

AD-A189 143

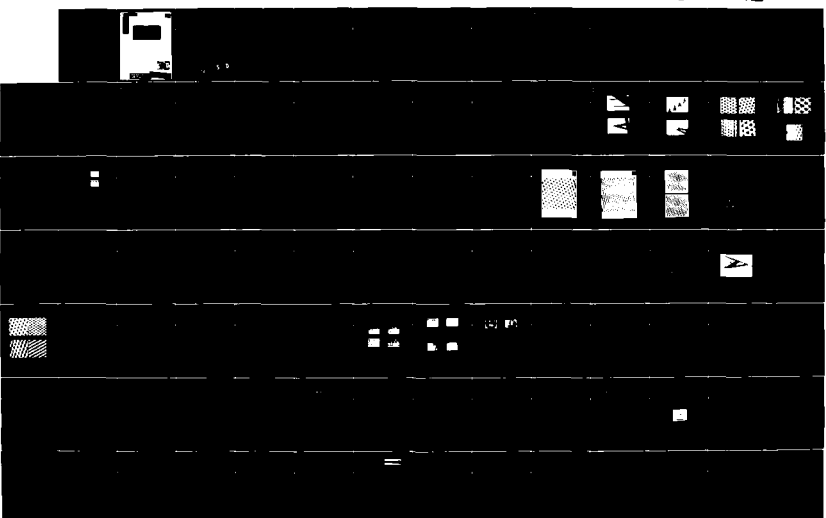
JOINT SERVICES ELECTRONICS PROGRAM APPENDIX(U) STANFORD 1/3
UNIV CA EDWARD L GINZTON LAB OF PHYSICS

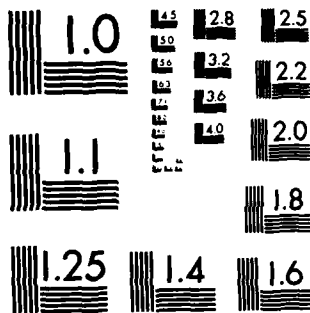
UNCLASSIFIED

D M BLOOM ET AL. 15 OCT 87 GL-4287 N00014-84-K-0327

F/G 9/1

ML





MICROCOPY RESOLUTION TEST CHART
NATIONAL BUREAU OF STANDARDS-1963-A

MC FILE COPY

(4)

AD-A189 143

Report Appendix

PUBLICATIONS CITING JSEP SPONSORSHIP

Joint Services Electronics Program

Contract N00014-84-K-0327

for the period ending

31 March 1987

Edward L. Ginzton Laboratory

OF THE

WW. HANSEN LABORATORIES OF PHYSICS

STANFORD UNIVERSITY, STANFORD, CALIFORNIA 94305



This document has been approved
for public release and makes its
distribution is unlimited.

87 12 8 014

4

Report Appendix

PUBLICATIONS CITING JSEP SPONSORSHIP

Joint Services Electronics Program

Contract N00014-84-K-0327

for the period ending

31 March 1987

Edward L. Ginzton Laboratory
Stanford University,
Stanford, California 94305



For the Faculty of the Edward L. Ginzton Laboratory
Professor S.E. Harris, Director

Accession For	
NTIS GRA&I	<input checked="" type="checkbox"/>
DTIC TAB	<input type="checkbox"/>
Unannounced	<input type="checkbox"/>
Justification	
By	
Distribution/	
Availability Codes	
Dist	Avail and/or Special

A-1

October 1987

This document has been approved
for public release and does not
contain recommendations or conclusions
of the DTIC.

DTIC
ELECTED
DEC 17 1987
S D
G E

87 12 8 014

JOINT SERVICES ELECTRONICS PROGRAM
Contract N00014-84-K-0327
Edward L. Ginzton Laboratory
STANFORD UNIVERSITY

TABLE OF CONTENTS

Publications Citing JSEP Sponsorship (Bibliographic Listing) 5

BOUND COPIES OF PUBLICATIONS CITING JSEP SPONSORSHIP

T.R. Albrecht and C.F. Quate	
Atomic Resolution with the Atomic Force Microscope.....	13
B.R. Hemenway, H.K. Heinrich, J.H. Goll, Z. Xu and D.M. Bloom	
Optical Detection of Charge Modulation in Silicon Integrated Circuits Using a Laser Diode Probe.....	27
J. Nogami, S. Park and C.F. Quate	
Observation of Dislocations in Graphite by Scanning Tunneling Microscopy (STM).....	31
T.R. Albrecht and C.F. Quate	
Atomic Resolution Imaging of a Nonconductor by Atomic Force Microscopy;.....	41
H.K. Heinrich	
A Noninvasive Optical Probe for Detecting Electrical Signals in Silicon Integrated Circuits.....	57
G.Q. Xiao and G.S. Kino	
A Real-Time Confocal Scanning Optical Microscope.....	59
B.L. Heffner	
A Switchable Fiber-Optic Tap Using the Acousto-Optic Bragg Interaction.....	67
B.Y. Kim and H.J. Shaw	
All-fiber-optic Gyroscopes.....	75
B.L. Heffner, W.P. Risk, B.T. Khuri-Yakub, and G.S. Kino	
Deposition of Piezoelectric Films on Single-Mode Fibers and Applications to Fiber Modulators.....	87
B.L. Heffner and G.S. Kino	
Switchable Fiber-Optic Tap Using Acoustic Transducers Deposited Upon the Fiber Surface.....	93

G.S. Kino, T.R. Corle, P.C.D. Hobbs and G.Q. Xiao	
Optical Sensors for Range and Depth Measurements;.....	97
D.P.E. Smith, A. Bryant, C.F. Quate, J.P. Rabe, Ch. Gerber, and J.D. Swalen	
Images of a Lipid Bilayer at Molecular Resolution by Scanning Tunneling Microscopy.....	107
H.K. Heinrich, B.R. Hemenway, K.A. McGrady, and D.M. Bloom	
Real Time Digital Signals in a Silicon Bipolar Junction Transistor Using a Noninvasive Optical Probe;...	111
A. Bryant., D.P.E. Smith, G. Binnig, W.A. Harrison and C.F. Quate	
Anomalous Distance Dependence in Scanning Tunneling Microscopy.....	113
J. Nightingale and R.L. Byer	
Monolithic Nd:YAG Fiber Laser.....	117
Kino, G.S. and B.T. Khuri-Yakub	
Optical Interactions with Solids;.....	121
B.L. Heffner, G.S. Kino, B.T. Khuri-Yakub and W.P. Risk	
Switchable Fiber-Optic Tap Using the Acousto-Optic Bragg Interaction.....	125
H.K. Heinrich, D.M. Bloom, and B.R. Hemenway	
Noninvasive Sheet Charge Density Probe for Integrated Silicon Devices;.....	129
B.L. Heffner and B.T. Khuri-Yakub	
Deposition of Oriented Zinc Oxide on an Optical Fiber;.....	135
G. Magel, D. Jundt, M. Fejer and R.L. Byer	
Low Loss Single-Crystal Sapphire Optical Fibers.....	137
B.H. Kolner and D.M. Bloom	
Electrooptic Sampling in GaAs Integrated Circuits;.....	143
J. Nightingale, and R.L. Byer	
A Guided Wave Monolithic Resonator Ruby Fiber Laser;.....	159
S.A. Elrod, A. Bryant, A.L. de Lozanne, S. Park, D. Smith and C.F. Quate	
Tunneling Microscopy from 300 to 4.2K;.....	165
M. Digonnet, M. Fejer and R.L. Byer	
Characterization of Proton Exchanged Waveguides in MgO:LiNbO ₃ ;.....	175

M. Fejer, G. Magel and R.L. Byer	
High Speed, High Resolution Fiber Diameter Measurement System.....	179
B.H. Kolner	
Picosecond Electro-Optic Sampling in Gallium Arsenide.....	185
B.L. Heffner, G.S. Kino and B.T. Khuri-Yakub	
7 GHz Acoustic Transmission through a Hertzian Contact.....	187
M. Fejer, J. Nightingale, G. Magel and R.L. Byer	
Laser Heated Miniature Pedestal Growth Apparatus for Single Crystal Optical Fibers.....	189
J.D. Kafka, B.H. Kolner, T.M. Baer and D.M. Bloom	
Compression of Pulses from a Continuous-wave Mode-Locked Nd:YAG Laser.....	195
B.H. Kolner and D.M. Bloom	
Direct Electrooptic Sampling of Transmission Line Signals Propagating on a GaAs Substrate.....	197
B.H. Kolner, J.D. Kafka, D.M. Bloom and T.M. Baer	
Compression of Mode-Locked Nd:YAG Pulses to 1.8 ps.....	199
M. Fejer, J. Nightingale, G. Magel and R.L. Byer	
Laser Assisted Growth of Optical Quality Crystal Fibers.....	205
S.W. Meeks and B.A. Auld	
Acoustic Wave Reflection from Ferroelastic Domain Walls.....	213
P.M. Fauchet, and A.E. Siegman	
Observations of higher-order laser induced surface ripples on (111) germanium.....	217
P.M. Fauchet and A.E. Siegman	
Evidence for a dense electron-hole plasma close to the melting phase transition in silicon.....	223
REPORT DOCUMENTATION PAGE (DD 1473).....	227

PUBLICATIONS CITING JSEP SPONSORSHIP

1 April 1984 through 30 September 1987

T.R. Albrecht and C.F. Quate, "Atomic Resolution with the Atomic Force Microscope," Proceedings of the STM '87, Second International Conference on Scanning Tunneling Microscopy, (September 1987), (To be published in the J. Vacuum Science and Technology A, March/April 1988).

* GL 4250: Supported by Joint Services Electronics Program on Contract N00014-84-K-0327 and the Advanced Research Projects Agency on Contract N00014-84-K-0624.

B.R. Hemenway, H.K. Heinrich, J.H. Goll, Z. Xu and D.M. Bloom, "Optical Detection of Charge Modulation in Silicon Integrated Circuits Using a Multimode Laser Diode Probe," IEEE Electron Device Letters, Vol. EDL-8, (8), (August 1987), 344-346.

GL 4215: Supported by Joint Services Electronics Program on Contract N00014-84-K-0327.

J. Nogami, S. Park and C.F. Quate, "Observation of Dislocations in Graphite by Scanning Tunneling Microscopy," Ginzton Laboratory Technical Report, (May 1987).

** GL 4199: Supported by Joint Services Electronics Program on Contract N00014-84-K-0327 and the Advanced Research Projects Agency on Contract N00014-84-K-0624.

T.R. Albrecht and C.F. Quate, "Atomic Resolution Imaging of a Nonconductor by Atomic Force Microscopy," Preprint, (May 1987), Submitted for publication in J. Appl. Phys..

* GL 4198: Supported by Joint Services Electronics Program on Contract N00014-84-K-0327 and the Advanced Research Projects Agency on Contract N00014-84-K-0624.

H.K. Heinrich, "A Noninvasive Optical Probe for Detecting Electrical Signals in Silicon Integrated Circuits," Dissertation, Stanford University, (April 1987).

** GL 4190: Supported by Joint Services Electronics Program on Contract N00014-84-K-0327.

* This material has been accepted for publication and will appear in the open literature as indicated above.

** This material is not in the open literature and copies are available only by contacting the author(s).

G.Q. Xiao and G.S. Kino, "A Real-Time Confocal Scanning Optical Microscope," Invited Paper, (March 1987), Presented at the 4th International Symposium on Optical and Optoelectronic Applied Science and Engineering, (March 30-April 3, 1987), The Hague, Netherlands.

* GL 4176: Supported by Joint Services Electronics Program on Contract N00014-84-K-0327.

B.L. Heffner, "A Switchable Fiber-Optic Tap Using the Acousto-Optic Bragg Interaction," Dissertation, Stanford University, (August 86)

** GL 4174: Supported by Joint Services Electronics Program on Contract N00014-84-K-0327.

B.Y. Kim and H.J. Shaw, "All-fiber-optic Gyroscopes," Invited paper, SPIE 10th Anniversary Conference, Fiber Optic Gyros, Vol. 719, (1986), 70-80.

GL 4121: Supported by Joint Services Electronics Program on Contract N00014-84-K-0327, the Air Force Office of Scientific Research and Litton Systems, Inc.

B.L. Heffner, W.P. Risk, B.T. Khuri-Yakub, and G.S. Kino "Deposition of Piezoelectric Films on Single-Mode Fibers and Applications to Fiber Modulators," Presented at the IEEE Ultrasonics Symposium, Williamsburg, Virginia (November 1986), Proceedings, 709-713.

GL 4112: Supported by Joint Services Electronics Program on Contract N00014-84-K-0327.

B.L. Heffner and G.S. Kino, "Switchable Fiber-Optic Tap Using Acoustic Transducers Deposited Upon the Fiber Surface," Optics Letters, Vol. 12, (March 1987), 208-210.

GL 4103: Supported by Joint Services Electronics Program on Contract N00014-84-K-0327.

G.S. Kino, T.R. Corle, P.C.D. Hobbs and G.Q. Xiao, "Optical Sensors for Range and Depth Measurements," Presented at ICALEO, Arlington, VA (November 1986). Preprint, October 1986.

GL 4060: Supported by Joint Services Electronics Program on Contract N00014-84-K-0327 and the Air Force Office of Scientific Research on Grant-84-0063B.

* This material has been accepted for publication and will appear in the open literature as indicated above.

** This material is not in the open literature and copies are available only by contacting the author(s).

D.P.E. Smith, A. Bryant, C.F. Quate, J.P. Rabe, Ch. Gerber, and J.D. Swalen, "Images of a Lipid Bilayer at Molecular Resolution by Scanning Tunneling Microscopy," Proc. Natl. Acad. Sci., Vol. 84, (February 1987), 969-972.

GL 4055: Supported by Joint Services Electronics Program on Contract N00014-84-K-0327 and the Advanced Research Projects Agency on Contract N00014-84-K-0624.

H.K. Heinrich, B.R. Hemenway, K.A. McGroddy, and D.M. Bloom, "Measurement of Real Time Digital Signals in a Silicon Bipolar Junction Transistor Using a Noninvasive Optical Probe," Electronics Letters, Vol. 22, (12), (June 1986), 650-652.

GL 4050: Supported by Joint Services Electronics Program on Contract N00014-84-K-0327.

A. Bryant., D.P.E. Smith, G. Binnig, W.A. Harrison and C.F. Quate, "Anomalous Distance Dependence in Scanning Tunneling Microscopy," Appl. Phys. Lett. Vol. 49, (October 1986), 936-938.

GL 4035: Supported by Joint Services Electronics Program on Contract N00014-84-K-0327 and the Advanced Research Projects Agency on Contract N00014-84-K-0624.

J. Nightingale and R.L. Byer, "Monolithic Nd:YAG Fiber Laser", Optics Letters, Vol. 11, (7), (July 1986), 437.

GL 4025: Supported by Joint Services Electronics Program on Contract N00014-84-K-0327, AFOSR on Contract F49620 85-C-0062 and NSF Grant DMR 83 16982

Kino, G.S. and B.T. Khuri-Yakub, "Optical Interactions with Solids," in the Twenty-fifth Annual Technical Report of the Center for Materials Research, Stanford University, (March 1986).

** GL 4012: Supported by Joint Services Electronics Program Contract N00014-84-K-0327, the Air Force Office of Scientific Research on Grant AFOSR-84-0638, Department Energy on Contract DOE DE-AT03-81ER10865, IBM Corporation on Contracts 607412 & 645416 and the Stanford Institute for Manufacturing and Automation.

** This material is not in the open literature and copies are available only by contacting the author(s).

B.L. Heffner, G.S. Kino, B.T. Khuri-Yakub and W.P. Risk, "Switchable Fiber-Optic Tap Using the Acousto-Optic Bragg Interaction," *Optics Letters*, Vol. 11, (July 1986), 476-478.

GL 4011: Supported by Joint Services Electronics Program on Contract N00014-84-K-0327.

H.K. Heinrich, D.M. Bloom, and B.R. Hemenway, "Noninvasive Sheet Charge Density Probe for Integrated Silicon Devices," *Appl. Phys. Lett.*, Vol. 48, (16), (April 1986), 1066-1068.

GL 4005: Supported by Joint Services Electronics Program on Contract N00014-84-K-0327.

B.L. Heffner and B.T. Khuri-Yakub, "Deposition of Oriented Zinc Oxide on an Optical Fiber," *Appl. Phys. Lett.*, Vol. 48, (21), (May 1986), 1422-1423.

GL 4003: Supported by Joint Services Electronics Program on Contract N00014-84-K-0327.

G. Magel, D. Jundt, M. Fejer and R.L. Byer, "Low Loss Single-Crystal Sapphire Optical Fibers", *Proceedings SPIE*, Vol. 618, (January 1986), 89-94.

GL 3998: Supported by Joint Services Electronics Program on Contract N00014-84-K-0327, AFOSR on Contract F49620 84-C-0062 and the Stanford Center for Materials Research

B.H. Kolner and D.M. Bloom, "Electrooptic Sampling in GaAs Integrated Circuits," Invited paper *IEEE J. Quantum Electron.* QE-22, (1), (January 1986), 79-83.

GL 4280: Supported by Joint Services Electronics Program on Contract N00014-84-K-0327 and the Air Force Office of Scientific Research, Air Force Systems Command, USAF on Grant AFOSR 87 0032

J. Nightingale, and R.L. Byer, "A Guided Wave Monolithic Resonator Ruby Fiber Laser", *Optics Commun.* Vol. 56, (1), (November 1985), 41-45.

GL 3914: Supported by Joint Services Electronics Program on Contract N00014-84-K-0327, the Air Force Office of Scientific Research, NSF Grant DMR 80 20248 and the Dept. of Energy on Lawrence Livermore Subcontract 8518101.

S.A. Elrod, A. Bryant, A.L. de Lozanne, S. Park, D. Smith and C.F. Quate, "Tunneling Microscopy from 300 to 4.2K," IBM J. Res. Develop., Vol. 30, (4), (July 1986), 387-395.

GL 3892: Supported by Joint Services Electronics Program on Contract N00014-84-K-0327, the Advanced Research Projects Agency on Contract N00014-84-K-0624, the Office of Naval Research on Contract N00014-84-K-0549 and the IBM Corporation on Contract 439514.

Bloom, D.M., R.L. Byer, G.S. Kino, C.F. Quate and S.E. Harris, "Annual Progress Report for Joint Services Electronics Program, Contract N00014-84-K-0327 for the period 1 April 1984 through 31 March 1985," Technical Report of the Ginzton Laboratory, Stanford University, (January 1986).

** GL 3891: Supported by Joint Services Electronics Program Contract N00014-84-K-0327.

M. Digonnet, M. Fejer and R.L. Byer, "Characterization of Proton Exchanged Waveguides in MgO:LiNbO₃," Optics Letters, Vol. 10, (5), (May 1985), 235-237.

GL 3849: Supported by Joint Services Electronics Program on Contract N00014-84-K-0327, the Air Force Office of Scientific Research and Litton Systems, Inc.

M. Fejer, G. Magel and R.L. Byer, "High Speed, High Resolution Fiber Diameter Measurement System," Applied Optics, Vol. 24, (15), (August 1985), 2362-2368.

GL 3839: Supported by Joint Services Electronics Program on Contract N00014-84-K-0327 and AFOSR on Contract F49620-84-C-0021.

B.H. Kolner, "Picosecond Electro-Optic Sampling in Gallium Arsenide," Dissertation, Stanford University, (August 1985).

GL 3912: Supported by Joint Services Electronics Program on Contract N00014-84-K-0327 and the Air Force Office of Scientific Research on Grant AFOSR 84-0139.

B.L. Heffner, G.S. Kino and B.T. Khuri-Yakub, "7 GHz Acoustic Transmission through a Hertzian Contact," Appl. Phys. Lett., Vol. 47, (1), (July 1985), 17-18.

GL 3838: Supported by Joint Services Electronics Program on Contract N00014-84-K-0327.

** This material is not in the open literature and copies are available only by contacting the author(s).

M. Fejer, J. Nightingale, G. Magel and R.L. Byer, "Laser Heated Miniature Pedestal Growth Apparatus for Single Crystal Optical Fibers, Rev. Sci. Instr. vol. 55, (November 1984), 1791-1796.

*** GL 3754: Supported by Joint Services Electronics Program on Contract N00014-75-C-0632, the Air Force Office of Scientific Research on Grant AFOSR-83-0193, Stanford Center for Materials Research and the Dept. of Energy Lawrence Livermore Subcontract 8518101.

J.D. Kafka, B.H. Kolner, T.M. Baer and D.M. Bloom, "Compression of Pulses from a Continuous-wave Mode-Locked Nd:YAG Laser," Opt. Lett. Vol. 9, (11), (November 1984), 505-506.

GL 4281: Supported by Joint Services Electronics Program on Contract N00014-84-K-0327.

B.H. Kolner and D.M. Bloom, "Direct Electrooptic Sampling of Transmission Line Signals Propagating on a GaAs Substrate," Elect. Lett. Vol. 20, (20), (September 1984), 818-819.

GL 4282: Supported by Joint Services Electronics Program Contract N00014-84-K-0327.

B.H. Kolner, J.D. Kafka, D.M. Bloom and T.M. Baer, "Compression of Mode-Locked Nd:YAG Pulses to 1.8 ps," in Proceedings of the Topical Meeting on Ultrafast Phenomena IV, D.H. Auston and K.B. Eisenthal, eds., 19-22 (New York: Spring-Verlag, June 1984).

GL 4283: Supported by Joint Services Electronics Program on Contract N00014-84-K-0327.

M. Fejer, J. Nightingale, G. Magel and R.L. Byer "Laser Assisted Growth of Optical Quality Crystal Fibers," SPIE Proceedings, Vol. 460, (Processing of Guided Wave Optoelectric Materials), (January 1984), 26-32.

*** GL 3697: Supported by Joint Services Electronics Program on Contract N00014-75-C-0632, the Air Force Office of Scientific Research on Grant AFOSR 83 0193 and Stanford Center for Materials Research.

S.W. Meeks and B.A. Auld, "Acoustic Wave Reflection from Ferroelastic Domain Walls," Proceedings IEEE 1983 Ultrasonics Symposium, (October 31 - November 2, 1983), 535-538.

*** GL 3649: Supported by Joint Services Electronics Program on Contract N00014-75-C-0632 and NSF MRL Grant Stanford Center for Materials Research.

P.M. Fauchet, and A.E. Siegman, "Observations of higher-order laser induced surface ripples on (111) germanium," *Appl. Phys. A*, Vol. 32, (1983), 135-140.

*** GL 3638: Supported by Joint Services Electronics Program on Contract N00014-75-C-0632 and the Air Force Office of Scientific Research on Contract F49620 82-K-0015

P.M. Fauchet and A.E. Siegman, "Evidence for a dense electron-hole plasma close to the melting phase transition in silicon," *Appl. Phys. Lett.*, Vol. 43, (December 1983), 1043-1045.

*** GL 3625: Supported by Joint Services Electronics Program on Contract N00014-75-C-0632 and Air Force Office of Scientific Research

*** These publications cite the predecessor JSEP Contract, but reprints were not available at the time that the Final Report was prepared, and they are therefore included here for completeness.

ATOMIC RESOLUTION WITH THE ATOMIC FORCE MICROSCOPE ON CONDUCTORS AND NONCONDUCTORS

Thomas R. Albrecht and Calvin F. Quate

Dept. of Applied Physics, Stanford University, Stanford, California 94305

ABSTRACT

The Atomic Force Microscope (AFM) has achieved atomic resolution on nonconducting as well as electrically conducting surfaces, opening a new class of materials to atomically resolved surface imaging. Images of boron nitride (a nonconductor) reveal that AFM can distinguish different atomic species. AFM images of molybdenum disulfide and graphite are also presented. Graphite AFM images appear identical to images obtained by scanning tunneling microscopy (STM), although AFM and STM probably respond to different atomic sites on the graphite surface. Microfabrication procedures for constructing low mass force-sensing cantilevers are discussed.

Proceedings of STM'87, the Second International Conference on
Scanning Tunneling Microscopy. To be published in the
Journal of Vacuum Science and Technology A, March/April 1988

I. INTRODUCTION

Atomic force microscopy (AFM)¹ has been introduced as a new technique for obtaining high resolution images of force contours near the surfaces of solids. Since its invention in 1985, AFM has been used to study attractive Van der Waals forces,¹⁻³ repulsive contact forces,⁴⁻⁶ lateral friction forces,⁷ and magnetic forces.^{8,9} One interesting application of AFM is atomic scale imaging of surface topography via force interactions, with resolution comparable to that obtained by scanning tunneling microscopy (STM).^{10,11} Unlike STM, however, AFM is not restricted to studying electrically conducting materials. Recent work has demonstrated that AFM can achieve atomic resolution on both conducting^{4,6} and nonconducting^{5,6} surfaces. Like STM, AFM can be used in air or at liquid/solid interfaces⁶ and should prove useful for low temperature measurements and for ultrahigh vacuum surface studies. This paper discusses atomic resolution imaging of surface topography on conducting and nonconducting surfaces in air by mapping repulsive contact forces with the AFM.

II. FABRICATION OF FORCE-SENSING MICROCANILEVERS

Force measurements are made in the AFM by monitoring the deflection of a flexible element (usually a cantilever) in response to the interaction force. Because of the magnitude of the forces involved, the cantilever should have a small force constant (10^{-2} - 10^2 N/m) in order to obtain a measurable response. In addition, a high mechanical resonance frequency is advantageous, since the imaging rate is limited by the speed of response of the cantilever. In our AFM, these requirements are met by using microfabrication techniques¹² to construct thin film SiO₂ microcantilevers with very low mass. The fabrication procedure is shown in Fig. 1. A thin film (1.5 μ m thick) of SiO₂ is thermally grown on both sides of a (100) Si wafer. Using photolithographic techniques, rectangular openings are etched in the oxide on both sides of the wafer. The orientation and size of the openings are chosen so that their edges define a volume of the wafer

bounded by (111) planes. A strip of oxide, which will serve as the cantilever, is left protruding into one of the openings. An anisotropic Si etchant is used to remove the exposed silicon. Because of the anisotropic nature of the etchant, the etching stops when the entire volume of Si removed is bound by (111) planes, which results in the geometry shown in Fig. 1(b), with the cantilever freely suspended over a hole through the wafer. One side of the lever is coated with a thin metal film and a small section of the wafer is cut out for positioning the lever in the AFM. Two types of levers fabricated by this procedure are shown in Fig. 2. Ideally the cantilever should have a sharp (perhaps single atom) point in order to restrict the interaction with the sample to a very small area. For the levers shown in Fig. 2, this is accomplished by tilting the levers so that only one corner comes into contact with the sample. The V-shaped cantilever shown in Fig. 2(b) provides a sharper corner than the rectangular style, and the additional rigidity of the V-shaped lever reduces lateral bending of the lever in response to frictional forces which are present when scanning over the sample. One difficulty in achieving atomic resolution with the AFM is obtaining a sufficiently sharp point on the cantilever. Only 25-50% of the levers of the types shown in Fig. 2 are usable for atomic resolution imaging. Fig. 3 shows two possible methods for forming sharp tips on cantilevers. Small sharp cones [Fig. 3(a)] grown by an evaporation technique¹³ can be formed on the ends of cantilevers. As an alternative method, diamond fragments [Fig. 3(b)] have been successfully attached to cantilevers with promising results.¹⁴

III. EXPERIMENTAL PROCEDURE

There are several modes for operating the AFM, depending on the nature of the forces involved. Deflection of the force-sensing cantilever can be measured by tunneling between the lever and a second electrode,^{1,4,5,6,9} by optical interferometry^{2,3,7,8} or by capacitive techniques.⁷ In our AFM, deflection is measured by tunneling between an electrochemically etched tungsten tip and a gold film on the back of the lever. The lever is mounted on a fixed support, and the sample and tunneling tip are brought into position

with separate mechanical approach systems. Both the tip and sample are mounted on piezoelectric tubes¹⁵ which control the X-Y scanning of the sample and the Z motion of the sample and tunneling tip. Each experiment begins by establishing a stable tunneling current between the cantilever and tunneling tip. The sample is then brought into contact with a corner of the cantilever and moved in further until the desired deflection (i.e., force) is obtained. Forces in the 10^{-8} - 10^{-7} N range were found to be satisfactory for atomic resolution. A feedback system with fast response can be used to keep the lever deflection constant while scanning (the "constant force" mode) or, if a slow feedback response is used, the average lever deflection can be held constant (the "variable deflection" mode). Because the lever remains in contact with the sample at all times, neither mode of operation can prevent lateral bumping on rough surfaces, an advantage which is realized in the "constant current" mode of STM operation. The variable deflection mode for the AFM is well suited to high speed imaging of relatively flat surfaces, since the feedback system only needs to respond rapidly enough to keep the tunneling tip and cantilever within tunneling range. When this mode is used, topographic information is obtained from rapid variations in the tunneling current as the lever deflection changes in response to surface corrugations while scanning. Our AFM uses a sinusoidal 2 kHz X scan and a 20 Hz triangle Y scan, producing real time images.

IV. ATOMIC RESOLUTION IMAGES

Fig. 4 shows four atomic resolution images of the (0001) surface of highly oriented pyrolytic graphite (HOPG). The largest corrugations observed on HOPG were approximately 0.15 Å in amplitude, which was calculated from the modulation of the tunneling current in the variable deflection mode. The surface of graphite is composed of carbon atoms occupying inequivalent A and B sites in a hexagonal array. Batra and Ciraci¹⁶ have shown that the AFM probably responds to A atoms on graphite, unlike STM which shows a greater response to B atoms. It is also important to note that the AFM responds to the total charge density in the contact region, unlike the STM which responds

only to charge density near the Fermi level. An ideal AFM image of graphite should show a dominant array of protrusions (assumed to be at the A sites) with 2.46 Å periodicity, similar to Fig. 4(a). The other images shown in Fig. 4 are probably caused by variations in the quality of the lever/sample contact area which can result in simultaneous imaging from multiple contact points. Mizes *et al.*¹⁷ have shown that such images differ from one another only in the relative amplitudes and phases of three dominant spatial Fourier components (with 2.46 Å period) which can be explained in terms of anisotropic responses caused by multiple point imaging. Therefore it is likely that all of the images in Fig. 4 show an appreciable response only to A atoms, unlike earlier interpretations⁴⁻⁶ which suggest that images similar to Fig. 4(c) show all six atoms per hexagon.

Figs. 5(a) and (b) are images of semiconducting 2H-MoS₂, a layered transition metal dichalcogenide. MoS₂ is easily cleaved in air, providing atomically flat surfaces composed of a close packed array of sulfur atoms with a 3.1604 Å lattice spacing.¹⁸ This material has previously been imaged by STM,^{19,20} but difficulties arise due to its highly anisotropic electrical conductivity.¹⁸ MoS₂, however, can be imaged as easily as graphite with the AFM, and its availability, ease of preparation, and large lattice constant make it a good candidate for initial evaluations of the performance of an AFM. The unusual shape of the protrusions seen in Fig. 5 is not well understood, but may be due to the properties of the lever/sample contact or some anisotropy in the material. Surface corrugations of 0.1-0.2 Å were observed on MoS₂ in the variable deflection mode.

Fig. 5(c) is an image of highly oriented pyrolytic boron nitride (HOPBN),²¹ an electrically insulating material which could not be imaged by STM. Similar to HOPG, HOPBN is a hexagonal layered material with a lattice constant of 2.504 Å. Adjacent sites in the plane are occupied alternately by boron and nitrogen atoms and the layers are stacked in direct registry (unlike graphite) with a boron atom above and below each nitrogen atom. The observed corrugation amplitude was 0.05 Å. The inequivalent atomic species are clearly differentiated by the AFM, with only one species appearing as dominant protrusions. A simple calculation⁵ suggested that the protrusions may be

attributed to nitrogen atoms on the surface, but a more extensive analysis is needed before a well established conclusion can be drawn. Difficulties arise in interpreting the images, since it is unknown whether the lever/sample force is confined to a single pair of atoms or distributed over a larger area, and the lever/sample interaction may cause appreciable perturbation of the charge density on the surface being studied. In addition, the extent and effects of any contamination present on the sample or lever in air are not well understood.

Future progress in AFM may make possible the routine imaging of nonconducting surfaces with atomic resolution. In particular, it may be possible to study biological and organic materials in liquid or air environments, which are often less destructive to these materials than the vacuum environments commonly encountered in SEM and TEM studies. Improvements in the construction of force-sensing cantilevers are expected to facilitate the application of AFM to a wide variety of studies.

ACKNOWLEDGEMENTS

We wish to thank G. Binnig and Ch. Gerber, who cooperated with us in our AFM work. We are also pleased to acknowledge fruitful discussions with I. Batra, W. Harrison, P. Hansma, O. Marti, H. Mizes, and D. Smith. The HOPBN and HOPG samples were provided by A. Moore of Union Carbide. This work was supported by the Joint Services Electronics Program, the Defense Advanced Research Projects Agency, and a National Science Foundation Graduate Fellowship.

REFERENCES

1. G. Binnig, C. F. Quate, and Ch. Gerber, *Phys. Rev. Lett.* **56**, 930 (1986).
2. Y. Martin, C. C. Williams, and H. K. Wickramasinghe, *J. Appl. Phys.* **61**, 4723 (1987).
3. G. M. McClelland, R. Erlandsson, and S. Chiang, *Rev. Prog. Quantit. Non-Destruct. Eval.* (Plenum, New York), Vol. 6 (to be published).
4. G. Binnig, Ch. Gerber, E. Stoll, T. R. Albrecht, and C. F. Quate, *Europhys. Lett.* **3**, 1281 (1987).
5. T. R. Albrecht and C. F. Quate, *J. Appl. Phys.* (to be published).
6. O. Marti, B. Drake, and P. K. Hansma, *Appl. Phys. Lett.* (to be published).
7. C. M. Mate, R. Erlandsson, G. M. McClelland, and S. Chiang, these proceedings.
8. Y. Martin and H. K. Wickramasinghe, *Appl. Phys. Lett.* **50**, 1455 (1987).
9. J. J. Sáenz, N. García, P. Grüter, E. Meyer, H. Heinzelmann, R. Wiesendanger, L. Rosenthaler, H. R. Hidber, and H. J. Güntherodt, *Appl. Phys. Lett.* (to be published).
10. P. K. Hansma and J. Tersoff, *J. Appl. Phys.* **61**, R1 (1987).
11. C. F. Quate, *Physics Today* **39**(8), 26 (1986).
12. K. E. Petersen, *Proc. IEEE* **70**, 420 (1982).
13. C. A. Spindt, I. Brodie, L. Humphrey, and E. R. Westerberg, *J. Appl. Phys.* **47**, 5248 (1976).
14. P. K. Hansma and O. Marti, private communication.
15. G. Binnig and D. P. E. Smith, *Rev. Sci. Instrum.* **57**, 1688 (1986).
16. I. P. Batra and S. Ciraci, these proceedings.
17. H. A. Mizes, S. Park, and W. A. Harrison, *Phys. Rev. B* (to be published).
18. J. A. Wilson and A. D. Yoffe, *Adv. Phys.* **18**, 193 (1969).
19. M. Weimer, J. Kramer, C. Bai, J. D. Baldeschwieler, and W. J. Kaiser, these proceedings.
20. T. R. Albrecht, unpublished.
21. A. W. Moore, *Nature* **221**, 1133 (1969).

CAPTIONS

FIG. 1. Fabrication of rectangular microcantilevers. Rectangular openings (a) are etched in an oxide film on both sides of a (100) Si wafer, leaving a thin strip of oxide intact. Anisotropic Si etching (b) removes a portion of the Si under the oxide strip, leaving it freely suspended as a cantilever. After metallization, which causes slight curvature of the lever, a small piece (c) of the wafer is cut out for mounting the lever in the AFM.

FIG. 2. SEM micrographs of force-sensing microcantilevers. The levers protrude from the edge of a silicon chip (right). When mounted in the AFM the top side contacts the sample at one corner and the bottom side is coated with a thin film of gold which serves as an electrode for the tunneling current. The longer rectangular lever shown in (a) is 180 μm long, 20 μm wide, and 1.5 μm thick; its force constant is calculated to be 0.16 N/m with a resonant frequency of 38 kHz. Each leg of the V-shaped lever shown in (b) is 100 μm long, 23 μm wide, and 1.5 μm thick, with a force constant of 2 N/m and a resonant frequency of 100 kHz.

FIG. 3. Two methods for forming sharp points on the ends of microcantilevers. Miniature cones (a) could be grown on levers by evaporation of material through a small hole. Diamond fragments (b) can be attached to levers with a small amount of glue.

FIG. 4. Grayscale images of graphite obtained with the AFM. The largest corrugation observed was 0.15 Å in amplitude. Several image variations including (a) round protrusions, (b) elliptical protrusions, (c) a hexagonal "honeycomb", and (d) triangular protrusions are seen. Such variations may be caused by simultaneous imaging with multiple contact points.

FIG. 5. AFM images of a semiconductor and a nonconductor. Sulfur atoms on the

cleaved surface of 2H-MoS₂ (a) appear as an array of protrusions. A greater magnification (b) of the same material reveals that the protrusions are anisotropic. Boron nitride (c) is a nonconductor and therefore could not be imaged by STM.

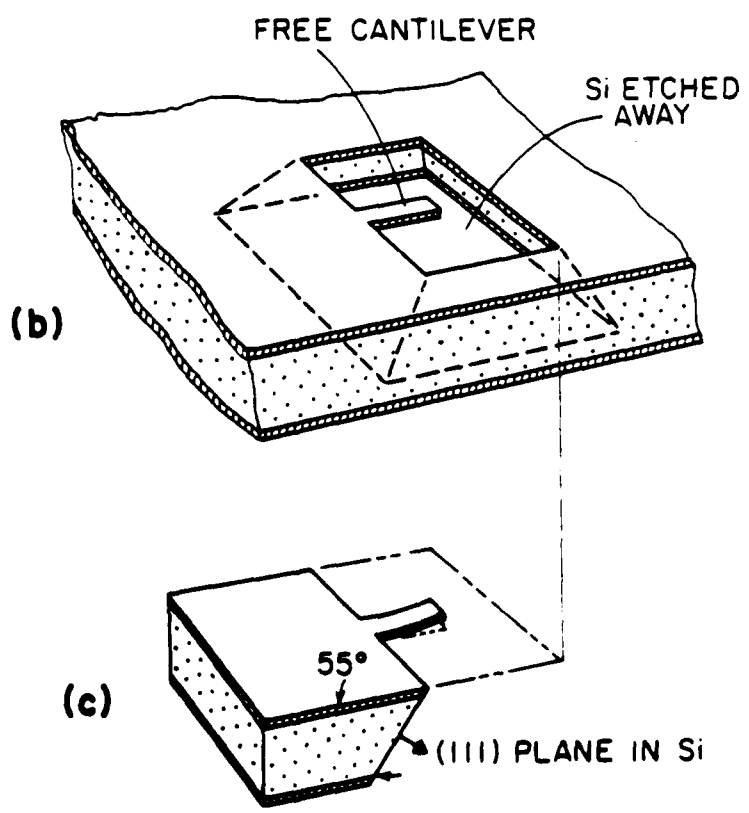
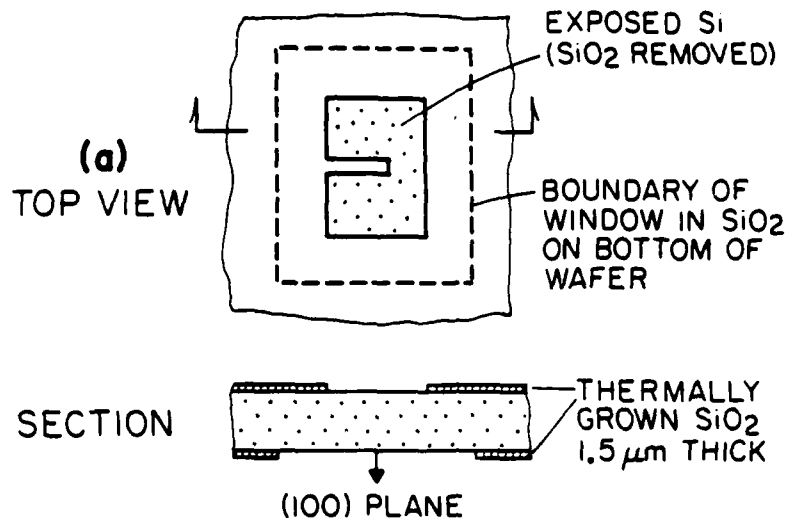
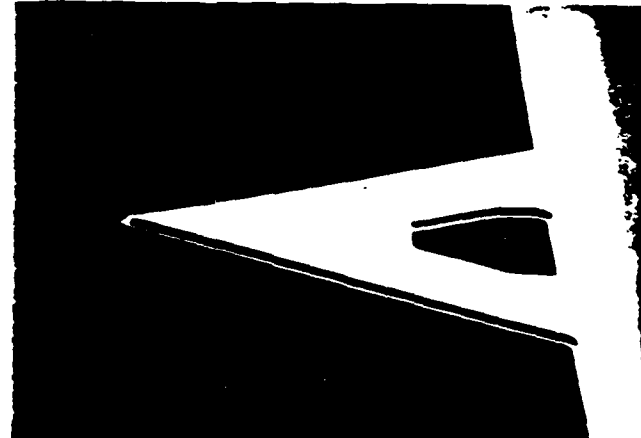


FIG. 1

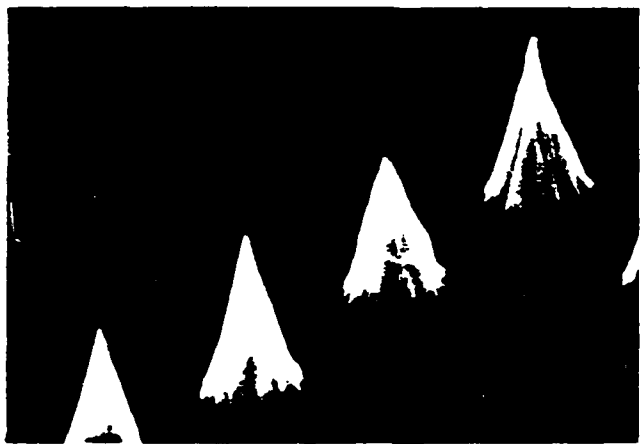


(a) $\longleftrightarrow 200 \mu \longrightarrow$



(b) $\longleftrightarrow 100 \mu \longrightarrow$

FIG. 2



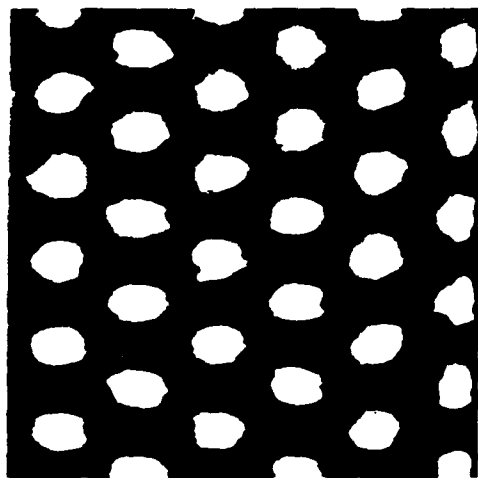
(a) $\longleftrightarrow 10 \mu \rightarrow$



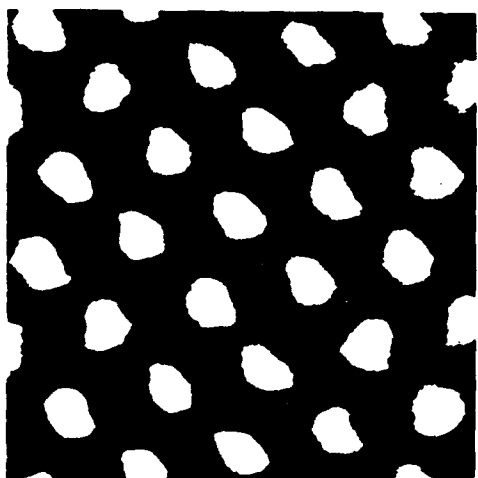
(b) $\longleftrightarrow 100 \mu \rightarrow$

FIG. 3

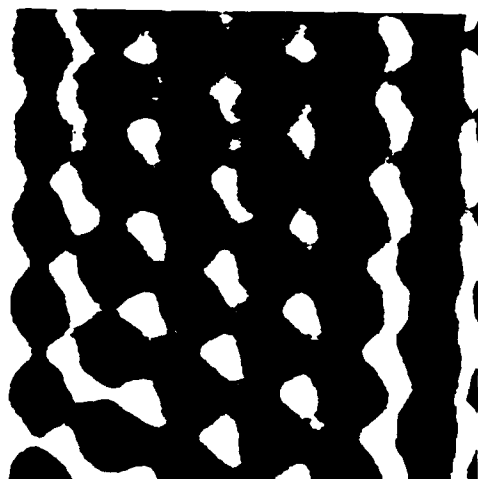
graphite



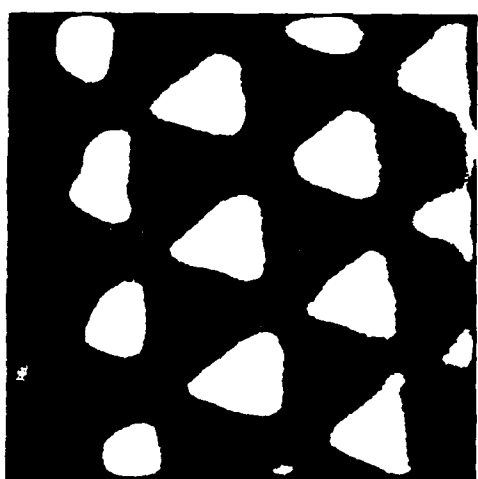
(a) $\longleftrightarrow 10 \text{ \AA} \longrightarrow$



(b) $\longleftrightarrow 10 \text{ \AA} \longrightarrow$



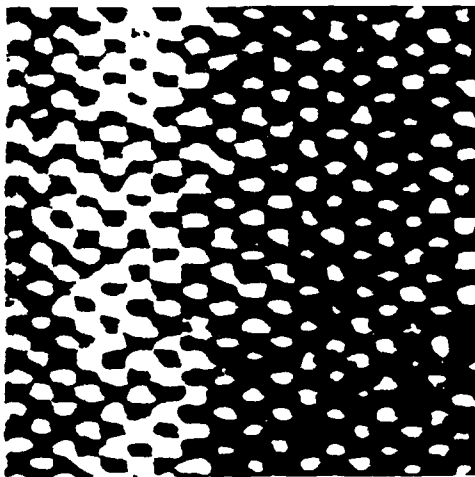
(c) $\longleftrightarrow 10 \text{ \AA} \longrightarrow$



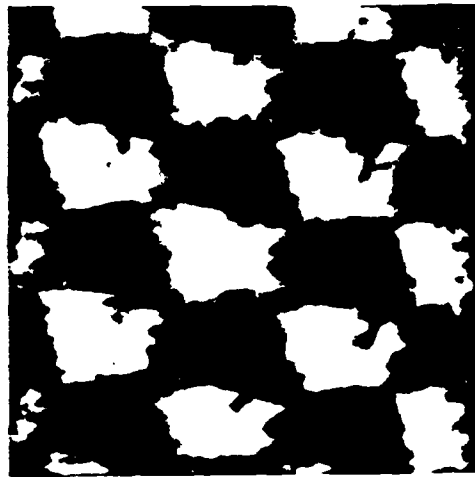
(d) $\longleftrightarrow 5 \text{ \AA} \longrightarrow$

FIG 4

molybdenum disulfide

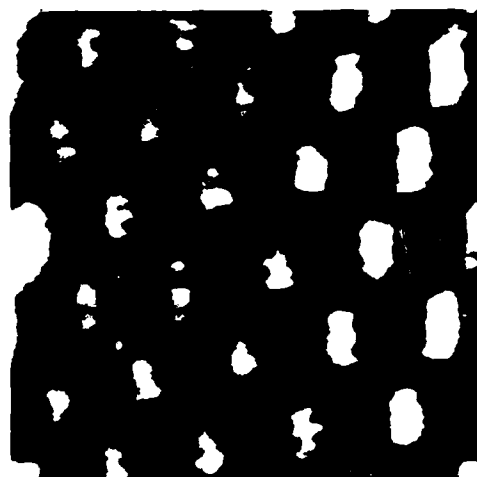


(a) $\blacktriangleleft 20 \text{ \AA} \blacktriangleright$



(b) $\blacktriangleleft 5 \text{ \AA} \blacktriangleright$

boron nitride



(c) $\blacktriangleleft 10 \text{ \AA} \blacktriangleright$

FIG 5

Optical Detection of Charge Modulation in Silicon Integrated Circuits Using a Multimode Laser-Diode Probe

B. R. HEMENWAY, H. K. HEINRICH, J. H. GOLL, Z. XU, AND DAVID M. BLOOM, FELLOW, IEEE

Abstract—This paper reports on the detection of sheet charge densities in silicon devices using an improved noninvasive optical probe based on the detection of free-carrier optical dispersion using a multilongitudinal-mode 1.3- μ m semiconductor laser. The improved system incorporates a differential detection technique and a Wollaston prism that allows the use of the multimode laser. These changes increase stability, sensitivity, and bandwidth, allow near shot-noise limited operation, reduce required optical power, and simplify the apparatus. The technique can be applied to probe electronic signals or, conversely, to modulate light using controlled electronic signals. Simple demonstrations of each application are presented.

WHILE the operation of standard semiconductor devices is well understood on the basis of highly developed models, corroborative experimental techniques that directly access the internal parts of the devices have not been available. Such techniques are especially appealing in the development of complex high-performance devices such as resonant tunneling diodes and quantum-well devices, where our understanding of the device physics is less mature. Also, noninvasive access to internal nodes within integrated circuits can help determine logic states, signal levels, and investigate latch-up, heating, and other problems. Recently [1], [2], we reported an optical probe which, working on the principle of free-carrier optical dispersion in semiconductors, provides information not available at the device terminals and thus makes new kinds of tests possible. This letter describes improvements made to the optical probe and demonstrates the detection of single-shot 25-Mbit/s modulation of sheet charge densities in a bipolar transistor. We now use a multimode 1.3- μ m semiconductor laser, and have increased sensitivity, stability, and noise performance. A second application—using electronic signals applied to the silicon to modulate light—has been identified. This is illustrated by an optical modulator based on a planar silicon n-p-n transistor. We observed a peak-to-peak amplitude modulation index of 9.8 percent at 25 Mbit/s with signal-to-noise ratio exceeding 6:1.

The improved optical probe is depicted in Fig. 1. New elements include a multilongitudinal-mode 1.3- μ m InGaAsP laser, a quartz Wollaston prism, coated high numerical aperture lenses, and two photodiodes for differential detection

Manuscript received March 24, 1987; revised May 21, 1987. This work was supported by the Joint Services Electronics Program under Contract N00014-84-k-0327.

The authors are with the Ginzton Laboratory, Stanford University, Stanford, CA 94305
IEEE Log Number 8715905.

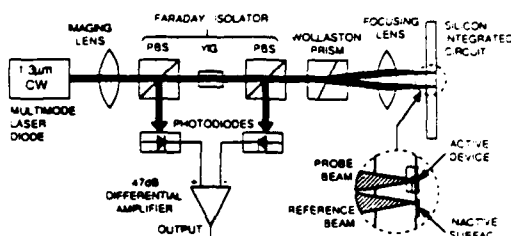


Fig. 1. Schematic diagram of improved charge-sensing optical system, with multimode laser, Wollaston prism, and differential detection

of the polarized optical beams. The Wollaston prism separates the incoming beam into two orthogonally polarized beams, with a divergence angle of 3.8 mrad. The relative phase shift between the two beams is adjusted by translation of the prism to a point of maximum sensitivity. Optimum sensitivity is achieved when, in the absence of a signal applied to the silicon device, the light returning to the Faraday isolator in Fig. 1 is circularly polarized. For a given laser mode, this is achieved when the relative phase shift induced by a round trip through the Wollaston prism and test wafer is an odd multiple of $\pi/2$. With multimode lasers, it is not possible to meet this condition simultaneously for all modes. However, when the relative phase shift for one mode is $\pi/2$ or a small odd multiple of $\pi/2$, the optimum bias condition can be met to good approximation for all modes. This can also be understood by noting that the path difference for the two beams should be short compared to the laser coherence length.

The "probe" beam is focused to a 3- μ m spot in a device area where the time-varying charge density modulates the phase of the beam by free-carrier dispersion. The "reference" beam is focused 30 μ m away, onto an inactive area where there is no modulation of the beam. Both beams reflect from the front surface and return through the substrate. The reflective surface of the wafer need not be metallized, but the back surface must be polished. The beams are recombined in the Wollaston prism. The relative phase shift induced by the charge in the silicon device results in elliptical polarization in the recombined beams. (That is, there is a deviation from the circular polarization with no signal on the silicon device.) This polarization modulation is converted to amplitude modulation by the polarizing beam splitters in the Faraday isolator. The detected signals at the two photodiodes are 180° out of phase.

The net relative phase shift of the two beams is found by integrating the local refractive index along their paths. The change in refractive index due to free-carrier dispersion is given by

$$\Delta n = -\frac{n_0 q^2 \lambda_0^2}{8 \pi^2 c^2 \epsilon_r} \left[\frac{N_e}{m_e^*} + \frac{N_h}{m_h^*} \right]$$

where q is the electronic charge, λ_0 is the vacuum wavelength, n_0 is the refractive index, ϵ_r is the material permittivity, N_e and N_h are the local time-dependent free electron and hole concentrations, and m_e^* and m_h^* are the carrier effective masses. The change Δn causes a modulation of the nominally circular polarization in the return beam and generates in the photodetectors two signals that are 180° out of phase. The signals pass through separate 46-dB gain 1-200-MHz low-noise amplifiers and are combined in a differential amplifier with 1-dB gain. Common-mode noise is virtually eliminated by this differential detection scheme.

Improvements in the probe performance are substantial. The Wollaston prism allows the use of a multimode laser diode. With a single wedge [2], static birefringence leads to a differential path delay between the two beams and mode partition noise from the laser renders the system useless. The Wollaston prism equalizes the path lengths and allows the use of a multimode laser. (The previous system used a Nd:YAG or a single-longitudinal-mode semiconductor laser.) The new system is much less sensitive to mode fluctuations giving a received signal that is more stable and depends to first order only on laser intensity. Differential detection has virtually doubled the signal voltage with only a 1.3-dB increase in the noise. Sensitivity to intensity noise in the laser is also greatly reduced. Finally, the coated lenses increase optical efficiency. The system noise floor can now be adjusted to within 2 dB of the Johnson noise limit, which in our system is about 7 dB above the shot-noise limit. The system exhibits some additional laser-induced noise caused by variations in temperature and optical feedback. A better isolator and temperature control should minimize this problem.

Modulation efficiency in this system is high enough to suggest that data communication could be accomplished using an on-chip silicon modulator. This was demonstrated using a planar silicon n-p-n transistor. We injected a 25-Mbit/s digital RZ data stream into the base of a common-emitter transistor circuit. The emitter area was $11 \times 11 \mu\text{m}^2$ and peak current was 130 mA. The applied base voltage is the lower trace in Fig. 2. The upper trace is the received optical signal after amplification without equalization when the probe beam was positioned in the base. The modulation index is 9.8 percent peak to peak relative to the static light level with a signal-to-noise ratio exceeding 6:1.

The baseline wander seen in Fig. 2 could cause timing or data errors in the receiver. This is caused by the 1-MHz low-end cutoff in the amplifier and also by heating; modulation of current changes the temperature profile near the beams and therefore the index of refraction. The dynamic response of this thermal modulation causes a frequency-dependent difference in the phase of the two beams. This appears in the received signal. The effect can be minimized by bringing the beams



Fig. 2. Lower trace: Real-time voltage signal input to base of transistor. Upper trace: Response of system at output of differential amplifier. Horizontal scale is 50 ns/div.

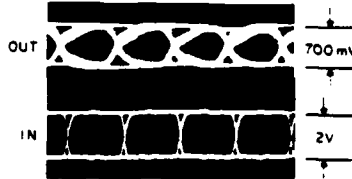


Fig. 3. Lower trace: Eye diagram of pseudorandom Manchester-coded bit stream input to base of transistor. Upper trace: Eye diagram of received optical signal. Horizontal scale is 20 ns/div.

closer together, placing them in approximately the same thermal environment. A computer model of the effect shows that, for our configuration, the thermal contribution to the observed signal is large at dc but has a corner frequency at approximately 1 MHz and then rolls off at 30 dB/decade. The thermal effect is therefore expected to be negligible at higher frequencies. This behavior is verified by experiment. However, in a different context, one may wish to use this dc sensitivity to examine remotely the temperature profile in an active integrated circuit.

Despite the thermal effect, one can use silicon as an efficient broad-band optoelectronic modulator by appropriately coding the input data stream. Manchester coding at clock rates above 5 MHz effectively eliminates the thermal effect because of the negligible spectral content of the data stream at frequencies where heating is important. The penalty is a maximum data rate reduced by half. Fig. 3 is the eye diagram of a pseudorandom optical Manchester-coded bit stream injected into the base at 25 Mbit/s using the same configuration as for Fig. 2. The lower trace is the input eye diagram, and the upper trace is the received eye diagram. The received eye is open, with a signal-to-noise ratio of greater than 6:1, indicating an expected bit error rate of less than 10^{-9} . The associated modulation index in this planar structure is 9.8 percent. (Modulation depth for 0.8-V ECL signals in the base is typically 3-4 percent.)

This experiment suggests that optical data communication could be implemented using on-chip modulators based on the plasma optical effect. Practical systems would likely require higher data rates and monolithic optical implementation. We are currently developing new monolithic device structures that do not require external optics to achieve intensity modulation and that can operate at higher data rates. In addition, all semiconductors exhibit free-carrier optical dispersion to some degree. For example, in GaAs the small values of the effective masses and relatively large bandgap suggest that the effect will

be easily seen, if care is taken to account for the electrooptic effect.

In summary, refinements to the charge-sensing optical probe system now allow the use of a multimode 1.3- μ m semiconductor laser. Differential detection increases the signal-to-noise ratio. We show that a planar silicon bipolar transistor can be used as an optical modulator using free-carrier dispersion and demonstrate a communications channel at 25 Mbit/s with a signal-to-noise ratio of 6:1 and a modulation index of 9.8 percent. We believe these improvements will lead to new methods in the testing of VLSI circuits and in the use of free-carrier dispersion for silicon optical modulators.

ACKNOWLEDGMENT

The authors wish to acknowledge M. Rodwell and R. Marsland for technical assistance.

REFERENCES

- [1] H. K. Heinrich, B. R. Hemenway, K. A. McGroddy, and D. M. Bloom, "Measurement of real-time digital signals in a silicon bipolar junction transistor using a noninvasive optical probe," *Electron Lett.*, vol. 22, no. 12, pp. 650-652, 1986
- [2] H. K. Heinrich, D. M. Bloom, and B. R. Hemenway, "Noninvasive sheet charge density probe for integrated silicon devices," *Appl. Phys. Lett.*, vol. 48, no. 16, pp. 1066-1068, Apr. 21, 1986; also "Erratum," *vol. 48, no. 26, p. 1811, June 30, 1986*

May 20, 1987

Observation of Dislocations in Graphite by Scanning Tunneling Microscopy

J. Nogami, Sang-il Park, and C.F. Quate
Ginzton Laboratory, Stanford University, Stanford CA 94305
and
A.W. Moore
Union Carbide Corporation, Parma Technical Centre, Parma OH 44130

Graphite is an attractive object for study by scanning tunneling microscopy (STM) since large areas of atomically flat surface are easily prepared by cleaving. These surfaces are relatively inert and have been imaged with STM in air[1], water[2], and vacuum[3]. The in-plane lattice spacing of 2.46 Å is easily resolved with this technique. We have observed networks of dislocations at the surface of graphite on a scale much finer than that previously seen by TEM studies. The width of the individual dislocations is less than 10 Å. Moreover, the dislocations outline hexagonal domains that are typically less than 25 Å across.

These domains were observed at room temperature on isolated areas of pyrolytic graphite that had been annealed at 3400 °C during preparation. These samples were being characterized as an alternate substrate to the more commonly studied highly oriented pyrolytic graphite (HOPG). To the naked eye, the sample surface was pebbled in appearance, with shiny convex areas of several square millimeters bounded by sharp lines where the surface was kinked. X-Ray measurements showed that the FWHM of the c-axis orientation distribution was 5°. (Less than 1° is typical of HOPG. [4]) On the submicron scale accessible to the STM, the great majority of the surface was atomically flat, and was a perfect single crystal over areas much larger than 100 Å square. There were occasional areas of unstable tunneling current that might be due to either gross structural defects on the surface or to surface contamination. It was not possible to say whether such areas occurred more frequently than on HOPG samples.

The images were taken in air with an instrument that has been described previously. [1] The tip to sample bias was 10 mV and the feedback maintained an average tunneling current of 5 nA. The images presented here were taken with a relatively high scanning rate in the variable current mode [1,5] to improve the signal to noise ratio. Constant current topographs were also taken to verify that there were no significant vertical corrugations of the surface at a dislocation.

Figure 1 shows an image of a defect-free area of the graphite surface taken under the same conditions as the images to follow. Every second surface atom appears as a bright spot in the image. These are the atoms which do not have a neighbour in the underlying plane of atoms.[6] It is important to point out that since the image is sensitive to the registration between the first and second atomic layers, a dislocation in either layer can have an equal effect on the apparent image of the surface.

Figure 2 shows an area exhibiting the hexagonal domain structure. The areas within each domain have the same appearance as normal graphite, whereas the boundary regions are blurred or streaked indicating that the registry between the first two layers is not well defined as would be the case if either or both of the layers had a dislocation across the boundary region. Figure 3a shows a smaller area centred on the boundary regions between three domains. This image was taken with the same sample and tip as figure 1. Figure 3b shows the same area as in 3a, with a triangular grid superimposed to clarify the spatial displacement of atoms across the boundaries. The grid has been position and scaled to provide a best fit to the atomic positions in areas of the lattice away from the boundary regions. One sees immediately that the position of the bright spots changes by a displacement of the type $a_0/6 <1\ 1\ \bar{2}\ 0>$ across any of the boundaries, which is half of a unit vector in the unit cell.

These real space images provide a direct measurement of the width of a basal dislocation in graphite. A previous measurement by convergent electron beam diffraction

suggested that partial dislocations are at least 20 to 30 unit cells wide.[7] Here the apparent width is less than 4 unit cells (10Å). The value is in rough agreement with other STM observations of isolated lines of dislocations in HOPG. [8,9] In particular Marti et al [8] report a reversal of the orientation of the three maxima in each unit cell across a dislocation boundary that is also apparent in our images.

Similar networks of dislocations have been observed at twist boundaries in graphite [10,11]. In fact a simple rotation of one hexagonal planar lattice of atoms with respect to another results in a regular array of hexagonal ordered areas of near a-a stacking. However the STM images clearly show that the graphite within the domains have the threefold pattern characteristic of normal a-b stacking and suggest that a-a stacking is strictly avoided even though this necessitates significant lateral displacement of atoms and the formation of a very dense network of in-plane dislocations.

It is important to note that the dislocations that are observed here have a different Burger's vector than the partials seen in previous work. TEM studies have shown that basal dislocations in graphite split into partials of the type $a_0/3<1\bar{1}00>$ (Figure 4). An example of this would be $A\sigma$ or σC , with $A\sigma + \sigma C \rightarrow AC$ being a typical decomposition of a dislocation. In the case of these new dislocations the displacement of atoms is along one of the unit cell directions, and is oriented parallel to the domain boundary. The dislocations are then pure screw in nature.

We have also observed transition regions between areas with these hexagonal domains and ordinary graphite. The transition seems to occur over a large distance over which there are areas of disordered graphite, periodic arrays of defects that appear as patches of unstable tunneling current, and a large vertical corrugation that spans the entire region. The structure of the different areas in the boundary, and their relationship to the ordered patterns on either side is unknown. The overall boundary region appears to be a stripe about 50Å wide, a value which corresponds to the width of a dislocation measured by other means.[7]

Perhaps then it is this entire boundary region that might be associated with the line of contrast at a dislocation as seen by TEM. However, since our images with atomic resolution after digitization were limited to about 100Å square, we were unable to measure along the boundary region for more than about 200Å so the actual larger scale geometry of the boundary is unknown. The possibility that the hexagonal domains are restricted to isolated regions of the sample rather than along an extended line cannot be ruled out.

This work was supported by the U.S. Defense Advanced Research Projects Agency and the U.S. Joint Services Electronics Program. We acknowledge helpful discussions with Howard Mizes.

References

- [1] Sang-il Park and C.F. Quate, *Appl. Phys. Lett.* **48**, 112 (1986)
- [2] R. Sonnenfeld and P.K. Hansma, *Science* **232**, 211 (1986)
- [3] G. Binnig, H. Fuchs, Ch. Gerber, H. Rohrer, E. Stoll, and E. Tosatti, *Europhys. Lett.* **1**, 31 (1986)
- [4] A.W. Moore, in Chemistry and Physics of Carbon, (Dekker, New York 1973) Vol. 11, pp. 69-176
- [5] A. Bryant, D.P.E. Smith and C.F. Quate, *Appl. Phys. Lett.* **48**, 832 (1986)
- [6] A. Selloni, P. Carnevali, E. Tosatti, and C.D. Chen, *Phys. Rev. B* **34**, 7406 (1986); errata concerning *Phys. Rev. B* **31**, 2602 (1985)
- [7] P. Goodman, *Acta. Cryst. A* **32**, 793 (1976)
- [8] O. Marti, G. Binnig, H. Rohrer, and H. Salemink, *Surf. Sci.* **181**, 230 (1987)
- [9] H.W.M. Salemink, I.P. Batra, H. Rohrer, E. Stoll, and E. Weibel, *Surf. Sci.* **181**, 139 (1987)
- [10] S. Amelinckx, P. Delavignette, and M. Heerschap, in Chemistry and Physics of Carbon, P.L. Walker Jr. ed. (Dekker, New York 1965), Vol. 1, Ch. 1, pp.1-71
- [11] G.K. Williamson, *Proc. Roy. Soc. A* **257**, 457 (1960)

Figure Captions

Figure 1: An STM image of graphite, presented as a greyscale map. Lighter areas indicate areas of greater tunneling current. Each hexagon of the lattice appears as three dots in the positions of atoms without a neighbour in the second layer nearest the surface. The spacing between the dots is equal to 2.46\AA , the basal lattice constant of graphite. The imaged area is approximately $30 \times 30 \text{\AA}$.

Figure 2: An image of an area showing the hexagonal domain structure. The size of the image is approximately $40 \times 50 \text{\AA}$.

Figure 3: A magnified view of several domains and the boundaries between them.
Figure 3a (Left) The imaged area is approximately $30 \times 30 \text{\AA}$.
Figure 3b (Right) The same image with a triangular grid overlaid to clarify the shift in the pattern of bright dots across the domain boundaries.

Figure 4: A diagrammatic representation of Figure 3b showing three domains and the pattern of dots within each. The upper left portion shows one possible position for the surface atoms along with the conventional notation for the basal plane lattice unit vectors. Note that the shift in position from domain to domain corresponds to displacements that are half of a unit vector such as AB or AC . $\text{A}\beta$ or $\text{A}\sigma$ are partial lattice vectors of the general type $a_0/3<1\bar{1}00>$ which have been observed by TEM.

Fig 1

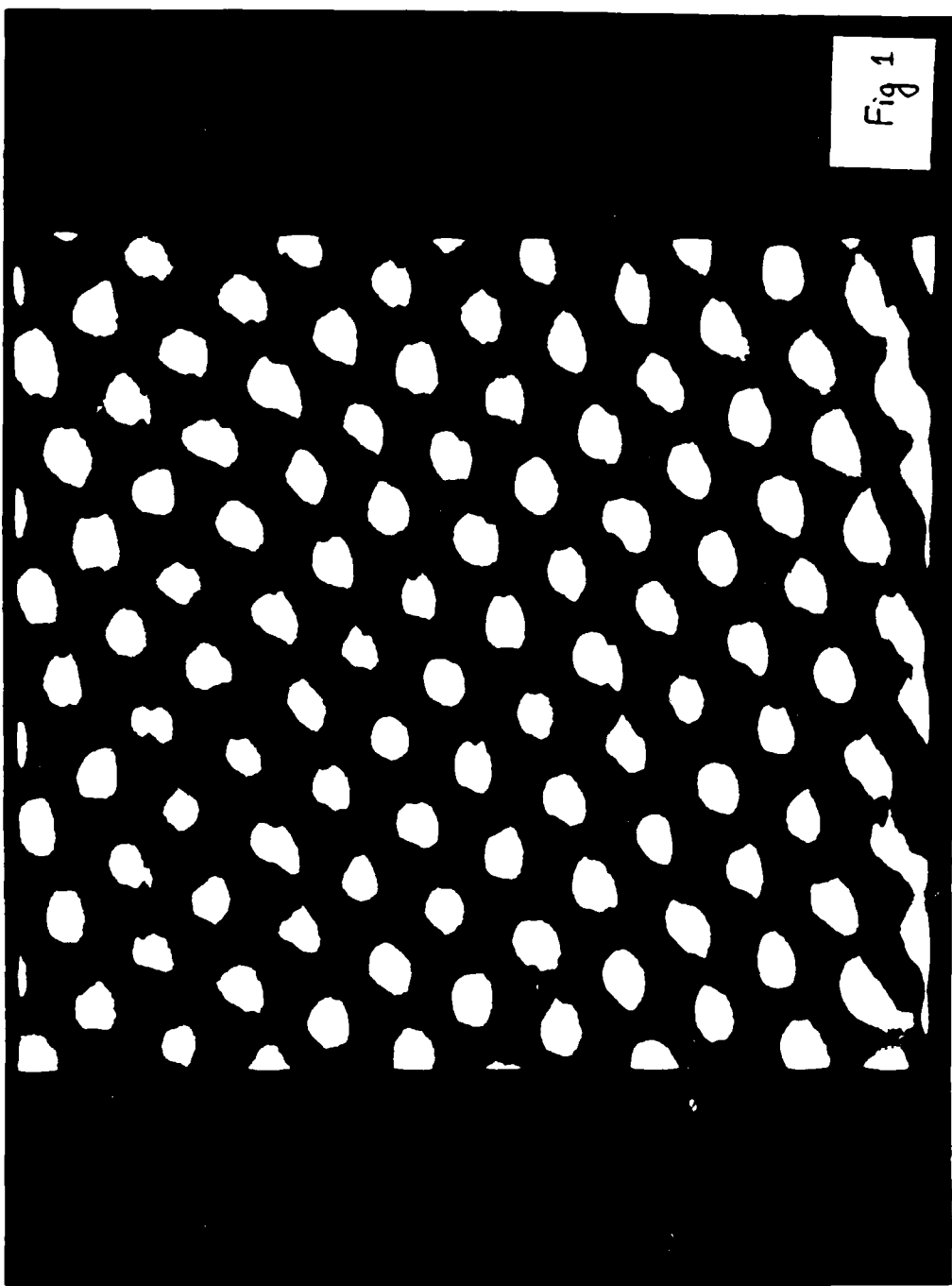


Fig 2

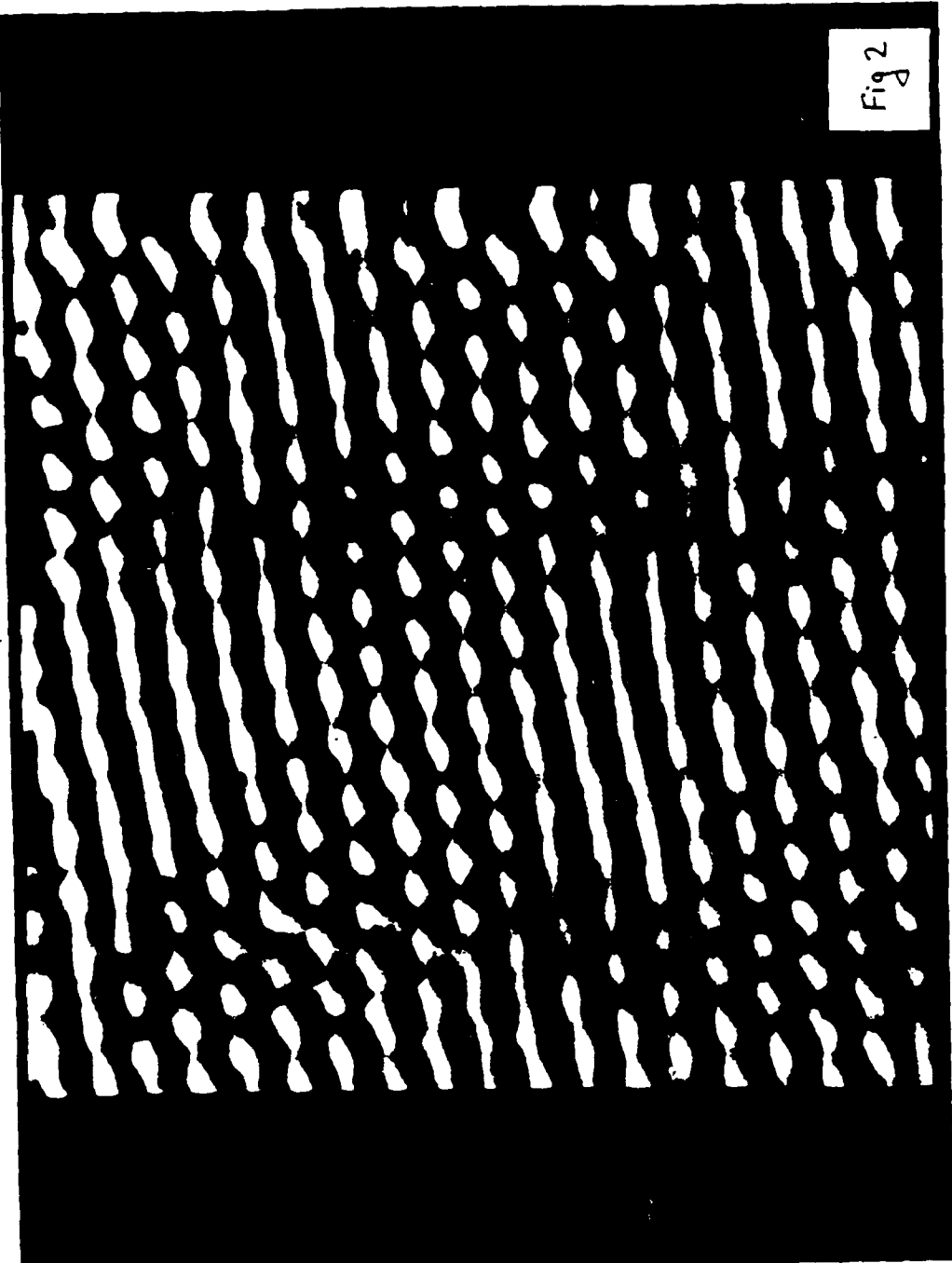
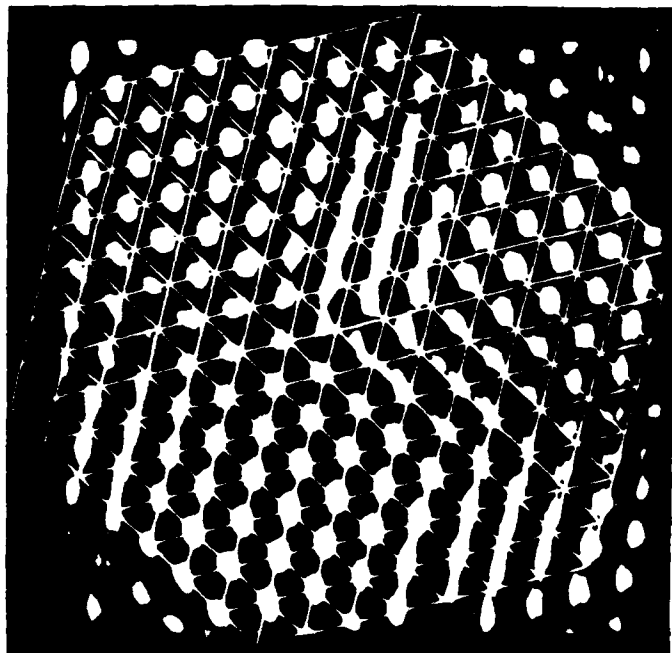


Fig 3

(b)



(a)

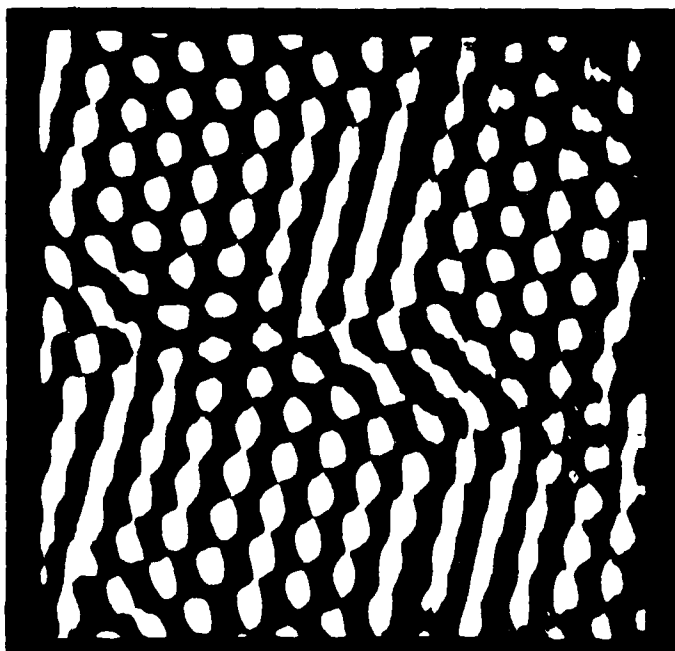
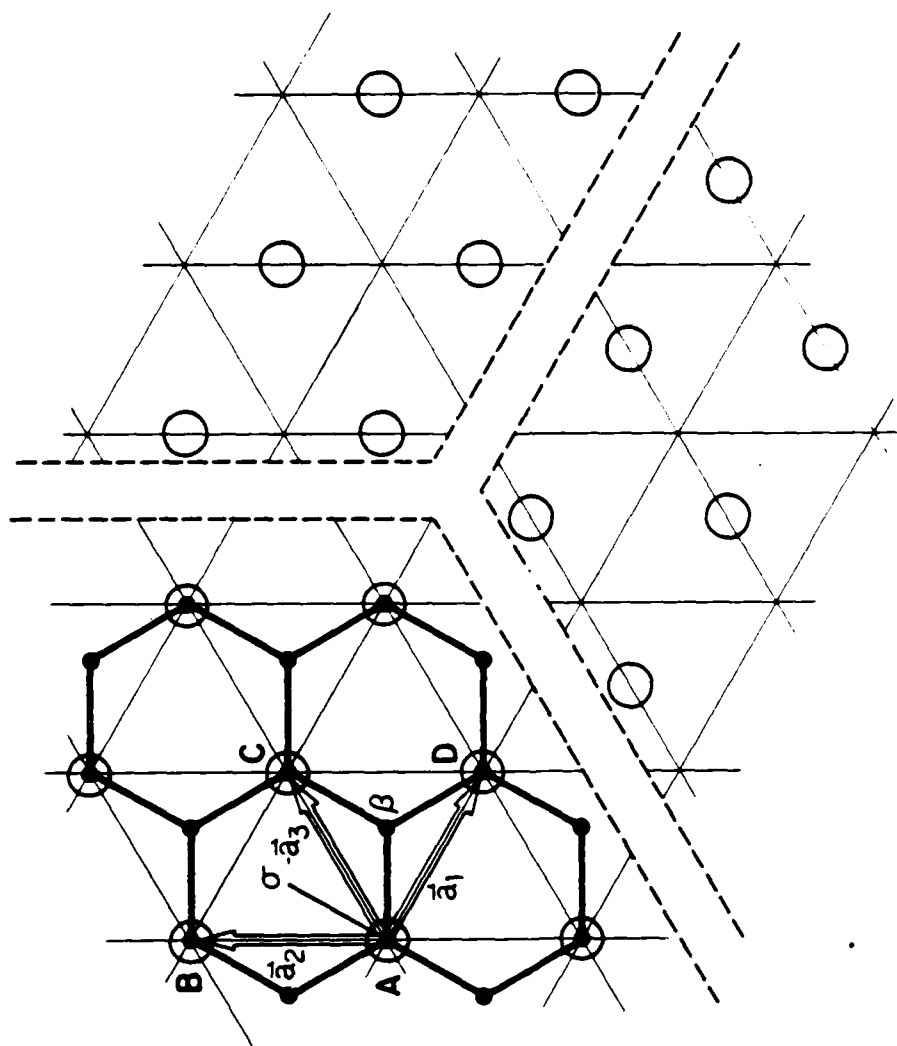


Fig. 1



Atomic resolution imaging of a nonconductor by Atomic Force Microscopy

T. R. Albrecht and C. F. Quate

Department of Applied Physics, Stanford University, Stanford, California 94305

ABSTRACT

We have demonstrated the capability of the Atomic Force Microscope to image the surface of an electrically insulating solid with atomic resolution. Images of highly oriented pyrolytic boron nitride taken in air show atomic corrugations with a lateral resolution better than 3 Å. Low noise images of graphite and molybdenum disulfide are also presented.

PACS numbers: 68.35.Bs, 61.16.Di

Submitted for publication in Journal of Applied Physics, May 1987

Atomic Force Microscopy (AFM)¹ has been proposed as a technique for extending the high resolution capabilities of Scanning Tunneling Microscopy (STM)^{2,3} to the imaging of nonconducting as well as conducting surfaces. The AFM profiles a surface by measuring the interatomic forces between a flexible stylus and the surface of interest. Several groups have reported AFM imaging with lateral resolutions on the order of 100 to 1000 Å.^{1,4,5} Others have mapped magnetic forces with the AFM, achieving similar resolution.^{6,7} Recently Binnig *et al.*⁸ and Marti *et al.*⁹ demonstrated atomic resolution on graphite. The latter group also profiled monatomic steps on an oil-covered surface of sodium chloride. Here we report AFM imaging of atomic corrugations on atomically flat surfaces of graphite, molybdenum disulfide, and highly oriented pyrolytic boron nitride (a nonconductor). The ability of the AFM to image nonconductors opens a new class of materials to atomic resolution surface imaging, complementing the work already being done with STM.

Our AFM (Fig. 1) senses repulsive contact forces between a fixed flexible microcantilever and the surface of the sample. The force is monitored by measuring the deflection of the lever with a tunneling current between a sharp tungsten tip and the back side of the lever. The sample is mounted on an X-Y-Z piezoelectric tube scanner.¹⁰ A second piezoelectric tube controls the Z motion of the tunneling tip. Separate mechanical systems using finely threaded screws and motion reduction levers¹¹ provide mechanical approach for the tip and sample. The apparatus rests on a stack of steel plates separated by rubber spacers, which provides adequate isolation from building vibrations. Because of the relatively long thermal path between the various elements of the AFM, a thermally insulated enclosure surrounding the AFM is necessary to reduce thermal drifts to an acceptable level.

The critical component of the AFM is the force-sensing microcantilever. It has previously been shown^{1,4,5} that the force-sensing element should have a low force constant ($\ll 100$ N/m) and a high mechanical resonant frequency. These requirements are met in our AFM by microfabrication

techniques^{8,12} which allow us to make structures with force constants between 10^{-2} and 10 N/m with corresponding resonances between 20 and 200 kHz. Our experience with several types of levers suggests that relatively stiff levers (1 to 10 N/m) with high resonances (~100 kHz) provide a superior signal to noise ratio. Others have achieved atomic resolution with a force constant as high as 40 N/m.⁹ We now use a V-shaped silicon dioxide lever (Fig. 2), consisting of two straight cantilevers intersecting at the free end at an angle of 60°. The lever has a calculated force constant of approximately 2 N/m and a resonant frequency near 100 kHz.¹² The V-shape reduces lateral bending of the lever in response to X-Y scanning of the sample. One side of the lever is covered with 400 Å of gold which serves as a conducting surface for the tunneling current between the tungsten tip and lever. Since we have not yet succeeded in constructing a protruding sharp tip on the end of the lever, the lever is tilted approximately 20° toward the sample, which restricts the contact area to the tip of the lever. The V-shape provides a macroscopically sharper point than the rectangular cantilevers used previously.⁸ Microscopic (perhaps monatomic) protrusions on the tip of the lever make atomic resolution imaging possible. Obtaining a sufficiently sharp tip on the lever appears to be the greatest difficulty in achieving atomic resolution with the AFM.

The control circuitry for the AFM is shown in Fig. 3. The first step in operating the AFM is to establish a stable tunneling current between the tip and lever. A feedback system identical to that used for high speed variable current STM imaging¹³ maintains a constant average tip-lever separation of a few angstroms by monitoring the tunneling current. With no sample in place, we observe rapid fluctuations of the tunneling current which are attributed to thermal excitations of the lever. Next, the sample is brought into contact with the lever using the mechanical approach system and a manually controlled DC voltage on the Z electrode of the sample piezo. Bringing the sample into contact with the lever significantly changes the mechanical properties of the lever, reducing the amplitude of its thermal vibrations. As a result, the initial contact between the sample and lever is detected as an abrupt reduction in noise in the tunneling current. Moving the sample in

further causes backward deflection of the lever, which is observed by monitoring the position of the tunneling tip as it follows the motion of the lever. The AFM is operated with a typical lever deflection of 1000 Å, which corresponds to a force of 2×10^{-7} N for the V-shaped lever. The amount of force exerted against the sample is not critical, since the average lever deflection can sometimes be changed by thousands of angstroms with little change in image quality. The sample is scanned at 1800 Hz in X and 18 Hz in Y. Slow feedback response prevents the tunneling tip from following the rapid changes in lever deflection in response to surface corrugations. The resulting modulation of the tunneling current is high-pass filtered to remove the effects of tilt in the background plane and is displayed as a television grayscale image using a video image processor and temporal filter.¹⁴ This "variable deflection" imaging mode produces real time images at a rate of 18 frames per second. Temporal filtering of the images improves the signal to noise ratio when the images are sufficiently stable.

Figure 4 shows AFM images of three different samples studied in air. All were taken with the same V-shaped lever. The scanning system was first calibrated by operating the apparatus as an STM with a bias voltage applied to a cleaved sample of highly oriented pyrolytic graphite (HOPG) and no force-sensing lever in place. The distance between equivalent sites in the graphite basal plane is known to be 2.46 Å. The AFM image of the same graphite sample shown in Fig. 4(a) confirmed that the scan calibration remains valid in the AFM mode. This AFM image of graphite is comparable in signal to noise ratio with the best STM images we have taken in air. The maximum modulation of the tunneling current between the tunneling tip and the lever was 30%, corresponding to lever motions in response to surface corrugation of 0.15 Å for an assumed tunneling barrier height of 4 eV. Helium scattering studies¹⁵ indicate a corrugation height of 0.21 Å on graphite. Both the nature of the image and the amount of modulation on the tunneling current changed occasionally, apparently due to variations in the quality of the lever-sample contact point and the condition of the tunneling tip. For example, in Fig. 4(a), inequivalent sites in the

graphite lattice are clearly distinguished, as only three bright maxima appear in each hexagon. At times, however, the complete hexagonal rings are seen with little distinction between inequivalent sites, although the individual atoms are not resolved as separate maxima.

Figure 4(b) is an AFM image of 2H-MoS₂, a layered semiconductor. MoS₂ can be cleaved by exfoliation in air to expose large atomically flat planes of sulfur atoms on its surface. The lattice is known to have threefold rotational symmetry with a spacing of 3.1604 Å between atoms in the sulfur planes.¹⁶ The observed lattice spacing is 3.2±0.2 Å. Because the electrical resistivity in the direction perpendicular to the planes may be as much as 10³ times greater than in the parallel direction ($\rho_{\perp} \sim 10 \Omega\text{-cm}$),¹⁶ our previous attempts to image MoS₂ by STM were only occasionally successful. With the AFM, however, MoS₂ proved no more difficult to image than graphite. Modulation of the tunneling current was similar to that observed on graphite. The image shown reveals an elongation of the atoms similar to the effect seen in STM images of TaSe₂.¹⁷ Rotating the sample also rotated the elongation direction, indicating that the anisotropy is a property of the sample and not generated by the imaging method. The AFM appears well suited for studies of the layered transition metal dichalcogenides, such as MoS₂, which have some unusual physical properties.¹⁶

The third sample imaged was highly oriented pyrolytic boron nitride (HOPBN), which was our first nonconducting sample to exhibit atomic resolution [Fig. 4(c)]. HOPBN is a hexagonal layered material similar to HOPG, with a spacing of 2.504 Å between equivalent sites in the same plane.¹⁸ Each hexagon contains three atoms of each species, alternating at adjacent vertices. The layers are stacked in direct registry, with a boron atom above and below each nitrogen atom. The sample was cleaved by exfoliation in air. The maximum modulation of the tunneling current was 10%, indicating surface corrugations of 0.05 Å, and the observed lattice spacing is 2.5±0.1 Å. All of the

HOPBN images showed three dominant bright spots per hexagon, indicating that height maxima occur over the atomic sites of one species only.

In order to determine how the observed corrugations correspond to atomic sites on the surface of HOPBN, we model the lever-sample repulsive potential using an overlap interaction between a single oxygen atom on the tip of the lever and a single boron or nitrogen atom on the surface of the sample. The interaction is approximated using the Gordon-Kim potential for the overlap of two neon atoms¹⁹ scaled for the B-O and N-O cases according to a method presented by Harrison.²⁰ While this approximation is inexact, it provides at least a qualitative comparison between the B-O and N-O cases. Harrison's overlap potential for two atoms separated by a distance d is

$$V_{12}(d) = \frac{\eta \hbar^2 d \mu_{12}^3}{2 m_e} \exp(-5 \mu_{12} d / 3)$$

where η is an empirical constant and $\mu_{12} = (1/2)(\mu_1 + \mu_2)$. The μ_i satisfy $E_{pi} = \hbar^2 \mu_i^2 / 2 m_e$ where E_{pi} is the p-state energy of an atom of species i . While this potential is quite successful in predicting V_{12} for d near the lattice spacing in a crystal, comparison with the more accurate Gordon-Kim potential reveals that it is less reliable in the strongly repulsive regime we are interested in. Hence the above is used only to compute scaling factors which relate V_{12} to the potential V_{Ne} for two Ne atoms:

$$V_{12}(d) = \left(\frac{\mu_{12}}{\mu_{Ne}}\right)^3 V_{Ne}(d) \exp[-5(\mu_{12} - \mu_{Ne})d/3]$$

At this point V_{Ne} is replaced by the Gordon-Kim potential, which in the range $d = 0.5$ to 1.3 Å can

be approximated by

$$V_{Ne}^{GK}(d) = A e^{-\kappa d}$$

where $A = 2800$ eV and $\kappa = 4.45 \text{ \AA}^{-1}$. In BN, the charge is distributed between the B and N atoms in the ratio 0.7:1.3 (Ref. 21). Taking this into account, the force in each case is

$$f_{BO}(d) = -0.7 \left(\frac{\partial V_{BO}}{\partial d} \right) = (3.7 \times 10^{-6}) e^{-3.34 d} \text{ N}$$

$$f_{NO}(d) = -1.3 \left(\frac{\partial V_{NO}}{\partial d} \right) = (1.1 \times 10^{-5}) e^{-3.68 d} \text{ N}$$

where d is in angstroms. If we assume the observed force of 2×10^{-7} N acts on only two atoms (one on the lever and one on the sample), the above would indicate $d = 0.88 \text{ \AA}$ when the tip of the lever is over a B atom and $d = 1.09 \text{ \AA}$ over a N atom, resulting in a lever deflection approximately 0.2 \AA greater on N atoms compared to B atoms. Similar calculations assuming a single silicon or carbon atom on the lever yielded qualitatively similar results. Based on this model, the height maxima in Fig. 4(c) are attributed to nitrogen sites on the surface of HOPBN. If the force is actually distributed over several atoms, however, this model would not apply.

Images of all three surfaces occasionally showed continuous parallel corrugations like those shown in Fig. 4(d). These features are attributed to simultaneous imaging by two separate sample-lever contact points. A similar effect is commonly encountered in STM due to simultaneous tunneling from more than one atom on a tunneling tip.²²

We have shown that the AFM is capable of low noise atomic resolution in imaging both conducting and nonconducting surfaces in air. Future refinements in the instrument, especially in

the force-sensing stylus, should establish the AFM as a valuable new analytical tool.

We wish to thank G. Binnig and Ch. Gerber for their interest, advice, and cooperation in our AFM work. We are also pleased to acknowledge useful conversations with W. A. Harrison, P. K. Hansma, and H. Mizes. The HOPBN and HOPG samples were provided by A. W. Moore of Union Carbide, and the MoS₂ sample was provided by T. H. Geballe of the Center for Materials Research at Stanford University.

This work was supported by the Defense Advanced Research Projects Agency, the Joint Services Electronics Program, and by a National Science Foundation Graduate Fellowship.

REFERENCES:

1. G. Binnig, C. F. Quate, and Ch. Gerber, *Phys. Rev. Lett.* **56**, 930 (1986).
2. C. F. Quate, *Physics Today* **39** (8), 26 (1986).
3. P. K. Hansma and J. Tersoff, *J. Appl. Phys.* **61**, R1 (1987).
4. G. M. McClelland, R. Erlandsson, and S. Chiang, to be published in *Rev. Prog. in Quantit. Non-Destruct. Eval.* **6** (Plenum, New York, 1987).
5. Y. Martin, C. C. Williams, and H. K. Wickramasinghe, to be published in *J. Appl. Phys.* (1987).
6. Y. Martin and H. K. Wickramasinghe, to be published (1987).
7. J. J. Sáenz, N. García, P. Grüter, E. Meyer, H. Heinzelmann, R. Wiesendanger, L. Rosenthaler, H. R. Hidber, and H.-J. Güntherodt, to be published (1987).
8. G. Binnig, Ch. Gerber, E. Stoll, T. R. Albrecht, and C. F. Quate, to be published in *Europhys. Lett.* (1987).
9. O. Marti, B. Drake, and P. K. Hansma, to be published (1987).
10. G. Binnig, and D. P. E. Smith, *Rev. Sci. Instrum.* **57**, 1688 (1986).
11. D. P. E. Smith, A. Bryant, C. F. Quate, J. P. Rabe, Ch. Gerber, and J. D. Swalen, *Proc. Natl. Acad. Sci. USA* **84**, 969 (1987).
12. K. E. Petersen, *Proc. IEEE* **70**, 420 (1982).
13. A. Bryant, D. P. E. Smith, and C. F. Quate, *Appl. Phys. Lett.* **48**, 832 (1986).
14. Arlynna TF5111 Temporal Filter and Image Store, Princeton Electronic Products, North Brunswick, New Jersey.
15. N. García, W. E. Carlos, M. W. Cole, and V. Celli, *Phys. Rev. B* **21**, 1636 (1980).
16. J. A. Wilson and A. D. Yoffe, *Adv. Phys.* **18**, 193 (1969).
17. A. Bryant, Ph. D. Thesis, Stanford University (1986).

18. E. Doni and G. Pastori Parravicini, *Nuovo Cimento B* **64**, 117 (1969).
19. R. G. Gordon and Y. S. Kim, *J. Chem. Phys.* **56**, 3122 (1972).
20. W. A. Harrison, *Phys. Rev. B* **23**, 5230 (1981).
21. E. Tegeler, N Kosuch, G. Wiech, and A. Faessler, *Phys. Status Solidi B* **91**, 223 (1979).
22. S. Park, J. Nogami, and C. F. Quate, to be published (1987).

CAPTIONS:

FIG. 1. (a) Diagram of the AFM apparatus showing the mechanical positioners and piezoelectric tubes for controlling the motion of the critical components. (b) Enlarged view showing the orientation of the tunneling tip and force-sensing microcantilever.

FIG. 2. SEM micrograph of the silicon dioxide V-shaped microcantilever used for sensing the force. Each leg of the structure is 1.5μ thick, 100μ long and 22μ wide. When mounted in the AFM, the top side is toward the sample. The bottom side is covered with a thin film of gold.

FIG. 3. The AFM control circuitry. Deflection of the force-sensing lever is monitored by a tunneling current between the tunneling tip and a gold film on the lever. As the sample is scanned, rapid changes in lever deflection in response to surface topography are observed as modulation of the tunneling current, which is displayed as a real time grayscale image.

FIG. 4. AFM grayscale images of (a) graphite, (b) molybdenum disulfide, and (c) boron nitride. A second image of boron nitride (d) shows the effects of multiple contact points between the sample and lever. White corresponds to raised areas on the surfaces.

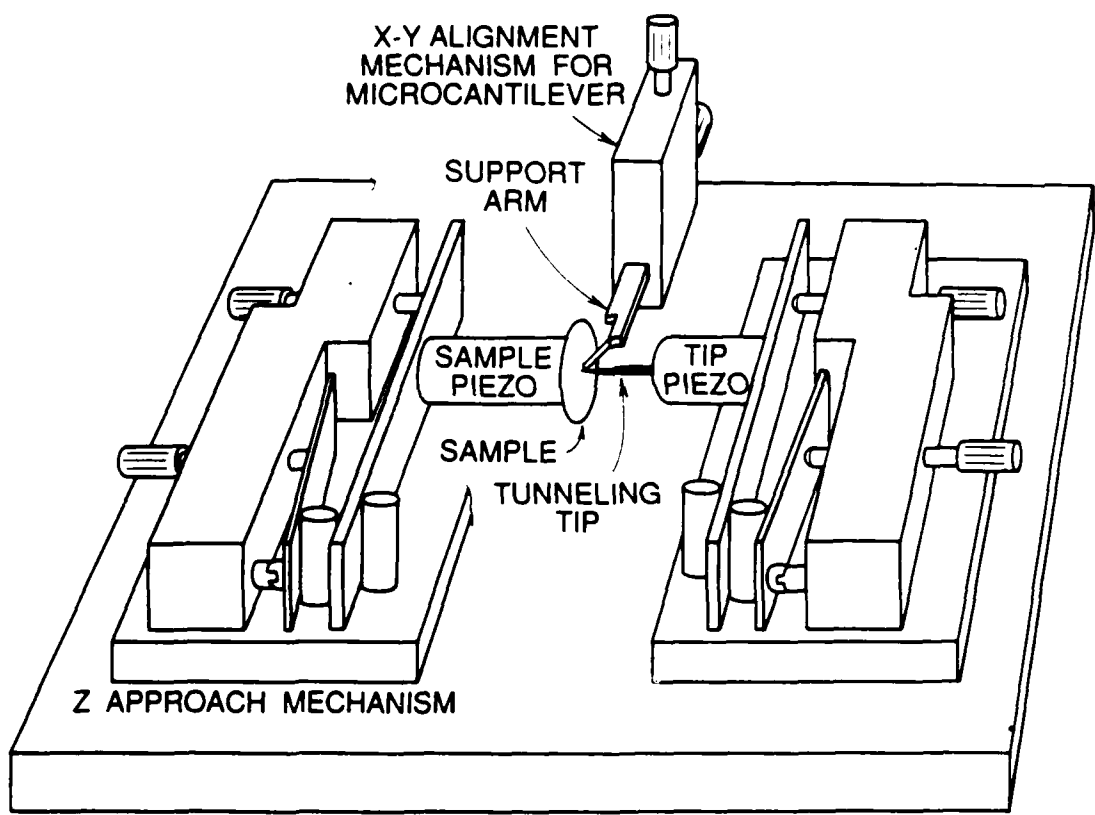


FIG. 1(a)

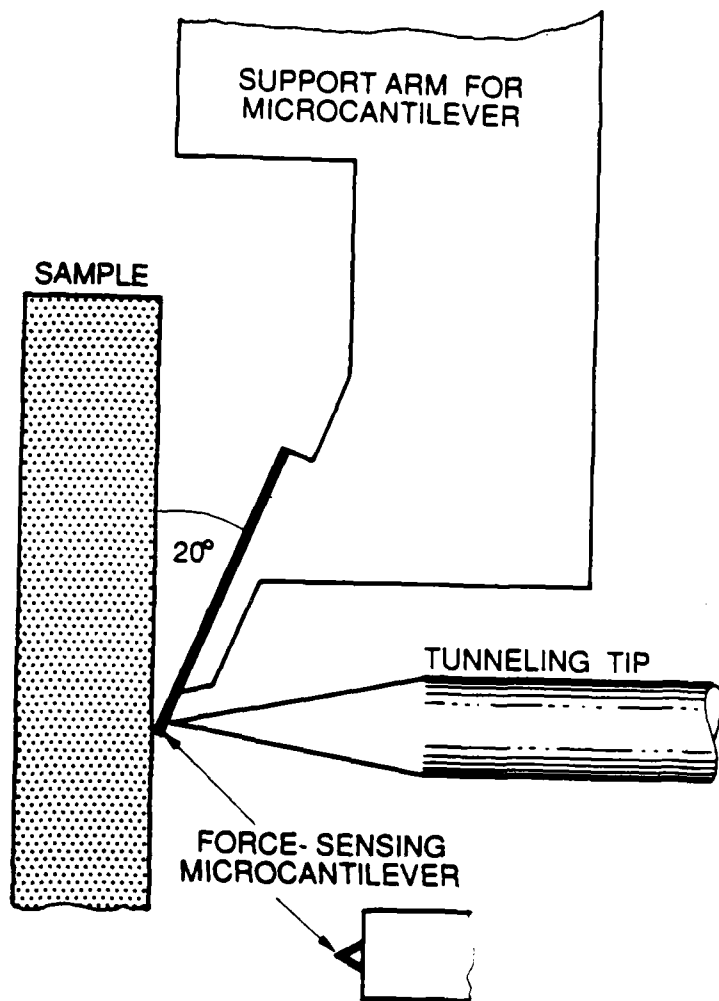


fig. 1(b)

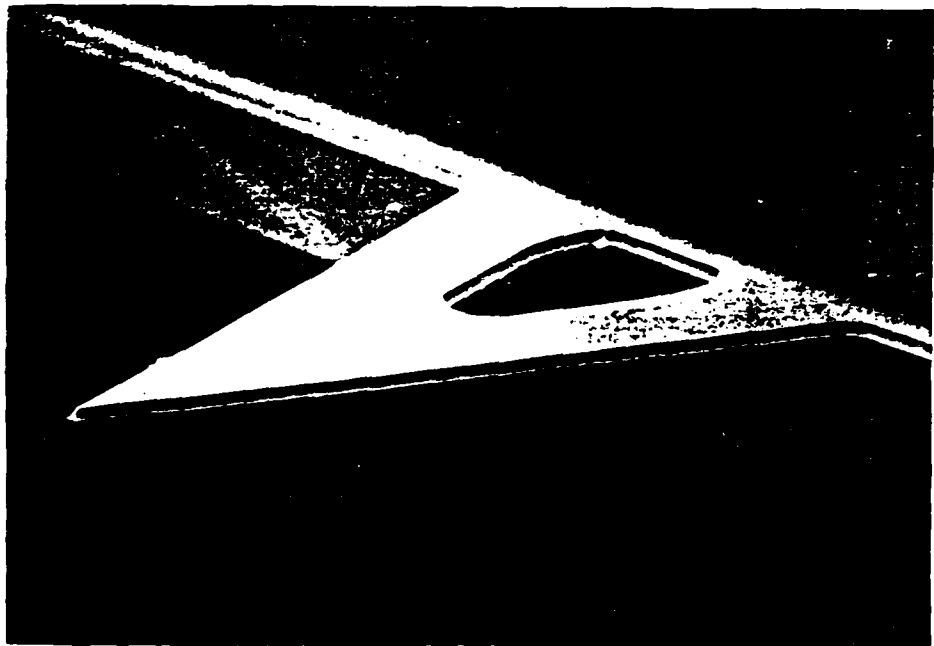


FIG. 2

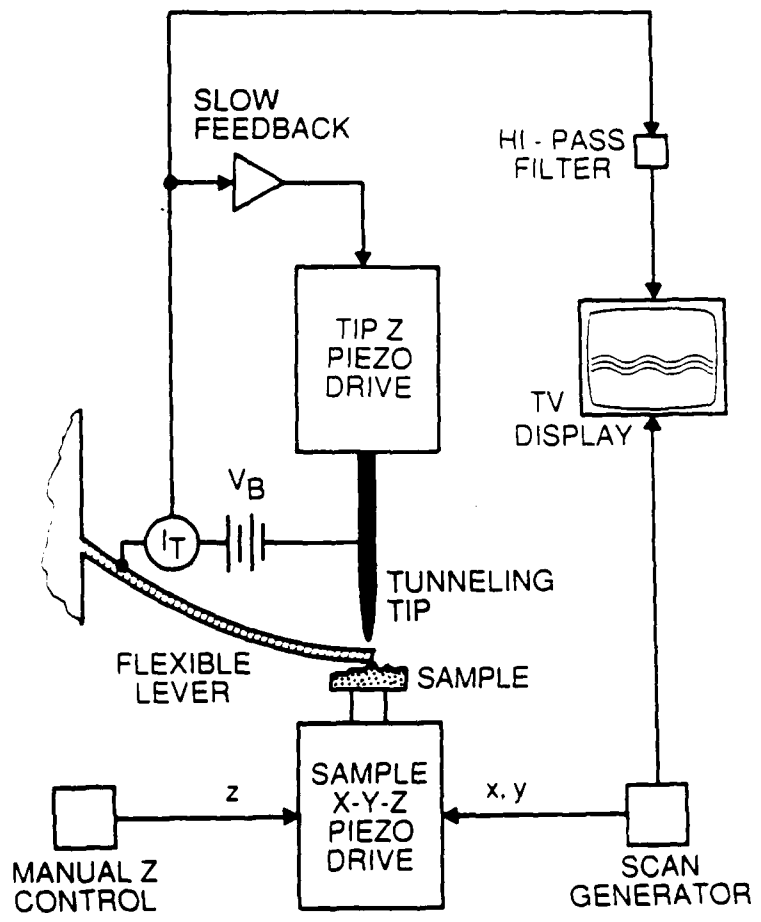


FIG. 3

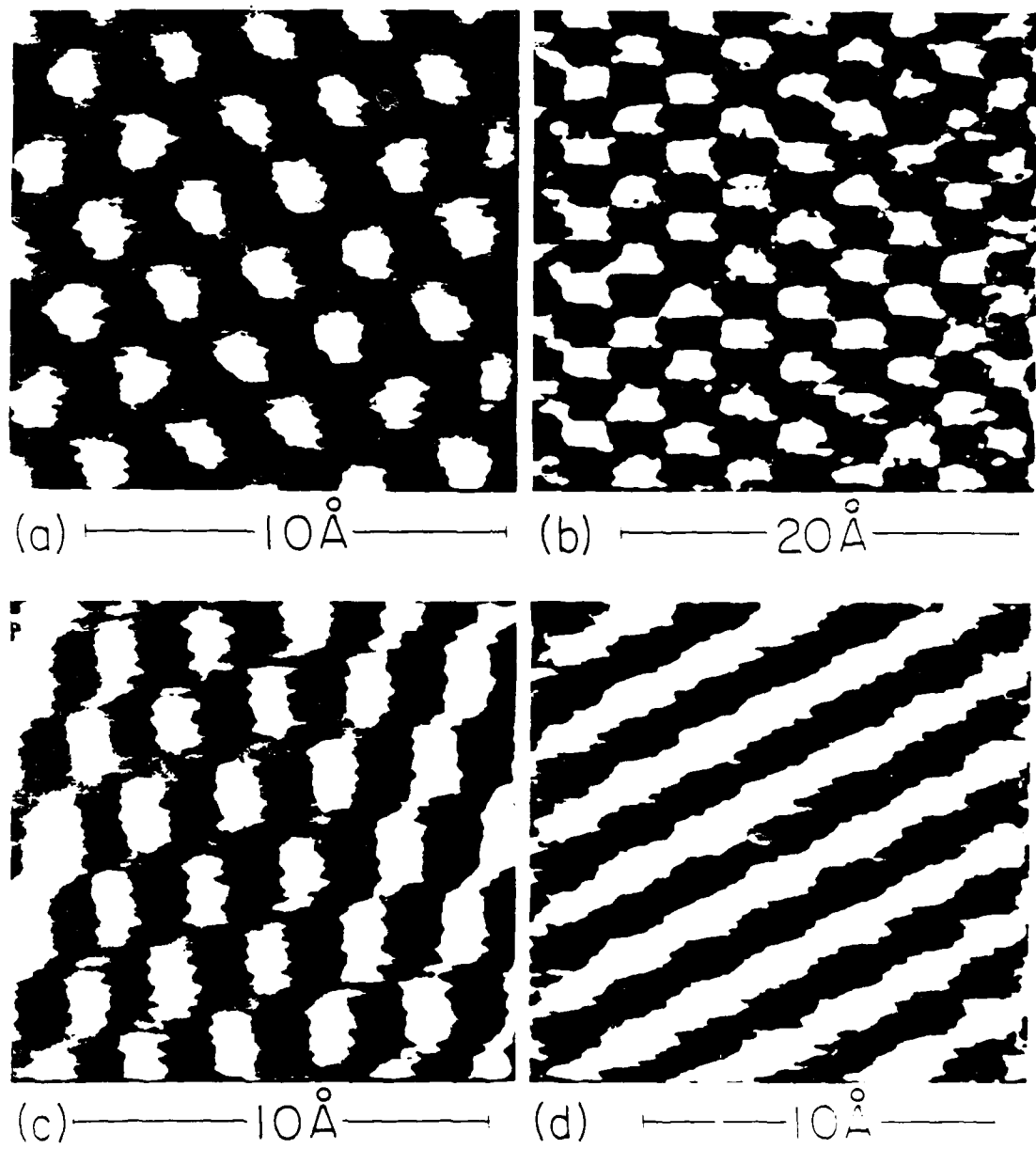


FIG. 4

**A NONINVASIVE OPTICAL PROBE
FOR DETECTING ELECTRICAL SIGNALS
IN SILICON INTEGRATED CIRCUITS**

by
Harley K. Heinrich

G. L. Report # 4190

A Dissertation

Supported by
JSEP Contract # N00014-84-K-0327

Picosecond Electronics Laboratory
Edward L. Ginzton Laboratory
W.W. Hansen Laboratories
Stanford University
Stanford, California 94305

April 1987

Abstract

As the bandwidth of silicon integrated circuits is pushed towards microwave frequencies, electrical measurements inside these circuits become more difficult to make. The best commercially available noncontact probing technique, the voltage contrast scanning electron microscope (SEM), is complex, and has a low sensitivity. Present optical probing techniques are less complex than the SEM but still produce weak signals. Probing systems based on silicon's nonlinear optical interactions produce even smaller signals than the SEM, since the electrooptic interactions in silicon are weak.

However, free carriers in an integrated active device introduce a significant perturbation in the index of refraction of the material. We have demonstrated a noninvasive $1.3\mu\text{m}$ (sub-silicon-bandgap) optical probing system which interferometrically senses the free-carrier concentration in active devices, with a sensitivity over an order of magnitude higher than the SEM. Because of this high sensitivity, we have experimentally measured real-time 0.8V digital signals applied to a bipolar junction transistor using a multimode InGaAsP semiconductor laser. This measurement was performed in a 200MHz detection bandwidth, and hence, it represents a wide-bandwidth optical interconnect between the probed device and the system detector.

In the future this probing system has the potential of simplifying complex microwave test systems, and since active devices in all semiconductor materials operate on the principle of charge control, we should be able to detect signals in IC's fabricated in any semiconductor material including GaAs, InGaAsP, Ge, and Si. In addition, because of the high spatial and temporal resolution capabilities of this system, we should be able to directly observe free-carrier dynamics in active devices. Finally, by optimizing a device which exploits the charge-optical interaction, we should be able to develop efficient integrated optical modulators for use in optical communication systems.

A REAL-TIME CONFOCAL SCANNING OPTICAL MICROSCOPE

G. Q. Xiao and G. S. Kino

Edward L. Ginzton Laboratory, W. W. Hansen Laboratories of Physics
Stanford University, Stanford, California 94305Abstract

A new type of real-time confocal scanning optical microscope, with the same measured resolution as a conventional confocal scanning optical microscope, is described. The system uses a rotating Nipkow disk with 150,000 pinholes etched in it, to yield a 640 frame/sec, 7000-line image. The transverse definition is of the order of 0.3 μ m, and the 3 dB range resolution, with a 0.8 N.A. objective lens, is better than 0.75 μ m.

Introduction

Recently we have developed a high-speed scanning technique for a scanning confocal optical microscope. We call the device "the spiral scanning optical microscope (SSOM)." The device operates at a rate of 640 frames/sec and produces an image with approximately 7000 lines. When viewed in real time by the naked eye, the definition is such that no scanning lines are observable in the image. Furthermore, the transverse definition of the microscope is better than that of a standard microscope, and it has extremely good depth definition, far superior to that of standard microscopes.

Our device is a development of the "tandem scanning optical microscope (TSOM)" of Petran et al.¹⁻³ Their microscope is extremely difficult to align because of its optical and mechanical complexity. Therefore, it provides fine performance, although perhaps not as good as that of a true confocal scanning optical microscope (CSOM).⁴ For these reasons, only a very small number of the devices have been made in the last twenty years. Ours eliminates the optical and mechanical difficulties in the design, is simple and relatively easy to construct, and makes it possible to realize the ultimate definition of a CSOM, as described below.

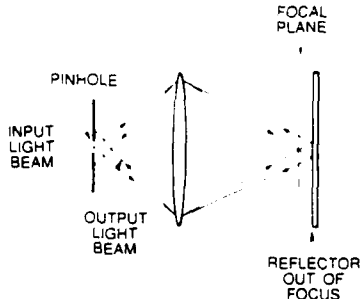


Fig. 1. An illustration of the principle of the confocal scanning optical microscope. The detector and laser source are not shown.

We will first describe the principles of the CSOM, as illustrated in Fig. 1. Light enters the objective lens of a microscope through a pinhole. An image of the pinhole is focused on the plane of the object. The beam impinging on the object is reflected from it, and an image of the illuminated spot on the object is, in turn, focused on the pinhole. The light passes through the pinhole to a detector (not shown). The output from the detector will be maximum when the object is located at the focus of the lens; otherwise the light received at the pinhole (dotted lines) is defocused, and the amplitude of the signal falls off very rapidly as the position of the object is changed. Thus, the system has a very short depth of focus. In addition, it has excellent transverse definition, with 3 dB points spaced at a distance approximately 70% of that for a conventional microscope. A CSOM also has very low sidelobe levels. This is because the lens is used in both transmit and receive mode so that the point spread function of the microscope is the square of the

point spread function of a single lens. Such a microscope can be mechanically scanned to form a raster image by moving the object or the pinhole. Typically, this is a relatively slow process. In a commercial example, the SiScan CSOM, the frame time for an image with 512×512 spots is 10 sec.⁵

The principle of the tandem scanning optical microscope is illustrated in Fig. 2. A circular disk, known as a Nipkow disk, has pinholes placed in it which are located on several interleaved spirals. These pinholes are illuminated by a light source from a mercury vapor arc, and are imaged on the sample by the objective lens. The reflected light from the object passes back through the conjugate pinholes, and an image of the pinholes is observed through a standard microscope eyepiece. The disk itself is rotated so as to form a raster scan, and thus fill in the spaces between the pinholes.

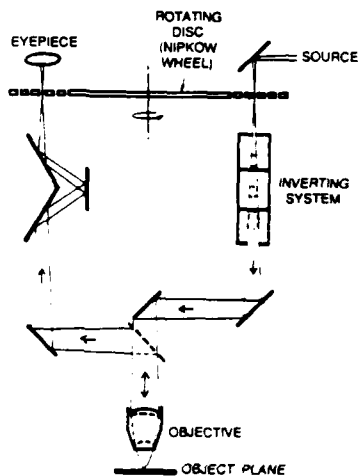


Fig. 2. A schematic of the tandem scanning optical microscope used by Petran et al.¹

It will be noted that if no additional precautions were taken, the reflected light from the disk would obscure the relatively weak image from the object formed by the approximately 1% of the light passing through the pinholes. Petran et al eliminated the reflected light by using a set of mirrors, a beam splitter, and an image inverter under the disk. This arrangement was used to pass light through a conjugate set of holes in the disk on the side of the axis opposite from the region illuminated by the light source. This made it extremely difficult to align the system, and therefore required the use of somewhat larger holes than the optimum size for a standard confocal microscope. The alignment difficulties, and hence the tolerances required, tend to degrade the transverse and range resolutions of the microscope. Furthermore, it is extremely difficult to duplicate the system because of the problem of mechanical alignment of the pinholes with their conjugate pairs, along with the necessity to adjust the large number of optical components in the path.

Therefore, we decided that the best way to eliminate these difficulties was by passing both the transmitted and reflected light through the same pinhole, so the alignment is guaranteed by the principles of optics. To do this, we have developed a new system which we have called "the spiral scanning optical microscope (SSOM)." The system is illustrated in Fig. 3. The 20 μm diameter holes are spaced, on average, about 9 hole diameters apart. In our case, the average radius of the spirals is 4 cm, and the spirals extend over a radial distance of 1.8 cm with a total of 150,000 holes. Either a mercury vapor arc lamp or a laser beam is used to illuminate a circular area, 1.4 cm in diameter, containing about 4000 holes. The incident beam converges to a 5 mm diameter on the back of the objective lens so 4000 points on the object are illuminated simultaneously. Because of the spacing of the image points, there is negligible interference between the different illuminated regions. The disk is rotated at 2400 rpm. Since the holes are arranged along spiral paths, the rotation of the disk forms a raster scan across the object, thus yielding a 7000-line, 640 frame/sec image.

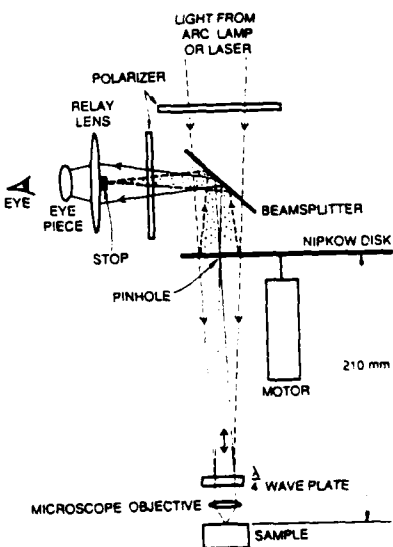


Fig. 3. A schematic of the spiral scanning optical microscope. the direct-view system is illustrated.

The light focused on the object is reflected from it and is, in turn, focused on the pinholes. An eyepiece and 1:1 transfer lens is used to observe the image of the pinholes, which corresponds to the image of the object. Thus, an instantaneous scanned image is received by the eye. Alternatively, an image can be, and has been, obtained on photographic film or a TV system. In the latter case, the transfer lens is used to form an image directly on the retina of the vidicon. The output of the vidicon can then be taken directly to a TV display system or an image processing system, which can be used to obtain line scans and to process the image in different ways.

We eliminate the reflected light from the disk by the following stratagems:

(1) We use the same hole for transmission and reception of the light. This measure made alignment relatively simple, in fact simpler than for a standard microscope. The eyepiece is focused on the pinholes using a light source behind the pinholes. The object can then be moved up or down to focus on the object plane. Since the pinholes are scanned, there are always pinholes within the field of view. Centering of the spirals is uncritical. Vibration is not a severe problem, provided that the disk vibrations have an amplitude much less than the depth of focus of the objective and transfer lenses at the pinholes, a distance greater than 1 mm in our case.

(2) We use a black emulsion photomask on glass for the disk (Petran et al used thin copper). This reduces the reflected light intensity to 4% of the incident light.

(3) We use a polarizer to polarize the light and an analyzer in front of the eyepiece rotated at 90° to reduce the background light intensity by 50 dB. A quarter-wavelength phase plate is used on the lower side of the disk to rotate the plane of polarization.

(4) A third technique, which we have not yet employed, is to place a small-diameter black mask at the focused image of the light source. This should completely eliminate the light directly reflected from the disk. With a collimated laser source, the mask need be only slightly larger than the diameter of the focused reflected beam. With an incoherent light source, the mask must block the reflected image of the light source.

It will be realized that this type of microscope should have the same range and transverse definitions as the standard single-pinhole CSOM. Its major disadvantage is that a much more powerful light source is required than for a standard CSOM. Approximately 1% of the light reaching the Nipkow disk passes through the pinholes. Furthermore, it is necessary to illuminate the complete field of view at one time. The advantages are the real-time imaging and the fact that it only requires a small, incoherent light source. This latter

property should make it possible to minimize the interference between waves reflected from the back and front surfaces of a transparent thin film, and to use a broadband light source extending over the whole optical wavelength range, thus yielding images in full color.

Experimental Results

The experimental system employed a 0.8 aperture 60X Nikon N-plan lens, a 100 watt mercury vapor arc source, and either a 15X eyepiece with a 1:1 transfer lens or a video camera or Nikon camera focused on the transferred image of the disk. We found the system to be extremely simple to align, far simpler than any confocal microscope with which we had worked in the past.

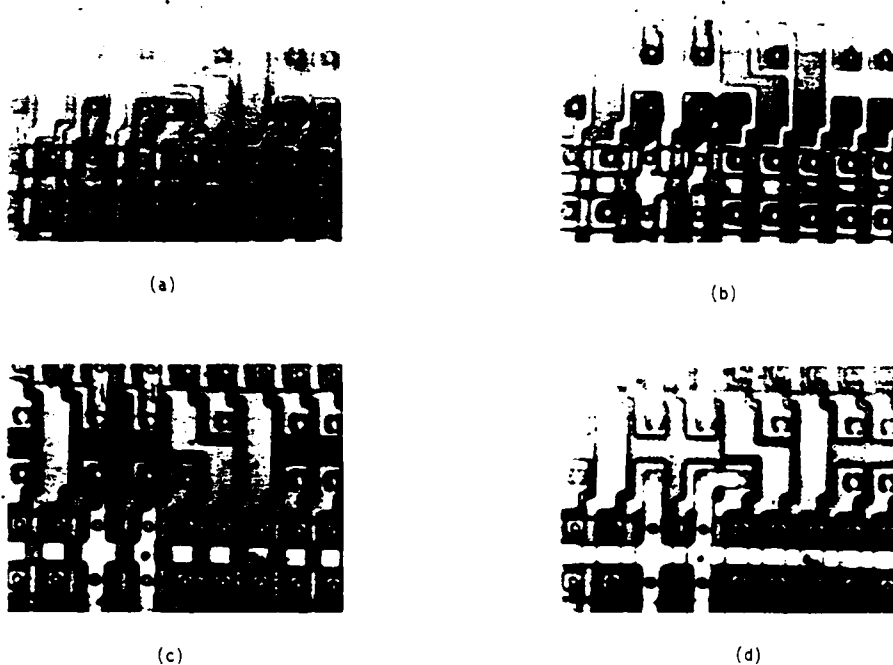


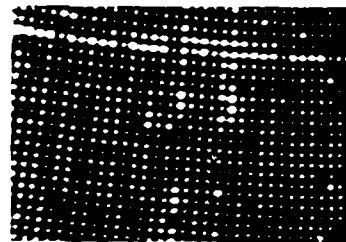
Fig. 4. Photographs of an integrated circuit as the sample is moved away from the objective. The sample is moved in incremental steps of: (a) 0 μ m, (b) 0.40 μ m, (c) 0.96 μ m, and (d) 1.77 μ m, respectively.

An image of a silicon integrated circuit, photographed from the video display screen, is shown in Fig. 4. The field of view is approximately 100 μ m across. Images 4a, 4b, 4c, and 4d were taken with the sample moved in steps away from the objective lens. It will be clearly seen that the images change as different planes of the object come into focus and then disappear. Figures 5a and 5b are images of the same sample with the disk rotating and stationary, respectively. The pinholes can be seen when the disk is stationary. The image taken compares favorably with that using a more conventional CSOM and a lens of the same aperture. The transverse resolution of the image and the contrast is somewhat better with the SSOM than with the use of a conventional microscope with a 0.95 objective lens. Furthermore, as the conventional microscope is defocused, it cannot pick out different layers of the object, as can the SSOM.

Photographs from the video screen of thin strips of SiO_2 on silicon 1 μ m wide and 0.6 μ m high are shown. A schematic of the sample is shown in Fig. 6a, with images of the sample in Figs. 6b and 6c. It is clear that the top and bottom surfaces of the SiO_2 layer can clearly be picked out when the system is focused on them.

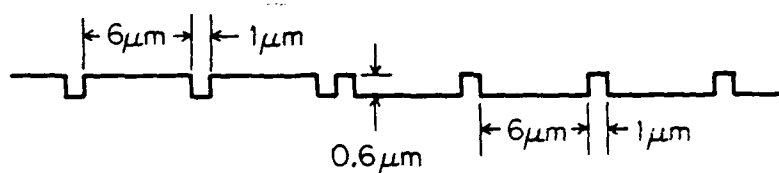


(a)



(b)

Fig. 5. Images of an integrated circuit with: (a) disk rotating, and (b) disk stationary.



(a)



(b)



(c)

Fig. 6. Images of 0.6 μm tall, 1 μm wide SiO_2 lines. (a) A schematic of the sample. (b) Beam focused on the top surface of the sample with (c) the sample moved 1.5 μm away from the objective.

To illustrate the resolution of the system, we have taken a set of photographs (Fig. 7) of a photoresist grating made for observation for an SEM. This grating is covered with a gold flash and is 0.5 μm deep. The form of the grating is also illustrated in Fig. 7. It will be seen that the 0.5 μm width can be clearly seen, while the 0.3 μm strip can barely be seen in the photograph. We have been able to observe, visually, 0.2 μm width strips. The calculated periodic spacing, which can just be resolved, is given by the Abbe criteria for this system by the relation

$$L = \frac{\lambda}{2 \sin \theta}$$

where λ is the wavelength. For $\lambda = 5500 \text{ \AA}$ and $\sin \theta = 0.8$, the calculated value of t is $0.35 \mu\text{m}$ or a strip width of $0.17 \mu\text{m}$, which compares well with the experimental value of $t = 0.4 \mu\text{m}$.



Fig. 7. Photograph of a grating of $1.0 \mu\text{m}$ and $0.6 \mu\text{m}$ period, with equal gap and strip widths.

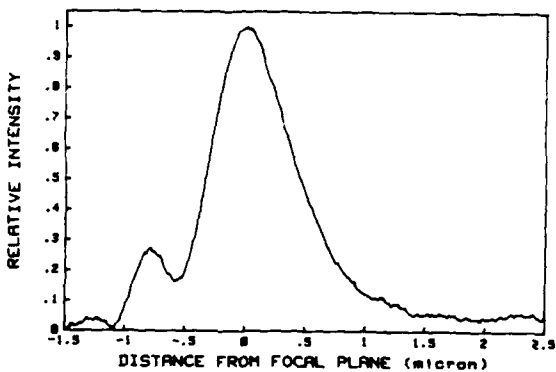


Fig. 8. A plot of intensity versus distance from the focus.

Finally, we show in Fig. 8 a plot of intensity at a photodetector placed in the image plane, versus defocus distance z , using a simple mirror as the object. The results were taken with the disk rotating, and are essentially identical to those obtained with the disk stationary. A simple theory indicates a range resolution between 3 dB points Δz (3 dB)

$$\Delta z(3 \text{ dB}) = \frac{.45 \lambda}{1 - \cos \theta}$$

For a 0.8 aperture lens and a wavelength of 5500 \AA , the calculated value of $\Delta z(3 \text{ dB})$ is 6125 \AA , where θ is the aperture angle, i.e., $\sin \theta = 0.8$. This value is close to the measured range definition of 7600 \AA . We believe that the slight discrepancy between experiment and theory is due to a slight tilting of the object with respect to the objective lens. Since the signal is being observed from point sources distributed over a region of the order of $80 \mu\text{m}$ in diameter, tilting would broaden the width of the intensity curve.

Conclusions

We have demonstrated a new type of real-time scanning optical microscope. This device operates in all respects like a confocal scanning optical microscope: the range and transverse definition appear to be of the same order as that of the conventional confocal scanning microscope. It is easy to construct and easy to line up. It can be used with an incoherent light source of small size and produces very high-quality images.

Acknowledgments

The authors would like to thank Tim Corle, who provided a great deal of help at all stages of the experiment. We would also like to thank Phil Hobbs, Jeff Fanton, and other members of our experimental microscopy group for numerous discussions on the basic ideas behind the microscope and for help with the experiments. In addition, we would like to thank Simon Bennett, Ian Smith, and Jim Lindow of SiScan for helpful discussions, for supplying us with samples, and for loaning us instruments. We are also grateful to Bob Bray and Steve Erasmus of Hewlett-Packard for supplying us with a number of useful samples, and to Frank Lundy and Viasta Cejna of Technical Instruments for useful discussions and for loaning us several lenses for use in our experiments.

This work was supported by the Office of Naval Research under the Joint Services Program, Contract No. N00014-84-K-0327.

References

1. M. Petran, M. Hadraovsky, M. D. Egger, and R. Galambos, "Tandem-Scanning Reflected-Light Microscope," *J. Opt. Soc. Amer.* 58, 661-664 (1968).
2. M. Petran, M. Hadraovsky, J. Benes, R. Kucera, and A. Boyde, "The Tandem Scanning Reflected Light Microscope, Part 1: The Principle and Its Design," *Proc. Roy. Microscopical Soc.* 20, 125-129 (1985).
3. A. Boyde, "The Tandem Scanning Reflected Light Microscope, Part 2: Pre-Micro '84 Applications at UCL," *Proc. Roy. Microscopical Soc.* 20, 131-139 (1985).
4. T. Wilson and C. Sheppard, *Theory and Practice of Scanning Optical Microscopy*, Academic Press, London (1984).
5. S. D. Bennett, J. D. Lindow, and I. R. Smith, "Integrated Circuit Metrology with Confocal Optical Microscopy," *Phil. Trans. Roy. Soc. London, Series A* 320, 307-313 (1986).

1271

**SWITCHABLE OPTICAL FIBER TAPS USING THE
ACOUSTO-OPTIC BRAGG INTERACTION**

A DISSERTATION
SUBMITTED TO THE DEPARTMENT OF ELECTRICAL ENGINEERING
AND THE COMMITTEE ON GRADUATE STUDIES
OF STANFORD UNIVERSITY
IN PARTIAL FULFILLMENT OF THE REQUIREMENTS
FOR THE DEGREE OF
DOCTOR OF PHILOSOPHY

By

Brian Lee Heffner

August 1986

Chapter 7

Conclusions and Summary

We now have an opportunity to highlight the main results of this dissertation so they will not be lost in the details of their initial presentation. All of the results quoted in this chapter will be original contributions unless specifically represented otherwise. A review of the wedge tap and the array tap will be followed by a review of the new physical relations resulting from the theory of Bragg diffraction from a thin fiber core. The chapter will close with a few suggestions for future research, based on the experience and knowledge gained from this work.

The contacting-wedge tap

The contacting-wedge tap was the first demonstration of a switchable optical fiber tap using the acousto-optic Bragg interaction. It exhibited for the first time some of the properties expected of a Bragg-diffracting fiber tap, such as the linear relationship between rf drive power and tap efficiency, and the resonant behavior of acoustic reflections within the fiber. The wedge tap demonstrated the feasibility of launching a high-frequency acoustic beam into a fiber through a direct Hertzian contact. This contact is nondestructive and completely reversible, so the position of the tap on the fiber can be adjusted simply by lifting the wedge and moving it to another desired tap location. In addition, no difficult preparation of the fiber is necessary, as the fiber cladding can

usually be exposed by stripping away the protective plastic jacket with a sharp knife. A D-fiber was used to facilitate the Hertzian contact, but it may be possible to make good contact to a standard cylindrical fiber by first polishing a cylindrical groove in the wedge. This would allow the tap to be used as a general-purpose nondestructive probe for fiber-optic systems.

As expected, the frequency response of the tap exhibited a periodic structure attributed to acoustic resonance within the fiber. Neglecting this resonance, the tap efficiency was measured to be $-38 \text{ dB} / \text{W}_{\text{input}}$, with a center frequency of 3.4 GHz. The bandwidth of the tap, limited by the acoustic transducer, was greater than 1 GHz, so the tap weighting could be adjusted in less than 1 ns. The characteristics of the guided mode in the D-fiber were not precisely known, but by estimating an effective width of $2 \mu\text{m}$ for the optical field at the core, an efficiency of $-41 \text{ dB} / \text{W}_{\text{input}}$ was predicted by the theory of chapter two.

Operation of the wedge tap was based on the possibility of acoustic transmission through a direct Hertzian contact. A transmission loss of 1.2 dB at 7 GHz was demonstrated through a contact between two sapphire pieces, and at the same time techniques were developed for alignment of the two pieces relative to one another. The alignment technique depended on the ability to monitor acoustic reflections, but the reflections within the wedge of the wedge tap arrived at the transducer at a large angle to the normal. A transducer in the shape of a grating had to be designed to allow these oblique reflections to be monitored. This grating transducer led to the idea of the acoustic array tap, where a phased array of acoustic transducers generates an acoustic beam in the fiber at the Bragg angle.

The acoustic array tap

It is possible to take advantage of the cylindrical shape of a standard optical fiber to focus an acoustic field onto the fiber core for more efficient acousto-optic interaction. The acoustic array tap employed a phased array of acoustic transducers fabricated directly on the surface of a cylindrical fiber. Fabrication of this device required the development of new technology both for the deposition of oriented zinc oxide and for photolithography on the surface of an optical fiber. In chapter five a phased array of transducers on the fiber surface was designed to generate an acoustic field at the fiber core which satisfied the Bragg condition.

The measured tap efficiency was $-24 \text{ dB/W}_{\text{input}}$, compared to a predicted efficiency of $-21.4 \text{ dB/W}_{\text{input}}$ as calculated according to the theory set forth in Chapters 2 and 5. In this initial device the center frequency of the transducer was a bit higher than expected, and it appears possible to achieve better than $-20 \text{ dB/W}_{\text{input}}$ efficiency simply by matching the transducer center frequency to the interaction center frequency. The device has been tested with input powers of up to 0.1 W . At higher power levels the carbon tetrachloride index-matching fluid begins to boil, so the absolute efficiency is limited to about -30 dB . This limit may be increased by using a less volatile matching fluid. The tap efficiency peaked at 3.3 GHz , and had a bandwidth of approximately 920 MHz .

The array tap is a monolithic device which requires no mechanical alignment. It is probably better suited to production in large quantities (as would be required for an adaptive signal processing system) than is the wedge tap, which would require careful mechanical adjustment at each tap. On the other hand, an array tap can only be fabricated on a fiber in a vacuum sputtering system, so it is not possible to tap an existing fiber in the field using this technique, or to move the tap to a new location on the fiber. The

array tap demonstrates a new technological capability to fabricate acoustic transducers directly on the side of an optical fiber, of a quality comparable to that of planar transducers.

The narrow-beam interaction

By analyzing acousto-optic Bragg diffraction as far-field radiation from the optical antenna formed by the wave interacion region, the characteristics of Bragg diffraction were shown in chapter two to fall into two regimes. The wide-beam regime applies to the traditional interaction geometry with a wide optical beam. The narrow-beam description applies to an interaction at a high acoustic frequency with a narrow optical beam (such as that guided by a fiber) and a relatively wide acoustic beam. The distinction between the two regimes is determined by geometric parameters:

$$\text{Wide-Beam Regime} \quad b \tan \psi / d \ll 1 \quad (2.61)$$

$$\text{Narrow-Beam Regime} \quad b \tan \psi / d \gg 1 \quad (2.62)$$

where b is the acoustic beamwidth, d is the optical beamwidth, and ψ is the deflection angle of the diffracted optical beam.

At the end of chapter two the properties of the narrow-beam interaction are compared to those of the wide-beam interaction, so there is no need for a similar review here. In a nutshell, there are two fundamental new results of the narrow-beam analysis, from which other results can be derived. One new result is that the angular resolution of the diffracted optical beam is determined by the acoustic beamwidth instead of by the optical beamwidth. This leads to a number of resolvable diffracted spots which is twice the time-bandwidth product of the interaction. The second fundamental new result is that

the wave interaction length L is given by $L = d / \sin \psi$, so it is proportional to the optical beamwidth instead of the acoustic beamwidth. The interaction length must be taken into account when calculating both the tap efficiency and the interaction bandwidth.

Future research

The conclusion of this dissertation would not be complete without a few brief suggestions of areas which might provide fertile grounds for research in the near future. In a sense, these suggestions summarize the potential uses for the contributions of the dissertation.

The wedge tap could be very useful as a nondestructive probe for *in situ* fibers, but its current design precludes its use on standard cylindrical fibers. If a cylindrical groove were machined in the contacting face of the wedge, a Hertzian contact might be made to standard fibers. Admittedly, polishing a groove of the required shape and dimensions would not be easy. Such a device would also be useful as a tap for high-bandwidth fiber communication lines. A new user could be connected to an existing fiber without breaking the fiber.

The wedge tap illustrates that the piezo-optic function of a Bragg cell can be separated from its propagation-delay function. In a traditional Bragg cell the acousto-optic medium serves as both the acoustic delay medium and the piezo-optic medium, forcing a trade-off between low acoustic attenuation and a high piezo-optic coefficient. Very high frequency Bragg cells might benefit from a geometry similar to that of the wedge tap, except that a highly piezo-optic planar waveguide could be deposited directly on the wedge, obviating the Hertzian contact (Fig. 7.1). The wedge material can be chosen for low acoustic attenuation regardless of its optical properties, making long propagation delays possible even at very high frequencies.

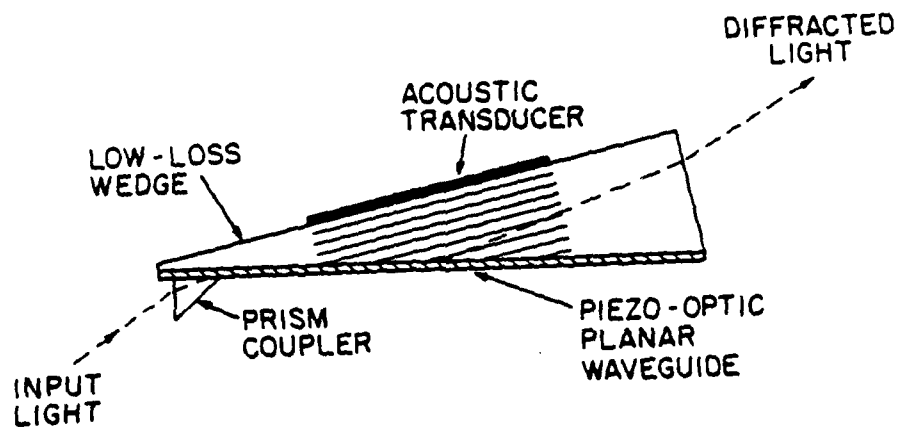


Fig. 7.1. A high-frequency Bragg cell in which a highly piezo-optic planar waveguide is deposited on a low-loss wedge.

Technology for the deposition of zinc oxide and for photolithography on the surface of an optical fiber was developed for fabrication of the array tap, but can be applied to other all-fiber acousto-optic modulators. At the time of writing, this technology is being used to fabricate a phase modulator with a large range of phase control. A transducer on the surface of a cylindrical fiber generates a focused acoustic beam, leading to efficient acousto-optic interaction at the fiber core. Unlike most fiber modulators, these devices are monolithic, with no need of adjustment or mechanical alignment. The design of new devices incorporating this technology and their application to fiber-optic systems may lead to many useful results.

Reprinted from SPIE Vol. 719—Fiber Optic Gyros: 10th Anniversary Conference
© 1987 by the Society of Photo-Optical Instrumentation Engineers, Box 10, Bellingham, WA 98227 0010 USA

Invited Paper

All-fiber-optic gyroscopes

B. Y. Kim and H. J. Shaw

Edward L. Ginzton Laboratory, W. W. Hansen Laboratories, STANFORD UNIVERSITY
Stanford University, Stanford, California 94305

Abstract

The development of all-fiber-optic gyroscopes at Stanford University is reviewed. Fiber-optic components for the gyroscopes are described. Techniques to suppress various error sources, and different approaches to a linear scale factor with wide dynamic range, are discussed. Fiber-optic single sideband frequency shifters for closed-loop operation of gyroscopes are described. A new approach to high birefringence fiber gyroscopes, with broadband optical source and birefringence modulation, is presented. Other approaches, including the pulsed reentrant fiber gyro, are shown.

Introduction

Soon after the first experimental demonstration of a Sagnac interferometer using optical fiber¹, it was realized that stability of the interferometer against environmental changes would be critical to achieving high performance in a fiber-optic gyroscope. Bulk optic components such as beam splitters, polarizers and birefringent plates used in the optical circuit could not provide alignment tolerances adequate for practical gyroscopes. One of the solutions for this problem was proposed and demonstrated at Stanford University. Single-mode fiber versions of these bulk optic elements were developed, in the form of fiber-optic directional couplers², polarizers³ and polarization controllers⁴. Along with fiber-optic phase modulators⁵, these made it possible to build an all-fiber gyroscope on a single strand of single-mode fiber⁶. This resulted in a low-loss interferometer combining the optical reciprocity^{7,8} of all-single-mode operation with the mechanical stability of all-fiber construction. With this system, it was possible to study other, more subtle noise mechanisms and to demonstrate low noise performance^{9,10}.

Being interferometers, the linear dynamic range of such gyroscopes was quite limited due to the non-linear (cosinusoidal) response of the output to rotation rate. One way to extend the linear dynamic range was to use electronic closed-loop operation of the gyro employing a single-sideband frequency shifter in the fiber sensing coil to neutralize the rotation induced Sagnac phase shift^{11,12}. The frequency shifters were not available in fiber-optic form. In order not to compromise the all-fiber-optic approach to the gyroscope, a considerable effort was made to use existing fiber phase modulators as feedback control elements in closed-loop gyroscopes, and a few such gyros have been demonstrated¹³⁻¹⁵. At the same time, the development of fiber-optic frequency shifters has been pursued at Stanford University using acousto-optic interaction in birefringent^{16,17,18} and two-mode^{19,20} optical fibers. Another successful demonstration of a gyro with an extended linear dynamic range was made using a synthetic heterodyne technique in an open-loop gyro with a phase modulator^{21,22}. The next stage of fiber gyro development at Stanford involved a high birefringence fiber gyro with a broadband optical source such as a superluminescent diode. A technique for accurate alignment of the birefringent axes in fiber-optic components was developed²³ in order to reduce the polarization cross-coupling in the fiber circuit. One of the current research efforts is directed at finding the optimum combination of available components which can produce the minimum nonreciprocal phase error²⁴. Another active research area is the development of an all-fiber acousto-optic frequency shifter using two-mode fiber, in which the optical wave and an acoustic flexural wave are both guided by the fiber^{19,20,25}.

Low-noise all-fiber-optic gyroscope

Figure 1 shows the schematic of an all-fiber-optic gyroscope. It is a reciprocal configuration in that, in the absence of rotation, the two counter-propagating waves travel exactly the same optical path^{7,8}. The basic fiber-optic components are directional couplers (DC)², a polarizer (P)³ and polarization controllers (PC)⁴, as shown in Fig. 2. The directional coupler was formed by bringing the cores of two fibers very close together so that the evanescent fields of the guided modes overlap. This involved removal of most of the cladding material on the mating side of each fiber by grinding and polishing. The optical power splitting ratio can be adjusted by adjusting the separation of the two cores. Polarizers with a very high extinction ratio were made by using evanescent coupling between the guided mode

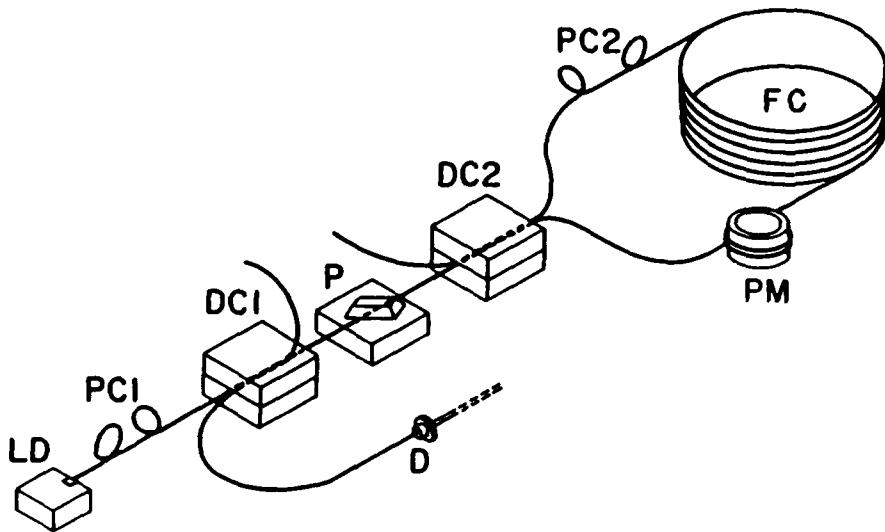


Figure 1: A schematic diagram of an all-fiber-optic gyroscope. LD: laser diode, PC: polarization controller, DC: directional coupler, P: polarizer, PM: phase modulator, FC: fiber coil, D: detector.

of the fiber and a birefringent crystal. The two orthogonal polarization modes of the fiber experience different effective refractive indices in the crystal such that one of the modes is no longer guided. Polarization controllers were necessary in order to compensate for the random birefringence in the fiber circuit and thus prevent signal fading due to drifting of the polarization. The polarization controllers consist of two fiber loops of controlled diameter to induce bending birefringence that corresponds to two quarter-wave retardation sections. The birefringence axes are perpendicular and parallel to the plane of the bend, whose orientation can be adjusted in order to transform any input polarization state to any arbitrary output polarization.

All these fiber components can be built on an uninterrupted length of single-mode fiber to form a complete optical circuit, or can be spliced together after being fabricated separately. Using these fiber-optic components developed at Stanford University, along with a fiber phase modulator, a fiber gyro with very low loss and excellent mechanical stability was constructed⁹.

The phase modulator located at one end of the sensing fiber coil provides a modulation in phase difference between the two counter-propagating optical waves. This non-reciprocal phase modulation was used to shift the operating point of the gyro from the zero sensitivity point to the maximum sensitivity region^{8,26}. It also removed electronic 1/f noise by translating the signal to a high frequency carrier and allowing the use of phase sensitive detection. Another important advantage of this detection technique is that the signal at zero rotation is independent of source optical power, amplitude of phase modulation and gain in the detection electronics, which led to substantial improvement in long term stability of the rotation measurement. An imperfect phase modulator, however, can generate phase modulation at harmonics of the modulation frequency, polarization modulation and amplitude modulation, which, constitute error sources. It was noticed that these error sources do not degrade the rotation measurements if a proper phase modulation frequency is used⁹. The appropriate period of this modulation signal corresponds to twice the transit time of the light through the sensing fiber coil, and provides the maximum differential phase modulation for a given modulation amplitude.

One of the major noise sources was shown to be coherent backscattering from the optical circuit that interferes with the main optical signal²⁷. The phase of the backscattered wave fluctuates in response to environmental changes, which results in noise in the rotation measurement. The use of a multi-mode laser diode⁹ drastically reduced this type of error. It was also noticed that, when the proper phase modulation frequency mentioned earlier was used, the coherent backscattering noise could be suppressed at zero rotation rate¹⁰. By employing these techniques, the coherent backscattering error could be made insignificant.

Other noise in the fiber gyroscope came from time-varying environmental perturbations (such as temperature,

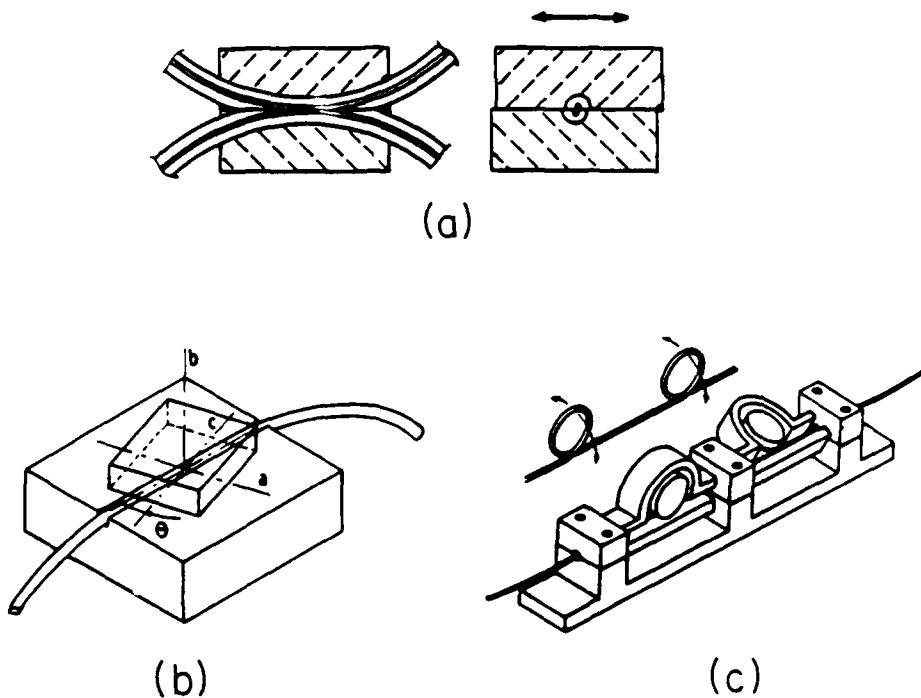


Figure 2: Fiber-optic components: (a) directional coupler, (b) polarizer, (c) polarization controller.

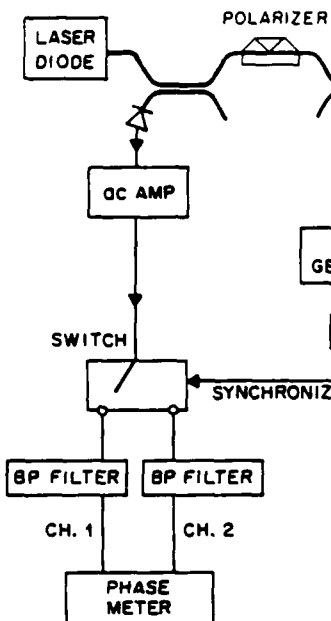
pressure and mechanical vibrations) acting directly and asymmetrically on the phases of the counter propagating optical waves in the sensing coil. When the perturbations change significantly during the transit time of light through the coil, the two counter propagating waves experience different phase changes, leading to an error. The solution, suggested elsewhere²⁸, was to minimize the difference in times at which the two optical waves pass through the location of the external perturbation by using an appropriate winding pattern for the fiber coil. In this scheme, the maximum time difference is reduced to the transit time of light once around the circumference of the winding spool. This substantially reduced time varying noise within the detection bandwidth.

The optical intensity dependent non-reciprocal phase error observed at MIT²⁹ had to be suppressed in order to achieve highly sensitive rotation measurement. This error is proportional to the optical intensity imbalance between the counter propagating beams. In order to suppress this error without imposing an unrealistic tolerance on the coupling ratio of the directional coupler, an intensity modulated optical source³⁰ or a source with proper spectral characteristics³¹ was used. Finally, the non-reciprocal Faraday effect due to Earth magnetic fields was suppressed simply by using a magnetic shield.

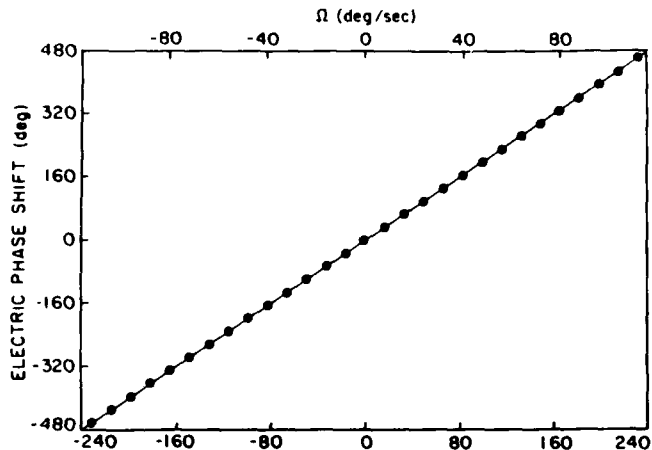
When all the measures described above were incorporated in the all-fiber-optic gyroscope, a mechanically stable gyroscope with inertial navigation grade sensitivity¹⁰ and good long-term bias stability⁹ was demonstrated in the laboratory environment. The performance demonstrated at that time(1981) still remains today as one of the best yet reported. Having achieved this performance near zero rotation rate, the direction of research at Stanford then was focused on developing techniques for achieving a linear, stable scale factor with wide dynamic range.

Linear scale factor

The basic output of the fiber gyroscope of Figure 1 has a highly non-linear (cosinusoidal) response to rotation rate, which limits its linear dynamic range. In order to achieve a linear response to rotation rate, the differential phase shift between the counter-propagating waves (Sagnac phase shift) needs to be measured in other ways, rather than inferring its value from the output intensity of the interferometer. Generally speaking, there are two categories



(a)

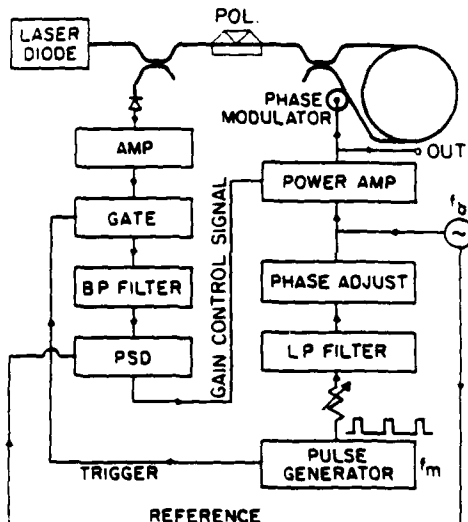


(b)

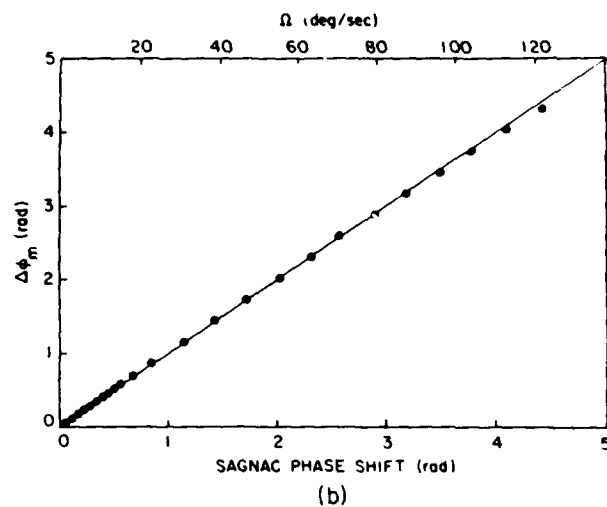
Figure 3: A schematic of a synthetic heterodyne open-loop gyroscope (a), and its measured scale factor (b).

of techniques to recover the optical phase information from the interferometer output: open-loop and closed-loop approaches. In the open-loop approach, electronic signal processing is applied to the detector current which contains quadrature information on the optical phase difference, in order to retrieve the Sagnac phase shift, which is linearly proportional to rotation rate. This approach usually utilizes signals in the detector current at odd and even harmonics of the phase modulation frequency applied to the gyroscope. The closed-loop approach, on the other hand, uses a non-reciprocal phase shifter in the fiber sensing coil that counteracts the rotation induced Sagnac phase shift. The rotation signal from the detector is fed back to the non-reciprocal phase shifter to keep the net phase difference between the counter-propagating waves at zero. In this case, the operating point of the gyroscope is maintained at the optimum point and the non-reciprocal phase shift introduced by the phase shifter is equal and opposite to the Sagnac phase shift. We have been investigating both approaches in all-fiber gyro configurations in order not to compromise the high performance of that configuration near zero rotation rate.

Figure 3 shows a schematic of an open-loop gyroscope, which we term a synthetic heterodyne gyroscope^{21,22}. The optical circuit is the same as the one shown in Figure 1 and no new optical elements are added. The same phase modulator as used for dynamically biasing the gyroscope was used to generate low frequency rf carriers at



(a)



(b)

Figure 4: The experimental setup (a) and results (b) of the gated phase modulation closed-loop gyroscope.

harmonic frequencies of the modulation frequency. In this case, the detector currents at odd and even harmonics of the modulation frequency are proportional to the sine and cosine of Sagnac phase shift, respectively. Using very simple electronic signal processing, these detector current components are combined at a common frequency, with proper phase relationship, to form two low-frequency rf signals with constant amplitude. The phase difference between these two rf signals is twice the Sagnac phase shift, and can be measured using conventional phase meters such as time interval counters. In essence, this synthetic heterodyne technique translates optical phase difference in an interferometer to phase difference of low frequency electronic signals that can be directly measured. Figure 3-b shows an experimental measurement of linear scale factor for such an all-fiber gyroscope. The same technique can be used to solve the signal fading problem in other types of interferometric sensor systems.

For closed-loop operation of fiber gyroscopes, electronic/optical control elements that can provide variable differential phase shift between the counter-propagating waves must be inserted into the fiber sensing coil. Although single sideband frequency shifters^{11,12} or broad bandwidth electro-optic phase modulators³² can be used for this purpose, no such components in fiber-optic form are available. In one attempt to retain the all-fiber configuration, we used an already existing fiber phase modulator³ as a control element. A sinusoidal phase modulation applied to the gyroscope cannot provide a non-reciprocal phase shift since the differential phase shift generated during one half cycle of the modulation waveform will be canceled by that produced in the next half cycle. However, if the detector current is gated off during every other half cycle of the modulation waveform, a net average differential phase shift can be achieved. This effective non-reciprocal phase shift is directly used for closed-loop operation of gyroscope¹⁴. By using two-frequency phase modulation, the linearity of the scale factor is improved significantly¹⁵. Figure 4 shows the schematic diagram of such a gyroscope and the experimentally measured response of the gyro to rotation rate. This class of control elements has the important feature of giving a scale factor which is independent of source wavelength change.

Fiber-optic frequency shifter

As mentioned earlier, a single sideband frequency shifter located in the fiber sensing coil can provide a differential phase shift for closed-loop operation of the gyroscope. Efforts have been made at Stanford University to realize fiber-optic frequency shifter using the acousto-optic effect in birefringent fibers and in two-mode fibers. Figure 5 shows a schematic of a fiber-optic frequency shifter using high birefringence single-mode fiber¹⁷. A surface acoustic

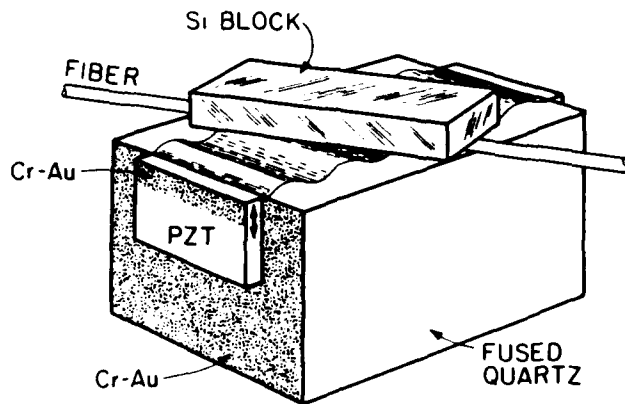
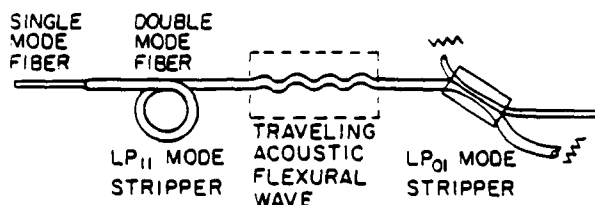


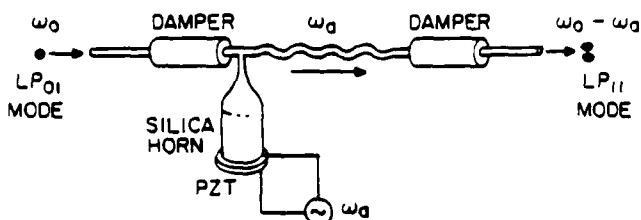
Figure 5: A fiber-optic frequency shifter using a birefringent optical fiber and surface acoustic wave.

wave provides a traveling periodic stress applied to the fiber at 45° with respect to its transverse birefringent axes, which couples optical signals from one polarization mode to the other and shifts the optical frequency by the amount of the applied acoustic frequency. For phase matching between the waves, the period of the applied stress must be approximately equal to the beat length between the two polarization modes. By properly angling the fiber with respect to the propagating direction of the surface acoustic wave, the operational acoustic frequency that provides proper phase matching can be made high enough to allow the desired tuning range for the frequency shift. Suppression of spurious signals by the order of 25 dB to 40 dB has been demonstrated. Alternatively, the angle between the fiber and the acoustic wave propagation direction can be made zero, with phase matching at high acoustic frequency achieved by cutting transverse grooves in the silicon block to give periodic coupling between the fiber and acoustic wave along the interaction region¹⁸. This allows a longer interaction region and a narrower acoustic beam. To achieve higher spectral purity in the shifted optical signal in birefringent fiber devices, suitable for high performance fiber-optic gyroscopes, however, very high accuracy of angular alignments of input and output polarization filters would have to be accomplished. Moreover, any static stress applied to the fiber in the process of coupling acoustic energy into the fiber alters the direction of the birefringent axes, and results in degradation of spectral purity.

In order to avoid these problems, a new type of all-fiber acousto-optic frequency shifter using a two-mode optical fiber was proposed and demonstrated^{19,20} (Figure 6). Two mutually orthogonal spatial modes guided by the fiber (LP_{01} and LP_{11}), instead of two polarization modes, are used. A traveling acoustic flexural wave guided in the same optical fiber provides a periodic coupling between the two optical modes. A very efficient excitation of the acoustic wave in the fiber is accomplished by an acoustic horn, bonded to the fiber with low melting temperature glass. The acoustic wavelength is approximately equal to the beat length between the LP_{01} and LP_{11} modes. Since the acoustic energy is confined within the same optical fiber that guides the optical signal, the coupling efficiency is very high and 100 % mode conversion is achieved with low electrical input power. For high spectral purity, good mode filters are necessary. It is well known that a tight bend with a proper diameter can eliminate the LP_{11} mode without causing significant loss for the fundamental, LP_{01} mode, and this is used to assure an initially pure LP_{01} mode excitation. To eliminate the remaining LP_{01} mode after mode conversion, however, a new modal filter is used. The new filter is an evanescent field directional coupler formed by a two-mode fiber and a single-mode fiber, where only the LP_{11} mode of the two-mode fiber couples to the single-mode fiber²¹. The input and output leads of this frequency shifter are single-mode fibers which can be directly spliced to any single mode system. Carrier and image sideband suppression, currently at the 35 dB level, appears to be limited only by the non-optimized fiber parameters used, and is not a critical function of fiber alignment. The next step is to obtain special fibers in attempts to realize higher extinction ratios needed for the most demanding gyroscopes.



(a)



(b)

Figure 6: An all-fiber acousto-optic frequency shifter using a two mode optical fiber and acoustic flexural wave guided in the fiber.

High birefringence fiber gyroscope

The use of high birefringence fiber in conjunction with a broadband optical source, such as a superluminescent diode, not only eliminates the problems of signal fading and coherent backscattering but it also provides further reduction of non-reciprocal phase error due to polarization cross coupling in the optical circuit³³. For the construction of fiber-optic components such as directional couplers and polarizers needed for a gyroscope, however, the birefringent axes of the fiber must be aligned with high accuracy in order to minimize polarization coupling in the components. We developed a technique for alignment of the fiber birefringent axes with the accuracy of a fraction of a degree that led to construction of directional couplers with -28 dB polarization cross coupling²³. This technique uses the elasto-optic effect which induces polarization cross coupling when the fiber is squeezed along directions not parallel to one of its birefringent axes. This alignment procedure has the advantage of aligning the fiber *in situ* during device fabrication, and is specific to the axis alignment inside the device interaction region.

Although a number of high birefringence fiber gyroscopes using superluminescent diode sources have been demonstrated by many research groups, sufficiently low bias drift for inertial navigation applications has not been demonstrated. A straightforward way in principle of reducing the bias drift errors would be to improve the extinction ratio of the polarizer and/or reduce the polarization mode coupling in the optical components such as directional couplers and optical fiber. However, this approach tends to push the state of the art of current technology. We are exploring the combination of several reciprocity enhancing effects in one gyroscope, to achieve better suppression of bias drift without imposing impractical requirements on any one of the optical components. One way to achieve reciprocal operation is to use a perfectly unpolarized optical source with no polarizing element in the optical circuit³⁴. In this case, the phase error term in one polarization mode has equal magnitude and opposite sign to that in the orthogonal polarization mode. Another way is to modulate the relative phase of the two orthogonal polarization components (birefringence modulation) at several places in the optical circuit³⁵. In this way, the error signals can be modulated in time and averaged to low values. A prototype of a high birefringence fiber gyroscope that contains the essential

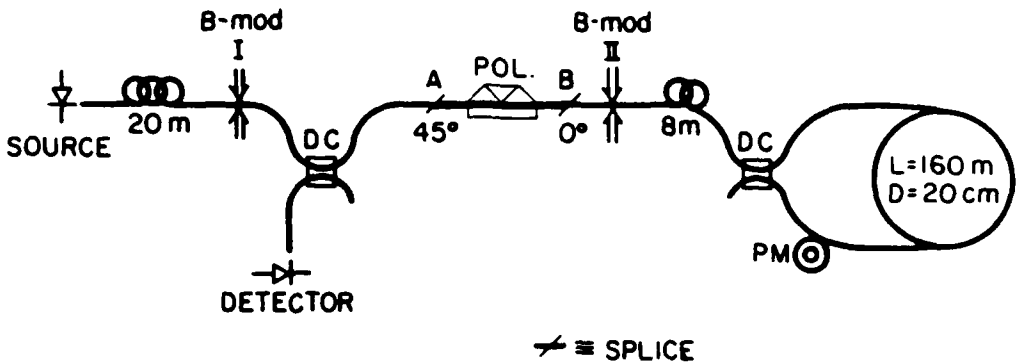


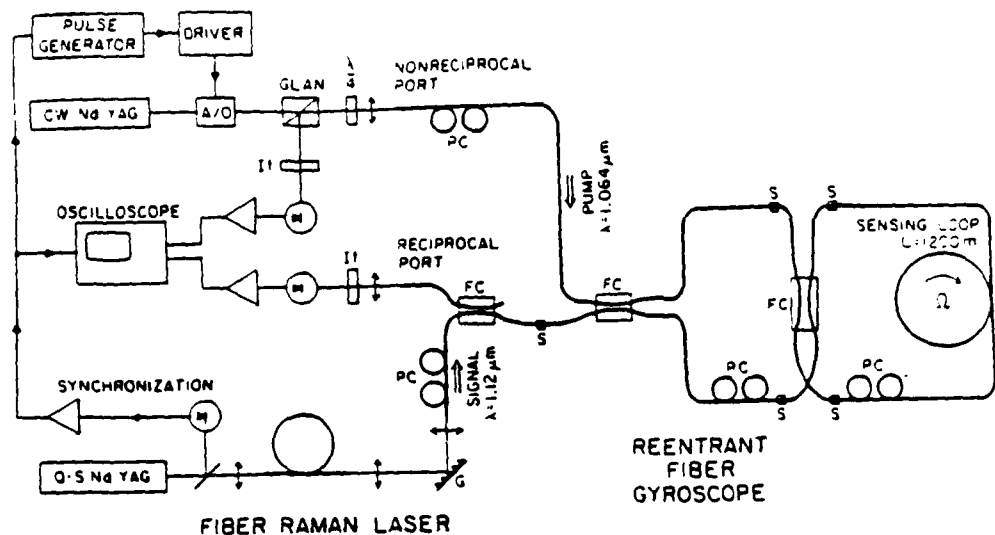
Figure 7: A schematic of a high birefringence fiber gyroscope with birefringence modulators and equal light excitation of the two polarization modes. B-mod: birefringence modulator.

elements of all three of these approaches is under construction²⁴. Figure 7 is the schematic of the gyroscope. Light from a superluminescent diode is directed to the polarizer with equal intensities along the transmission and cutoff axes of the polarizer. This polarizer has a finite extinction ratio. After the polarizer, the main polarization component and the component that leaked through the cutoff axis of the polarizer are made to be incoherent, within the detection bandwidth of the gyro, by a birefringence modulator and a long length of a birefringent fiber. The birefringence modulator is constructed directly on the high birefringence fiber by squeezing the fiber parallel to one of its birefringent axes using a piezo-electric modulator. In this case, the non-reciprocal phase errors in the two orthogonal polarization modes, which are already reduced by the polarizer, have equal magnitude but opposite sign due to equal light excitation of the two polarizer axes, leading to further suppression of bias drift error. Preliminary experimental results show the reduction of bias drift by orders of magnitude by the combination of equal excitation and birefringence modulation.

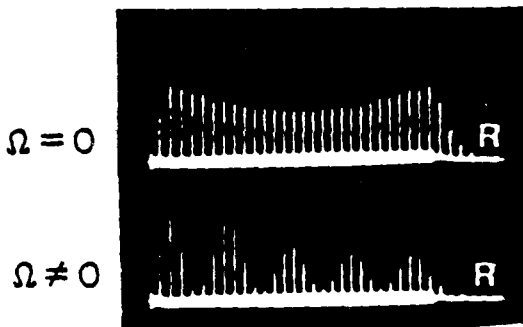
Other approaches

Other approaches to fiber-optic gyroscopes have been explored at Stanford University. One interesting approach, referred to as a pulsed reentrant fiber gyro^{7,36,37}, uses optical pulses rather than continuous waves. One input pulse is split into two counterpropagating pulses that recirculate around the fiber sensing coil many times, and the Sagnac phase shift is enhanced in proportion to the number of recirculations. The round-trip signal loss can be neutralized by an optical amplifier inserted in the fiber sensing coil, allowing many recirculations with substantially zero loss of signal intensity. The schematic diagram of a re-entrant fiber gyro is shown in figure 8-a, where optical amplification is provided by stimulated Raman scattering in the glass fiber³⁷. For a single input optical pulse, a portion of the signal is monitored after each transit of the fiber coil, producing a long train of output pulses whose envelope is sinusoidally modulated. The modulation frequency is the same as the beat frequency of a ring laser gyroscope and can be used as a digital measure of rotation angle with large linear dynamic range. Figure 8-b shows a typical output from this gyroscope.

Another approach investigated at Stanford is a passive ring resonator gyro³⁸ using a fiber-optic resonator³⁹. A coherent optical source is used and the rotation rate is determined by measuring the difference in resonant frequencies of the coil in the two propagation directions. This difference is linearly proportional to rotation rate, leading to a linear scale factor over a wide dynamic range. One of the attractive features of this approach is that the length of the fiber can be much shorter than in a regular fiber gyro, and the coil may be a single turn loop. The use of a long coherence source, however, makes it non-trivial to suppress the coherent backscattering noise and frequency lock-in effect. Precise polarization control inside and outside of the resonator is necessary to achieve a sensitive rotation measurement.



(a)



(b)

Figure 8: (a) A re-entrant fiber gyroscope with optical amplification provided by Stimulated Raman Scattering. (b) Experimental results with and without rotation input.

Conclusion

The development of all-fiber-optic gyroscopes and related components are reviewed. Techniques to suppress noise and bias drift, approaches to extended linear dynamic range, and fiber-optic frequency shifters are described. Current research efforts are focused on determining the optimum optical circuit for inertial navigation grade gyroscopes and developing a fiber-optic frequency shifter for wide linear dynamic range of rotation sensing.

Separate parts of Stanford University work described herein were supported by the Joint Services Electronic Program, the Air Force Office of Scientific Research, and Litton Systems, Inc.

References

1. Vali, V. and Shorthill, R. W., "Fiber-ring interferometer," *Appl. Opt.*, Vol. 15, 1099-1100. 1976.
2. Bergh, R. A., Kotler, G. and Shaw, H. J., "Single-mode fiber-optic directional coupler," *Electron. Lett.*, Vol. 16, 260-261. 1980.
3. Bergh, R. A., Lefevre, H. C. and Shaw, H. J., "Single-mode fiber-optic polarizer," *Opt. Lett.*, Vol. 5, 479-481 1980.
4. Lefevre, H. C., "Single-mode fiber fractional wave devices and polarization controllers," *Electron. Lett.*, Vol. 16, 778-780. 1980.
5. Davies, D. E. N. and Kingsley, S. A., "Method of phase-modulating signals in optical fibers: application to optical telemetry systems," *Electron. Lett.*, Vol. 10, 21-22. 1974.
6. Bergh, R. A., Lefevre, H. C. and Shaw, H. J., "All-single-mode fiber-optic gyroscope," *Opt. Lett.*, Vol. 6, 198-200. 1981.
7. Arditty, H. J., Shaw, H. J., Chodorow, M. and Kompfner, R., "Re-entrant fiberoptic approach to rotation sensing," *Proc. Soc. Photo-Opt. Instrum. Eng.*, Vol. 157, 138-148. 1978.
8. Ulrich, R., "Fiber-optic rotation sensing with low drift," *Opt. Lett.*, Vol. 5, 173-175. 1980.
9. Bergh, R. A., Lefevre, H. C. Shaw, H. J., "All-single-mode fiber-optic gyroscope with long term stability," *Opt. Lett.*, Vol. 6, 502-504. 1981.
10. Lefevre, H. C., Bergh, R. A. and Shaw, H. J., "All-fiber gyroscope with inertial navigation short-term sensitivity," *Opt. Lett.*, Vol. 7, 454-456. 1982.
11. Davis, J. L. and Ezekiel, S., "Techniques for shot-noise-limited inertial rotation measurement using a multi-turn fiber Sagnac interferometer," *Proc. Soc. Photo-Opt. Instrum. Eng.*, Vol. 157, 131-136. 1978.
12. Cahill, R. F. and Udd, E., "Phase-nulling fiber-optic laser gyro," *Opt. Lett.*, Vol. 4, 93-95. 1979.
13. Kim, B. Y., Lefevre, H. C., Bergh, R. A. and Shaw, H. J., "Response of fiber gyros to signals introduced at the second harmonic of the bias modulation frequency," *Proc. Soc. Photo-Opt. Instrum. Eng.*, Vol. 425, 86-89. 1983.
14. Kim, B. Y. and Shaw, H. J., "Gated phase modulation feedback approach to fiber-optic gyroscope," *Opt. Lett.*, Vol. 9, 263-265. 1984.
15. Kim, B. Y. and Shaw, H. J., "Gated phase modulation approach to fiber-optic gyroscope with linearized scale factor," *Opt. Lett.*, Vol. 9, 375-377.
16. Risk, W. P., Younquist, R. C., Kino, G. S. and Shaw, H. J., "Acousto-optic frequency shifting in birefringent fiber," *Opt. Lett.*, Vol. 9, 309-311. 1984.
17. Risk, W. P., Shaw, H. J. and Kino, G. S., "Fiber-optic frequency shifter using a surface acoustic wave incident at an oblique angle," *Opt. Lett.*, Vol. 11, 115-117. 1986.
18. Risk, W. P., Kino, G. S., "Acousto-optic frequency shifter using periodic contact with a copropagating surface acoustic wave," *Opt. Lett.*, Vol. 11, 336-338. 1986.
19. Kim, B. Y., Blake, J. N., Engan, H. E. and Shaw, H. J., "All-fiber acousto-optic frequency shifter," *Opt. Lett.*, Vol. 11, 389-391. 1986.
20. Blake, J. N., Kim, B. Y., Engan, H. E. and Shaw, H. J., "All-fiber acousto-optic frequency shifter using two-mode optical fibers," *Proc. Soc. Photo-Opt. Instrum. Eng.*, Vol. 719 (this volume), 1986.
21. Kim, B. Y. and Shaw, H. J., "All-fiber-gyroscope with linear scale factor using phase detection," *Proc. Soc. Photo-Opt. Instrum. Eng.*, Vol. 478, 142-148. 1984.
22. Kim, B. Y. and Shaw, H. J., "Phase-reading all-fiber-optic gyroscope," *Opt. Lett.*, Vol. 9, 378-380. 1984.

23. Carrara, S. L. A., Kim, B. Y. and Shaw, H. J., "Elasto-optic alignment of birefringent axes in polarization holding optical fiber," *Opt. Lett.*, Vol. 11, 470-472. 1986.
24. Carrara, S. L. A., Kim, B. Y. and Shaw, H. J., "Fiber gyroscope with birefringence modulation," *Proc. Soc. Photo-Opt. Instrum. Eng.*, Vol. 719 (this volume), 1986.
25. Sorin, W. V., Kim, B. Y. and Shaw, H. J., "Highly selective evanescent modal filter for two-mode optical fibers," *Opt. Lett.*, Vol. 11, 581-583. 1986.
26. Arditty, H., Papuchon, M., Puech, C. and Thyagarapan, K., "Recent developments in guided wave optical rotation sensors," *Digest of Topical Meeting on Integrated and Guided Wave Optics*, Paper TuC2, OSA, Washington, D. C. 1980.
27. Cutler, C. C., Newton, S. A. and Shaw, H. J., "Limitation of rotation sensing by scattering," *Opt. Lett.*, Vol. 5, 488-500. 1980.
28. Shupe, D. M., "Thermally induced nonreciprocity in the fiber-optic interferometer," *Appl. Opt.*, Vol. 19, 654-655. 1980.
29. Ezekiel, S., Davies, T. L. and Hellworth, R. W., "Observation of intensity-induced nonreciprocity in fiber-optic gyroscopes," *Opt. Lett.*, Vol. 7, 457-459. 1982.
30. Bergh, R. A., Lefevre, H. C. and Shaw, H. J., "Compensation of the optical Kerr effect in fiber-optic gyroscopes," *Opt. Lett.*, Vol. 7, 282-284. 1982.
31. Bergh, R. A., Culshaw, B., Cutler, C. C., Lefevre, H. C. and Shaw, H. J., "Source statistics and the Kerr effect in fiber-optic gyroscopes," *Opt. Lett.*, Vol. 7, 563-565. 1982.
32. Lefevre, H. C., Graindorge, Ph., Arditty, H. J., Vatoux, S. and Papuchon, M., "Double closed-loop hybrid gyroscope using digital phase ramp," *Tech. Digest of the 3rd International Conf. Optical Fiber Sensors*, San Diego, Postdeadline paper, PSD7. 1985.
33. Burns, W. K., Chen, C.-L. and Moeller, R. P., "Fiber-optic gyroscopes with broad-band source," *J. Lightwave Technol.*, Vol. LT-1, 98-104. 1983.
34. Pavlath, G. and Shaw, H. J., "Unpolarized reciprocal operation of fiber-optic rotation sensors," *Technical Digest, Conference on Lasers and Electro Optics*, Washington, D. C., 126-127. 1981.
35. Fredrics, R. J. and Ulrich, R., "Phase error bounds of fiber gyro with imperfect polarizer/depolarizer," *Electron. Lett.*, Vol. 20, 330-332. 1984.
36. Pavlath, G. and Shaw, H. J., "Re-entrant fiber optic rotation sensors," in *Fiber-Optic Rotation Sensors and Related Technologies*, Springer Series in Optical Science, Vol. 32, 364-367, Springer-Verlag, 1982.
37. Desurvire, E., Kim, B. Y., Fesler, K. A. and Shaw, H. J., "Reentrant fiber Raman gyroscope," *Technical Digest, Conference on Lasers and Electro-Optics*, Postdeadline Papers, p. 40, San Francisco, 1986.
38. Ezekiel, S. and Balsamo, S. R., "Passive ring resonator laser gyroscope," *Appl. Phys. Lett.*, Vol. 30, 478-480. 1977.
39. Stokes, L. F., *Single-mode optical-fiber resonator and application to sensing*, Ph. D. dissertation, Stanford University, 1983.

111

DEPOSITION OF PIEZOELECTRIC FILMS ON SINGLE-MODE FIBERS AND APPLICATIONS TO FIBER MODULATORS

B. L. Heffner,* W. P. Risk,* B. T. Khuri-Yakub, and G. S. Kino

Edward L. Ginzton Laboratory, W. W. Hansen Laboratories of Physics
Stanford University, Stanford, CA 94305

ABSTRACT

Techniques are described by which an oriented, piezoelectric zinc oxide film is sputtered directly on one side of an 80- μm -diameter fused silica single-mode fiber. These techniques have been used to fabricate piezoelectric transducers in the 0.5-5 GHz frequency range. Acoustic transducers fabricated directly on a fiber produce fields focused on the fiber core for efficient acousto-optic interaction, making possible many new all-fiber modulators and taps. An all-fiber phase modulator with a center frequency of approximately 850 MHz is demonstrated.

I. Introduction

Although originally developed as a simple optical waveguide, optical fiber has found wide application in a variety of new devices. Compared to similar devices realized using bulk optics, these fiber-optic devices offer the advantages of small size, light weight, and lack of optical coupling loss to other fiber or integrated optic devices. Increased levels of sophistication in all-fiber systems are made possible by the addition of new inventions to the inventory of proven fiber-optic components.

Acoustic waves have been coupled to fibers to make fiber-optic frequency shifters [1], switchable fiber taps [2], and amplitude and phase modulators [3]. In this paper we report the use of a piezoelectric zinc oxide film deposited directly on the surface of a fiber to make an acousto-optic all-fiber phase modulator for operation in the 850 MHz range.

Unlike previous fiber devices relying on acoustic fields, this phase modulator employs a thin film zinc oxide transducer which is fabricated directly on the fiber cladding. This results in a monolithic device in which no mechanical contact is necessary to couple an external acoustic source to the fiber. Aside from eliminating the usual problems of mechanical alignment to the external transducer, fabrication of a zinc oxide transducer on the fiber cladding makes possible all-fiber acousto-optic interactions at much higher acoustic frequencies than have previously been feasible. Zinc oxide transducers have been demonstrated in the 200 MHz to 30 GHz range using identical thin film technology on planar substrates.

II. Description of Device and Fabrication Techniques

The optical fiber used for the phase modulator was an ITT 1601 fused silica fiber which supported a single propagation mode at the 633-nm wavelength used in this experiment. The cladding diameter was 80 μm and the core diameter was 4 μm . An acoustic transducer was fabricated on one side of the cylindrical fiber surface by sputtering and evaporating thin films directly on the fiber, using projection photolithography to define the boundaries of the transducer. The transducer was fabricated on a 5-cm length of fiber and rf power was applied to the device by soldering a coaxial transmission line directly to gold metallizations on the fiber.

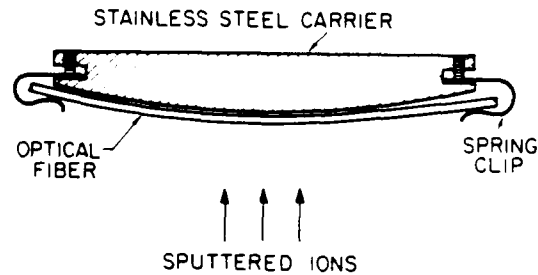


Fig. 1. Method of holding an optical fiber for depositing the metal electrodes and zinc oxide film. The fiber is free to move at one end during thermal cycling.

Two of the authors have published a description of the film deposition techniques [4], so this aspect of fabrication will be presented in a condensed form. A reactive planar magnetron sputtering system was used to deposit the zinc oxide film. We were able to use a low substrate temperature (100-200°C) and sputtering power to obtain low residual stress in the fiber. Due to the difference in thermal expansion coefficients between fused silica and stainless steel, the fiber cannot be simply stretched against a thermally-controlled surface and clamped in place during sputtering, as this arrangement will break the fiber during thermal cycling. Instead, the stiffness of the fiber was exploited to force the fiber against the cylindrical surface of a polished stainless steel bar. As shown in Fig. 1, the

fiber was clamped at one end with a spring clip. The other end was forced upward by the stiffness of the fiber, but the fiber was free to slide along the second clip. In this way, the fiber was held against a thermal reference while being free to move during thermal expansion. The fiber orientation was maintained by using the steel bar to carry the fiber through the entire fabrication process. It was found that photoresist could be spun onto the fiber by spinning the steel bar with the fiber attached, coating one side of the fiber with a thin film of resist suitable for photolithography. Only after the completion of the entire fabrication process was the fiber detached, ready for soldering to the rf line.

The acoustic transducer consisted of a piezoelectric zinc oxide film sandwiched between two gold electrodes on one side of the single-mode fiber, as shown in Fig. 2. After masking one end of the fiber with a metal foil, a 250-nm gold film was evaporated onto the fiber over a flash coating of titanium used to improve adhesion. A 1.6- μ m film of oriented zinc oxide was then sputtered over the bottom electrode. At this point a thin film of photoresist was spun onto the fiber and an image of the top electrode was projected onto the fiber through a microscope. An aperture stop in the microscope was employed to increase the depth of field of the image in order to accommodate the curved surface of the fiber. After developing the resist, a 120-nm gold film was deposited and lifted off to define the upper transducer electrode. The resulting acoustic transducer was 40 μ m wide and 600 μ m long. The gold metallizations were soldered with indium directly to the end of a semirigid coaxial transmission line, through which the rf drive signal was applied.

III. Theory of Operation

Other authors have considered the effect of an external perturbation on the propagation of modes in an optical fiber. It can be shown [5] that if the perturbation causes a change ($\delta\epsilon$) in the permittivity of the waveguide, the change in the propagating constant of a mode having electric field E and magnetic field H is given by:

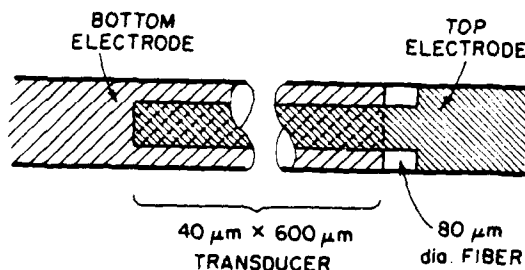


Fig. 2. Top view of the phase modulator transducer fabricated on the side of a single-mode fiber. A piezoelectric zinc oxide film separates the two electrodes.

$$\Delta B = \omega \epsilon_0 \int \mathbf{E}^* \cdot (\delta\epsilon) \cdot \mathbf{E} dS \quad (1)$$

where the integral is taken over the fiber cross section and it is assumed that the fields are normalized such that:

$$\int (\mathbf{E} \times \mathbf{H}^* + \mathbf{E}^* \times \mathbf{H}) \cdot \hat{a}_z dS = 1 \quad (2)$$

where z is the direction of propagation. In the weakly-guiding approximation [6], the electric field components of the LP_{01} mode can be written as:

$$E_x = E_0 F(r), \quad E_y = 0, \quad E_z = 0 \quad (3)$$

and the magnetic field components by:

$$H_x = 0, \quad H_y = \frac{n}{Z_0} E_0 F(r), \quad H_z = 0 \quad (4)$$

where $F(r)$ is the transverse profile of the field, n is the index, and Z_0 is the impedance of free space.

If a uniform strain S_1 is applied to the fiber, the resulting perturbation is:

$$[\delta\epsilon] = \begin{bmatrix} -n^4 p_{11} S_1 & 0 & 0 \\ 0 & -n p_{12} S_1^4 & 0 \\ 0 & 0 & -n^4 p_{12} S_1 \end{bmatrix} \quad (5)$$

where p_{11} and p_{12} are photoelastic coefficients. Inserting this result into Eq. (1), we find that the expected change in propagation constant is:

$$\Delta B = -\frac{\pi}{\lambda_0} n^3 p_{11} S_1 \quad (6)$$

where λ_0 is the optical wavelength in free space. This is identical to the result obtained by assuming that the optical fields are plane waves. According to Eq. (6), the degree of phase modulation is proportional to the acoustic strain. A phase modulation efficiency measured in rad/ \sqrt{W} can therefore be associated with a device to indicate the modulation expected for any given rf input power.

The optical spectrum of the output of the phase modulator consists in general of a number of sidebands spaced by the modulation frequency and having Bessel function amplitudes, e.g., the output electric field will be:

$$E_x \left(\sum_{n=-\infty}^{\infty} J_n(\Delta BL) e^{-j(\omega_0 + n\omega_a)t} \right) \quad (7)$$

where ω_0 is the original optical frequency and ω_a is the acoustic frequency. The ratio R of the power in the first sideband at frequency $\omega_0 + \omega_a$ to the power in the carrier at ω_0 will be $J_1^2(\Delta BL)/J_0^2(\Delta BL)$, where ΔB is given above and L is the interaction length of the device. For small phase modulation ($\Delta BL \ll 1$), R is approximately $(\Delta BL/2)^2$, and is therefore proportional to the acoustic power density. Hence, by measuring the ratio of the amplitudes of these two sidebands, the degree of phase modulation can be determined.

If the input polarization is not aligned with the direction of acoustic strain, the phase modulation efficiency is different. In particular, if the optical polarization is at right angles to the strain, $\Delta B = -\pi/\lambda_0 n p_{12} S_1$. In general,

$$R = \left(\frac{\pi L}{\lambda_0 n S_1} \right)^2 (p_{11}^2 \sin^2 \theta + p_{12}^2 \cos^2 \theta) \quad (8)$$

where θ is the angle between the acoustic wave-front and the input polarization. Since $p_{12} > p_{11}$, it is desirable to align the input polarization perpendicular to the direction of acoustic strain ($\theta = 90^\circ$) for the most effective phase modulation.

Finally, the assumption that the strain is uniform is not correct and is only a valid approximation when the acoustic wavelength is large compared to the extent of the optical mode. When the acoustic wavelength is comparable to or smaller than the size of the mode, the effect is reduced, as the positive and negative phase modulations average spatially over the mode. For an example, consider the case where $S_1(x) = S_1 \cos Kx$. Then, using Eq. (1), we obtain:

$$\Delta B = -\frac{\pi}{\lambda_0} n^3 p_{11} S_1 \frac{\int_0^{\infty} F^2(r) r J_0(Kr) dr}{\int_0^{\infty} F^2(r) r dr} \quad (9)$$

For K approaching 0, the quantity in parentheses goes to 1. This is the long wavelength case (approaching uniform strain) discussed above. For larger values of K , the J_0 term reduces the value of the integral in the numerator, and the phase modulation is decreased.

IV. Experiment

To evaluate the performance of the ZnO phase modulator, the set-up of Fig. 3 was used. Light from a single-mode, linearly-polarized helium neon laser at 633 nm was coupled into the fiber after first passing through a $\lambda/2$ plate, which could be used to adjust the angle of the input polarization with respect to the direction of acoustic strain. A suspension of carbon powder in glycerin was placed on the unjacketed fiber to strip cladding modes. The light emerging from the fiber was collimated and directed into a scanning confocal interferometer, and then into a photomultiplier tube. The scanning confocal interferometer and the photomultiplier tube acted as an optical spectrum analyzer to allow direct observation of the optical sidebands. As explained in the preceding section, by measuring the ratio of the height of the first sideband to the height of the carrier, the amount of phase shift produced by the modulator can be inferred.

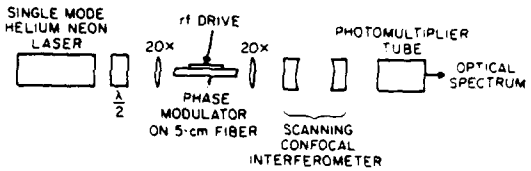


Fig. 3. Experimental measurement system showing coupling of the device to an optical spectrum analyzer.

The modulator was driven CW from an rf synthesizer. Although the transducer resonance was centered at 1.3 GHz, the spatial averaging effect described in the preceding section causes the most efficient operation to be at lower frequencies, around 850 MHz. Although the transducer itself is broadband, the performance of the phase modulator exhibits peaks at intervals of 34 MHz due to acoustic resonances of the fiber. The zinc oxide transducer is a resonator coupled both to the rf input line and to the fiber resonator. At a series of frequencies determined by the coupled resonance, the rf power is efficiently matched into the device, leading to peaks in the phase modulator frequency response. Figure 4 shows the variation of the phase modulation with frequency in the vicinity of one of these resonances with +1.5 dBm of available rf power delivered to the device. Roughly 90 mrad of phase shift was obtained at the peak.

When greater powers are supplied to the modulator, thermal effects become evident. The variation of phase modulation with frequency is shown in Fig. 5, for power levels of +1.5 dBm, +10.5 dBm, and +12.5 dBm. At low powers, the trace is reversible and continuous. At higher power levels, sudden jumps in the phase modulation appear due to heating of the device as a resonance is approached. In addition, the frequency of maximum response increases, and a sort of hysteresis appears: the variation of phase modulation with frequency is different going up in frequency from that obtained going

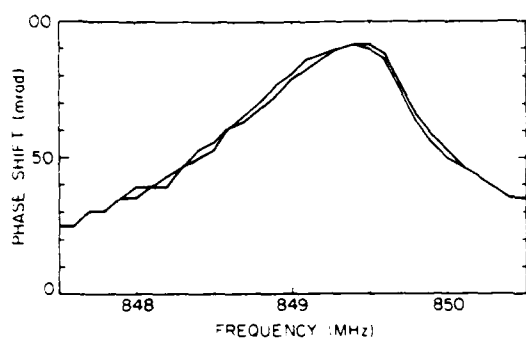


Fig. 4. Phase modulator frequency response at 1.5 dBm input power. The two traces represent nearly identical data taken at increasing and decreasing frequencies.

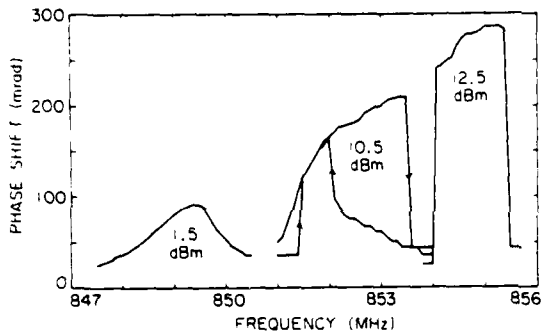


Fig. 5. Phase modulator frequency responses at three input power levels. Thermal feedback causes hysteresis effects at the two highest power levels.

down in frequency. Apparently this hysteresis is caused by thermal feedback. When a frequency is reached at which the input impedance presented by the coupled resonators (transducer and fiber) approaches the conjugate rf source impedance, power into the device increases, raising the temperature of the coupled resonators and changing their resonant characteristics. The peak phase modulation measured was roughly 285 milliradians with +12.5 dBm supplied to the transducer at 855 MHz. Application of higher power destroyed the transducer. Higher order sidebands were not observed.

From the theory previously presented, we expect the degree of phase modulation to be proportional to the acoustic strain. The small signal modulation efficiency, measured at 849 MHz and 1.5 dBm, was 76 mrad peak phase shift per $\sqrt{\text{mW}}$ of rf power. At high powers, where heating of the device

became significant, slightly lower efficiencies were observed. An efficiency of 57 mrad/ $\sqrt{\text{mW}}$ was observed at the highest power level of 14.5 dBm, on the borderline of thermal overload. This saturation of the modulation efficiency may occur because the zinc oxide transducer is less efficient at high temperatures. A transducer efficiency of approximately -7.4 dB was measured using purely acoustic means. If acoustic reflections within the fiber are neglected, a theoretically predicted modulation efficiency of 27 mrad/ $\sqrt{\text{mW}}$ can be calculated. The measured value was two to three times that predicted in the absence of reflections in the fiber, confirming that the acoustic resonance in the fiber contributes to a more efficient device.

The polarization dependence of the transducer was also investigated. This is shown in Fig. 6. When the input polarization is perpendicular to the direction of acoustic strain, the phase modulation is the highest. As the input polarization is rotated, the modulation decreases. From the results of the preceding section, the ratio of the perpendicular and parallel values should be $\phi_{\perp}/\phi_{\parallel} = p_{12}/p_{11}$. Using the values for bulk glass, this should give a ratio of about 2.23. The actual measured ratio is closer to 1.2. This may be a manifestation of the spatial variation of the focused acoustic wave, which we have neglected in the theory. In any case, the phase modulation does not depend strongly on the angle of input polarization.

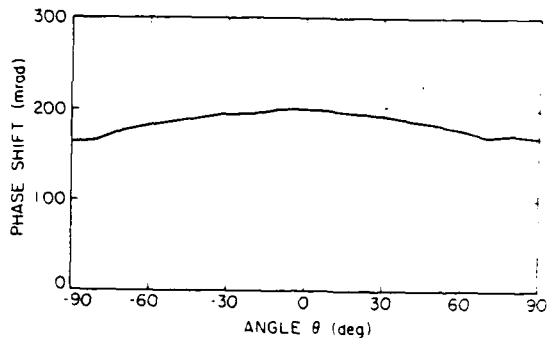


Fig. 6. Optical phase shift versus input polarization angle at 10.5 dBm input power.

V. Conclusions

We have demonstrated an all-fiber acousto-optic phase modulator using a zinc oxide acoustic transducer fabricated directly on the side of a single-mode fiber. Techniques for the deposition of oriented zinc oxide on a fiber and for photolithography on the side of a fiber were developed to allow fabrication of the all-fiber phase modulator. Measurements yielded a small signal modulation efficiency of 76 mrad peak modulation per $\sqrt{\text{mW}}$ of rf power at 849 MHz, but this efficiency decreased at drive powers above 1 mW. A peak modulation of 285 mrad was obtained with the device driven CW at 855 MHz.

with 28 mW rf power. The transducer input impedance variations associated with acoustic resonance within the fiber allowed an efficient rf match to the device only over a narrow frequency range, limiting the device bandwidth to approximately 1 MHz. The maximum phase modulation was limited by the thermal dissipation of the device, and the effects of heating were quite apparent.

This device, though not perfected, demonstrates that it is possible to construct all-fiber acousto-optic modulators using zinc oxide transducers deposited directly on fibers. These transducers excite acoustic fields which are focused on the fiber core for efficient acousto-optic interaction. The maximum acoustic field attainable by such a device is currently limited by thermal dissipation. We are developing techniques to heat sink the device to allow operation at higher powers. Judging by our experience with planar transducers, we can expect to operate a transducer at 1 GHz with over one watt of CW power.

Acknowledgment

This work was supported by the Office of Naval Research under Contract No. N00014-84-K-0327.

* Current address for B. L. Heffner is Bell Communications Research, Red Bank, NJ 07733. Current address for W. P. Risk is IBM Almaden Research Center, San Jose, CA 95120.

References

1. W. P. Risk, R. C. Youngquist, G. S. Kino, and H. J. Shaw, "Acousto-Optic Frequency Shifting in Birefringent Fiber," *Opt. Lett.* 9, 309 (1984).
2. B. L. Heffner, G. S. Kino, B. T. Khuri-Yakub, and W. P. Risk, "Switchable Fiber-Optic Tap Using the Acousto-Optic Bragg Interaction," *Opt. Lett.* 11, 476 (1986).
3. W. P. Risk and G. S. Kino, "Acousto-Optic Polarization Coupler and Intensity Modulator for Birefringent Fiber," *Opt. Lett.* 11, 48 (1986).
4. B. L. Heffner and B. T. Khuri-Yakub, "Deposition of Oriented Zinc Oxide on an Optical Fiber," *Appl. Phys. Lett.* 48, 1422 (1986).
5. J. Sakai and T. Kimura, "Birefringence and Polarization Characteristics of Single-Mode Optical Fibers Under Elastic Deformations," *IEEE J. Quantum Elect.* QE-17, 1041 (1981).
6. D. Gloger, "Weakly Guiding Fibers," *Appl. Opt.* 10, 2252 (1971).

Switchable fiber-optic tap using acoustic transducers deposited upon the fiber surface

B. L. Heffner* and G. S. Kino

Edward L. Ginzton Laboratory, W. W. Hansen Laboratories of Physics, Stanford University, Stanford, California 94305

Received October 20, 1986; accepted December 12, 1986

A new electronically switchable fiber-optic tap is demonstrated. The tap consists of an array of acoustic transducers fabricated directly upon the side of a cylindrical single-mode fiber. The transducer array generates an acoustic field that is focused on the fiber core and that satisfies the Bragg condition, allowing light to be deflected out of the fiber by the acousto-optic Bragg interaction. The amount of light tapped is linearly proportional to the rf power driving the transducer array. The bandwidth of the tap is 920 MHz centered at 3.3 GHz, with a maximum tap efficiency of 0.4% per watt of rf input.

It has been demonstrated that single-mode fiber can be used as an extremely wide-bandwidth, low-loss delay medium for signal-processing applications.^{1,2} For these applications, fiber taps are required in order to deflect part of the guided light out of the fiber to one or more photodetectors, which generate an electronic output signal. Two techniques have been used to extract light mechanically from a fiber: the cladding can be etched or polished away to expose the evanescent field³ or the fiber can be bent to induce coupling to radiation modes that are detectable outside the fiber.⁴ In both of these techniques the tap weighting is determined mechanically and cannot be rapidly controlled or switched. The acousto-optic tap described here permits the amount of light taken from the fiber to be varied electronically. Because of the large acousto-optic bandwidth available at the high acoustic frequency used, the tap can be adjusted or switched in times of the order of a nanosecond. Potential applications for this device include simple switchable taps and programmable tapped delay lines for use as filters, correlators, convolvers, and word generators.

The authors previously reported an electronically switchable tap to an optical fiber that employs a 4-GHz acoustic transducer fabricated upon a wedge that is brought into contact with the fiber.^{5,6} Using a wedge to couple an acoustic beam into an optical fiber allows the fiber to be tapped in a fairly direct manner, but this configuration does not lend itself to designs yielding high acousto-optic diffraction efficiencies. Much higher diffraction efficiencies can be attained by fabricating acoustic transducers directly upon the surface of a cylindrical fiber, eliminating the coupling wedge altogether. The resulting curved transducers generate an acoustic field that is focused on the fiber core. An optical fiber is manufactured with the core well centered within the cladding to facilitate splicing to other fibers. This allows the acoustic transducer to cover a large angular sector of the fiber surface, with correspondingly tight focusing and large acoustic fields in the core. The monolithic nature of this device circumvents problems associated with mechanical

stability and alignment of the wedge. Furthermore, material loss in the wedge, coupling loss through a Hertzian contact, and diffraction loss are completely eliminated.

Conservation of momentum in a photon-phonon interaction can be shown⁷ to lead to the Bragg condition, which specifies the required angle α between an acoustic wave front and the optical propagation vector \mathbf{k}_1 :

$$\sin \alpha = k_a / k_1, \quad (1)$$

where k_a is the acoustic wave's propagation constant. Though the advantages of fabricating an acoustic transducer directly upon the surface of a cylindrical fiber are attractive, the acoustic field produced by a simple transducer does not satisfy the Bragg condition for acousto-optic diffraction since a finite component of acoustic momentum in the direction of the fiber axis is required to obtain a finite angle α . The acoustic beam generated by a simple transducer upon a fiber surface propagates normal to that surface and has no axial momentum. Fortunately, a Bragg-diffraction fiber tap can be realized by constructing a phased array of acoustic transducers upon the fiber surface designed to excite an acoustic field that satisfies the Bragg condition. This array, which takes the form of an interdigital transducer deposited upon the curved surface of the fiber, is shown in Fig. 1. Note that although the array is similar in form to a surface wave transducer, its operating frequency is far above that necessary to excite surface waves.

The array was designed to excite longitudinal waves efficiently only at angles $\pm\beta$ to the normal, given by

$$\sin \beta = 2\pi / k_a d, \quad (2)$$

where d is the period of the array. Equating the angles α and β in Eqs. (1) and (2) and letting V_a denote the acoustic velocity, we obtain the center frequency f_{ao} of the acousto-optic interaction:

$$f_{ao} = V_a \sqrt{k_1 / \pi d}. \quad (3)$$

The highest possible center frequency is desired in order to obtain the greatest tap bandwidth and to increase material loss to reduce the effect of acoustic reflections within the fiber. An upper frequency limit was set by the resolution of the lift-off photolithography used to fabricate the device, which determined the smallest possible array period d . Using an optical projection system, we found that $4 \mu\text{m}$ was a realistic lower limit to the element width and the spacing between elements. As an array period includes two oppositely phased elements and two spaces, the minimum array period is $d = 16 \mu\text{m}$. From this figure and the physical parameters of fused silica, Eq. (3) yields a center frequency of 3.20 GHz at the 633-nm He-Ne optical wavelength.

It should be emphasized that the array does not produce an acoustic beam that tracks the Bragg angle's variation with frequency to increase the acousto-optic bandwidth, as has been demonstrated in other applications.⁸ In the array tap, although both the angle of the acoustic beam and the Bragg angle vary with frequency, they vary in an opposite sense. In fact, diffracted beam's angular variation usually associated with the Bragg interaction is exactly canceled by the acoustic beam's angular variation, and the deflection angle ψ between the diffracted and undiffracted beams is given by $\cos \psi = 1 - 2\pi k_1 d$. The array tap does not generate an acousto-optic Fourier transform, as does a Bragg cell.

The introduction of electrical signals into the transducer array poses a problem, because it is not possible to make conventional wire bonds to metallizations on an 80- μm -diameter fiber. Fortunately, only two connections need be made to a two-phase array if the ground plane is left floating (unconnected). Because the inputs to the two sides of the array are 180° out of phase, the net current from the ground plane sums to zero, and a ground connection is superfluous. Connections to the two sides of the array are made by extending the upper electrode metallizations of each side to cover about 1 mm of the fiber next to the device. The rf signal leads can then be soldered with indium directly to the gold-coated fiber. As illustrated in Fig. 1, signals travel from the input leads soldered to each end of the fiber through gold metallizations to 40 array elements, which are interleaved in an

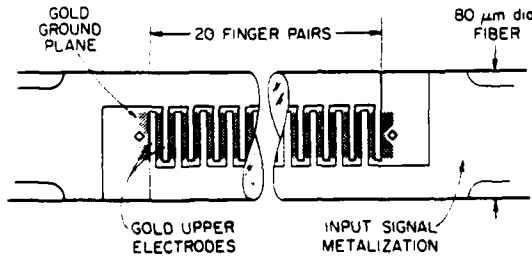


Fig. 1. The acoustic array tap, consisting of an array of bulk wave transducers fabricated upon the cylindrical surface of a single-mode fiber. A piezoelectric ZnO film is sputtered between the ground plane and the upper electrodes.



Fig. 2. Micrograph of one end of the transducer array, showing 4- μm wide array elements. The sides of the fiber are not in focus.

interdigital pattern with 20 elements connected to each input phase. The element dimensions are 4 μm by 30 μm , defined by the overlap of the top metallizations with the floating ground plane underneath. The total length of the array is 316 μm , which allows it to fit conveniently within the field of view of the microscope used for projection lithography.

The physical geometry of the array is defined by photolithographic masking of the device for chemical etching or lift-off of films. We found that photoresist could be spun on the side of a fiber by spinning the fiber on top of a flat substrate. A drop of resist on a fiber lying flat on a smooth surface can be spun to coat the fiber with a high-quality thin film suitable for photolithography. After spinning, capillary forces hold the fiber against the substrate, even if the substrate is not perfectly flat. Any technique used to form an optical image on the photoresist on a fiber must have a depth of focus adequate to accommodate the curvature of the fiber surface. In this case, array fingers 30 μm long plus the gaps at their ends require a 22- μm depth of field over which 4- μm lines must be resolvable. It was found that these requirements could be satisfied by an optical projection microscope with an internal aperture stop to increase the depth of focus. Significantly finer resolution was probably not possible with the present projection system.

In previous devices using relatively rugged, flat substrates, piezoelectric zinc oxide (ZnO) films had been successfully deposited by using a reactive planar magnetron sputtering system. We have extended this technology to permit deposition upon the curved surface of a fiber, and these results were reported previously.⁹ An oriented 80-nm gold film was sputtered upon the fiber, and the ground plane was defined by using photolithography and chemical etching. An oriented 505-nm ZnO film was then sputtered over the gold film. The gold 80-nm top array electrodes were defined by photolithographic lift-off. Figure 2 is a photograph of one end of the array tap on a fiber, showing the 4- μm array elements interleaved over the ground plane.

The frequency response of the tap was measured by focusing the diffracted light onto an avalanche photodiode. Reflecting the geometry of the wave interaction region, the diffracted beam is wedge shaped, with a large angular extent perpendicular to the plane of incidence. Carbon tetrachloride was used as an index-matching fluid to allow the tapped light to escape the fiber cladding. A lens of large numerical aperture

was used to focus the wedge-shaped beam onto a photodiode. The diffracted beam was clearly visible to the eye, and by sighting along the lens it could be seen that only a negligible fraction of the diffracted beam was not focused and detected.

After the tapped light was measured and numerical corrections for small amplitude and phase imbalances were made, the frequency response of the acoustic array tap was plotted (Fig. 3). The periodic structure of the array-tap frequency response is a result of acoustic reflections within the fiber. The reflections can be clearly revealed by computing a discrete Fourier transform of the frequency-response magnitude data to obtain the autocorrelation of the tap impulse response. Assuming the presence of acoustic reflections in the fiber, the impulse response is expected to be a decaying series of pulses spaced by an acoustic delay time of 26.8 nsec. In this case the autocorrelation will be a series of identically spaced pulses of amplitude $A_K = \sum h_n h_{n+k}$, where h_n is the amplitude of the n th impulse-response pulse. The calculated autocorrelation has precisely this structure, and solving for h_n we obtain the normalized impulse response $h_1 = 1$, $h_2 = 0.207$, and $h_3 = 0.0414$. The impulse response exhibits the exponential decay expected of reflections in a lossy medium, with a reduction between consecutive reflections of 13.7 dB.

We have therefore demonstrated a new method of forming an electronically switchable tap to an optical fiber by using a phased array of acoustic transducers fabricated directly upon the surface of a standard cy-

lindrical fiber. This arrangement takes advantage of acoustic focusing to achieve high fields in the acousto-optic interaction region. The measured tap efficiency was $-24 \text{ dB/W}_{\text{input}}$, with a bandwidth of 920 MHz centered at 3.3 GHz. Purely acoustic measurements indicate that the transducer center frequency was 3.9 GHz instead of the 3.2-GHz center frequency imposed by Eq. (3), and it appears possible to achieve better than $-20 \text{ dB/W}_{\text{input}}$ ($1\%/\text{W}_{\text{input}}$) efficiency simply by matching the transducer center frequency to the interaction center frequency. The device has been run cw with input powers of up to 200 mW, and we soon expect to heat sink the device to permit higher-power operation. The array tap is a monolithic device that requires no mechanical alignment. It demonstrates a new technological capability to fabricate acoustic transducers directly upon the side of an optical fiber, of a quality comparable with that of planar transducers.

This research was supported by the U.S. Office of Naval Research under contract no. N00014-84-K-0327. The research of Brian Heffner was supported by a fellowship from the Fannie and John Hertz Foundation.

*Present address, Bell Communications Research, Red Bank, New Jersey 07701.

References

1. K. Wilner and A. P. van den Heuvel, Proc. IEEE 64, 805 (1976).
2. K. P. Jackson, S. A. Newton, B. Moslehi, M. Tur, C. C. Cutler, J. W. Goodman, and H. J. Shaw, IEEE Trans. Microwave Theory Tech. MTT-33, 193 (1985).
3. R. A. Bergh, G. Kotler, and H. J. Shaw, Electron Lett. 7, 260 (1980).
4. K. P. Jackson, J. E. Bowers, S. A. Newton, and C. C. Cutler, Appl. Phys. Lett. 41, 139 (1982).
5. B. L. Heffner, G. S. Kino, B. T. Khuri-Yakub, and W. P. Risk, in *Proceedings of the IEEE Ultrasonics Symposium* (Institute of Electrical and Electronics Engineers, New York, 1985).
6. B. L. Heffner, G. S. Kino, B. T. Khuri-Yakub, and W. P. Risk, Opt. Lett. 11, 476 (1986).
7. See, for example, A. Yariv, *Optical Electronics*, 3rd ed. (Holt, Rinehart and Winston, New York, 1985), pp. 385-390.
8. L. Palmieri, G. Socino, and E. Verona, Appl. Phys. Lett. 47, 463 (1985).
9. B. L. Heffner and B. T. Khuri-Yakub, Appl. Phys. Lett. 48, 1422 (1986).

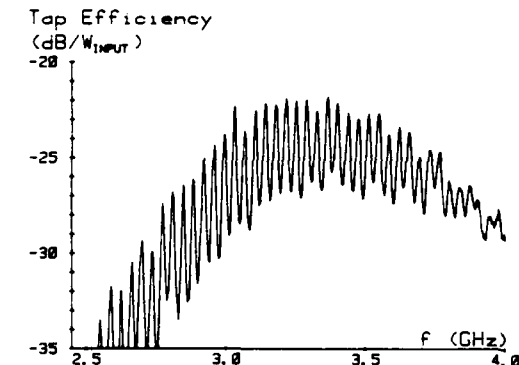


Fig. 3. Acousto-optic frequency response of the array tap.

OPTICAL SENSORS FOR RANGE AND DEPTH MEASUREMENTS

G. S. Kino, T. R. Corle, P. C. D. Hobbs, and G. Q. Xiao

Edward L. Ginzton Laboratory; Stanford University
Stanford, California 94305Abstract

A new type of optical range sensor is being developed which makes use of the shallow depth of field of a type II confocal scanning optical microscope. The range resolution is of the order of 2 μm at a 10-20 cm distance from the lens. We have shown that the system works well on rough surfaces, although with a much decreased output signal. In another set of experiments employing microscope lenses, various versions of the system are being used to measure the thickness of transparent films with a thickness of the order of 100 nm to 5 μm with good accuracy and with transverse resolutions in the 150-500 nm range. We can scan the beam electronically with a Bragg cell, or mechanically, to measure the profiles of objects.

Introduction

We will describe in this paper several new techniques for making accurate range measurements with good transverse definition. In microscopy, this involves the measurement of profiles and the thickness of transparent and opaque films in integrated circuits. On a more macroscopic scale, the techniques can be used for robot position sensors and for measuring profiles of machined parts, to which no direct contact need be made.

Research in the area of distance measurements has been carried out for many years using several different methods [1]. One approach is to use interferometry, which requires a high-quality laser. The method yields excellent range accuracy, but suffers from phase wraparound; thus, without additional complexity, such as the use of two laser frequencies or the employment of extremely high-frequency modulation, it is not possible to make noncontinuous distance measurements [2]. An alternative technique is to use a triangulation; however, this method does not usually provide very good transverse resolution.

In this paper, we describe several new optical techniques which are based upon the type II confocal microscope [3,4]. With one system using a camera lens, we have made absolute distance measurements with a range accuracy of 2 μm and a transverse definition of 10 μm at a working distance of 15 cm. The system is stable, easy to align, and largely insensitive to the tilt and roughness of the object. With microscope systems, we have measured film thickness and range accuracies of the order of 1 nm, and have obtained transverse resolutions in certain applications of the order of 15 nm.

We have developed two distinct methods for directly measuring film thickness or range with confocal systems. One method is to determine when the system is focused on a reflecting surface by looking for the maximum reflected amplitude. When this method is applied to thin film measurements, as the microscope lens is moved up and down, maxima will be observed

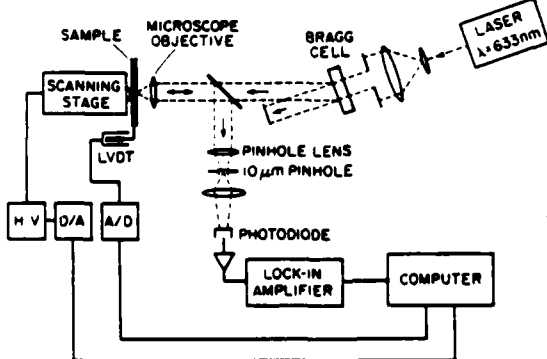


Fig. 1. Schematic diagram of a basic type II microscope system.

at the upper and lower surfaces of a transparent reflecting film. This technique works most easily when the film thickness is considerably larger than the depth of focus of the microscope, and works very well as a direct method for measuring the range of a reflecting object.

A second technique is to measure phase directly and to determine the thickness from the phase shift of the reflected beam through the film. Such a technique is at its best when the film thickness is less than an optical wavelength, i.e., well within the depth of focus. It is particularly simple to apply when the films themselves are opaque and the technique is used to measure surface profiles or the thickness of opaque films on transparent or opaque substrates. An additional advantage of being able to make measurements of optical amplitude and phase directly is that the resultant data obtained can be inverse filtered to improve the transverse definition or to obtain more accurate information on the width of surface features.

Basic System

The basic type II microscope system with which we are working is shown in Fig. 1 [4]. The microscope objective lens is illuminated by a collimated laser beam which produces a diffraction-limited spot on the surface of the object to be examined. The beam reflected from the surface of the object passes back through the microscope objective lens to a beam splitter and through a second lens. This lens focuses the beam onto a pinhole through which it passes to a detector. A Bragg cell is used to modulate the beam so that ac detection techniques may be employed.

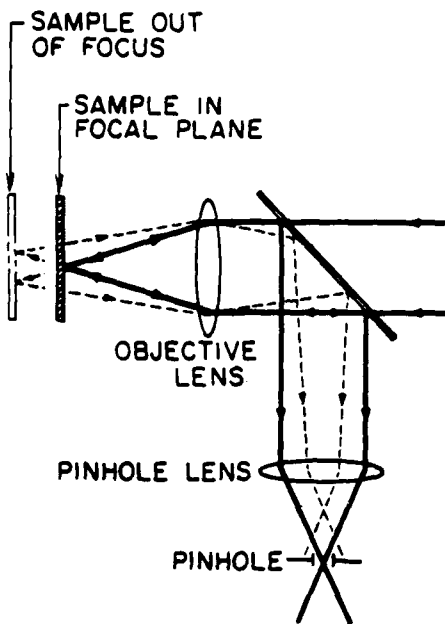


Fig. 2. Schematic illustrating depth discrimination properties of a type II confocal optical microscope.

The ranging properties of this apparatus can be most easily understood by referring to Fig. 2. If the object is in the focal plane of the lens, the reflected rays are focused at the pinhole and a maximum in the output signal is obtained. If the sample moves out of the focal plane, the amount of light transmitted by the pinhole is reduced and the signal at the photodiode decreases. We therefore expect the signal output from the detector to have a strong dependence on the position of the object.

Because a focused beam is employed, and the phase changes between the different rays comprising the beam are very small, the phase fluctuations of the laser are unimportant. Therefore, a semiconductor laser, or even an incoherent source, can be used. Furthermore, since the objective lens is used twice, once to focus the incoming wave to a point and a

second time to image that point onto the pinhole, the transverse amplitude response of the system is the square of the point spread function of the lens. Thus, when the sample is at the focal plane, the output from the detector is of the form $j_{10}(2\pi/\lambda) r \sin \theta_0$, where $j_{10} x = 2J_1(x)/x$. $J_1(x)$ is a Bessel function of the first kind, r is the distance from the optical axis, the aperture angle of the lens is θ_0 , and λ is the optical wavelength. Thus, the 3 dB resolution of this type of microscope is better by a factor of approximately 1.4 than a standard microscope, and the sidelobe level and speckle associated with the device are negligible.

To calculate the ranging response of this system when a plane reflector is scanned in the axial (z) direction, we assume a lens with a pupil function $P(\theta)$ where θ is the angle between the ray from the pupil plane to the focal point and the axis. By following the derivation of Richards and Wolf for vector fields, with some minor changes, it can be shown that the normalized field of the reflected wave at the pinhole is of the form [5]:

$$V(z) = \frac{\int_0^{\theta_0} \frac{(1 + \cos \theta) \sin \theta}{(\cos \theta)^{1/2}} e^{-2jkz \cos \theta} P(\theta) R(\theta) d\theta}{\int_0^{\theta_0} \frac{(1 + \cos \theta) \sin \theta}{(\cos \theta)^{1/2}} P(\theta) d\theta}$$

where the output signal from the detector is proportional to

$$I(z) = |V(z)|^2 \quad (2)$$

In these expressions, $R(\theta)$ is the reflection coefficient of the plane reflector, k is the wave number $(2\pi/\lambda)$, and $\sin \theta_0$ is the numerical aperture of the lens.

Assuming a plane reflector with $R(\theta) = 1$ and uniform excitation at the lens, [$P(\theta) = 1$ for $\theta < \theta_0$], $ka \gg 1$ and $(1 + \cos \theta)/\cos \theta^{1/2} \approx 2$, an approximate expression for $V(z)$ has been derived [6],

$$V(z) = e^{-jkz(1 + \cos \theta_0)} \frac{\sin kz(1 - \cos \theta_0)}{kz(1 - \cos \theta_0)} \quad (3)$$

This expression accurately predicts the shape of the central lobe and the phase change of the reflected signal. The result fails to account for asymmetries in the sidelobes which are caused by lens aberrations. The depth of focus is given by the 3 dB points of the central lobe in Eq. (3).

$$(\Delta z)_{3 \text{ dB}} = \frac{0.443 \lambda}{1 - \cos \theta_0} \quad (4)$$

Experimental results with mechanically-scanned systems

Mechanically-scanned microscope

The object itself can be moved in the transverse and range directions by piezoelectric pushers or stepping motors. We use piezoelectric pushers for the microscope and stepping motors to demonstrate the principles of the macroscopic range sensor. Sometimes the object is mounted on an additional piezoelectric transducer which can vibrate the sample in and out periodically. Alternatively, as will be described later, the focus is periodically moved back and forth by an electro-optic device or with an electrically-controlled deformable mirror.

A result taken with the mechanically-scanned microscope is shown in Fig. 3. It will be observed that there is good agreement between theory and experiment, and that the 3 dB range resolution of a 0.9 aperture lens using a He-Ne laser is about 0.6 μm . It will be noted that the sidelobes are not at the same level or as symmetric as the simple theory indicates. A more sophisticated theory, which takes phase aberrations and amplitude weighting of the lens into account, explains the discrepancy in the sidelobe behavior [4].

Results taken on photoresist films of the order of 1.8 μm and 4.86 μm thick are shown in Figs. 4 and 5. Two peaks are obtained corresponding to the reflections from the top and bottom surfaces of the film. It is relatively easy to modify the theory to take

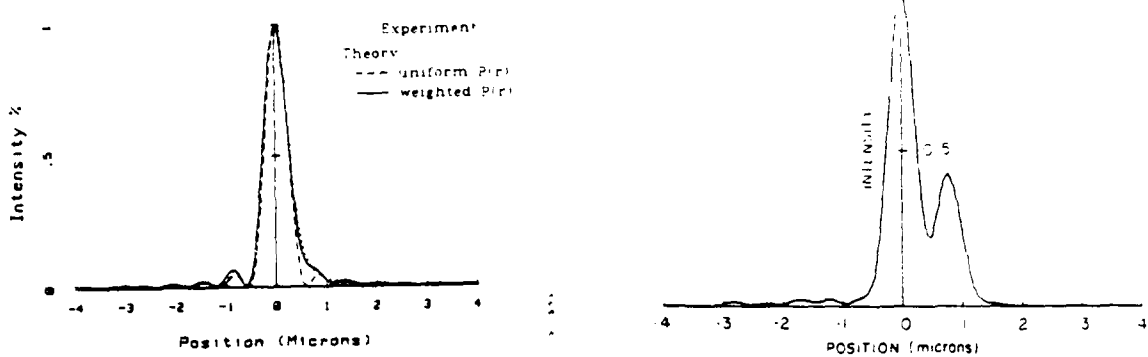


Fig. 3. $|V(z)|^2$ curve for objective of numerical aperture 0.9. Experimental data: dotted line. Theoretical calculations: solid and dashed lines.

Fig. 4. $|V(z)|^2$ curve of 1.8 μm photoresist on silicon.

account of this effect, and the results are extremely accurate for films thicker than 3 μm . However, for thinner films, where the two peaks overlap, the results obtained tend to be accurate as a measure of film thickness to only the order of a half wavelength ($\sim 2500 \text{ \AA}$). This uncertainty is primarily due to the unknown phase difference between the reflection from the top and bottom surfaces of the film. Use of phase measurements, as described below, can eliminate the difficulties. Direct comparison on calibrated samples can also eliminate this problem.

It is apparent that it would be useful to measure the position of the maximum of the reflectivity function with as high an accuracy as possible. To do this, we have adopted a simple stratagem. We vibrate the sample at a frequency Ω using a vibration amplitude comparable to or less than the depth-of-focus of the beam. In this case, we obtain an output from the photodetector at a frequency Ω , which passes through zero when the average value of $|V(z)|^2$ at the detector passes through a maximum. Thus, by looking for the zero or the minimum at a frequency Ω , we can determine the position of the focal point with very good accuracy. The result taken on the 4.86 μm photoresist film is shown as the full line in Fig. 5. When the depth-of-focus is of the order of 1 μm , we can determine the position of the maximum, and hence the film thickness, to within a few nanometers.

Optical range sensors

A schematic diagram of the optical range finder is shown in Fig. 6; this arrangement is slightly different from that of the microscope. The first lens after the beamsplitter focuses the laser beam to a spot of the order of 5 μm diameter, so that most of the beam passes through a 10 μm diameter pinhole. A camera lens placed beyond the pinhole focuses the light onto a point on the object. If the object is in the front focal plane of the camera lens and the pinhole is at the back focus, the reflected light passes back through the pinhole and is detected by the photodetector. When the object moves out of the focal plane, the amount of light passing through the pinhole is reduced. Hence, as we have already seen, the signal output from the detector has a strong dependence on the position of the object. Furthermore, the employment of a focused beam implies that the transverse definition of the system is excellent.

We used a 4 mW He-Ne laser with a wavelength of 6328 \AA in these experiments. A semiconductor laser could have been employed equally well; we chose to work with the gas laser initially only because of its availability and the greater ease of working with visible light in the early experiments. We found it convenient to use a Bragg cell for amplitude modulation of the incident light; with a semiconductor laser, we could directly modulate the laser itself.

To demonstrate the usefulness of this system for obtaining accurate distance measurements, we used a mirror as the reflecting object and scanned it in the axial (z) direction.

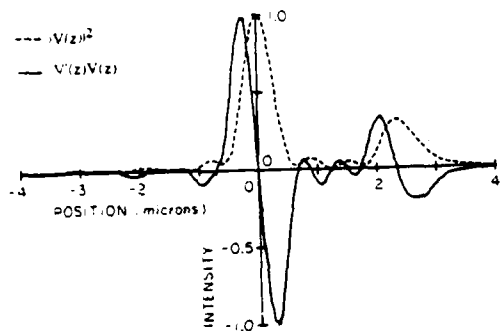


Fig. 5. $|V(z)|^2$ and $V'(z)V(z)$ curves of 4.86 μm photoresist on silicon.

Figure 7 shows the dependence of the signal on the position of the object. The numerical aperture of the optical system is 0.054, the corresponding depth of focus is 188 μm , and the spot size is about 10 μm . The experimental curve fits the theoretical curve very well, except for some discrepancies in the sidelobes which are believed to be caused by aberrations in the optical system. By determining the position of the peak of this curve, we can determine the position of the object very accurately.

To determine the sensitivity of our measurement technique, we scanned the focused beam over a tilted mirror, as shown in Fig. 8. The straight line represents the mirrored surface and the dots are experimental results. The estimated accuracy is about 2 μm . As we tilted

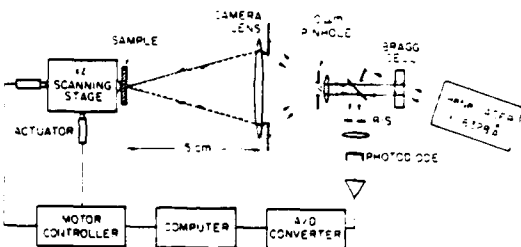


Fig. 6. Experimental arrangement of optical range finder.

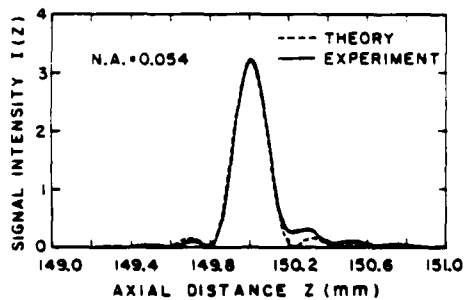


Fig. 7. $|V(z)|^2$ curve for camera lens in optical range finding system. Numerical aperture = 0.054.

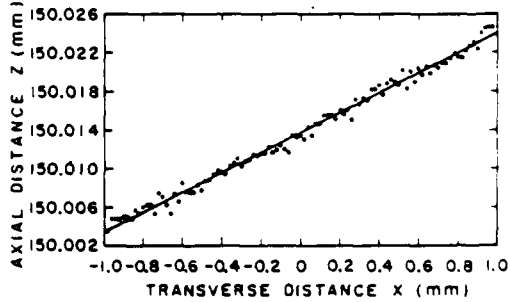


Fig. 8. Transverse scan over a tilted front surface mirror.

the mirror, the height of the central lobe decreased and the depth of focus increased. This is because less light could be collected by the camera lens, so the effective numerical aperture decreased.

The results of a scan over a 220 μm step on a specular reflector are shown in Fig. 9. The transverse spacing between adjacent points is 5 μm . Except for the overshoot near the step, the accuracy of the range measurement is about 2 μm . The overshoot is due to shadowing and interference effects.

This system is not only suitable for measurements on smooth surfaces, but also for measurements on rough surfaces. This behavior arises because when the light is focused to a point on a rough surface, the reflected light will be scattered in all directions, but an image of the point can still be obtained at the pinhole. We pay a price for this convenient result in that the light reaching the pinhole is greatly reduced in intensity; the advantage is that the alignment of the rough surface is relatively uncritical. To demonstrate this

effect, we measured a sample of sheet aluminum, as supplied by the manufacturer. The results we obtained are shown in Fig. 10. The central lobe of this curve is unchanged from the central lobe obtained using a mirror. As expected, the detected signal from this rough surface is much weaker than that for a smoother surface, but it is still strong enough to be easily detected with a narrowband receiving system. The results obtained were insensitive to the tilt of the object, essential for the measurement of ordinary machined parts.

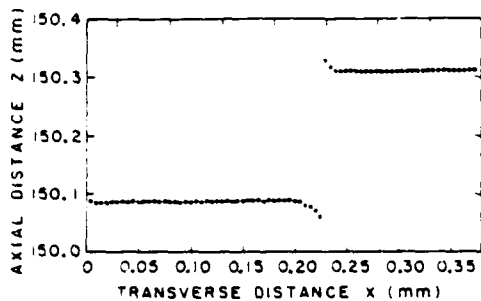


Fig. 9. Transverse scan over a step of aluminum on aluminum. Points represent peaks in intensity response.

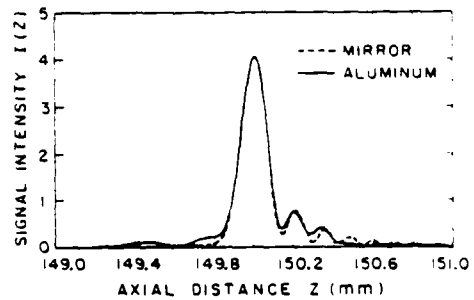


Fig. 10. $|V(z)|^2$ axial scan using a mirror (dashed line) and rough aluminum (solid line) surface as in the reflecting plane.

Phase measurements

A second microscope technique with which we have been working for some time [7] is shown in Fig. 11. A laser beam is incident on an acousto-optic Bragg cell. Part of the beam travels straight through the Bragg cell, but part is deflected at an angle which varies linearly with the driving frequency f_B of the Bragg cell. This technique has the advantages of great speed, repeatability, and random access. The Bragg cell is positioned at the pupil plane of an optical microscope, so the two outgoing beams are focused onto the object being examined and produce two focused spots. One spot is fixed and the other scans as the frequency f_B of the Bragg cell is varied. The beams are reflected from the sample, retrace their paths through the Bragg cell, and interfere on a photodiode, as shown. A lens images the center of the Bragg cell on the photodiode so that the spot does not wander off the detector as the beam is scanned.

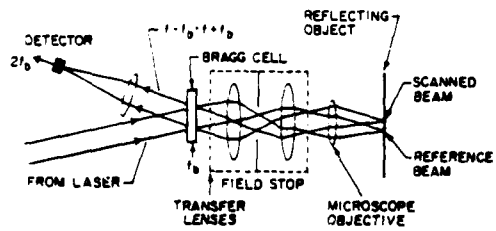


Fig. 11. Schematic diagram of the electronically-scanned microscope.

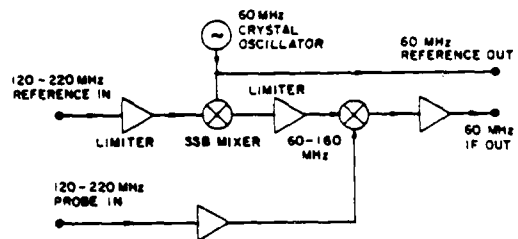


Fig. 12. Block diagram of the analog signal processing subsystem.

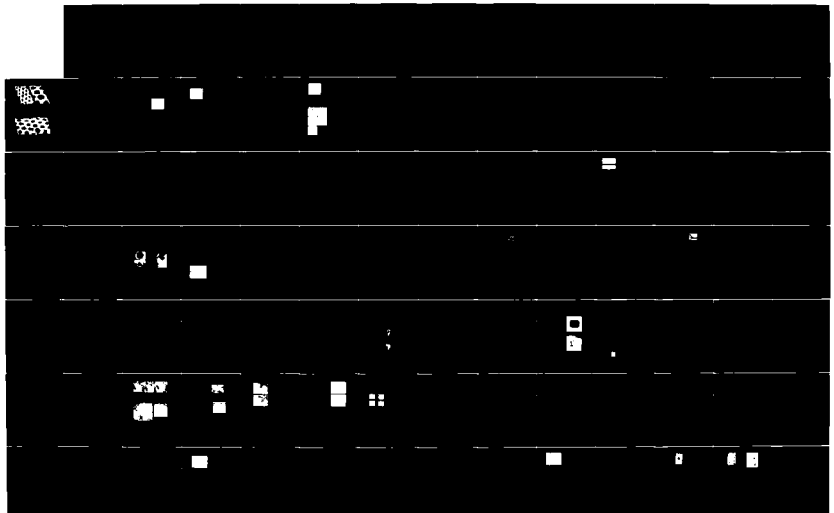
The beam reaching the photodiode from the scanned spot is upshifted by a frequency f_B , and the one from the fixed spot is downshifted by the same frequency f_B . When the beams interfere on the photodiode (a square-law device), we obtain an output product term at a frequency $2f_B$, whose phase is the optical phase difference between the fixed reference spot and the scanned spot. Since the amplitude of the fixed spot is constant, the amplitude of the output signal varies linearly with the amplitude of the scanned spot.

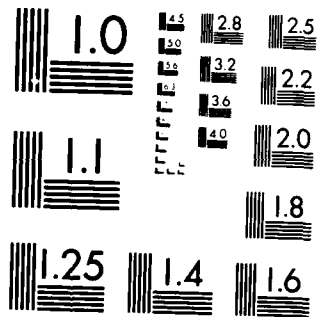
We are using a modified Leitz microscope, kindly supplied to us and modified by the E. Leitz Company, with an Inrad (Matsushita) Bragg cell. The Bragg cell has a frequency range of approximately 50-100 MHz and is capable of providing about 340 resolvable spots (equivalent to 680 after our post-processing).

AD-A189 143

JOINT SERVICES ELECTRONICS PROGRAM APPENDIX(U) STANFORD 2/3
UNIV CA EDWARD L GINZTON LAB OF PHYSICS

D M BLOOM ET AL. 15 OCT 87 CL-4287 NO 0014-84-K-0327
UNCLASSIFIED F/G 9/1 NL





MICROCOPY RESOLUTION TEST CHART
NATIONAL BUREAU OF STANDARDS 1963 A

OPTICAL SENSORS FOR RANGE AND DEPTH MEASUREMENTS

G. S. Kino, T. R. Corle, P. C. D. Hobbs, and G. Q. Xiao

Edward L. Ginzton Laboratory; Stanford University
Stanford, California 94305

Abstract

A new type of optical range sensor is being developed which makes use of the shallow depth of field of a type II confocal scanning optical microscope. The range resolution is of the order of 2 μm at a 10-20 cm distance from the lens. We have shown that the system works well on rough surfaces, although with a much decreased output signal. In another set of experiments employing microscope lenses, various versions of the system are being used to measure the thickness of transparent films with a thickness of the order of 100 nm to 5 μm with good accuracy and with transverse resolutions in the 150-500 nm range. We can scan the beam electronically with a Bragg cell, or mechanically, to measure the profiles of objects.

Introduction

We will describe in this paper several new techniques for making accurate range measurements with good transverse definition. In microscopy, this involves the measurement of profiles and the thickness of transparent and opaque films in integrated circuits. On a more macroscopic scale, the techniques can be used for robot position sensors and for measuring profiles of machined parts, to which no direct contact need be made.

Research in the area of distance measurements has been carried out for many years using several different methods [1]. One approach is to use interferometry, which requires a high-quality laser. The method yields excellent range accuracy, but suffers from phase wraparound; thus, without additional complexity, such as the use of two laser frequencies or the employment of extremely high-frequency modulation, it is not possible to make noncontinuous distance measurements [2]. An alternative technique is to use a triangulation; however, this method does not usually provide very good transverse resolution.

In this paper, we describe several new optical techniques which are based upon the type II confocal microscope [3,4]. With one system using a camera lens, we have made absolute distance measurements with a range accuracy of 2 μm and a transverse definition of 10 μm at a working distance of 15 cm. The system is stable, easy to align, and largely insensitive to the tilt and roughness of the object. With microscope systems, we have measured film thickness and range accuracies of the order of 1 nm, and have obtained transverse resolutions in certain applications of the order of 15 nm.

We have developed two distinct methods for directly measuring film thickness or range with confocal systems. One method is to determine when the system is focused on a reflecting surface by looking for the maximum reflected amplitude. When this method is applied to thin film measurements, as the microscope lens is moved up and down, maxima will be observed

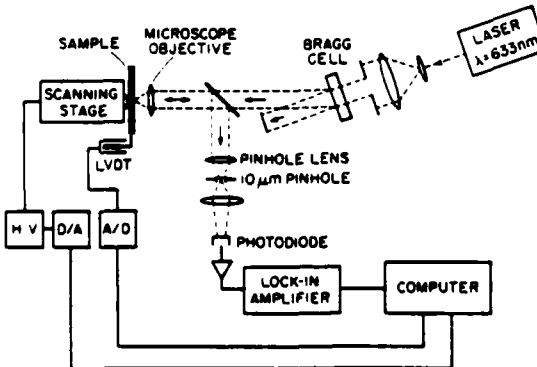


Fig. 1. Schematic diagram of a basic type II microscope system.

Invited paper: Presented at ICALEO, Arlington Virginia, November, 1986

at the upper and lower surfaces of a transparent reflecting film. This technique works most easily when the film thickness is considerably larger than the depth of focus of the microscope, and works very well as a direct method for measuring the range of a reflecting object.

A second technique is to measure phase directly and to determine the thickness from the phase shift of the reflected beam through the film. Such a technique is at its best when the film thickness is less than an optical wavelength, i.e., well within the depth of focus. It is particularly simple to apply when the films themselves are opaque and the technique is used to measure surface profiles or the thickness of opaque films on transparent or opaque substrates. An additional advantage of being able to make measurements of optical amplitude and phase directly is that the resultant data obtained can be inverse filtered to improve the transverse definition or to obtain more accurate information on the width of surface features.

Basic System

The basic type II microscope system with which we are working is shown in Fig. 1 [4]. The microscope objective lens is illuminated by a collimated laser beam which produces a diffraction-limited spot on the surface of the object to be examined. The beam reflected from the surface of the object passes back through the microscope objective lens to a beam splitter and through a second lens. This lens focuses the beam onto a pinhole through which it passes to a detector. A Bragg cell is used to modulate the beam so that ac detection techniques may be employed.

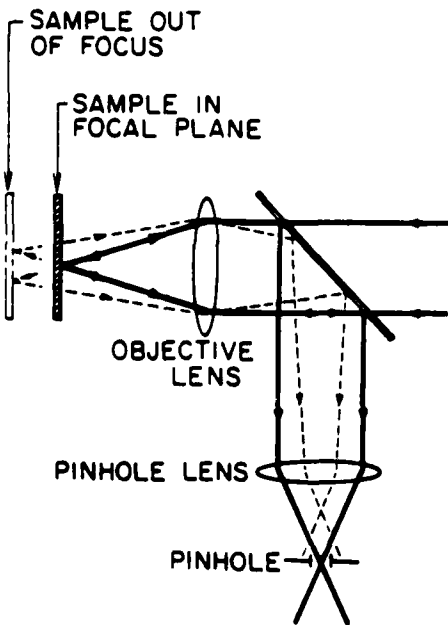


Fig. 2. Schematic illustrating depth discrimination properties of a type II confocal optical microscope.

The ranging properties of this apparatus can be most easily understood by referring to Fig. 2. If the object is in the focal plane of the lens, the reflected rays are focused at the pinhole and a maximum in the output signal is obtained. If the sample moves out of the focal plane, the amount of light transmitted by the pinhole is reduced and the signal at the photodiode decreases. We therefore expect the signal output from the detector to have a strong dependence on the position of the object.

Because a focused beam is employed, and the phase changes between the different rays comprising the beam are very small, the phase fluctuations of the laser are unimportant. Therefore, a semiconductor laser, or even an incoherent source, can be used. Furthermore, since the objective lens is used twice, once to focus the incoming wave to a point and a

second time to image that point onto the pinhole, the transverse amplitude response of the system is the square of the point spread function of the lens. Thus, when the sample is at the focal plane, the output from the detector is of the form $jinc^4(2\pi/\lambda) r \sin \theta_0$, where $jinc x = 2J_1(x)/x$. $J_1(x)$ is a Bessel function of the first kind, r is the distance from the optical axis, the aperture angle of the lens is θ_0 , and λ is the optical wavelength. Thus, the 3 dB resolution of this type of microscope is better by a factor of approximately 1.4 than a standard microscope, and the sidelobe level and speckle associated with the device are negligible.

To calculate the ranging response of this system when a plane reflector is scanned in the axial (z) direction, we assume a lens with a pupil function $P(\theta)$ where θ is the angle between the ray from the pupil plane to the focal point and the axis. By following the derivation of Richards and Wolf for vector fields, with some minor changes, it can be shown that the normalized field of the reflected wave at the pinhole is of the form [5]:

$$V(z) = \frac{\int_0^{\theta_0} \frac{(1 + \cos \theta) \sin \theta}{(\cos \theta)^{1/2}} e^{-2jkz \cos \theta} P(\theta) R(\theta) d\theta}{\int_0^{\theta_0} \frac{(1 + \cos \theta) \sin \theta}{(\cos \theta)^{1/2}} P(\theta) d\theta}$$

where the output signal from the detector is proportional to

$$I(z) = |V(z)|^2 \quad (2)$$

In these expressions, $R(\theta)$ is the reflection coefficient of the plane reflector, k is the wave number $(2\pi/\lambda)$, and $\sin \theta_0$ is the numerical aperture of the lens.

Assuming a plane reflector with $R(\theta) = 1$ and uniform excitation at the lens, $[P(\theta) = 1 \text{ for } \theta < \theta_0]$, $ka \gg 1$ and $(1 + \cos \theta)/\cos \theta^{1/2} = 2$, an approximate expression for $V(z)$ has been derived [6].

$$V(z) = e^{-jkz(1 + \cos \theta_0)} \frac{\sin kz(1 - \cos \theta_0)}{kz(1 - \cos \theta_0)} \quad (3)$$

This expression accurately predicts the shape of the central lobe and the phase change of the reflected signal. The result fails to account for asymmetries in the sidelobes which are caused by lens aberrations. The depth of focus is given by the 3 dB points of the central lobe in Eq. (3).

$$(\Delta z)_{3 \text{ dB}} = \frac{0.443 \lambda}{1 - \cos \theta_0} \quad (4)$$

Experimental results with mechanically-scanned systems

Mechanically-scanned microscope

The object itself can be moved in the transverse and range directions by piezoelectric pushers or stepping motors. We use piezoelectric pushers for the microscope and stepping motors to demonstrate the principles of the macroscopic range sensor. Sometimes the object is mounted on an additional piezoelectric transducer which can vibrate the sample in and out periodically. Alternatively, as will be described later, the focus is periodically moved back and forth by an electro-optic device or with an electrically-controlled deformable mirror.

A result taken with the mechanically-scanned microscope is shown in Fig. 3. It will be observed that there is good agreement between theory and experiment, and that the 3 dB range resolution of a 0.9 aperture lens using a He-Ne laser is about 0.6 μm . It will be noted that the sidelobes are not at the same level or as symmetric as the simple theory indicates. A more sophisticated theory, which takes phase aberrations and amplitude weighting of the lens into account, explains the discrepancy in the sidelobe behavior [4].

Results taken on photoresist films of the order of 1.8 μm and 4.86 μm thick are shown in Figs. 4 and 5. Two peaks are obtained corresponding to the reflections from the top and bottom surfaces of the film. It is relatively easy to modify the theory to take

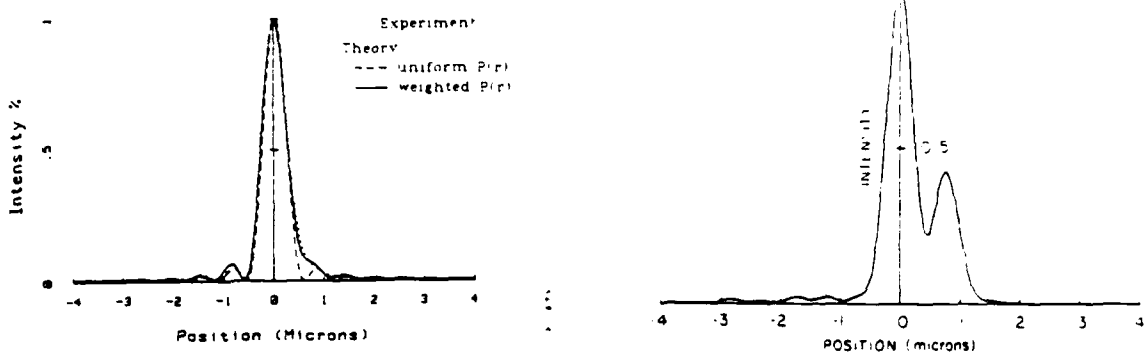


Fig. 3. $|V(z)|^2$ curve for objective of numerical aperture 0.9. Experimental data: dotted line. Theoretical calculations: solid and dashed lines.

Fig. 4. $|V(z)|^2$ curve of 1.8 μm photoresist on silicon.

account of this effect, and the results are extremely accurate for films thicker than 3 μm . However, for thinner films, where the two peaks overlap, the results obtained tend to be accurate as a measure of film thickness to only the order of a half wavelength ($\sim 2500 \text{ \AA}$). This uncertainty is primarily due to the unknown phase difference between the reflection from the top and bottom surfaces of the film. Use of phase measurements, as described below, can eliminate the difficulties. Direct comparison on calibrated samples can also eliminate this problem.

It is apparent that it would be useful to measure the position of the maximum of the reflectivity function with as high an accuracy as possible. To do this, we have adopted a simple stratagem. We vibrate the sample at a frequency Ω using a vibration amplitude comparable to or less than the depth-of-focus of the beam. In this case, we obtain an output from the photodetector at a frequency Ω , which passes through zero when the average value of $|V(z)|^2$ at the detector passes through a maximum. Thus, by looking for the zero or the minimum at a frequency Ω , we can determine the position of the focal point with very good accuracy. The result taken on the 4.86 μm photoresist film is shown as the full line in Fig. 5. When the depth-of-focus is of the order of 1 μm , we can determine the position of the maximum, and hence the film thickness, to within a few nanometers.

Optical range sensors

A schematic diagram of the optical range finder is shown in Fig. 6; this arrangement is slightly different from that of the microscope. The first lens after the beamsplitter focuses the laser beam to a spot of the order of 5 μm diameter, so that most of the beam passes through a 10 μm diameter pinhole. A camera lens placed beyond the pinhole focuses the light onto a point on the object. If the object is in the front focal plane of the camera lens and the pinhole is at the back focus, the reflected light passes back through the pinhole and is detected by the photodetector. When the object moves out of the focal plane, the amount of light passing through the pinhole is reduced. Hence, as we have already seen, the signal output from the detector has a strong dependence on the position of the object. Furthermore, the employment of a focused beam implies that the transverse definition of the system is excellent.

We used a 4 mW He-Ne laser with a wavelength of 6328 \AA in these experiments. A semiconductor laser could have been employed equally well; we chose to work with the gas laser initially only because of its availability and the greater ease of working with visible light in the early experiments. We found it convenient to use a Bragg cell for amplitude modulation of the incident light; with a semiconductor laser, we could directly modulate the laser itself.

To demonstrate the usefulness of this system for obtaining accurate distance measurements, we used a mirror as the reflecting object and scanned it in the axial (z) direction.

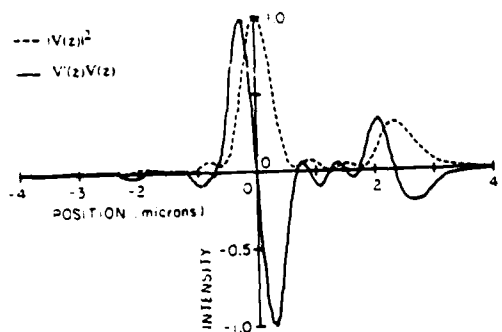


Fig. 5. $|V(z)|^2$ and $V'(z)V(z)$ curves of $4.86 \mu\text{m}$ photoresist on silicon.

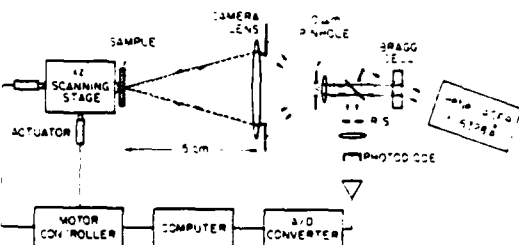


Fig. 6. Experimental arrangement of optical range finder.

Figure 7 shows the dependence of the signal on the position of the object. The numerical aperture of the optical system is 0.054 , the corresponding depth of focus is $188 \mu\text{m}$, and the spot size is about $10 \mu\text{m}$. The experimental curve fits the theoretical curve very well, except for some discrepancies in the sidelobes which are believed to be caused by aberrations in the optical system. By determining the position of the peak of this curve, we can determine the position of the object very accurately.

To determine the sensitivity of our measurement technique, we scanned the focused beam over a tilted mirror, as shown in Fig. 8. The straight line represents the mirrored surface and the dots are experimental results. The estimated accuracy is about $2 \mu\text{m}$. As we tilted

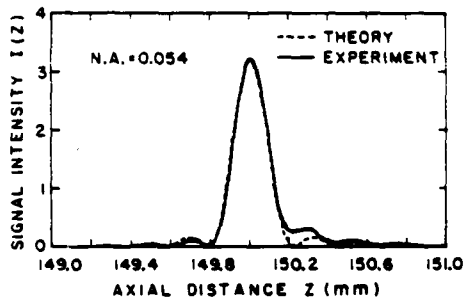


Fig. 7. $|V(z)|^2$ curve for camera lens in optical range finding system. Numerical aperture = 0.054 .

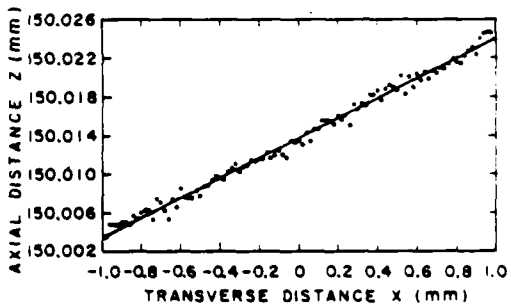


Fig. 8. Transverse scan over a tilted front surface mirror.

the mirror, the height of the central lobe decreased and the depth of focus increased. This is because less light could be collected by the camera lens, so the effective numerical aperture decreased.

The results of a scan over a $220 \mu\text{m}$ step on a specular reflector are shown in Fig. 9. The transverse spacing between adjacent points is $5 \mu\text{m}$. Except for the overshoot near the step, the accuracy of the range measurement is about $2 \mu\text{m}$. The overshoot is due to shadowing and interference effects.

This system is not only suitable for measurements on smooth surfaces, but also for measurements on rough surfaces. This behavior arises because when the light is focused to a point on a rough surface, the reflected light will be scattered in all directions, but an image of the point can still be obtained at the pinhole. We pay a price for this convenient result in that the light reaching the pinhole is greatly reduced in intensity; the advantage is that the alignment of the rough surface is relatively uncritical. To demonstrate this

effect, we measured a sample of sheet aluminum, as supplied by the manufacturer. The results we obtained are shown in Fig. 10. The central lobe of this curve is unchanged from the central lobe obtained using a mirror. As expected, the detected signal from this rough surface is much weaker than that for a smoother surface, but it is still strong enough to be easily detected with a narrowband receiving system. The results obtained were insensitive to the tilt of the object, essential for the measurement of ordinary machined parts.

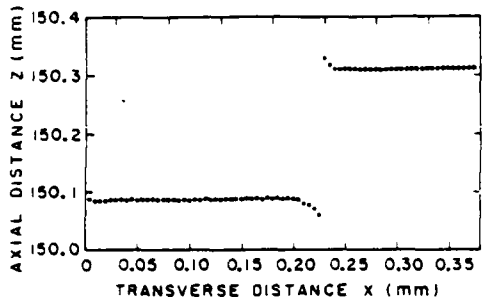


Fig. 9. Transverse scan over a step of aluminum on aluminum. Points represent peaks in intensity response.

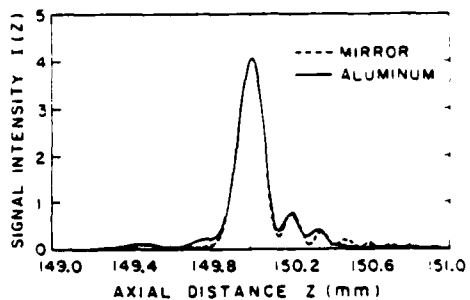


Fig. 10. $|V(z)|^2$ axial scan using a mirror (dashed line) and rough aluminum (solid line) surface as in the reflecting plane.

Phase measurements

A second microscope technique with which we have been working for some time [7] is shown in Fig. 11. A laser beam is incident on an acousto-optic Bragg cell. Part of the beam travels straight through the Bragg cell, but part is deflected at an angle which varies linearly with the driving frequency f_B of the Bragg cell. This technique has the advantages of great speed, repeatability, and random access. The Bragg cell is positioned at the pupil plane of an optical microscope, so the two outgoing beams are focused onto the object being examined and produce two focused spots. One spot is fixed and the other scans as the frequency f_B of the Bragg cell is varied. The beams are reflected from the sample, retrace their paths through the Bragg cell, and interfere on a photodiode, as shown. A lens images the center of the Bragg cell on the photodiode so that the spot does not wander off the detector as the beam is scanned.

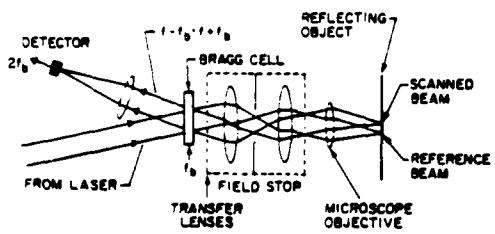


Fig. 11. Schematic diagram of the electronically-scanned microscope.

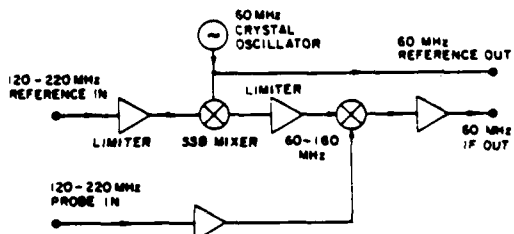


Fig. 12. Block diagram of the analog signal processing subsystem.

The beam reaching the photodiode from the scanned spot is upshifted by a frequency f_B , and the one from the fixed spot is downshifted by the same frequency f_B . When the beams interfere on the photodiode (a square-law device), we obtain an output product term at a frequency $2f_B$ whose phase is the optical phase difference between the fixed reference spot and the scanned spot. Since the amplitude of the fixed spot is constant, the amplitude of the output signal varies linearly with the amplitude of the scanned spot.

We are using a modified Leitz microscope, kindly supplied to us and modified by the E. Leitz Company, with an Inrad (Matsushita) Bragg cell. The Bragg cell has a frequency range of approximately 50-100 MHz and is capable of providing about 340 resolvable spots (equivalent to 680 after our post-processing).

We measure the amplitude and phase of the rf signal (100-200 MHz) by mixing down to a 60 MHz IF, as shown in Fig. 12, and then using the digital detectors shown in Fig. 13. These circuits are capable of making amplitude and phase measurements at a rate of about 50,000 points per second, with an accuracy of one or two tenths of a degree in phase, and about a tenth of a percent in amplitude.

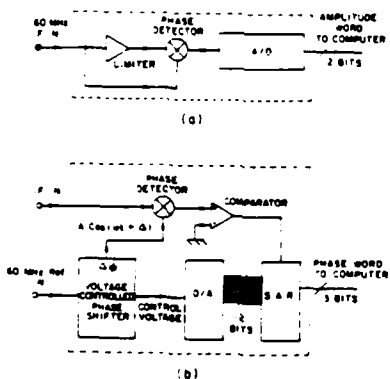


Fig. 13. (a) Amplitude digitizer. (b) Successive approximation phase digitizer.

On this basis, we expect to measure heights with sensitivities on the order of a thousandth of a wavelength or better, i.e., a few Angstroms. Results taken with this type of system are shown in Figs. 14a and 14b. The sample was a periodic array of 200 Å tall, 0.40 μm wide lines and 0.33 μm spaces on crystalline quartz. Note the great improvement due to the deconvolution (see below). The amplitude changes as the beam is scanned over the edge of the film show the reflection coefficient change between the films and the substrates.

The amplitude response is exactly the intensity response of a standard microscope. The 3 dB definition of this microscope, without post-processing, is approximately 1.4 times better than a standard microscope's.

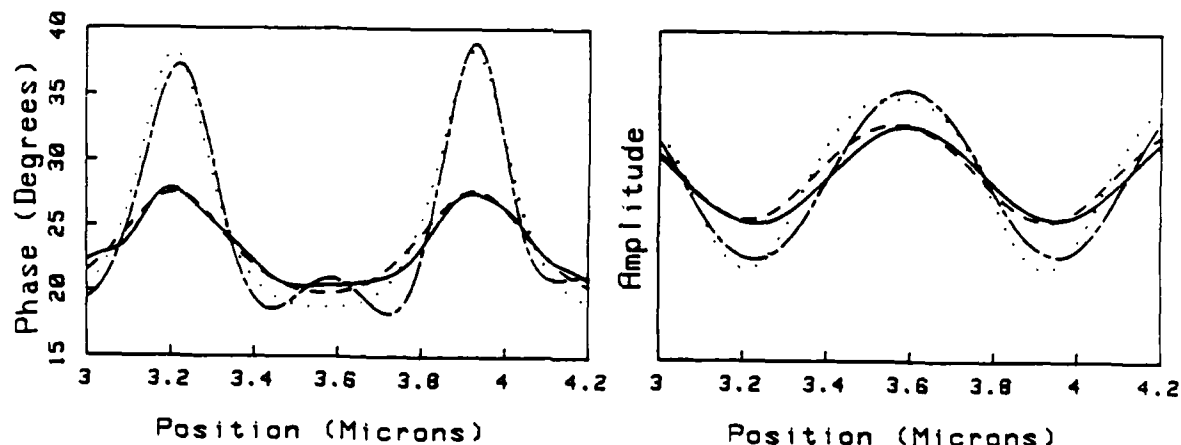


Fig. 14. Scan data from a periodic array of 200 Å tall, 0.4 μm wide aluminum lines and 0.33 μm spaces. The substrate was silica quartz. (a) Phase. (b) Amplitude. Legend: solid = raw data, dashed = simulation, dash-dot = deconvolved data, and dotted = deconvolved simulation.

As the point spread function is squared, the spatial frequency bandwidth is twice that of a standard type 1 microscope. The transfer functions of the type 1 and type 2 microscopes are shown in Fig. 15, plotted in normalized spatial frequency. These correspond to the Fourier transforms of the linespread function of the microscope. Since we have both

amplitude and phase information available, and twice the bandwidth, we can use linear deconvolution to improve the resolution to twice that of a type 1 microscope at the expense of introducing sidelobes. This is done by digital filtering in a personal computer (it typically takes 20 seconds for 1024 points), so we can change the filter very easily. The curve marked $F(s)$ in Fig. 15 is the approximate transfer function we have obtained after processing. The roll-off at the high end reduces the noise gain of the filter. By choosing various filters, one can trade off lateral resolution against ringing or sidelobe response.

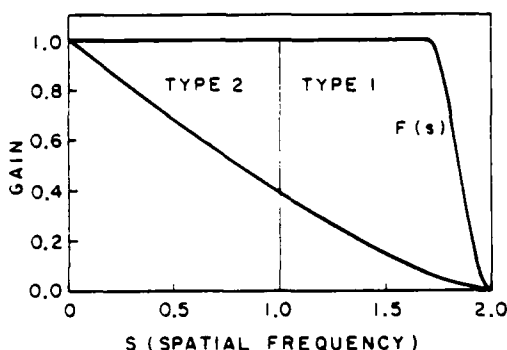


Fig. 15. Comparison of the theoretical transfer function of a type 1 microscope with that of the electronically-scanned type 2 before and after post-processing.

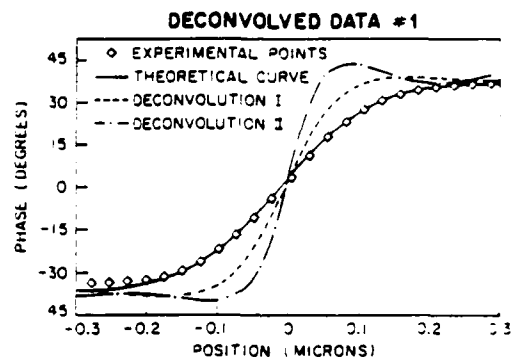
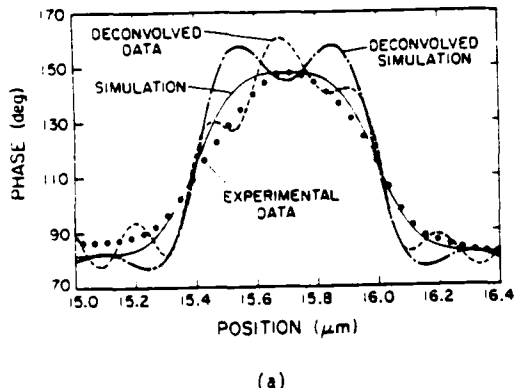
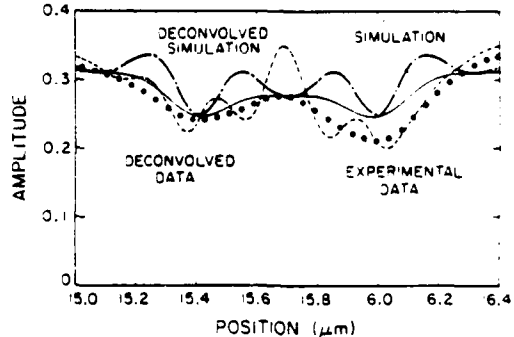


Fig. 16. Data from a single scan of a 900 Å step of aluminum on aluminum taken with the electronically-scanned microscope. The experimental results are compared with theory, along with deconvolved scan data made by using two different inverse filters.

Figure 16 shows this trade-off clearly [7]. The original data (diamonds) is plotted with the theoretical curve (solid) and two deconvolved experimental curves. The raw data shows a 10-90% rise interval of 0.23 μm . Deconvolution I used a relatively gentle filter to achieve 0.13 μm edge response (10-90%) with little added ringing. Deconvolution II used a different filter to achieve 0.10 μm edge response (10-90%), but with extra ringing added. Thus, we have demonstrated an edge resolution of better than $\lambda/5$.



(a)



(b)

Fig. 17. Data from a scan of a 0.61 μm line of Au on Si taken with the electronically-scanned microscope and compared with theory. Wavelength was 514 nm. (a) Phase. (b) Amplitude.

The results shown in Fig. 17 are for a gold film on silicon, 1000 Å thick and 0.61 μm wide, taken using laser illumination of 0.51 μm wavelength. When the spot is partly on the film and partly on the substrate, the two parts do not add in phase at the detector. This results in amplitude dips at the edges of the film, even though the film and substrate

reflection coefficients are almost the same. By carrying out the same inverse filtering process, we can sharpen up the phase response of the film a great deal and get a good measure of the width and thickness of the film. The measured width is $0.64 \mu\text{m}$ (our scanning steps are $.04 \mu\text{m}$ apart), which agrees very well with the high-voltage SEM value of $0.61 \mu\text{m}$. The very sharp edges in the phase curve permit unambiguous measurements of width.

Related techniques

We have described here two basic techniques for measuring height and width. We have shown that deconvolution techniques can improve the resolution of the microscope and that by vibrating the sample, we can obtain a very sensitive measure of the position of the focal point. We have recently begun to work with other techniques for moving the focal position back and forth. One is a modified Zernike phase contrast microscope, illustrated in Fig. 18. An rf voltage of frequency Ω is applied to a transparent center electrode deposited on an electro-optic cell of PLZT. The electro-optic cell is placed in the back focal plane of the lens. It may be shown that an ac output at the frequency Ω is obtained from the detector as the phase through the central region of the beam is varied. When the beam is focused on the surface of a reflecting object, the rf signal amplitude passes through zero. This zero occurs because small phase variations do not affect the amplitude of the $V(z)$ curve when it is at its maximum. When the beam is defocused, there is a static phase shift between the rays at the center of the beam and those at the outside, resulting in an ac output. Hence, it is very easy to determine when the beam is defocused. Furthermore, the phase of the rf output from the detector reverses in sign as the focus moves past the reflector. A simple result of this kind is shown in Fig. 19. A similar system, which operates with a reflecting mirror in the optical path, employs a flexible spherical mirror made of a piezoelectric cantilever material. We prefer the transmission system because it is simpler.

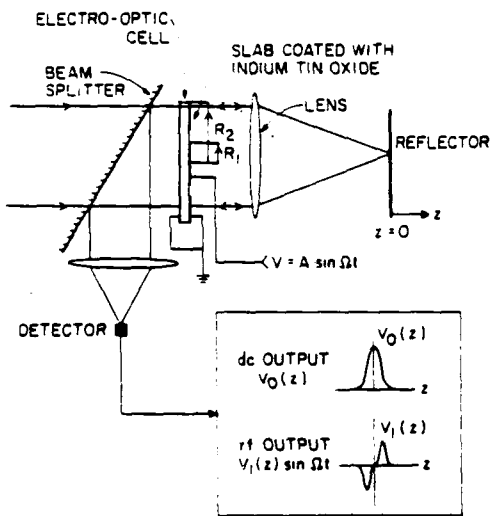


Fig. 18. Schematic diagram of electro-optic cell placed in standard type II microscope, thus creating a phase contrast system.

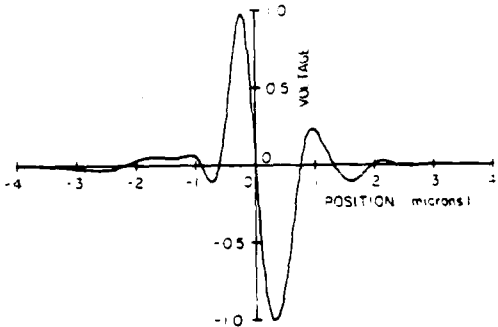


Fig. 19. Curve demonstrating the effect of defocus of a plane reflector in the modified Zernike phase contrast microscope.

We are presently developing high-speed one- and two-dimensional scanners for the optical range sensor and scanned optical microscope. One technique is to employ two crossed Bragg cells for a high-speed two-dimensional scan. A second technique, which we believe will give us a great deal of flexibility, is that used in the Tandem Scanning Microscope by Petran et al [8]. They use many pinholes placed in a rotating Nipkow disk, instead of only one pinhole, and illuminate a $1.5 \text{ cm} \times 1.5 \text{ cm}$ area with a broad, intense light source. An objective lens focuses an image of the pinholes on the object, and the reflected light passes back through the same lens, a beam splitter, and a set of mirrors to a conjugate set of pinholes on the disc. The pinholes themselves are located on spiral curves, so that when the disc is rotated rapidly, a raster scan is generated. Since many pinholes are employed, and the disc can be rotated at high speed, an image with several thousand lines is obtained.

with a high frame rate. The image itself can be viewed directly with a microscope eyepiece; it has good depth discrimination, since it is a modified type II microscope. We are developing a simplified form of this rapid-scan system, which should be adaptable to the applications we have already described.

Conclusion

We conclude that it is possible to modify the standard microscope, turn it into a scanning system, and obtain better resolution and more quantitative information than has been available with optical microscopy techniques in the past.

Acknowledgment

This work was supported by the Air Force Office of Scientific Research under Contract No. AFOSR-84-0063B, by the Office of Naval Research under Contract No. N00014-84-K-0327, and by the Stanford Institute for Manufacturing and Automation. Two of us, Phil Hobbs and Tim Corle, were supported by IBM Graduate Predoctoral Fellowships.

References

1. Strand, T. C. (January/February 1985). OPT. ENGINEERING 24 (1), pg. 33.
2. Williams, C. C. and H. K. Wickramasinghe (accepted for publication). J. APPL. PHYS.
3. Sheppard, C. J. R. (1980). Scanned Image Microscopy, Edited by E. A. Ash, Academic Press, London. pg. 201-225.
4. Corle, T. R., C-H. Chou, and G. S. Kino (accepted for publication). OPT. LETT.
5. Richards, B. and E. Wolf (1959). PROC. R. SOC. LONDON A. 253, pg. 358.
6. Liang, K. K., G. S. Kino, and B. T. Khuri-Yakub (March 1985). IEEE TRANS. ON SONICS AND ULTRASONICS, Spec. Issue on Acoustic Microscopy SU-32 (2), pg. 213.
7. Hobbs, P. C. D., R. L. Jungerman, and G. S. Kino (August 1985). PROC. SPIE 565, pg. 74.
8. Petran, M. et al (May 1985). PROC. R. MICRO. SOC. 20 (3), pg. 124.

Gordon S. Kino is Professor and Associate Chairman of Electrical Engineering at Stanford University. He has published over three hundred papers in the fields of plasmas, acoustics, microwave tubes, and optics. Professor Kino is a Fellow of the IEEE, the American Physical Society and AAAS, and a member of the National Academy of Engineering

Timothy R. Corle received a B.A. in Physics with honors from the University of Colorado, Boulder in 1983. From 1982 until 1984 he worked for the Coatings R & D Group at Rockwell International. Mr. Corle is currently a Ph.D. candidate at Stanford University. His research interests include microscopy and opto-electronics.

P. C. D. Hobbs received a B.Sc. in Astronomy and Physics with honors from the University of British Columbia in 1981. From 1981 to 1983 he was an RF design engineer at Microtel Pacific Research Ltd. He is currently working towards a Ph.D. in Applied Physics at Stanford University. His research interests include microscopy, signal processing, and electromagnetic theory.

Mr. G. Q. Xiao received a B.S. in Physics from Peking University, People's Republic of China in 1983. He is currently a Ph.D. candidate at Stanford University. His research interests include range sensing, fiber and integrated optics, and opto-electronics.

Images of a lipid bilayer at molecular resolution by scanning tunneling microscopy 4035

(biological membranes/cadmium isocanoate/graphite)

D. P. E. SMITH*, A. BRYANT*, C. F. QUATE**†, J. P. RABE‡§, CH. GERBER‡¶, AND J. D. SWALEN‡

*Department of Applied Physics, Stanford University, Stanford, CA 94305; ‡IBM Almaden Research Center, San Jose, CA 95120; and †IBM Research Laboratory, Zürich, Switzerland

Contributed by C. F. Quate, September 23, 1986

ABSTRACT The molecular structure of a fatty acid bilayer has been recorded with a scanning tunneling microscope operating in air. The molecular film, a bilayer of cadmium isocanoate (arachidate), was deposited onto a graphite substrate by the Langmuir-Blodgett technique. The packing of the lipid film was found to be partially ordered. Along one axis of the triclinic unit cell the intermolecular distance varied randomly around a mean of 5.84 Å with a SD of 0.24 Å. Along the other axis the mean distance was 4.1 Å and appeared to vary monotonically over several intermolecular distances, indicating that a superstructure of longer range may exist. The molecular density was one molecule per 19.4 Å². The surprising ability of the scanning tunneling microscope to image the individual molecular chains demonstrates that electrons from the graphite can be transferred along the molecular chains for a distance of 50 Å.

Molecular monolayers, bilayers, and multilayers are important in the fields of biology and technology. In biology where they occur as lipid membranes the details of the two-dimensional packing are important for our understanding of their biological function (1). The proposed technological uses of Langmuir-Blodgett films as thin film dielectrics make it necessary to characterize them if we are to optimize the interactions that occur within the film and at the interfaces with the environment (2). In recent years a number of techniques have been applied toward the problem of determining the structure, orientation, and packing of molecular monolayers and bilayers. The methods that have been used to characterize these films include infrared spectroscopy (3), Raman spectroscopy (4), electron diffraction (5), x-ray diffraction (6), and fluorescence microscopy (7). However, even for the simple cases of pure fatty acids, it is difficult to unambiguously determine the packing structure. The most direct way to study molecular packing is with a microscope that is capable of resolving the intermolecular distances, which in the case of the fatty acids is about 5 Å. In this report we will demonstrate that the scanning tunneling microscope (STM) is useful for this purpose. A preliminary report on this work has been presented elsewhere (25).

The technique of scanning tunneling microscopy has been used to image the distribution of electronic charge density for a variety of conducting and semiconducting solid surfaces (8-10). Viruses (11) and DNA (G. Binnig, H. Rohrer, E. Courtenes, H. Gross, and J. Sogo, personal communication) deposited on conducting substrates have also been imaged with the STM, but the resolution in these experiments was only about 50 Å. In this report we present STM studies of a fatty acid bilayer deposited on a graphite substrate; we are able to reproducibly image the individual molecules in the film with a resolution of about 2 Å. By using the STM in a

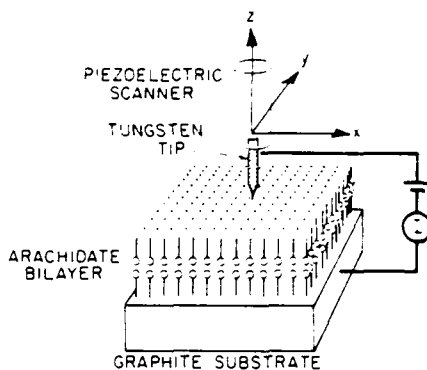


FIG. 1. Schematic of the STM experiment. A fine tungsten tip is brought to within several angstroms of the sample surface. With a voltage applied to the tip, electrons can tunnel across the gap, and a current is detected at the sample. If the tip is now rapidly scanned over the sample in the x and y directions, the variations in the tunnel current correspond to the atomic corrugation of the surface.

high-speed mode we have obtained several thousand pictures that can be assembled into a "movie." The lipid film, prepared by the Langmuir-Blodgett technique, consists of two monomolecular layers of cadmium isocanoate (cadmium arachidate: CdAch), each 27 Å thick. High resolution imaging of organic molecules has been possible with the STM because, to our surprise, the bilayer of closely packed fatty acid molecules had sufficiently high electrical conductivity.

The STM experiment is shown schematically in Fig. 1. A finely sharpened tungsten tip is brought to within several angstroms of the surface of our sample by means of a coarse mechanical approach and a fine piezoelectric transducer. With a voltage applied to the tip, electrons can tunnel across the gap, and a current is induced. This current decreases exponentially as the gap spacing increases and provides an extremely sensitive measure of the tip-to-sample distance. Height changes of 0.1 Å are easily detected. In our method of imaging (12) we raster scan the tip over a flat area of the sample while maintaining the tip at an average distance. The detected tunnel current then contains variations that correspond to the atomic corrugation of the surface. The current variation, representing surface contour, is converted to a video signal that maps the surface over which the tip scans. In this way we take television "movies" of the atomic surface structure at a rate of about 10 frames per sec.

Abbreviations: STM, scanning tunneling microscope; CdAch, cadmium isocanoate (cadmium arachidate).

*To whom reprint requests should be addressed.

†Present address: Max-Planck-Institut für Polymerforschung, Postfach 3148, D-6500 Mainz, Federal Republic of Germany.

The publication costs of this article were defrayed in part by page charge payment. This article must therefore be hereby marked "advertisement" in accordance with 18 U.S.C. §1734 solely to indicate this fact.

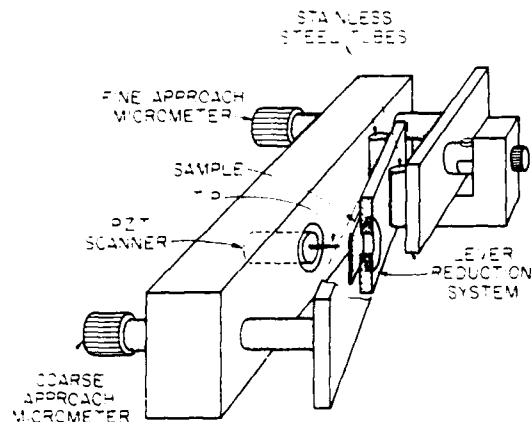


FIG. 2. The STM used in this study. The sample is moved toward the tungsten tip using a pair of micrometers and a lever reduction system. The fine-distance control and the scanning are performed by a single piezoelectric tube with four electrodes on the outside and one on the inside.

The microscope itself is quite simple (Fig. 2). The coarse-approach mechanism is a pair of micrometers whose motion is reduced by a system of levers. The sample can be brought toward the tip from several millimeters away with a resolution of about 200 Å. The fine-distance control and the scanning is performed by a single piezoelectric tube with four equally spaced electrodes on the outside and one electrode on the inside. Motion in three orthogonal directions is possible by applying voltage to the proper electrodes (13). To filter out ambient vibrations, the microscope is mounted on top of stacked metal plates separated by pieces of rubber. The microscope can operate in air at room temperature.

Graphite was chosen as the substrate in this work because previous STM studies have shown that cleaving gives large regions that are atomically flat (11, 12, 14, 15). Moreover, in air the surface appears to remain clean over long periods of time. The fatty acid bilayers were fabricated using the Langmuir-Blodgett technique (16), shown schematically in Fig. 3. Icosanoic (arachidic) acid dissolved in chloroform was spread on the surface of water and compressed to a surface pressure of $30 \text{ mN} \cdot \text{m}^{-1}$ in order to create a monolayer. The water contained $2.5 \times 10^{-4} \text{ mol/liter}$ of CdCl_2 at a pH of 7 to stabilize the monolayer as the cadmium salt. Freshly cleaved samples of highly oriented pyrolytic graphite (provided by A. W. Moore, Union Carbide, Parma, OH) were lowered into the water at a speed of about 3 mm/min. Because graphite is hydrophobic, one monolayer was deposited on the way into the water, and a second one was added on the way out. The transfer of the monolayer on the downstroke was somewhat smaller than unity and was close to unity on the way up. The presence of the film was checked by ellipsometry; the average thickness was found to be close to a double layer. Attempts to transfer a single layer were unsuccessful because graphite is too hydrophobic to allow a transfer with the hydrophilic head group on the graphite. The configuration with the head groups facing the air is also unstable. Recently it has been shown that the STM can operate underwater (17). This should make imaging of a monolayer possible by having the hydrophobic tail on the graphite and the hydrophilic head in the water where it would be stable.

Fig. 4 shows a comparison of an image of cleaved pristine graphite and an image of a CdAch bilayer deposited onto cleaved graphite. Images such as these have been repeated several times with different samples. In both pictures in Fig. 4 the tip voltage was 40 mV, positive with respect to the sample, and the average current was held to 2.0 nA. The picture was

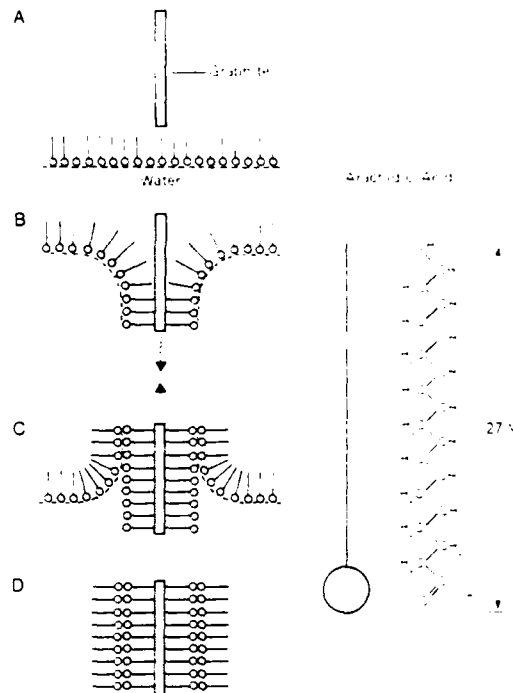


FIG. 3. Sample fabrication with the Langmuir-Blodgett technique. Arachidic acid dissolved in chloroform is spread on a water surface (A). The graphite substrate is lowered into the water, and because it is hydrophobic, it gains a monolayer on the way down (B). A second monolayer is transferred on the way up (C), giving a CdAch bilayer in air (D).

scanned at 2 kHz in the horizontal direction and 80 Hz in the vertical direction. The image was converted to a video signal and stored on video tape using an Arlynva image-processing system (Princeton Electronics Products, North Brunswick, NJ). It was then temporally filtered using the same machine and spatially filtered by a digital computer. The distortion introduced into the picture due to scanner nonorthogonality and unequal scan ranges was removed by linearly transforming the graphite image to agree with its known hexagonal structure (18); the transformation required to correct for scanner imperfections is constant with time. The same transformation was applied to the image of the Langmuir-Blodgett film. Because the experimental parameters in the two images are the same (the same tip was used), the corrected graphite image serves as a calibration for the Langmuir-Blodgett picture.

The CdAch film in the eyes of the STM looks qualitatively different from the graphite substrate onto which it is deposited. The graphite has a very uniform structure, while the Langmuir-Blodgett film shows irregularities in both the apparent size of the molecules and the distances between them. To show the larger-scale structure of the molecular packing we have assembled a sequence of four images of the Langmuir-Blodgett film (Fig. 5). These four images were taken from a video recording that showed the gradual movement of the Langmuir-Blodgett film through the viewing field of the microscope. Whereas the graphite shows a variation in lattice spacing of only about 1%, the Langmuir-Blodgett film shows a significantly greater variation and more anisotropy. The observed packing fits a triclinic unit cell. The intermolecular distances along one axis, the *a* axis, are larger than along the other axis, the *b* axis.

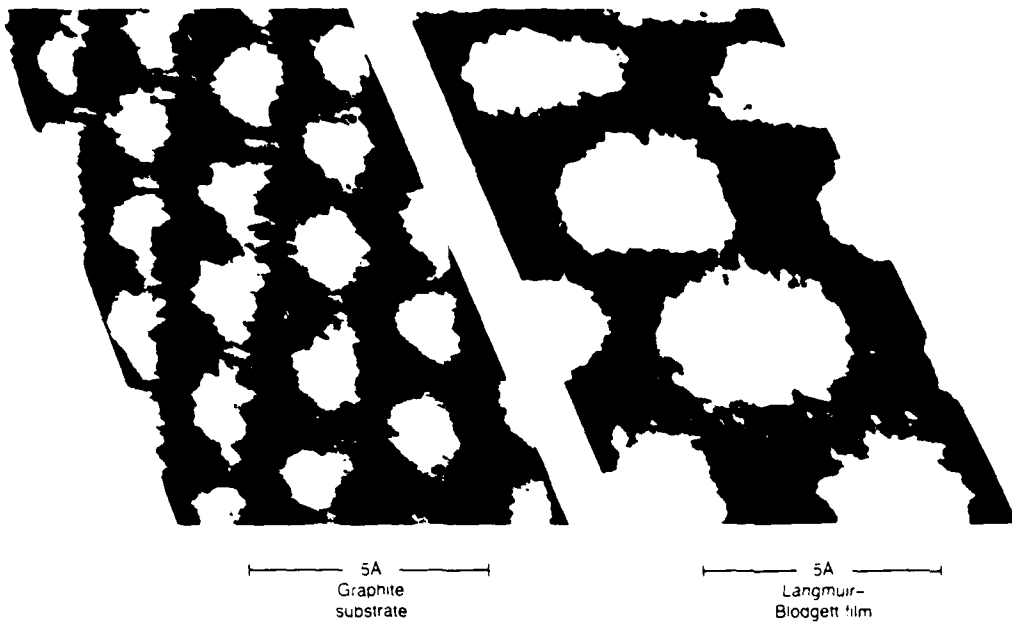


FIG. 4. Images of a cleaved graphite sample obtained with a STM. *Left*, pristine graphite. *Right*, graphite coated with CdACh bilayer. Brightness indicates higher tunneling current and therefore represents higher topography, or increased conductivity.

The two axes form a mean angle of 128° with a SD of 2° . The variation along the a axis is random, but the distances along the b axis vary monotonically. Using the graphite C-C bond length of 1.42 \AA from Fig. 4 as a distance calibration, we find the average intermolecular distance along the a axis to be 5.84 \AA with a SD of 0.24 \AA , or 4% . The variation of the lattice spacing is consistent with the electron diffraction linewidth

for lipid monolayers on silicon oxide surfaces, where coherence lengths of 50 to 100 \AA were observed (16). This coherence length would predict a 5% variation in the intermolecular distances, and this is consistent with our findings. The spacings along the b axis are smaller, with a mean of 4.1 \AA and a SD of 0.43 \AA . However, this average is not meaningful since the b axis spacings decrease monotonically from the bottom

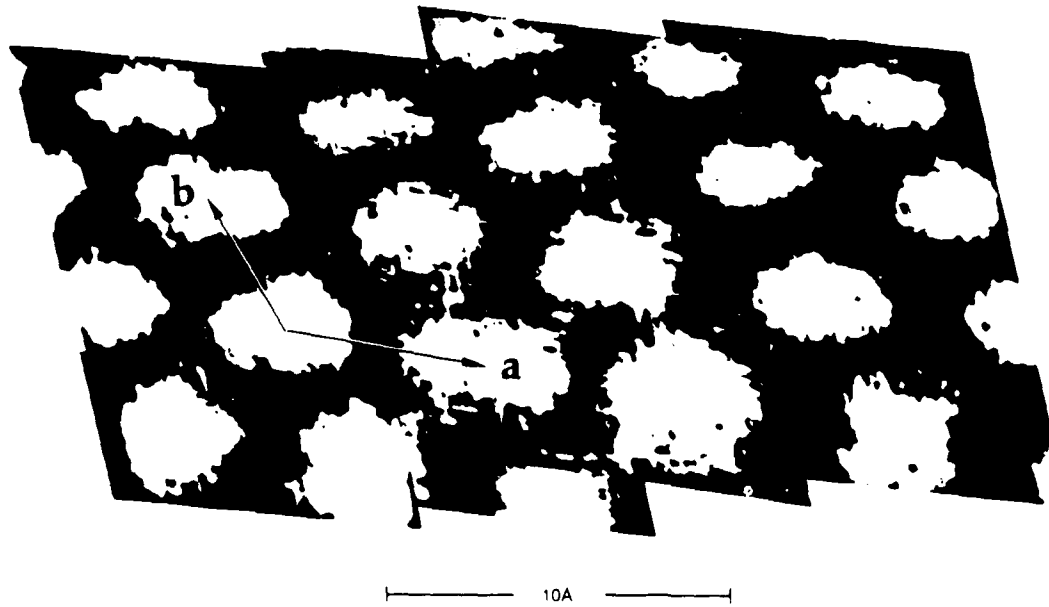


FIG. 5. STM image of a CdACh bilayer. The variation along one axis (*a*) of the triclinic unit cell is random with an average of 5.84 \AA and a SD of 0.24 \AA . The spacings along the other axis (*b*) are smaller, about 4 \AA , and monotonically decrease from the bottom to the top of the image. The mean area of the unit cell is 19.4 \AA^2 .

to the top of the image. Larger areas need to be investigated in order to find whether a possible superstructure exists (19). The mean molecular density is one molecule per 19.4 \AA^2 . This agrees very well with the calculated density of molecules on the water surface from pressure-area curves (ref. 16, p. 186).

The ordered Langmuir-Blodgett film was consistently observed to flow across the viewing field of the STM. In the sequence shown in Fig. 5 the CdAch lattice appeared to move at a rate of about $4 \text{ \AA}/\text{sec}$. Because images of pristine graphite were free from drift over several minutes, the Langmuir-Blodgett film might be actually sliding across the graphite substrate. Some areas of the samples coated with the Langmuir-Blodgett molecules showed no ordered packing of the molecules; in these areas large unidentifiable lumps of material were seen sitting on top of the graphite substrate. The lumps were observed to move relative to the stationary graphite lattice and may be disassociated CdAch molecules. In some places only the graphite substrate was visible on the coated sample. In contrast to images of pristine graphite that were very stable, the clarity and resolution of the Langmuir-Blodgett images would change suddenly. These effects indicate that the film is nonuniform over the whole sample, possibly because of weak bonding to the substrate. No edge separating the ordered molecular film from the graphite substrate could be located.

The morphology of these lipid films, which was the focus of this study, is not the only interesting feature of the Langmuir-Blodgett films. We found that current at the position of the tip could be easily measured, and this suggests that the STM technique is useful for studying charge transfer in organic solids. Hopfield (20) has described the transfer of charge along molecular chains where the electronic states are localized at the position of the atomic sites. The electronic properties of these molecular assemblies are very different from those in crystalline solids. The high degree of periodicity that gives long-range order in crystalline solids is nonexistent in molecular solids, and as a result, the electrons are believed to be confined to the molecular chains. This condition is evident in our images, because they show little conduction in the regions between the molecules. Another effect to consider is the weak van der Waals forces between chains that can lead to fluctuations in the molecular conformations along the chains. We found that the current was significantly noisier when imaging the Langmuir-Blodgett films than it was with pristine graphite; this may be a manifestation of molecular fluctuations within the film.

With the STM we were able to examine well-defined areas of the sample and control the gap spacing precisely. Let us consider that the total current was conducted along a CdAch filament with a cross-section of 20 \AA^2 , the approximate resolution we observed. Then for a current of 2 nA and voltage of 40 mV the resistivity of the 50 \AA chains was $10^3 \Omega\text{-cm}$. In contrast to this fairly low resistivity, other experiments (21, 22) have suggested that the conduction through fatty acid monolayers on oxidized metal substrates occurs by tunneling through an insulator with a resistivity ranging from 10^9 to $10^{15} \Omega\text{-cm}$. While these results using planar tunneling junctions show that the electron affinity of the films acts to significantly lower the tunneling barrier, it would appear unlikely that tunneling alone could account for the high conductivity we observed. Baró *et al.* (11) in their STM experiments with viruses have also found surprisingly high conductivity through thick organic materials. They propose the existence of conduction levels lower than the kinetic energy of the electrons, so that the electrons can propagate, rather than tunnel, through the specimen. Duke has dealt with this question at length in his theoretical treatment of conduction through organic materials (23) and in his discussion of field emission from clean surfaces covered with absorbed molecules (24).

Our results, which display the structure of the lipid bilayers in a way that is not possible with other techniques, demonstrate the advantages of using the STM to study organic molecules. In particular, we are able to obtain a resolution of several angstroms using a simple instrument. In conventional electron microscopy it is often necessary to "decorate" the molecules with metal atoms to render them visible to the microscope. With the STM this procedure is unnecessary. The high energy of the electrons, usually keV, in electron microscopes often damages the specimen. In contrast, the low energy of tunneling electrons, on the order of 10 meV , makes it possible to probe the structure without disrupting the sample. Another attractive feature of the STM is its ability to take real time movies and observe dynamical behavior. Finally, the images are taken in air rather than the vacuum environment demanded by most high-resolution techniques. Our results, combined with the recent report of the operation of the STM in water (17), suggest that it is possible to image organic molecules in an aqueous solution. This is the natural environment for many organic molecules, and it should open up a variety of interesting examinations of structural and electrical properties. Biological membranes, close relatives of the Langmuir-Blodgett films, should be particularly appropriate subjects for study.

The research at Stanford University was supported by the Defense Advanced Research Projects Agency and the Joint Services Electronics Program. The research at IBM was partially supported by a grant from the Army Office of Research.

1. Sackmann, E. (1978) *Ber. Bunsen-Ges. Phys. Chem.* **82**, 891-909.
2. Roberts, G. G. (1985) *Adv. Phys.* **34**, 475-512.
3. Rabolt, J. F., Burns, F. C., Schlotter, N. F. & Swalen, J. D. (1983) *J. Chem. Phys.* **78**, 946-952.
4. Rabe, J. P., Rabolt, J. F. & Swalen, J. D. (1987) *J. Chem. Phys.* in press.
5. Fischer, A. & Sackmann, E. (1984) *J. Phys. (Les Ulis Fr.)* **45**, 517-527.
6. Seul, M., Eisenberger, P. & McConnell, H. M. (1983) *Proc. Natl. Acad. Sci. USA* **80**, 5795-5797.
7. Losche, M., Rabe, J., Fischer, A., Rucha, B. U., Knoll, W. & Mohwald, H. (1984) *Thin Solid Films* **117**, 269-280.
8. Binnig, G. & Rohrer, H. (1986) *IBM J. Res. Dev.* **30**, 355-369.
9. Quate, C. F. (1986) *Phys. Today* **39**, 26-33.
10. Golovchenko, J. (1986) *Science* **232**, 48-53.
11. Baró, A. M., Miranda, R., Alamán, J., García, N., Binnig, G., Rohrer, H., Gerber, Ch. & Carrascosa, J. L. (1985) *Nature (London)* **315**, 253-254.
12. Bryant, A., Smith, D. P. E. & Quate, C. F. (1986) *Appl. Phys. Lett.* **48**, 832-834.
13. Binnig, G. & Smith, D. P. E. (1986) *Rev. Sci. Instrum.* **57**, 1688-1689.
14. Binnig, G., Fuchs, H., Gerber, Ch., Rohrer, H., Stoll, E. & Tosatti, E. (1986) *Europhysics Lett.* **1**, 31-36.
15. Park, S.-I. & Quate, C. F. (1986) *Appl. Phys. Lett.* **48**, 112-114.
16. Gaines, G. L. (1966) *Insoluble Monolayers at Liquid-Gas Interfaces* (Interscience, New York).
17. Sonnenfeld, R. & Hansma, P. K. (1986) *Science* **232**, 211-213.
18. Selloni, A., Carnevali, P., Tosatti, E. & Chen, C. D. (1985) *Phys. Rev. B* **31**, 2602-2605.
19. Garoff, S., Deckman, H. W., Dunsmuir, J. H., Alvarez, M. S. & Bloch, J. M. (1986) *J. Phys. (Les Ulis Fr.)* **47**, 701-709.
20. Hopfield, J. J. (1977) in *Electrical Phenomena at the Biological Membrane Level*, ed. Roux, E. (Elsevier, New York), p. 471.
21. Mann, B. & Kuhn, H. (1971) *J. Appl. Phys.* **42**, 4398-4405.
22. Polymeropoulos, E. E. (1977) *J. Appl. Phys.* **48**, 2404-2407.
23. Duke, C. B. & Gibson, H. W. (1982) in *Encyclopedia of Chemical Technology* (Wiley, New York), Vol. 18, pp. 755-793.
24. Duke, C. B. & Fauchier, J. (1972) *Surf. Sci.* **32**, 175-204.
25. Rabe, R., Gerber, Ch., Swalen, J. D., Smith, D. P. E., Bryant, A. & Quate, C. F. (1986) *Bull. Am. Phys. Soc.* **31**, 289.

MEASUREMENT OF REAL-TIME DIGITAL SIGNALS IN A SILICON BIPOLAR JUNCTION TRANSISTOR USING A NONINVASIVE OPTICAL PROBE

Indexing terms Measurement, Bipolar devices, Electro-optics, Optical measurement

We report optical charge sensing of real-time 0.8 V digital signals in a silicon bipolar transistor in a 20 MHz bandwidth using a 1.3 μm semiconductor laser, and in a 100 MHz bandwidth using a 1.3 μm Nd:YAG laser. The probe is noninvasive, inducing a transistor base current of less than 10 nA.

Earlier techniques for using noninvasive optical probes to measure electrical signals in an integrated circuit relied on sensing an induced electric field in an external electro-optic crystal brought near the circuit.¹ Later work done in this field relied directly on the birefringence of the GaAs substrate. Using this technique, direct electro-optic sampling of both analogue and digital electrical signals in GaAs integrated circuits has been demonstrated.^{2,3} Direct electro-optic detection in silicon is not possible because of its crystalline symmetry. Alternative techniques used to measure signals in silicon integrated circuits include the voltage-contrast scanning electron microscope⁴ and the scanning photoexcitation probe.⁵ However, the voltage-contrast SEM has a low sensitivity and is very expensive. The photoexcitation probe uses an above-bandgap optical source to photoconductively perturb internal nodes within an integrated circuit. This probe is invasive and only measures the logic states of the circuit. Other higher-order interactions such as the optical Kerr and Franz-Keldysh effects are not large enough to be of practical value in silicon. However, free carriers perturb the index of refraction in all materials because of their intrinsic polarisability. This is the basis of our present work. Earlier researchers have used this concept to make both absorptive⁶ and refractive modulators.⁷ We have previously described a technique for detecting this free carrier density, and have demonstrated a shot-noise-limited sensitivity of $2.6 \times 10^8 \text{ e cm}^2 \text{ Hz}$ for 1 mA of photocurrent.⁸ This letter describes the application of this concept to the measurement of real-time 0.8 V digital signals in silicon bipolar junction transistors.

The system used for optically detecting charge density modulation in silicon integrated devices is shown in Fig. 1. The output from a 1.3 μm laser passes through a Faraday isolator to minimise reflections which cause instabilities in the laser. The optical beam continues through a polarising beam splitter and a birefringent Nomarski prism. This prism separates the incoming beam into two beams which diverge from each other by about 4 mrad. The objective lens focuses these two beams into two spots separated by about 74 μm in the integrated circuit. These two beams are focused through the backside of a polished silicon wafer (see the inset in Fig. 1). One beam travels through the device [the emitter, base and collector of the vertical NPN bipolar junction transistor (BJT)] in which the charge density is being electrically modulated. The reference beam travels through a nearby region in which no charge is being modulated. The two beams then reflect off front surface metal and travel back through the substrate. The Nomarski prism recombines the two beams and the polarising beam splitter directs the interference products from the charge density modulation on to an infra-red detector. Two different continuous-wave 1.3 μm lasers were used for this experiment—a C³ laser⁹ and an Nd:YAG laser. The C³ laser provided a compact stable source. By properly adjusting the bias current in the laser, it can be operated in a single longitudinal mode with a high side-mode suppression ratio. This dramatically reduces the impact of laser partition noise on the system noise floor. The Nd:YAG laser provides a high output power for making wideband digital measurements.

Fig. 2 displays a real-time 20 MHz-bandwidth measure-

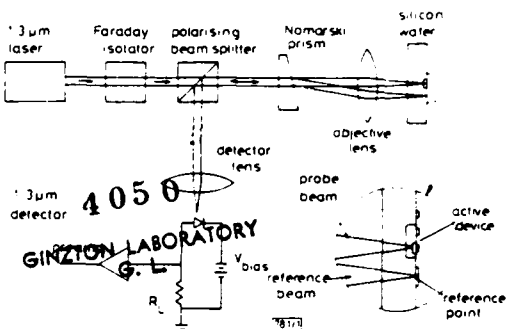


Fig. 1 Schematic diagram of system used to sense charge density modulation in silicon

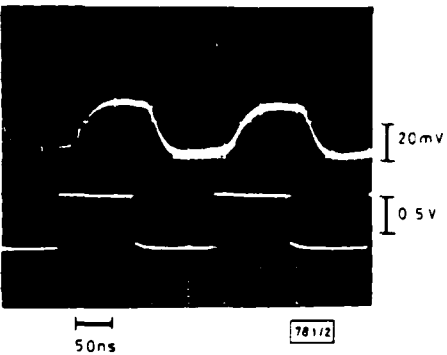


Fig. 2 Real-time 20 MHz bandwidth measurements of a 0.8 V logic signal applied to a bipolar junction transistor made with C³ semiconductor laser

Upper trace is signal detected with optical probe, and lower trace is signal applied to transistor

ment of a 0.8 V logic signal applied to a bipolar junction transistor made with a C³ semiconductor laser. The NPN bipolar transistor tested in this experiment had an $11 \times 11 \mu\text{m}^2$ emitter and an f_T of approximately 1 GHz. The rise and fall times shown in this Figure are limited by the bandpass 1–20 MHz noise filter used after the photodetector, and not by the device. Note that the detected signal has sufficient signal noise that single-shot detection of this signal should be achievable with a very low error rate, even though the measurement of Fig. 2 was performed with a detected photocurrent of only 100 μA . At this level of optical power, the noise floor of the system is not dominated by the shot noise from the photocurrent, but rather by the noise figure of the preamplifier and the stability of the C³ laser.

Fig. 3 displays an Nd:YAG laser measurement of a 100 MHz-bandwidth 0.8 V digital signal applied to the same bipolar junction transistor. The detected photocurrent in this experiment was 10 mA. The signal noise level shown in this Figure is sufficient that single-shot signals should be detectable in real time with a very low error rate. The measurement suggests that additional signal bandwidth could have been attained before the error rate performance of a single-shot detection system would significantly degrade. However, to eliminate the effect of mode partition noise below 500 kHz and laser cavity mode oscillations at 400 MHz, we limited the signal to a passband of 1–100 MHz with an electrical filter after the photodiode. Theoretical calculations for this structure assuming $f_T = 1 \text{ GHz}$, operating at a collector current of $I_c = 1 \text{ mA}$ and a detected system photocurrent of 10 mA, predict a minimum detectable signal of $2.5 \mu\text{V} \text{ Hz}^{-0.5}$. Hence, for a 100 MHz-bandwidth detection system, the signal-referred noise floor of the probe should be only 25 mV.

Since the 1.3 μm wavelength used in this experiment is well below the bandgap of silicon, this probe is noninvasive. We have experimentally measured its effect on the device which we are probing. Using the Nd:YAG laser operating at an

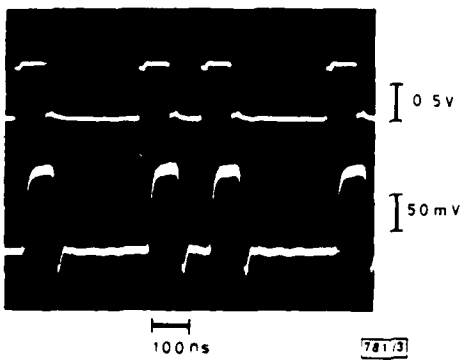


Fig. 3 Real-time 100 MHz bandwidth measurements of a 0.8 V logic signal applied to a bipolar junction transistor made with CW Nd:YAG laser

Upper trace is signal applied to transistor, and lower trace is signal detected with optical probe

incident power of 20 mW, the common-collector transistor DC characteristics were observed to be perturbed by less than 1 μ A. If we assume that this optical power is completely absorbed within the base region of the transistor, the effective base current would be only 6.6 nA. An equivalent electrical probe would need an input impedance of over 100 M Ω . In a carefully designed system, the single-shot detection capabilities of this probe could be extended up into the gigahertz regime. This would provide one of the only tools available for making noninvasive high-frequency real-time measurements of signals in silicon integrated circuits.

In conclusion, we have demonstrated the capability to measure 0.8 V digital signals in a 20 MHz bandwidth using a 3 mW C³ semiconductor laser and in a 100 MHz bandwidth using a 100 mW Nd:YAG laser. This probe is noninvasive even in comparison with a high-impedance electrical probe. Using a mode-locked 1.3 μ m laser system, charge detection in both silicon and GaAs integrated circuits could be performed with sampling bandwidths up to the millimetre range and with microvolt sensitivity. Such a system could greatly simplify high-frequency testing of silicon and GaAs integrated circuits. By designing a device which optimises the interaction between free carriers in a semiconductor device and an optical

beam, high-speed integrated optical modulators could be developed for potential use in fibre-optic communication links or optical interconnects.

Acknowledgment: We would like to thank C. Burrus and J. Bowers of AT&T Bell Laboratories for supplying the C³ semiconductor laser used in this experiment, C. Sue of Hewlett-Packard for donating the bipolar junction transistor, and R. Mortensen and R. Wallace of Lightwave Electronics for their technical assistance. H. Heinrich wishes to acknowledge a Hewlett-Packard fellowship. This research is supported by Joint Services Electronics Program contract N00014-84-K-0327.

H. K. HEINRICH
 B. R. HEMENWAY
 K. A. McGRODDY
 D. M. BLOOM
*E. L. Ginzton Laboratory
 Stanford University
 Stanford, CA 94305, USA*

6th May, 1986

References

- VALDANIS, J. A., MOUROU, G., and GABEL, C. W. 'Subpicosecond electrical sampling', *IEEE J. Quantum Electron.*, 1983, **QE-19**, pp 664-667
- WEINGARTEN, K. J., RODWELL, M. J. W., HEINRICH, H. K., KOLSFR, B. H., and BLOOM, D. M. 'Direct electro-optic sampling of GaAs integrated circuits', *Electron. Lett.*, 1985, **21**, pp 765-766
- FREEMAN, J., DIAMOND, S. K., FONG, H., and BLOOM, D. M. 'Electro-optic sampling of planar digital integrated circuits', *Appl. Phys. Lett.*, 1985, **47**, pp 1083-1084
- FEUERBAH, M. H. P. 'Electron beam testing: methods and applications', *Scanning*, 1983, **5**, pp 14-24
- HENLEY, F. J. 'Functional testing and failure analysis of VLSI using a laser probe', *IEEE custom integrated circuits conf.*, May 1984, pp 181-186
- GIBSON, A. F. 'Injected absorption in germanium', *Proc. R. Soc. London*, 1953, **B66**, pp 588-596
- MIKAMI, O., and NAKAGOME, H. 'InGaAsP/InP optical waveguide switch operated by a carrier-induced change in the refractive index', *Opt. & Quantum Electron.*, 1985, **17**, pp 449-455
- HEINRICH, H. K., BLOOM, D. M., and HEMENWAY, B. R. 'Noninvasive sheet charge density probe for integrated silicon devices', *Appl. Phys. Lett.*, 1986, **48**, pp 1066-1068
- TSANG, W. T., OLSSON, N. A., and LOGAN, R. A. 'High-speed direct single-frequency modulation with large tuning rate and frequency excursion in cleaved-coupled-cavity semiconductor lasers', *ibid.*, 1983, **42**, pp 650-652

Anomalous distance dependence in scanning tunneling microscopy

A. Bryant, D. P. E. Smith, G. Binnig,¹⁾ W. A. Harrison, and C. F. Quate
Edward L. Ginzton Laboratory, Stanford University, California 94305

(Received 27 June 1986; accepted for publication 13 August 1986)

In this work it is found experimentally that the appearance of surfaces in scanning tunneling microscope (STM) images can change drastically as the distance between the STM tip and sample is varied. Defects are found on gold-sputtered graphite samples which appear as protrusions in charge density when the spacing exceeds a critical value. At smaller distances the protrusions are not evident in the images. It is possible to model these defects as gold atoms which lie just below the surface layer. We discuss possible mechanisms that give rise to the distance dependence.

It is well known that scanning tunneling microscopes (STM) probe the spatial distribution of surface electrons with energies close to the Fermi energy; the images do not necessarily reflect the positions of the atomic nuclei on the surface.¹ The local density of states at the Fermi level as first defined by Tersoff and Hamann is in many cases distributed equally among the atoms and concentrated near the nuclei of each atom.¹ For those cases, the STM images which represent the contours of constant charge density give us the atomic positions with great accuracy.^{1,2} In other more heterogeneous systems, the STM images do not represent the simple topographic mapping of the atomic positions since the charge density can have strong variations from atom to atom. In one extreme case, Lang has shown that it is possible for an adatom to appear as a depression on the surface.^{3,4} Another example is graphite where, even though all the atoms in the surface layer are at the same level, the STM images show bumps only on every second atom in the uppermost layer.^{5,6} In one striking example given by Feenstra, the difficulties of interpreting STM images are clearly evident.⁷ He has probed the local density of states at various energies on a silicon (111) surface and found that the "apparent" topography changes sharply as the energy of the tunneling electrons is changed by varying the voltage between the tip and the silicon sample.

In this work we find that the STM images can change in a significant way, not with a change in the electron energy, but rather when the spacing between the tip and sample, or gap spacing, is changed. The sample is graphite on which gold atoms have been deposited. Defects are found on this surface which perturb the charge density in nearby regions in such a way that they show up with strong contrast when the tip-to-surface spacing is larger than a critical value. For spacings less than the critical value the defects disappear and the carbon atoms dominate the image. In this letter we demonstrate this effect and discuss possible mechanisms that can account for the image variations that we observe.

The STM used in this experiment has been described elsewhere.⁸ It is a high-speed device operating in air in the variable current mode to achieve real time imaging. In the variable current mode, STM images represent a cross section of the electron charge density at the Fermi energy at a particular distance from the surface as opposed to the conven-

tional constant current mode in which surfaces of constant charge density are imaged.

The sample under study was highly oriented pyrolytic graphite (HOPG) from Union Carbide.⁹ We deposited approximately 5 Å of gold on this substrate by sputtering a gold target with argon atoms at 2 keV. After sputtering, the presence of gold was verified with an Auger analysis.

We expect to find some areas that are free of atomic gold. Such an area is shown in Fig. 1. It is an STM image of an area 12 Å by 20 Å showing the atomic arrangement of the carbon atoms with the usual appearance of graphite in the STM. The true hexagonal structure appears distorted and this is a result of distortions due to the piezoelectric scanner. We want to point to the spreading between carbon atoms in the center of the image. This is an example of a scanner aberration which occurs in all of the images. The image of Fig. 1 was recorded with an average tunneling current of 2 nA while a positive 38 mV was applied to the STM probe with respect to the sample. The bright regions in the image represent increased tunneling current. The variations in brightness correspond to approximately a 0.1-nA modulation in the tunneling current.

Our high-speed capabilities allowed us to search over large areas with a modest investment of time. We were able to locate several regions where protrusions were present on the surface. In Fig. 2(a) we show an STM image of one such area. As before, the average tunneling current was 2 nA and the probe voltage was a positive 38 mV. In the lower half of the image near site 2 we find the typical pattern of carbon atoms; however, this pattern is disrupted in the upper half about the site labeled 1.

At first glance there is nothing unusual about this image. It could be interpreted as an image of gold atoms adsorbed on the graphite surface. However, this conclusion does not stand up when we examine the images with different spacings between the tip and the sample. In Fig. 2(b) we show the image of the same area with the STM probe moved close to the sample. In Fig. 2(c) the spacing was decreased still further so that the average tunneling current increased to 4 nA. The gray scale modulation at site 2 increased to 0.15 nA.

The result is surprising. The character of the image is changed with this simple variation of spacing between the STM probe and the sample surface. We find that the image of the protrusion at site 1 is no longer observed and in its

¹⁾On leave from IBM Research Laboratory, Zurich, Switzerland.

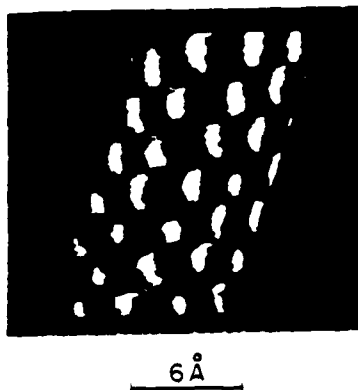


FIG. 1. Area of gold-sputtered graphite sample which is free of atomic gold. Average tunneling current is 2 nA and gap voltage is 38 mV. Variable current method is used at a scan rate of 2 kHz. Deviations from a hexagonal pattern are a result of scanner distortion.

place we have the normal pattern of carbon atoms. The sequence is reversed in Figs. 2(d) and 2(e). There we retract the STM probe back toward its original position. The gold atom reappears in a form similar to that of Fig. 2(a). The

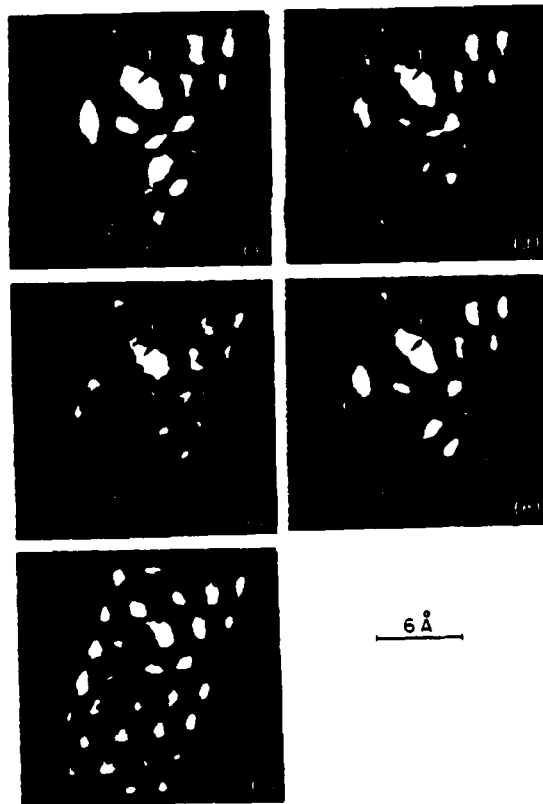


FIG. 2. STM images of gold atoms deposited on graphite. The sequence of images shows the changes as the distance between tip and sample is varied. The tip is furthest from the sample in (a), closer in (b), closest for (c), and the process is reversed for (d) and (e).

process is reproducible and the surface structure is unchanged by the imaging process.

The sequence of STM images shown in Fig. 2 shows that close to the defect at site 1 the charge density does not deviate significantly from that of a perfect graphite lattice. As the distance between the STM probe and sample is increased, the presence of the defect becomes extremely visible. This clearly demonstrates that the predominant effect is to locally alter the rate at which electronic states decay away from the surface. We have found that it is possible to predict the observed gap spacing dependence by using a model where gold atoms lie just below the surface layer.

We should point out that in principle an adatom can become "invisibile" or could appear as a depression to the STM. This was first put forth in general by Baratoff and clearly demonstrated by Lang for a helium atom adsorbed on a metal surface.^{4,10} However, if the special case of the noble gases is excluded, Lang's calculations show that there is always an increase in the charge density due to an atom adsorbed on metals.¹⁴ We, therefore, expect this to be true for a gold atom lying on top of the graphite surface. Furthermore, we expect that a gold atom in the surface plane of graphite would significantly alter the charge density and alter atomic positions.

Since we cannot explain the results in Fig. 2 by placing gold atoms on the surface or by incorporating them into the surface layer of graphite, we are left with the possibility that the effect is caused by gold atoms lying below the surface. We expect that such gold atoms will lose some of their electronic charge to the graphite and be positively charged. The screening of the charge by the surface layer is not expected to be complete, and a noticeable electric field penetrates through the surface layer. Thus, the local surface potential is lowered and consequently results in an increase in the decay length of wave functions.

The simplest way to imagine and to calculate the effect of gold atoms below the surface is by using a linear combination of atomic orbitals approach. In that theory, the new perturbed electronic states are described as an add-mixture of the known atomic gold states and the π states of graphite. The rate of decay into the vacuum for the shallower s-like component will be slower than for the graphite π states. In such a situation, where the gold atom is sitting below the surface, the variations in charge density near the sample surface are dominated by the carbon atoms. However, as we move the tip away from the surface, the carbon charge density decays rather quickly and we are left with the slowly decaying component of the s-like state. We believe this accounts for the change in contrast in Fig. 2.

We test these arguments with a simple calculation. We consider a single graphite layer and allow for a gold atom situated just below the layer. The gold atom is situated laterally at a position equivalent to site 1 in Fig. 2 and lies halfway between the first two layers. This position in which the gold atom is cradled by three carbon atoms on the surface and three in the second layer has been previously proposed as an interstitial site.¹¹ The gold s state is coupled by a V_{so} matrix element to each of the π states on its three neighboring carbon atoms. It is this resulting s orbital added to the π states

which we believe is responsible for the effects here. We calculate the coefficients of the added orbital in perturbation theory using tight-binding parameters.¹² We estimate the charge density from the orbitals by a form $e^{-i\mu r}$ with μ related to the atomic energy by $\epsilon_i = -\hbar^2\mu^2/2m$.

In Fig. 3, we plot the calculated charge density profiles along the (2110) direction when the tip to sample spacing is 2, 3, and 4 Å. The curves are normalized to their peak values and they are presented in arbitrary units. The model shows the trend that is observed in our results. When the tip is spaced 4 Å from the surface the gold atom appears as a strong protrusion in the profile. In contrast, when the tip is spaced 3 Å from the surface the profile shows only the corrugations of the carbon atoms similar to what is observed in Fig. 2(c). In the experimental observations we found the strong change in the image occurs when we changed the spacing by approximately 0.3 Å. A more rigorous self-consistent calculation which would include the effects of screening would certainly yield more accurate predictions. However, we believe that the change predicted with the model used in Fig. 3 will also be evident in the results of such a calculation.

We should point out that the distance dependence we have observed may be accentuated in the case of graphite. In graphite, which is an anisotropic two-dimensional semimetal, the electrons at the Fermi energy have a large component of momentum in the basal plane and a small component normal to the surface.¹³ As a result, the electronic states at the Fermi energy decay away from the surface at an unusually high rate.¹ On the other hand, point defects with an isotropic structure will include states that decay away from the surface at a slower rate than the electronic states of graphite. This effect has not been included explicitly in our analysis; however, the resulting change in decay length will only accentuate the effect seen in Fig. 3.

In this work we have demonstrated that the appearance of surfaces in STM images can change drastically with gap spacing. Our analysis indicates that a gold atom below the surface layer of graphite will appear as a protrusion in the charge density when the spacing between the tip and the sample is adjusted to above a critical value. These results indicate that we should exercise care in choosing both the correct spacing and the correct voltage when we carry out detailed studies of new samples.

We are grateful to Jerry Tersoff and Norton Lang for sharing their theoretical insight with us, and to Christoph Gerber for many helpful discussions. We also thank Bob Wilson for doing the Auger analysis of our sample, William Holmes for sputtering the gold, Matthew Richter for preparing the STM tips, and Morris Dovek for help with the mea-

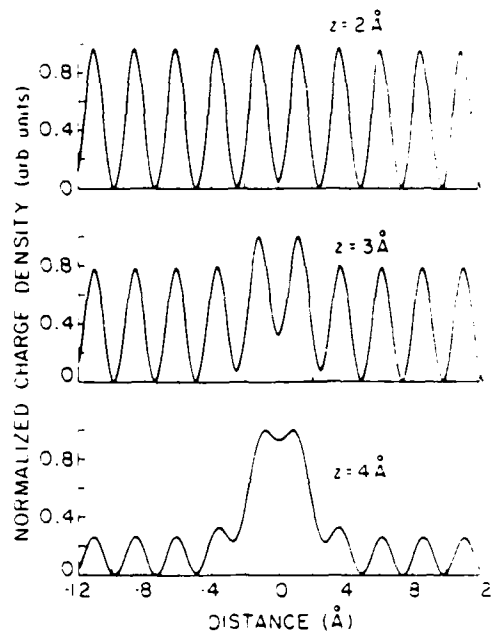


FIG. 3. Calculated charge density profiles at several distances from the surface. A gold atom is below a single graphite layer at the position marked zero.

surements. Many thanks to Russell Becker for providing us with his image processing software. This work was supported in part by the Defense Advanced Research Projects Agency and in part by the Joint Services Electronics Program.

- ¹J. Tersoff and D. R. Hamann, *Phys. Rev. Lett.* **50**, 1998 (1983).
- ²G. Binnig, H. Rohrer, Ch. Gerber, and E. Weibel, *Surf. Sci.* **131**, L179 (1983).
- ³N. D. Lang, *Phys. Rev. Lett.* **55**, 230 (1985).
- ⁴N. D. Lang, *Phys. Rev. Lett.* **56**, 1164 (1986); *IBM J. Res. Dev.* **30**, 374 (1986).
- ⁵A. Selloni, P. Carnaval, E. Tosatti, and C. D. Chen, *Phys. Rev. B* **31**, 2602 (1985).
- ⁶S. I. Park and C. F. Quate, *Appl. Phys. Lett.* **48**, 112 (1986).
- ⁷R. M. Feenstra, W. A. Thompson, and A. P. Fein, *Phys. Rev. Lett.* **56**, 608 (1986).
- ⁸A. Bryant, D. P. E. Smith, and C. F. Quate, *Appl. Phys. Lett.* **48**, 452 (1986).
- ⁹We are grateful to A. R. Moore for providing HOPG samples.
- ¹⁰A. Baratoff, *IBM J. Res. Dev.* Sept. (1986).
- ¹¹W. N. Reynolds, *Physical Properties of Graphite* (Elsevier, New York, 1968), p. 144.
- ¹²W. A. Harrison, *Electronic Structure and Properties of Solids* (Freeman, New York, 1980).
- ¹³G. S. Painter and D. E. Ellis, *Phys. Rev. B* **1**, 4747 (1970).

Monolithic Nd:YAG fiber laser

J. L. Nightingale* and R. L. Byer

Department of Applied Physics, Edward L. Ginzton Laboratory of Physics, Stanford University, Stanford, California 94305

Received January 6, 1986; accepted April 4, 1986

A single-crystal Nd:YAG fiber with polished and coated endfaces has been operated as a monolithic, guided-wave laser oscillator. The 47- μm -diameter, 7-mm-length fiber oscillator operated with a threshold of 3.7 mW and a slope efficiency of 10.5%. Seventy-five percent of the laser power was in the fundamental spatial mode.

Single-crystal optical fibers offer the promise of compact, rugged, and highly efficient end-pumped laser oscillators. An advantage of the fiber geometry is the inherent excellent spatial overlap between the confined pump radiation and the oscillator's fundamental optical mode. This offers the potential for simple butt coupling of fiber oscillators to laser-diode and light-emitting-diode pump sources.

Short crystal fiber lengths previously have been used to make miniature Nd:YAG,¹⁻³ Nd:Y₂O₃,⁴ and ruby⁵ lasers. These lasers employed external mirrors adjacent to the fiber to form the resonator cavity. The finite mirror thickness precluded efficient butt coupling to LED pump sources² and complicated laser-diode pumping.³ For most of these lasers the fiber's length was less than or comparable with the Rayleigh length of the fiber's lowest-order spatial mode. Thus the mode interacted only weakly with the fiber surface, so that fiber diameter variations were not a significant loss mechanism and pump-beam confinement was limited. Miniature monolithic Nd:YAG lasers using small, 2-mm-diameter laser rods have also been demonstrated.⁶ In these miniature lasers the beam waist is determined by endface curvature, not by the fiber radial dimension as is the case for fiber lasers.

We have extended the earlier work and demonstrated the first reported monolithic single-crystal fiber oscillators. These laser oscillators are guided-wave devices with a fiber length five times the Rayleigh length of the fiber's fundamental spatial mode. In these oscillators the resonator structure is formed by the fiber waveguide and the polished and coated fiber endfaces. The first monolithic fiber oscillators were made in ruby cooled to 77 K.⁷ In this Letter we describe a Nd:YAG monolithic fiber oscillator that had significantly improved laser performance compared with that of the earlier ruby system.

The Nd:YAG fibers used in the laser tests were grown by the miniature pedestal growth technique by using an apparatus developed in our laboratory.⁸ The fibers were grown with active diameter control and had a rms diameter variation of 0.5%.⁹ Improvements in the endface polishing method reduced the endface losses to approximately 2%. As a result, the Nd:YAG fiber lasers had thresholds as low as 3.7 mW with a maximum slope efficiency of 10.5%. Seventy-five per-

cent of the laser output power was in the fiber's fundamental spatial mode.

The fibers were grown from a 450- μm -diameter YAG rod doped with 1.1 wt. % neodymium. Two growths, each with a three-to-one diameter reduction, were necessary to reduce the fiber diameter to approximately 50 μm . The neodymium dopant does not evaporate during YAG fiber growth, and thus the fiber's dopant concentration equaled that of the source rod.¹ Examination of thin fiber cross sections revealed no coring or stress birefringence.^{1,10}

The fiber endfaces were fabricated by using the polishing fixture shown in Fig. 1. Several slots were cut into a YAG block and fibers inserted in these slots. The slots were perpendicular to the block endface to within 0.5 mrad. An unslotted block was placed on top of the slotted block, the two blocks were mechanically clamped together, and the entire assembly was polished using conventional techniques. A 5- μm -thick gold layer vapor deposited on the block faces cushioned the fibers in the slots and accommodated small irregularities in either the slot or the fiber dimensions. The gold eliminated the need for any waxes or epoxies in the polishing fixture. The absence of these organic materials permitted application of multilayer dielectric coatings to the fiber endfaces while the fibers remained in the polishing fixture.

The 590-nm radiation from a cw dye laser was used as the pump source for the monolithic Nd:YAG fiber

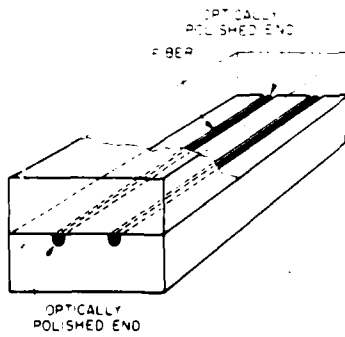


Fig. 1. Schematic of the fixture used to polish the fiber endfaces.

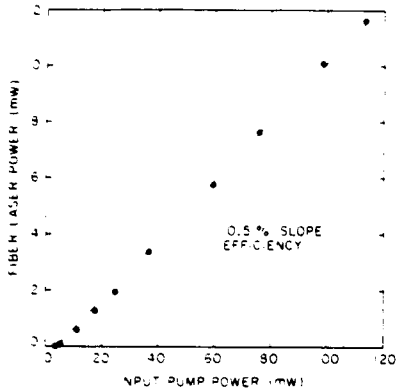


Fig. 2. Nd:YAG single-crystal fiber oscillator output power as a function of the absorbed pump power.

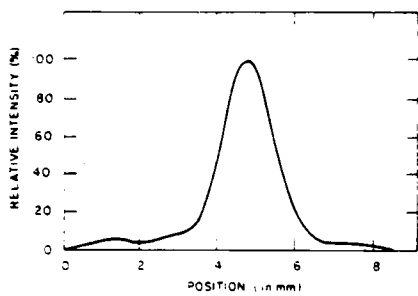


Fig. 3. Spatial mode profile of a monolithic Nd:YAG fiber laser 4.3 cm from the end of the fiber. Seventy-five percent of the power is in the central Gaussian peak.

laser tests. The radiation was focused into the fiber through the high-reflector endface. Laser radiation at 1064 nm was observed from the opposite fiber endface. The fibers remained mounted in the polishing fixture during these laser tests.

All Nd:YAG single-crystal fibers mounted and fabricated in the polishing fixture reached threshold and oscillated. However, some fibers had high cavity losses owing to badly chipped fiber endfaces. As shown in Fig. 2, the best fiber had a slope efficiency of 10.5% with a laser threshold of 3.7 mW of absorbed 590-nm pump radiation.

Figure 3 illustrates the spatial mode profile 43 mm away from the fiber. The profile consists of a central Gaussian mode above a background of higher-spatial-frequency modes. Seventy-five percent of the laser output power is in this central lobe. The width of this lobe was measured as a function of distance from the laser. As predicted from Gaussian beam theory, the beam width expands linearly with position in the far field. Calculating the beam waist at the fiber laser from the measured beam divergence yields a beam waist of 14 μm . This is consistent with the 15- μm beam waist calculated from the fiber waveguide dimensions.¹¹

The resonator losses were calculated by using the

measured laser slope efficiency and relaxation oscillation period as a function of pump power. The slope efficiency η and relaxation oscillation period τ are given by the relations²

$$\eta = \lambda_p T / \lambda_1 (T + 2L) \quad (1)$$

and

$$\tau = 2\pi [2\ln t_f / [c(2L + T)(r - 1)]]^{1/2}, \quad (2)$$

where λ_p is the pump wavelength, λ_1 is the laser wavelength, T is the mirror transmission, L is the single-pass loss, t_f is the upper-state lifetime, l is the fiber length, n is the fiber index of refraction, c is the speed of light in vacuum, and r is the number of times the pump power is above threshold. As shown in Fig. 4, the functional dependence of the relaxation oscillation period on pump power is consistent with Eq. (2). By using the measured slopes from Figs. 2 and 4, and Eqs. (1) and (2), the values of L and T are calculated to be 7 ± 2 and $3.4 \pm 0.8\%$, respectively.

The fiber losses can also be estimated by equating the calculated gain coefficient and resonator loss at threshold. The unsaturated single-pass gain coefficient is given by the expression³

$$g = \sigma t_f \lambda_p P / hc A_p, \quad (3)$$

where σ is the laser cross section, which is taken to be $3.3 \times 10^{-19} \text{ cm}^2$,¹² t_f is the upper-state lifetime taken to be 230 μsec , P is the absorbed pump power, h is Planck's constant, c is the speed of light in vacuum, and A_p is the effective pump area. The effective pump area is defined by the relation¹³

$$A_p = A_f / F_{\kappa\mu km}, \quad (4)$$

where A_f is the fiber area, $F_{\kappa\mu km}$ is the overlap factor, and the index pairs (κ, μ) and (k, m) characterize the signal and pump modes, respectively. In our case we are interested in the overlap of the fundamental signal and pump modes. The F_{0101} coefficient that describes this overlap equals 2.098.¹³ Evaluating Eq. (3) at threshold gives a calculated single-pass gain of $10.0 \pm$

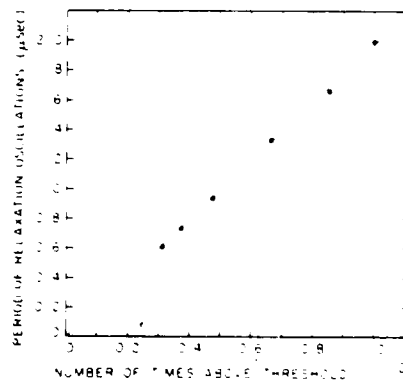


Fig. 4. The relaxation oscillation period as a function of the number of times above threshold. The linear dependence observed is predicted by theory.

Table 1. Summary of Loss Formulas for a Monolithic Fiber Laser

Type of Loss	Expression for Loss	Deviation from Ideal for 1% Loss
Tilted end-face	$L = 43.7$ $[(2k\alpha a)^2]^{1/2}$	$\alpha = 0.53$ mrad
Curved end-face	$L = 3.19$ $2k^2 a^4 / R^2 c_0$	$R = 13$ mm
Chipped end-face	$L = 771 \delta^{3/2}$	$\delta = 0.11$
Waveguide	$L/l \sim 70$ $(\delta a/a)^2 a^{-1} c_0$	$(\delta a/a) \sqrt{l}$ $\sim 0.006 \text{ cm}^{-1/2}$

3%. This is consistent with the single-pass loss and transmission of 8.7% determined by the slope efficiency and the relaxation oscillation period.

This loss is consistent with a theoretical analysis of monolithic fiber laser losses. Loss mechanisms include radiation scattering losses due to fiber diameter variations and endface reflection losses due to curved, tilted, or chipped endfaces. The fiber waveguide losses are estimated from the work of Marcuse.¹⁴ Calculated endface losses are based on the overlap integral of the fundamental fiber mode with the reflected wave from the fiber endface.

The result of the theoretical loss analysis is summarized in Table 1. The expressions for loss listed in this table are all first-order approximations valid in the low-loss regime. The variables are defined as follows: a is the fiber radius, $2k$ is the fiber propagation constant, α is the deviation in the endface orientation from the plane perpendicular to the fiber axis, R is the endface curvature, b is the effective endface reflecting radius, and δa is the deviation about the mean diameter. The fiber laser parameters used in the computation of the right-hand column are $a = 25 \mu\text{m}$ and $2k = 11.8 \text{ cm}^{-1}$.

Based on these calculations, endface chipping contributes a 1% loss to the monolithic fiber oscillator experimentally studied. Endface orientation, measured to be perpendicular to within 0.7 mrad of the fiber axis, gives rise to a 2% loss. Fiber endface curvature should be comparable with polishing-block endface curvature. In this case the loss from endface curvature is negligible. The 0.5% rms variations in fiber diameter give rise to an estimated 1% loss. Assuming no material losses, this gives a total calculated single-pass loss of 4%. The difference between this value and the measured value of 7% probably stems from an underestimation of the waveguide losses.

In conclusion, the monolithic, single-crystal, Nd:YAG fiber oscillator described in this Letter represent a significant step toward realization of practical

optical devices using single-crystal fibers. It demonstrates a relatively low-loss waveguide and reflector structure without the use of cumbersome external mirrors. The laser had a threshold of 3.7 mW with a slope efficiency of 10.5%. Seventy-five percent of the output power was in the fiber's fundamental transverse mode. The next step in this research is demonstration of a butt-coupled, laser-diode-pumped Nd:YAG fiber laser.

We gratefully acknowledge many useful discussions with M. M. Fejer, T. J. Kane, M. J. T. Digonnet, and C. J. Gaeta. We are thankful to L. C. Goddard and J. J. Vrheil of Ginzton Laboratory, T. Roderick of Veeco Custom Optics, and J. Radcliffe of Hewlett-Packard, Inc., who all contributed to the fabrication of the fiber lasers.

This research was supported by U.S. Office of Air Force Scientific Research contract F49620-85-C-0062, the Joint Services Electronics Program contract N00014-84-K-0327, and National Science Foundation contract DMR-83-16982.

J. L. Nightingale acknowledges the support of the Newport Corporation through the Newport Research Award.

* Present address, Crystal Technology, Inc., 1035 East Meadow Circle, Palo Alto, California 94303.

References

1. C. A. Burrus and J. Stone, *Appl. Phys. Lett.* **26**, 318 (1975).
2. J. Stone and C. A. Burrus, *Fiber Integr. Opt.* **2**, 19 (1979).
3. M. J. T. Digonnet and H. J. Shaw, "Diode-pumped fiber laser," Final Tech. Rep. TR-83-1110 for AFWAL (July 1983).
4. J. Stone and C. A. Burrus, *J. Appl. Phys.* **49**, 2281 (1978).
5. C. A. Burrus and J. Stone, *J. Appl. Phys.* **49**, 3118 (1978).
6. B. Zhou, T. J. Kane, G. J. Dixon, and R. L. Byer, *Opt. Lett.* **10**, 62 (1985).
7. J. L. Nightingale and R. L. Byer, *Opt. Commun.* **56**, 41 (1985).
8. M. M. Fejer, J. L. Nightingale, G. A. Magel, and R. L. Byer, *Rev. Sci. Instrum.* **55**, 1791 (1984).
9. G. A. Magel, M. M. Fejer, J. L. Nightingale, and R. L. Byer, in *Digest of Conference on Lasers and Electro-Optics* (Optical Society of America, Washington, D.C., 1985), p. 178.
10. D. O'Meara, Edward L. Ginzton Laboratory, Stanford University, Stanford, Calif. 94305 (personal communication).
11. R. Abrams, *IEEE J. Quantum Electron.* **QE-8**, 838 (1972).
12. A. A. Kaminskii, *Laser Crystals* (Springer-Verlag, Berlin, 1981), p. 332.
13. M. J. T. Digonnet and C. J. Gaeta, *Appl. Opt.* **24**, 333 (1985).
14. D. Marcuse, *Bell Syst. Tech. J.* **48**, 3187 (1969).

11

Twenty-Fifth Annual Technical Report
for
The Center for Materials Research

March 1986

Edward L. Ginzton Laboratory
Hansen Laboratories of Physics
Stanford University
Stanford, California 94305

OPTICAL INTERACTIONS WITH SOLIDS
G. S. Kino, Professor, Electrical Engineering

Professional Associates:

C. H. Chou
B. T. Khuri-Yakub

Graduate Students:

T. Corle
J. D. Fox*
B. Heffner
P. C. D. Hobbs
K. K. Liang*
D. K. Peterson*
D. Patterson
R. G. Stearns*

* Received Ph.D./report period.

Agency Support:

AFOSR-84-00638
DOE DE-AT03-81ER10865
IBM
ONR N00014-84-K-0327
SIMA

Nondestructive Testing

Technical Objective:

To use scanning optical and scanning photoacoustic techniques to make quantitative profile measurements, to measure range, and to measure the thickness of transparent and opaque films. It is also of interest to determine material properties such as adhesion and internal electronic properties of semiconductors.

Approach:

During the last year, we have mainly concentrated on optical measurement methods. Our aim has been to turn the optical microscope into a quantitative measurement tool by using internal electronically-controllable components inside the optical system.

Research Report:

We have been carrying out research with two types of optical microscopes: one is mechanically scanned and the other is electronically scanned.

The mechanically-scanned microscope passes a collimated laser beam through an objective lens to illuminate a single point on the object. The reflected image of this point is focused on a pinhole through which the light is passed to a photodetector. Because the image at the pinhole is defocused if the surface of the object being observed is not at the focal point, the amplitude of the light passing through the pinhole decreases very rapidly with the distance of the surface z from the focus. Therefore, the range definition of the microscope is very good, about $0.7 \mu\text{m}$ between 3 dB points for a 0.9 aperture lens illuminated by a 5100 \AA laser beam. There is no speckle, and the transverse definition of the beam is about a factor of 1.4 better than standard optical microscopes.

Various electronically-controllable optical components have been used with this microscope. One example is a development of the Zernike phase contrast microscope using a PLZT plate in the back focal plane of the lens. By applying an rf signal to a transparent center electrode, an rf output is obtained from the detector at the same frequency, which is zero when the beam is focused on the surface of the reflecting object. A second, closely related device uses a cantilever made of two bonded pieces of PZT bonded, in turn, to a thin mirror. This mirror is flexed by an rf voltage to move the focus in and out. Using this system, we have demonstrated a range resolution of 0.01 \AA . We have used devices based on the principles to measure the thickness of $1.5 \mu\text{m}$ zinc oxide films. A third device uses a Bragg cell placed in the optical path to obtain two focal spots side by side which can be scanned electronically or mechanically over the surface of an object. The phase of the signal received at the detector is proportional to the slope of the surface being examined. The technique is, therefore, a powerful one for the measurement of the position of sharp edges and for determining the slope of the outer surface of a hole.

A second microscope uses a Bragg cell for scanning the optical beam. This device has been built into a high-quality Leitz optical microscope. The system produces one stationary spot on the sample and one spot which can be scanned by changing the frequency of the signal applied to the Bragg cell. The output signal from the detector is obtained at a frequency of 60 MHz . The amplitude and phase of this signal correspond to the amplitude of the scanned optical beam and the optical phase difference between the two reflected spots, respectively. With it, we can measure changes in height to accuracies of a few Angstroms. Because we have optical phase and amplitude available, we can also use sophisticated processing of the data to improve the transverse resolution. We have

measured steps 900 Å high with a 10-90% transverse resolution of 0.25 μm ; after inverse filtering, the resolution improves to 0.13 μm . This is a far better resolution than is obtainable with a standard microscope.

A third photoacoustic system uses a laser beam modulated at frequencies in the 100 Hz to 2 MHz range to heat a surface. Thermal waves are generated which heat the air above the surface. The thermal expansion and contraction of the air generates an acoustic wave which can be detected by very high-frequency acoustic transducers built in our laboratory. By measuring the phase of the generated acoustic wave as a function of frequency, we can determine the thickness of opaque and transparent films of the order of 1000 Å to 1 μm thick. The amplitude of the signal gives information on adhesion or thermal bonding. No contact is made to the sample. We have used this photoacoustic technique to measure the thickness of ferrite-filled epoxy films of the type used in magnetic recording discs, the thickness of SiO_2 layers, and thermal bonding of silicon samples to a metal heat sink.

Fiber-Optic Devices

Technical Objective:

To modulate the light passing through an optical fiber or to form an electronically-controllable optical tap.

Approach:

Zinc oxide is sputter deposited on single-mode optical fiber to make an acoustic transducer.

Research Report:

A gold film is deposited on the glass fiber. Zinc oxide is deposited on this film and interdigital electrodes are deposited, in turn, on the zinc oxide. The device is operated at a frequency of 3 GHz . At this frequency, we obtain Bragg diffraction of the light from the optical waveguide to a beam which passes through the cladding. The measured efficiency is 2% per watt. As far as we are aware, this is the first time that anyone has succeeded in sputter depositing zinc oxide and performing photolithography, with this resolution, on an 8 μm diameter optical fiber.

Switchable fiber-optic tap using the acousto-optic Bragg interaction

B. L. Heffner, G. S. Kino, B. T. Khuri-Yakub, and W. P. Risk

Edward L. Ginzton Laboratory, W. W. Hansen Laboratories of Physics, Stanford University, Stanford, California 94305

401.1

Received March 26, 1986; accepted May 6, 1986

A new type of electronically switchable optical-fiber tap using acousto-optic Bragg diffraction is demonstrated. An acoustic transducer on a wedge launches an acoustic beam through a Hertzian contact into a D-shaped optical fiber, diffracting light out through the side of the fiber. The bandwidth of the tap is greater than 1 GHz centered at 3.5 GHz, with a tap efficiency of 0.01% per watt of rf power. The tap does not damage the fiber and is completely reversible, so its location on the fiber can easily be adjusted.

The usefulness of single-mode optical fiber as a delay medium for high-speed, high-bandwidth signal-processing systems has been clearly demonstrated.¹ The low loss and low dispersion of optical fibers makes them well suited to this application.² However, realization of the optical fiber's full potential as a delay medium requires a method to tap a fraction of the guided light out of a fiber at discrete points. Before the development of the acousto-optic tap described here, light could be extracted from a length of fiber by one of two techniques. First, the fiber cladding could be polished or etched to expose the evanescent field, which could then be detected or used to couple energy into a propagating mode of a similarly prepared fiber.³ Second, the fiber could be bent to induce coupling to radiation modes outside the fiber, which could be received by a remote detector.⁴ Both of these techniques have been used to produce tapped delay lines and other signal-processing networks.

In neither of the techniques mentioned above can the amount of light extracted from the fiber be varied rapidly, since the coupling must be changed mechanically. The acousto-optic tap described here permits the amount of light taken from the fiber to be varied electronically. Because of the large acousto-optic bandwidth available at the high acoustic frequency used, the tap can be adjusted or switched in times of the order of a nanosecond. Potential applications for this device include simple switchable taps and programmable tapped delay lines for use as filters, correlators, convolvers, and word generators.

Wideband switching of light has been demonstrated in Ti:LiNbO₃ waveguides, and low-loss connections have been made to optical fibers from these waveguides.⁵ However, the interface loss may limit the usefulness of this device, and no adjustment can be made to the placement of the device on the fiber.

We have developed a new method to tap light from a fiber by using the acousto-optic Bragg interaction. Our technique uses acoustic transducers fabricated on a wedge of yttrium aluminum garnet (YAG). Pressing this wedge against an optical fiber allows an acoustic

beam to be launched from the wedge into the fiber at the angle necessary to satisfy the Bragg condition. For a sufficiently large acoustic frequency or small acoustic wavelength Ω , the angle ϕ between the Bragg-diffracted wave and the fiber axis can exceed the maximum internal angle of acceptance of the fiber, allowing the diffracted beam to propagate through the cladding and out of the fiber through the high-index YAG wedge. For an optical wavelength λ , the angle ϕ between the fiber axis and the diffracted beam at mid-band is given by

$$\sin \phi = \frac{\lambda}{\Omega} \left(1 - \frac{\lambda}{2\Omega} \right)^2. \quad (1)$$

The contact formed between the wedge and the fiber is nondestructive and completely reversible, so the location of the tap can be adjusted simply by moving the wedge to another point on the fiber.

Figure 1 is a diagram of the device in operation. Part of the light guided by the fiber core is diffracted away from the core by the acousto-optic Bragg interaction. This tapped light is emitted from the fiber through the YAG wedge and is received by a photodetector. Intensity of the tapped light is proportional to acoustic power, and the wide bandwidth of the tap allows it to be switched at very high speeds.

The acoustic beam generated by a transducer on the YAG wedge is coupled into the optical fiber through a Hertzian contact. A Hertzian contact is formed when two solids are pushed together and elastically deformed to come into contact over a finite area. The authors have demonstrated transmission of acoustic waves through such a contact and have measured a transmission loss of approximately 1.2 dB for 7-GHz longitudinal waves in sapphire.⁶

Dimensions of Hertzian contacts have been calculated for certain special cases.⁷ The small radius of a conventional cylindrical fiber would make it impossible to obtain a suitably large contact area, so a special D-shaped fiber was used. This fiber is manufactured with a flat surface 50 μm wide parallel to the fiber axis. The spherical face of the YAG wedge (radius $R = 2 \text{ m}$)

0146-9592/86/070476-03\$2.00/0

© 1986, Optical Society of America

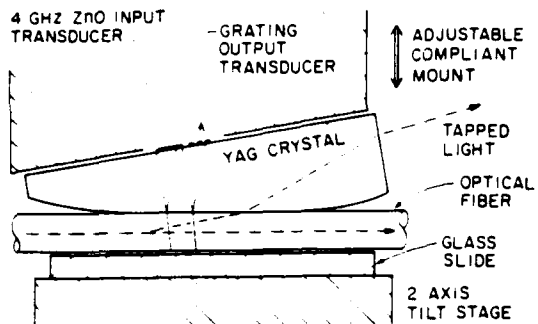


Fig. 1. Acousto-optic fiber tap. Part of the acoustic beam is shown reflected to the output transducer. Light in the fiber is scattered upward by the Bragg interaction.

is pressed against the flat side of the D fiber, resulting in a contact much longer than the width of the fiber. The properties of the contact closely approximate those of a cylinder pressed against a flat, in which case the length s of the contact is approximately

$$s = 8(DFR/3\pi)^{1/2}, \quad (2)$$

where F is the force per unit width and D is a parameter derived from the elastic properties of the fiber and wedge. In our experiment, the force used was approximately $2N$, $D = \times 10^{-12} \text{ m}^2 \text{ N}^{-1}$, and the fiber width was $50 \mu\text{m}$, yielding a contact length of approximately 1 mm.

A YAG wedge was used in order to launch an acoustic beam through the fiber at the Bragg angle. YAG was chosen for its low acoustic loss and nearly isotropic characteristics. The wedge was polished from a YAG étalon of diameter 6.4 mm. The angle of the wedge was nominally 12.4° , and the bottom surface was spherically polished to a radius of approximately 2 m.

Operation of the acousto-optic tap depends on precise alignment of the wedge relative to the fiber to allow the acoustic beam to intersect the fiber core. Once the wedge was aligned, we found that moving it as little as $10 \mu\text{m}$ in a direction perpendicular to the fiber axis caused a significant reduction in tap efficiency. It is convenient to use an alignment technique that does not depend on acousto-optic diffraction to set up the device initially. For this purpose, we excited the transmitting acoustic transducer with a series of microwave pulses and used a second receiving transducer to monitor acoustic echoes from the spherical face of the wedge while adjusting the mechanical alignment. A reduction in the amplitude of these echoes indicated that part of the acoustic signal was being coupled into the fiber. Both transducers employed zinc oxide films deposited in a reactive planar magnetron sputtering system, and the receiving transducer was constructed with fingers in the shape of a grating to make it sensitive to acoustic waves arriving at 24.8° from the normal.

The design and placement of acoustic transducers on the wedge were guided by our desire to maximize acousto-optic diffraction efficiency over a wide band-

width. The transducers were placed as close as possible to the thin edge of the wedge in order to minimize diffraction of the acoustic beam. By measuring the timing of acoustic echoes, the thickness of the wedge at the transmitting transducer was found to be about $440 \mu\text{m}$. At this thickness, a numerical analysis of diffraction shows the optimal transducer width to be of the order of $30 \mu\text{m}$ at 3.5 GHz . A transmitting transducer of width $30 \mu\text{m}$ and length $90 \mu\text{m}$ was used to achieve broadband rf matching to a $50\text{-}\Omega$ line.

The tapped optical power of the acousto-optic fiber tap shown in Fig. 1 was measured over the frequency range 2-4 GHz using a computer-controlled data-acquisition system. Light from a 5-mW He-Ne laser was coupled into the fiber, and an avalanche photodiode was used to detect the tapped light. Owing to elastic deformation of the fiber, a small amount of light was detected with no rf power applied, i.e., with the tap turned off. To eliminate any error due to this background light, the rf drive was modulated by a 10-kHz square wave, and a lock-in amplifier was used to detect the modulation on the photodiode output. Tapped light was downshifted by the acoustic frequency, so signals produced by coherent interference with the background light were well above the upper frequency limit of the photodiode and did not contribute to the detected signal. The measurement procedure incorporated calibrations to account for capacitive feedthrough of the modulation and rf power variations over the frequency range. Absolute calibration of the tap efficiency was accomplished by mechanically chopping the input light and using the same avalanche photodiode and lock-in amplifier to detect the chopped light guided by the fiber core. A precision optical filter was used to attenuate the light to a level comparable with that of the tapped light in order to avoid saturating the photodiode.

Tap efficiency expressed in units of $\text{dB}/W_{\text{input}}$ over a 2-4-GHz frequency range is shown in Fig. 2. Diffraction efficiency is proportional to acoustic power for a Bragg interaction at low efficiencies, and the tap efficiency plotted in Fig. 2 is that resulting when an available rf power of 1 W is used to drive the tap. Our

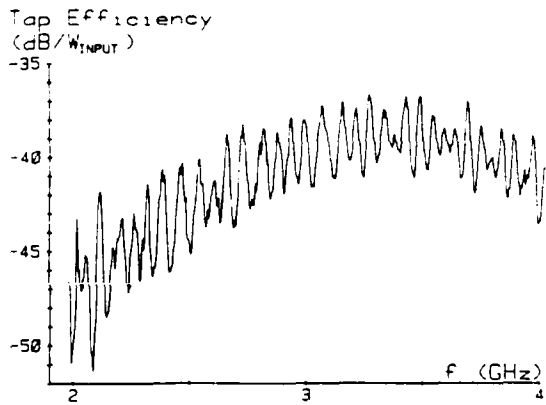


Fig. 2. Frequency response of the fiber tap.

acoustic transducers could tolerate slightly more than 1 W of power.

The periodic structure of the tap frequency response is caused by acoustic reflections within the fiber. The autocorrelation of the tap impulse response was obtained by computing the Fourier transform of the frequency response. The autocorrelation revealed acoustic reflections approximately 10 dB below the main beam arriving approximately 16 nsec after the main response. This indicates that echoes are reflected twice by the cylindrical surface of the D fiber. It should be possible to reduce these echoes greatly by acoustically backing the fiber with glass or indium. If this is accomplished, then the periodicity of the frequency response will be eliminated, yielding a 3-dB acousto-optic bandwidth of greater than 1 GHz. This implies a tap switching time of the order of 1 nsec. The unbacked fiber has a similar switching time but suffers a -10-dB ghost image of the switching signal delayed by 16 nsec.

In a traditional Bragg cell, the acoustic beam width is made large to increase the diffraction efficiency by providing a long region for coupling to the diffracted beam. We have found that when a thin optical waveguide is used, the width of the guide (instead of the acoustic beamwidth) determines the acousto-optic coupling length and hence determines the diffraction efficiency. The number of resolvable spots over the range of the diffracted beam can be shown to be twice the time-bandwidth product.³

We have demonstrated wide-bandwidth Bragg diffraction from an optical fiber. Acoustic waves are launched into the fiber at the Bragg angle through a Hertzian contact to a YAG wedge on which ZnO acoustic transducers have been fabricated. At the present time, the efficiency is low (0.01%), although it is adequate for certain types of tapped delay line devices. The wide bandwidth of the tap implies a switching time of approximately 1 nsec.

Depositing a piezoelectric material such as ZnO directly upon a standard optical fiber of circular cross section will increase efficiency and obviate mechanical

alignment. By using an interdigital transducer, we can excite acoustic waves focused on the center of the fiber at the correct angle for Bragg interaction, radically improving the efficiency. Such a device has been constructed, and its properties are currently being measured.

Finally, by using acoustic focusing through a low-loss material onto an optical waveguide with a large piezo-optic coefficient, it should be possible to obtain strong Bragg interaction, permitting construction of efficient Bragg devices at frequencies of the order of 10 GHz.

The authors are grateful to R. B. Dyott of Andrews Corporation for providing a sample of D fiber. Brian Heffner is supported by a fellowship from the Fannie and John Hertz Foundation. This research was supported by the U.S. Office of Naval Research under contract no. N00014-84-K-0327 and by Litton Systems, Inc.

References

1. K. P. Jackson, S. A. Newton, B. Moslehi, M. Tur, C. C. Cutler, J. W. Goodman, and H. J. Shaw, *IEEE Trans. Microwave Theory Tech.* **MTT-33**, 193 (1985).
2. K. Wilner and A. P. van den Heuvel, *Proc. IEEE* **64**, 905 (1976).
3. R. A. Bergh, G. Kotler, and H. J. Shaw, *Electron. Lett.* **7**, 260 (1980).
4. K. P. Jackson, J. E. Bowers, S. A. Newton, and C. C. Cutler, *Appl. Phys. Lett.* **41**, 139 (1982).
5. S. K. Korotky, G. Eisenstein, R. C. Alferness, J. J. Veselka, L. L. Buhl, G. T. Harvey, and P. H. Read, *IEEE J. Lightwave Technol.* **LT-3**, 1 (1985).
6. B. L. Heffner, G. S. Kino, and B. T. Khuri-Yakub, *Appl. Phys. Lett.* **47**, 17 (1985).
7. See, for example, L. D. Landau and E. M. Lifshitz, *Theory of Elasticity*, translated by J. B. Sykes and W. H. Reid (Pergamon, New York, 1959), pp. 30-37.
8. B. L. Heffner, G. S. Kino, B. T. Khuri-Yakub, and W. P. Risk, in *Proceedings of the IEEE Ultrasonics Symposium* (Institute of Electrical and Electronics Engineers, New York, 1985).

Noninvasive sheet charge density probe for integrated silicon devices

H. K. Heinrich, D. M. Bloom, and B. R. Hemenway

Stanford University, Edward L. Ginzton Laboratory, Stanford, California 94305

(Received 20 January 1986; accepted for publication 25 February 1986)

We report a sensitive new technique for probing dynamic sheet charge density variations in integrated silicon devices. Using a specially designed noninvasive Nomarski phase contrast interferometer a sheet charge density sensitivity of $2.6 \times 10^6 \text{ e/cm}^2/\sqrt{\text{Hz}}$ is extracted from experimental data for 1 mA of detected photocurrent. This charge density sensitivity makes possible μV signal level detection in an active device, and with digital signals the corresponding signal/noise level is sufficiently high that multimegabaud data can be captured in real time. **STANFORD UNIVERSITY** 4005 **G. L.** **GINTON LABORATORY**

Optical techniques have been used effectively to noninvasively measure both analog and digital signals in GaAs integrated circuits.^{1,2} These measurements have been shown to have a very high spatial resolution and a bandwidth which is limited only by the device under test. While this approach is adequate for measuring voltage waveforms it is limited to circuits fabricated on electro-optic substrates. Other workers have used an external electro-optic crystal to measure the signals in an integrated circuit.^{1,3} While these approaches are generally applicable to any type of integrated circuit, these techniques rely on either bonding the signal out to the electro-optic crystal or on bringing a piece of the crystal near the point to be measured. Hence these approaches introduce unwanted parasitics into the circuit. Electro-optic detection in silicon is not possible since it is a symmetric crystal. In addition, the optical Kerr effect and the Franz-Keldysh effect are too small to be of practical value. However, free carriers in an active device perturb both the index of refraction and the absorption coefficient near the device.⁴ Modulators employing absorption by free carriers have been demonstrated.^{5,6} However, free-carrier absorption is insignificant in the near infrared,⁷ where small optical spot sizes can be achieved and sensitive optical detectors are available. The phase shift produced by the index perturbation, on the other hand, varies more slowly with wavelength ($\phi \propto \lambda$) than the λ^2 dependence for the free-carrier absorption. Thus significant phase modulation of the optical beam can be achieved in the near infrared even when no free-carrier absorption can be detected.

In this letter, we report shot noise limited interferometric detection of refractive index variations from free-carrier modulation in silicon devices and propose its potential use in measuring internal device characteristics and μV signals noninvasively in an integrated circuit. Since this technique relies on free carriers, it is applicable to integrated circuits fabricated in any semiconducting material. Simple electromagnetic theory¹⁰ predicts that these carriers will perturb the index of refraction according to the relationship

$$n = n_0 \sqrt{1 - w_p^2/w^2},$$

where w_p is the plasma resonant frequency given by $w_p^2 = q^2 N / \epsilon m^*$, N is the carrier concentration, and m^* is the combined reduced mass for the electrons and holes given by

$$m^* = \frac{m_e m_h}{m_e^* + m_h^*}.$$

For a charge density level of $N = 10^{16} \text{ e/cm}^3$ the plasma frequency is $w_p = 4 \text{ THz}$ which is well above any present electronic signals, yet far below the wavelength of infrared optical sources. Thus, by modulating the charge in an integrated circuit device, a small modulation occurs in the index of refraction. This index change can readily be detected by placing the device in one arm of a high resolution interferometer and then detecting the resulting amplitude modulation with a photodiode placed at the output of the interferometer. If the system is designed to be shot noise limited at the optical receiver, the minimum detectable sheet charge density will be given by

$$\frac{\delta N}{\sqrt{\text{Hz}}} = \frac{4\pi^2 \epsilon m^*}{q^2 n_0 \lambda_0} \left(\frac{2q}{I_0} \right)^{1/2},$$

where I_0 is the average photocurrent in the photodiode, n_0 is the optical index of refraction, λ_0 is the vacuum wavelength of the optical probe beam, and δN is given by the integral of the charge density over the wafer thickness. For a photocurrent of $I_0 = 1 \text{ mA}$ the minimum detectable sheet charge density will be $\delta N = 2.47 \times 10^6 \text{ e/cm}^2/\sqrt{\text{Hz}}$. If the capacitance/area of the device under test is known this sheet charge density can be expressed as a voltage modulation by the simple relation

$$\delta V = q \delta N / C',$$

where C' is the capacitance/area. Applying this relationship to a simple reverse-biased diode with a junction capacitance of $4.5 \times 10^{-8} \text{ F/cm}^2$ gives a minimum detectable signal of $\delta V = 880 \mu\text{V}/\sqrt{\text{Hz}}$ for 1 mA of photocurrent. For a forward-biased diode with a minority-carrier lifetime of $\tau = 500 \text{ ns}$ at a bias current density of $I_{dc} = 40 \text{ mA/cm}^2$, $C' = 7.7 \times 10^{-7} \text{ F/cm}^2$ (Ref. 11) which gives a minimum detectable signal of $\delta V = 51 \mu\text{V}/\sqrt{\text{Hz}}$ for 1 mA of photocurrent. Hence this technique is capable of detecting microvolt signal fluctuations in active devices.

The measurement system used to detect the charge induced phase fluctuations is shown in Fig. 1. A 1.3- μm continuous wave neodymium-doped yttrium aluminum garnet (cw Nd:YAG) laser was chosen because the absorption coefficient at this wavelength is a minimum⁹ and yet a spot size of about 2.5 μm can be achieved. The output from this laser is directed through a polarizing beamsplitter cube into a 1.5° calcite Nomarski¹² wedge whose crystal axes are placed at 45° to the direction of polarization defined by the polarizing

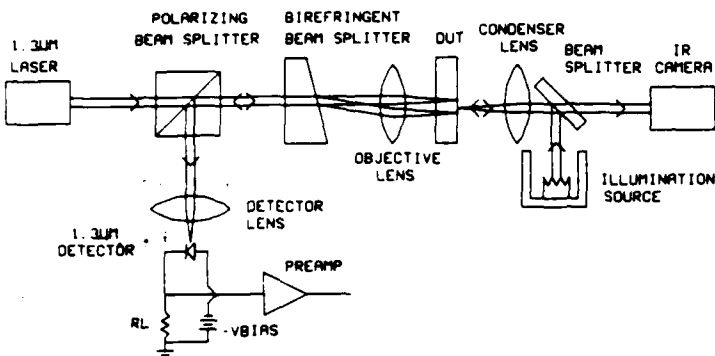


FIG. 1. Block diagram of electrical and optical system to sense charge density modulation in silicon

beamsplitter cube. For maximum signal gain the Nomarski wedge has been set to provide a round trip differential phase shift of an odd multiple of $\pi/2$ between the two orthogonal polarizations. Because of the birefringence of the wedge, two beams of orthogonal polarization are produced with an angle of 4.2 mrad between them. The objective lens converts the slight angular separation produced by the wedge into a spatial separation at the device under test (DUT). The two beams enter the backside of the wafer and pass through the sample to the front surface where one beam is reflected from metallization over an active device and the other beam is reflected from metallization over a reference point on the circuit. If the birefringent wedge and the DUT are at the front and back focal planes of the objective lens, the reflected beams from the DUT will return along the same optical path, and hence the Nomarski wedge will recombine the two beams into a single beam. The polarizing beamsplitter then mixes these two orthogonal polarizations and causes them to produce intensity modulated interference products at the Ge photodiode. The intensity modulated signal at the detector will be linear with respect to charge density to within 1% over a dynamic range of over 128 dB. In addition, since both beams follow highly overlapping optical paths, the interferometer is insensitive to temperature fluctuations and vibrations. The condenser lens, IR camera, and illumination source provide the means whereby the DUT can be visually aligned to the probe beam.

For our first experimental demonstration of charge detection in silicon we used a large area ($0.5 \text{ mm} \times 0.5 \text{ mm}$) abrupt junction *pn* diode. The measured series resistance of the diode was 250Ω . The zero bias junction capacitance/area of this device was measured to be $4.5 \times 10^{-8} \text{ F/cm}^2$ which gives a corresponding theoretical minimum detectable signal of $880 \mu\text{V}/\sqrt{\text{Hz}}$ for 1 mA of photocurrent. This calculation agrees well with the observed minimum detectable signal of $930 \mu\text{V}/\sqrt{\text{Hz}}$ at 0 V dc bias. In the forward-biased condition, the injected charge storage significantly increases the capacitance/area and the minimum detectable signal is reduced to $51 \mu\text{V}/\sqrt{\text{Hz}}$ for 1 mA of photocurrent. Figure 2 shows a plot of the small-signal transfer function from the diode voltage to the optically received and amplified output signal (45 dB gain following a 50Ω photodiode load resistor) as a function of the dc bias applied to the diode. The data show excellent agreement with the simple the-

ory presented here at reverse biases, and at forward biases below the signal gain saturation level. This saturation level occurs when the voltage applied across the diode series resistance is much larger than the small-signal voltage across the diode. Beyond this dc bias, the experimental results are probably best explained by current crowding within the DUT. For reverse-biased operation, the theory and data required no parameter fitting. For forward-biased operation, the minority-carrier lifetime, which has not yet been measured, was adjusted to fit the data.

Figure 3 shows a photograph of the output from the photodiode preamplifier when a 0.8-V emitter coupled logic (ECL) signal was applied to the ($0.5 \text{ mm} \times 0.5 \text{ mm}$) diode. The signal was bandwidth limited to 20 MHz and displayed on an oscilloscope. The rise and fall times shown are a direct result of diode series resistance and the active charge stored within the device from the minority-carrier injection. Since the sensitivity scales directly with the bias current density and carrier lifetime, a typical bipolar junction transistor ($A = 25 \mu\text{m}^2, f_T = 1 \text{ GHz}$), operating at bias currents greater than $30 \mu\text{A}$, would produce a signal greater than that shown in Fig. 3. This suggests that multimegabaud data could be captured with a high signal/noise ratio in real time. We have also observed charge detection of digital signals on an *N*-channel metal-oxide-silicon (NMOS) inverter. However, since the capacitance/area in this device was governed by gate capacitance ($t_{ox} = 1000 \text{ \AA}$), the signals in this device were much smaller than for the forward-biased diode and

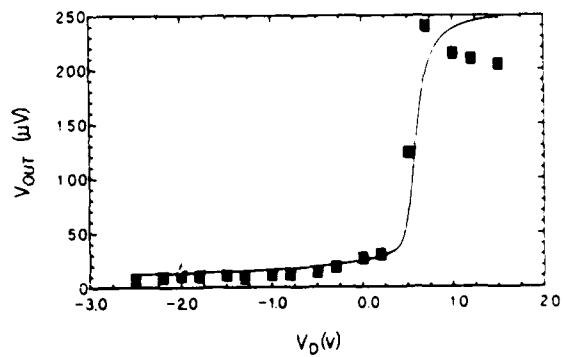


FIG. 2. Comparison of experimental and theoretical small-signal transfer functions. Experimental (solid boxes) and theoretical (solid line)

ERRATA

Erratum: Noninvasive sheet charge density probe for integrated silicon devices [Appl. Phys. Lett. 48, 1066 (1986)]

H. K. Heinrich, D. M. Bloom, and B. R. Hemenway
Stanford University, Edward L. Ginzton Laboratory, Stanford, California 94305

The third equation in this letter should read as follows:

$$\frac{\delta N}{\sqrt{\text{Hz}}} = \frac{4\pi c^2 \epsilon m^*}{q^2 n_0 \lambda_0} \left(\frac{2q}{I_0} \right)^{1/2},$$

where the factor c^2 has been inserted into the numerator of the right-hand side of the equation and π^2 changed to π

STANFORD UNIVERSITY

4005

GINZTON LABORATORY
G. L.

ERRATA

Erratum: Noninvasive sheet charge density probe for integrated silicon devices [Appl. Phys. Lett. 48, 1066 (1986)]

H. K. Heinrich, D. M. Bloom, and B. R. Hemenway
Stanford University, Edward L. Ginzton Laboratory, Stanford, California 94305

The third equation in this letter should read as follows:

$$\frac{\delta N}{\sqrt{\text{Hz}}} = \frac{4\pi c^2 \epsilon m^*}{q^2 n_s \lambda_0} \left(\frac{2q}{I_0} \right)^{1/2}$$

where the factor c^2 has been inserted into the numerator of the right-hand side of the equation and π^2 changed to π .

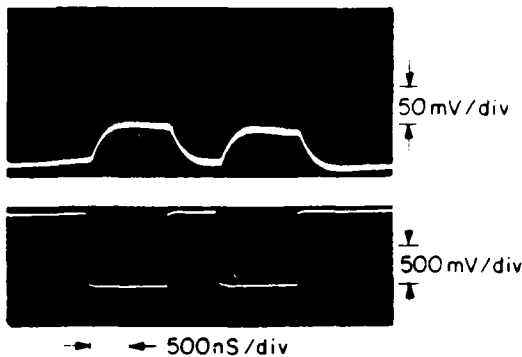


FIG. 3 Real time display of a digital signal measured from a forward-biased *pn* junction diode. Upper trace is the optically detected and amplified signal displayed on a 20-MHz bandwidth oscilloscope. Lower trace is a 0.8-V 1-MHz emitter coupled logic signal applied to the diode. The limited rise and fall times in the measured response are a result of the large area diode (0.5 mm \times 0.5 mm) junction capacitance and series resistance.

about the same size as for the reverse-biased *pn* junction diode. With thinner gate oxides correspondingly larger signals will be observed.

In conclusion, we have experimentally demonstrated optical detection of charge density modulation in silicon. We have observed a sheet charge sensitivity of 2.6×10^6 $e/cm^2/\sqrt{Hz}$. We have used this approach to measure internal node voltages in a silicon IC, and we have demonstrated the ability to sense μV signal levels in a forward-biased diode and digital signals in an NMOS inverter. With an appropriately designed receiver, this optical detection technique has a sufficient signal to noise ratio to allow transient capture logic analysis at rates of several tens of MHz (with a bit error rate

of less than 10^{-9}). The ability to achieve low error rate data capture suggests a potential use of this technique in optical interconnects. In addition, the bandwidth capabilities of this system are sufficiently high that F_T measurements on state-of-the-art high-frequency transistors will be limited only by the device under test. This charge sensing tool allows a device designer the ability to directly observe spatial variations in charge density modulation within a device.

This work was supported under a Joint Services Electronics Program research contract No. N00014-84-K-0327 and the Hewlett-Packard fellowship program. Such support does not imply endorsement of the content by any of the above parties.

- ¹B. H. Kolner and D. M. Bloom, *Electron. Lett.* **20**, 818 (1984).
- ²J. Freeman, S. K. Diamond, H. Fong, and D. M. Bloom, *Appl. Phys. Lett.* **47**, 1083 (1985).
- ³J. A. Valdmanis, G. Mourou, and C. W. Gabel, *Appl. Phys. Lett.* **41**, 211 (1982).
- ⁴J. A. Valdmanis, G. Mourou, and C. W. Gabel, *Soc. Photo-opt. Instrum. Eng.* **439**, 142 (1983).
- ⁵K. E. Meyer and G. A. Mourou, in *Picosecond Electronics and Optoelectronics*, edited by G. Mourou, D. M. Bloom, and C. H. Lee, Springer-Verlag Series on Electrophysics (Springer, New York, 1985), Vol. 21, pp. 46-49.
- ⁶H. Y. Fan and R. J. Collins, *Phys. Rev.* **101**, 566 (1956).
- ⁷R. B. McQuistan and J. W. Schultz, *J. Appl. Phys.* **35**, 1243 (1964).
- ⁸D. W. Peters, *Appl. Opt.* **6**, 1033 (1967).
- ⁹H. Y. Fan and M. Becker, *Phys. Rev.* **78**, 178 (1950).
- ¹⁰S. Ramo, J. R. Whinnery, and T. Van Duzer, *Fields and Waves in Communication Electronics* (Wiley, New York, 1965), pp. 338-342.
- ¹¹S. M. Sze, *Physics of Semiconductor Devices*, 2nd ed. (Wiley, New York, 1981), pp. 158-160.
- ¹²M. G. Normarski, *J. Phys. Radium* **16**, 99 (1955).
- ¹³Subsequent measurements on a high-speed bipolar junction transistor have demonstrated measurement bandwidths > 100 MHz.

Deposition of oriented zinc oxide on an optical fiber

B. L. Heffner and B. T. Khuri-Yakub

Edward L. Ginzton Laboratory, W. W. Hansen Laboratories of Physics, Stanford University, Stanford, California 94305

S. L.

(Received 10 March 1986; accepted for publication 31 March 1986)

Techniques are described by which an oriented zinc oxide film is sputtered directly on one side of an 80- μm -diam fused silica single-mode optical fiber. A 4-GHz piezoelectric transducer incorporating this film demonstrates that the film is oriented. Evidence of acoustic waves in the fiber is given by the swept-frequency vector input impedance of the transducer. Acoustic transducers fabricated directly on a fiber produce fields focused on the fiber core for efficient acousto-optic interactions, making possible many new fiber-optic signal processing devices.

Over the last few years, several attempts have been made at developing acoustic fiber modulators by mechanically contacting the fiber with one or an array of contacting points coupled to an acoustic transducer.^{1,2} While some of these modulators have been successful, the need for mechanical contact and alignment leads to fracture of the fibers and difficulty in reproducing results. We address the problem of modulating fibers by depositing a piezoelectric material directly on the fiber. The advantages gained by direct deposition of a piezoelectric material are many: a monolithic structure is obtained with no mechanical alignment problems, operation at high frequency and with large bandwidths is possible, multiple taps are relatively easy to accomplish, and enhanced interaction between the acoustic and optical beams is obtained because the acoustic beam is focused on the fiber core.

We have, in the past, worked on several different systems for the deposition of zinc oxide (ZnO) as a piezoelectric material for applications in monolithic surface wave devices and bulk transducers. Presently, we use a reactive planar magnetron sputtering system for depositing ZnO for all of our device applications. The major concerns related to the deposition of oriented ZnO on optical fibers include residual stress that can lead to the fracture of the film and fiber, proper alignment of the crystallites around the fiber, and the need to thermally heat the fiber during deposition of both the ZnO and the metal back electrode. An argon-oxygen atmosphere is used for depositing the ZnO, which allows us to use a low substrate temperature (50–200 °C), and sputtering power (200 W) for deposition, resulting in low residual stress. Several of our experiments have demonstrated that the orientation of the ZnO is independent of the orientation of the plane of the substrate with respect to the plane of the target, if the substrate is located in the middle of the plasma. A later publication will present the results of that work. We also find that the temperature of the substrate can be varied over a wide range without deterioration of the quality of the ZnO film. The above results encouraged us to deposit the ZnO directly on optical fibers to make monolithic acoustic fiber-optic modulator structure.

The low thermal conductivity of an optical fiber makes it difficult to hold the fiber at a known elevated temperature, as is usually required for rf sputtering. The conductivity of fused silica is approximately 3.5×10^{-3} cal $\text{cm}/\text{cm}^2 \cdot \text{s} \cdot ^\circ\text{C}$. This low conductivity, combined with the 5.0×10^{-4} cm^2

cross-sectional area of an 80- μm -diam fiber, makes it necessary to keep the fiber in good contact with a thermal reference along the entire length of the sputtered film. A stainless-steel substrate was used as the thermal reference, with the surface contacting the fiber machined and polished to form a convex cylindrical surface of 30 cm radius.

Holding the delicate fiber in good contact with the thermal reference proved to be a challenge. Due to the difference in thermal expansion coefficients between fused silica and stainless steel, the fiber cannot be simply stretched against the thermal surface and clamped in place, as this arrangement will break the fiber during thermal cycling. Instead, the stiffness of the fiber was exploited to force the fiber against the cylindrical surface. As shown in Fig. 1, the fiber was clamped at one end with a spring clip. The other end was forced upward, but was free to slide along the second clip. In this way, the fiber was held against a thermal reference while being free to move during thermal expansion.

In Fig. 2 the normalized vector input impedance S_{11} is shown over 4.0–4.8 GHz, as measured with a network analyzer. The acoustic signal within the fiber is reflected back to the transducer after a delay of $160 \mu\text{m}/5970 \text{ ms}^{-1} = 26.8 \text{ ns}$. As the frequency is swept, this delay causes the input impedance to exhibit an acoustic resonance response with a 37.3-MHz periodicity. Given the fiber's dimensions, this resonance and periodicity are characteristic of acoustic reflections. The plot of S_{11} yields a transducer efficiency of –9 dB at 4.15 GHz, assuming a material loss of 4.2 dB at this frequency. However, loss in the matching elements is significant at these frequencies, and techniques to make a good microwave connection to a device on a fiber have yet to

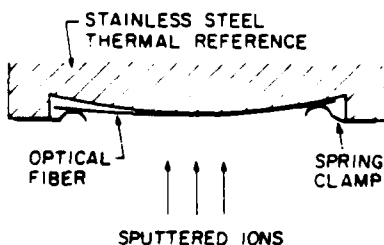


FIG. 1. Method of holding an optical fiber for depositing the back metal electrode and ZnO film. The fiber is free at one end to move during thermal cycling.

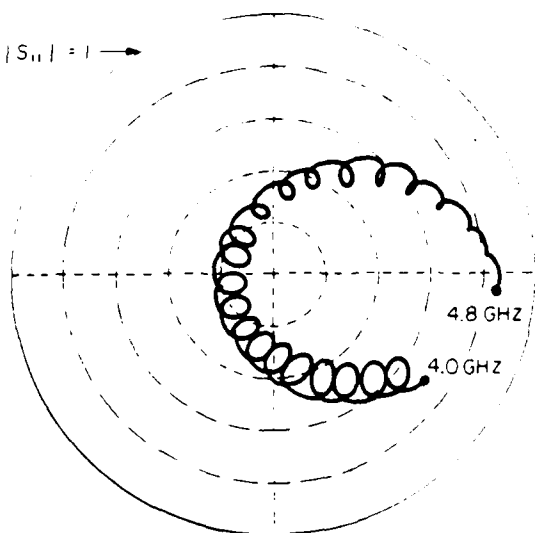


FIG. 2. Measured S_{11} of a ZnO transducer on an 80- μm -diam fiber over 4.0-4.8 GHz. Phase is uncalibrated

be perfected, so improvements in transducer efficiency can be expected.

We have therefore demonstrated a new technology for fabricating acoustic transducers directly on the surface of an optical fiber. This technology makes possible many new fiber-optic signal processing devices using monolithic acous-

tic transducers that produce an acoustic field focused on the fiber core for efficient interaction. The low loss, low dispersion, and extremely high modulation bandwidth of single-mode fiber makes it an attractive delay medium for high-speed processing.⁴ An acoustic transducer on such a fiber can be used to construct an electronically switchable tap or modulator. A description of the first acousto-optic device to be constructed using this technology will soon be available.

The authors are grateful to Harrison Ransom and Professor Gordon Kino for many helpful discussions, and to Lance Goddard for performing the sputtering. Brian Heffner is supported by a fellowship from the Fannie and John Hertz Foundation. This work was supported by the Office of Naval Research through the Joint Services Electronics Program on contract No. N00014-84-K-0327.

¹W. P. Risk, G. S. Kino, H. J. Shaw, and R. C. Youngquist, Proc. IEEE Ultrasonics Symp. 318 (1984).

²B. L. Heffner, G. S. Kino, B. T. Khuri-Yakub, and W. P. Risk, Proc. IEEE Ultrasonics Symp. (1985).

³CRC Handbook of Chemistry and Physics, 66th edition, R. C. Weast, ed. Section E (CRC, Boca Raton, FL, 1985).

⁴K. P. Jackson, S. A. Newton, B. Moslehi, M. Tur, C. C. Cutler, J. W. Goodman, and H. J. Shaw, IEEE Trans. Microwave Theory Tech. MTT-33 (3), 193 (1985).

Low-loss single-crystal sapphire optical fibers

C.A. Magel, D.H. Jundt, M.M. Fejer and R. STANFORD UNIVERSITY
Applied Physics Department, Stanford University
Stanford, California 94305

Abstract

GINZTON LABORATORY
G. L.

Single-crystal sapphire (α -Al₂O₃) fibers are potentially useful in a wide variety of optical applications, particularly those involving high-power or high temperature light-guiding, over the wavelength range from 0.24 μ m in the ultraviolet to 4.0 μ m in the mid-infrared. These fibers are routinely grown at rates of up to 8 mm/min, and with diameter stability of better than 0.5% rms under feedback control. Recent measurements on unclad 150 μ m diameter fibers show fundamental mode scattering losses of about 0.3 dB/m in the visible and less than 0.07 dB/m at 3.39 μ m.

Introduction

Single-crystal sapphire (α -Al₂O₃) has long been recognized as a good material for optical windows, because of its wide range of high transmission (0.24–4.0 μ m), its low bulk scattering, its durability and hardness, and its resistance to chemical attack. These same properties make sapphire an interesting candidate for an optical fiber material. In addition, the high melting point of sapphire fibers, ~ 2045°C, makes them potentially useful for light-guiding or thermometry in high-temperature environments, or for the transmission of high average power laser light in industrial or medical applications.

In this paper, we first briefly review the method we have used to grow optical-quality single-crystal sapphire fibers. We then summarize fiber growth results, including improved diameter stability attained through the active control of fiber diameter during growth. After a discussion of recent measurements of the scattering losses of unclad fibers at several wavelengths from the UV to the mid-IR, we conclude with a summary of the present state of development of sapphire optical fibers and suggestions for further research.

Growth method

The process we have chosen to produce single-crystal refractory oxide fibers, known as laser-heated miniature pedestal growth,¹ is illustrated in Fig. 1. The tip of a rod of source material is heated by focused radiation from a CO₂ laser, forming a molten liquid droplet. An oriented seed crystal is then dipped into this droplet, and withdrawn slowly until the molten zone assumes the shape, governed by surface tension, shown in the figure. To grow a fiber, the seed pulls material out of the molten zone while fresh source material is being moved into the melt. The fiber can be grown slightly more than a factor of three smaller in diameter than the source by appropriate choice of the translation rates. This limit to the diameter reduction in a single growth step is dictated by instability of the growth process at higher diameter reduction ratios.

Several features of this process should be noted. First, materials with a high melting temperature can be grown. Second, as this is a technique using no crucibles or dies, the purity of the grown fiber may be limited only by the purity of the source material. Finally, since the material is melted and not just softened, diameter fluctuations at the freezing interface that arise from unstable heating or translation are permanently frozen into the fiber.

A block diagram of our fiber growth apparatus,²⁻⁵ as configured for these experiments, is presented in Fig. 2. We have used this same apparatus to grow fibers of Nd:YAG and LiNbO₃. The controlled atmosphere chamber contains atmospheric-pressure air and is currently used in sapphire growth merely to prevent perturbation of the growth by wind currents. The copper focusing mirrors are designed to symmetrically heat the molten zone and the fiber translators are of a continuous belt-driven design which can grow unlimited lengths of fiber, and which are driven by phase-locked dc motors for accurate constant speed.

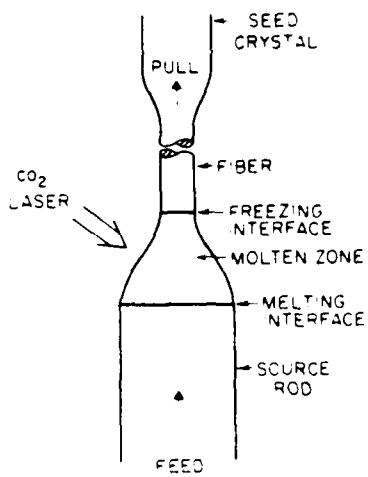


Fig. 1--The laser-heated miniature pedestal growth process

and diameter-controlled fibers have been grown as long as 150 m sapphire fiber from a 500 m source rod is approximately 3 watts. Sapphire is an easy material to grow with this technique; we have grown more than 100 sapphire fibers since June of 1983.

In spite of all these design provisions, fibers of better diameter uniformity than were obtained without feedback were required. To this end, we constructed a real-time, in-situ diameter variation monitoring system. The fiber diameter measurement system has a diameter resolution of better than 0.1%, a working distance of 160 mm, a measurement rate of 100 kHz, and an axial resolution of less than 11 μ m along the fiber length. As indicated in Fig. 3, this system can be used in conjunction with a simple analog proportional controller to feed back to the pull feed motor speed ratio in order to stabilize the diameter of a growing fiber.

Growth results

Sapphire fibers are typically grown with a diameter reduction of 3:1 from a centerless ground single crystal source rod of 500 m in diameter. It is possible to use these fibers as source material for further growth steps if more diameter reduction is required. Fibers can be grown with either the c or a crystallographic axis along the fiber axis. Our research fibers are typically 4.5 cm long, but both open-loop

and diameter-controlled fibers have been grown as long as 150 m sapphire fiber from a 500 m source rod is approximately 3 watts. Sapphire is an easy material to grow with this technique; we have grown more than 100 sapphire fibers since June of 1983.

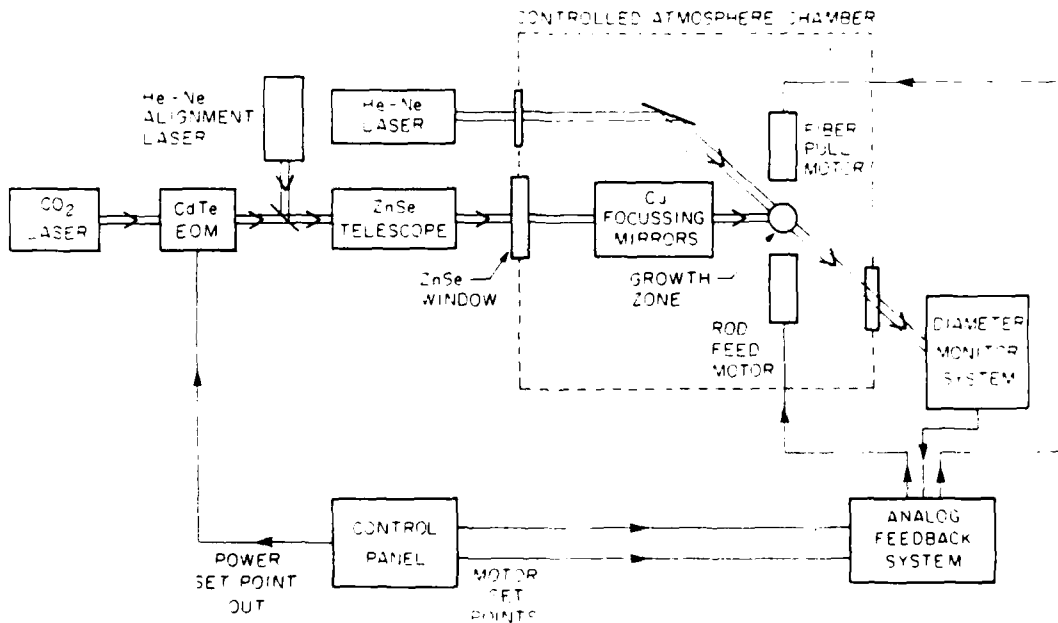


Fig. 2--Block diagram of the growth apparatus

The cross-sectional geometry of single crystal sapphire fibers, as shown in Fig. 3, reflects the crystal symmetry, as it does in bulk crystal growth. The cloudy areas in the centers of these fibers are regions of tiny "bubbles", or microvoids, which occur at growth speeds of over 8 mm/min (or 0.5 m/h). Nightingale⁵ has proposed that microvoid formation may be the result of constitutional supercooling. If this is the case, then measures taken to steer the temperature gradient at the freezing interface, such as growth in a helium atmosphere to increase convective heat loss from the fiber, could increase the threshold speed for microvoid formation and allow higher growth rates. The fibers used in these studies were grown at 1 mm/min, and therefore do not exhibit microvoids.

Figure 4 shows a 150 μm c-axis sapphire fiber bent into a loop 7.8 mm in diameter. Upon being released, the bent fiber immediately springs straight. This fiber sample finally broke when the loop was pulled to a diameter of 5 mm. This bending radius corresponds to a maximum strain of 3%, approaching the theoretical cohesive strength of solid matter,⁶ and achieving the maximum strength measured in much smaller sapphire whiskers.⁷ In addition to attesting to the crystalline perfection and smoothness of the sapphire fiber, this experiment also suggests its inertness, since this unclad and uncotted fiber was exposed to the atmosphere for almost a year before the bending test.



Fig. 3--Polished cross-sections of 150 μm diameter sapphire fibers grown at 23.2 mm/min. (a) c-axis along fiber axis; (b) a-axis along fiber axis. Note microvoids (see text) near fiber centers. [From Ref.5].

Fig. 4--Demonstration of flexibility of a 150 μm c-axis sapphire fiber. (Ruler is marked in inches).

The effect of feedback control on diameter stability⁷ is illustrated in Fig. 5. This figure compares the plots of diameter vs length, obtained by the diameter monitoring system during growth, for a 1 cm section from each of two 150 μm c-axis fibers grown at 1 mm/min on the same day. Sample S-213, represented by the dashed line, exhibits the 2% rms diameter fluctuations typical of fibers grown without feedback. It is believed that the rough periodicity observed reflects a natural resonance of the pedestal growth process. Fiber S-209, represented by the dark solid line, was grown under nominally identical conditions, except that a proportional feedback gain corresponding approximately to a 44% speed change of the fiber pulling motor per 1% fiber diameter change was used. (Applying much higher feedback gain results in diameter oscillations which exponentially increase in amplitude until the fiber pinches off, terminating growth). This fiber exhibits fluctuations of under 0.2% rms amplitude, and the fluctuations appear less periodic, or at least of higher frequency. In both cases, the CO_2 laser power was held constant. The residual diameter noise on S-209 may largely be due to the 1% fluctuations in laser power.

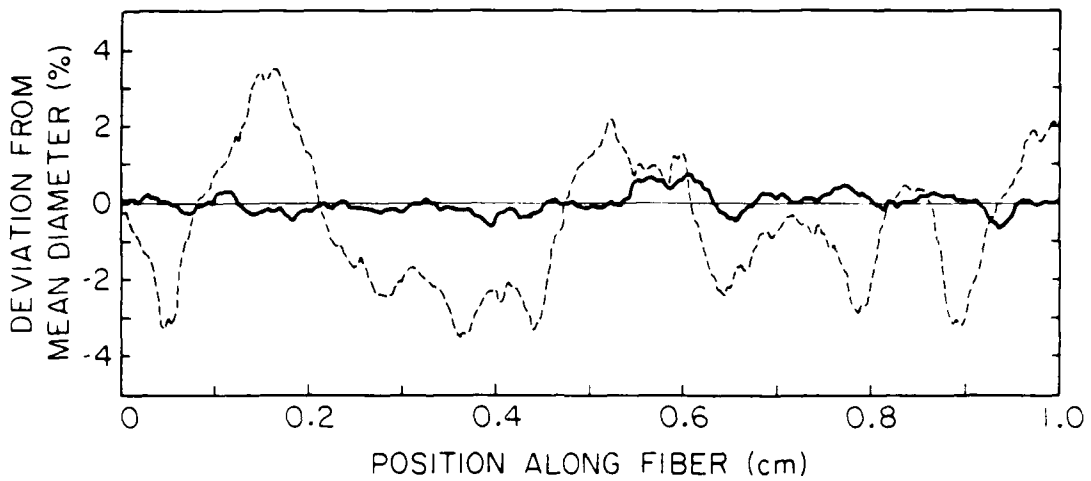


Fig. 5--Effect of feedback control on diameter stability. Dashed line shows 2% rms fluctuations on S-213, a 150 μm fiber grown without feedback; dark solid line shows tenfold improvement for S-209, grown using feedback diameter control.

Because of the unique ability of the crystal growth process to "freeze-in" diameter or composition fluctuations along an optical fiber, we have considered the possibility of making fiber structures with intentionally-modulated diameters or dopant levels. These structures may find eventual application in fiber devices with distributed Bragg filters or mirrors. The result of our first experiment along these lines⁷ is shown in Fig. 6. Application of a 3-Hz sinusoidal modulation in fiber pull speed (around a mean pull rate of 1 mm/min) resulted in diameter modulation with a spatial period of about 5 μm . It is reasonable to believe that practical first-order gratings could be made by using an increased modulation frequency, a slower mean pull rate, laser power modulation, or some combination of the above.

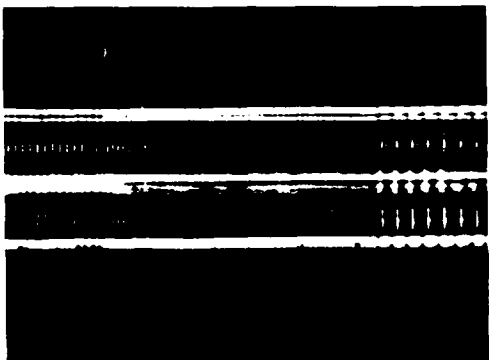


Fig. 6--Intentional periodic modulation of fiber diameter. The shortest period ripples (center) have a spacing of ~5 μm .

collect small-angle forward scattering; a baffle in the sphere prevents the detector from seeing direct light from the fiber. Light from a laser source is chopped and directed at the polished input face of the fiber. Care is taken to block light which is not launched into the fiber from entering the sphere. The fiber and sphere are translated and tilted as a unit to optimize the coupling to the fundamental mode of the fiber. This optimal condition can be observed both as a minimum in the scattering signal and as a narrow far-

Scattering losses

Earlier optical measurements⁸ led us to the conclusion that total fiber attenuation in the visible was dominated by surface scattering resulting from diameter non-uniformity. Bulk scattering should be negligible in a single-crystal material with no grain boundaries, inclusions, or micro-voids, and a small deviation from perfect roundness should not contribute to the loss of low-order modes if the cross-sectional shape is constant along the length of the fiber. The availability of diameter-controlled fibers motivated us to make a more quantitative investigation and to extend our experiments to both shorter and longer wavelengths.

The apparatus used in our scattering loss measurements is indicated schematically in Fig. 7. The fiber under test is cleaned and threaded through a custom 25-mm diameter integrating sphere.¹⁰ The output plug has a small hole in it to pass the fiber, yet

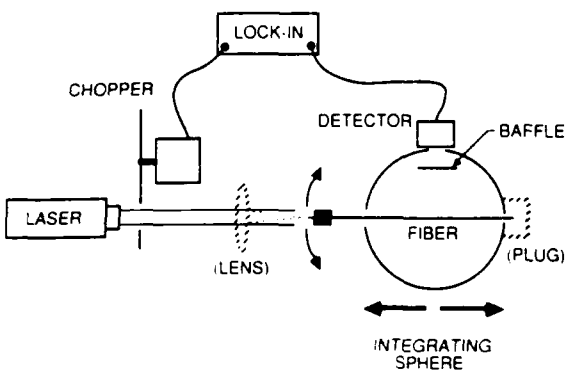


Fig. 7--Schematic diagram of the scattering loss measurement apparatus.

frequency was 440 Hz. The most consistent results were obtained with no light-launching lens, and fundamental-mode launching conditions. Since the fiber was capable of supporting many guided modes, careful adjustment of the fiber tilt was required to obtain single-mode propagation. A factor of approximately two greater loss was measured when launching multiple modes.

At the 3.392 μm wavelength, a diffuse gold coated sphere and pyroelectric detector were used for the measurement. The chopping frequency was 10 Hz to optimize the detector performance. The low laser power, small scattered signal, low detector sensitivity, and high detector noise necessitated the use of a lens to increase the signal, and a lock-in time constant of 100 s. It was thus difficult to optimize the fiber tilt for single-mode launching.

The results of the scattering loss measurements are plotted in Fig. 8. The UV to near-IR losses cluster around 0.3 dB/m. The measured value at 3.392 μm of 0.07 dB/m should properly be considered an upper bound to the actual value for the reasons just stated. Many factors could explain the apparently higher scattering loss of the diameter-controlled fiber, but considering the error bars, perhaps it is best simply to say that diameter control did not lead to a significant lowering of scattering loss. The drop in loss at 0.325 μm could be due to incomplete guiding of the light in the short (4.5 cm) fiber samples.

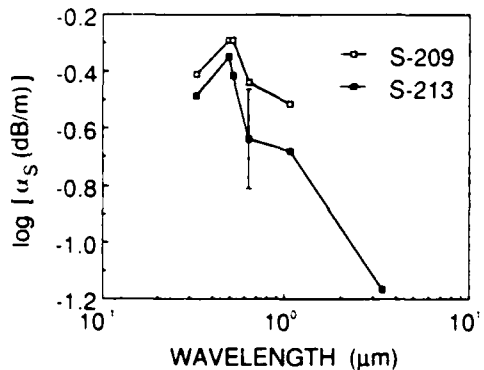


Fig. 8--Measured scattering losses vs wavelength. Closed squares are for fiber grown without feedback diameter control. Error bar applies to all points except longest wavelength point, which is an upper bound.

field mode pattern on a screen at the polished output end of the fiber. The detected scattered light is measured with a lock-in amplifier. Then without disturbing the launching conditions, the sphere is translated so as to just bring the output end of the fiber into the integrating sphere, and a solid plug is placed in the output port. In this position, scattered light plus fiber throughput is measured. By taking the proper ratio, the scattering loss is obtained. The input coupling efficiency, detector sensitivity, and sphere throughput all cancel using this technique.

This measurement was performed on 150 μm c-axis samples S-209 and S-213 (the two samples of Fig. 5) at the 0.325, 0.488, 0.5145, 0.6328 and 1.064 μm laser wavelengths using a barium sulfate coated sphere and silicon photodiode. The chopping

were obtained with no light-launching lens, and fundamental-mode launching conditions.

These scattering values are still seven orders of magnitude greater than Brillouin scattering, which is theoretically predicted to be the largest contribution to bulk scattering in single crystals.¹¹ We calculate that a minimum total loss of 0.08 dB/m should occur at 2.7 μm , using our interpolated scattering loss data, and assuming published values of the intrinsic bulk absorption.^{11,12} This is a reasonable assumption since the only obvious extrinsic absorption found in our source material, using Fourier transform infrared spectroscopy was a group of narrow peaks between 3.0 and 3.1 μm , possibly attributable to OH. Better values for absorption will be obtained using a fiber calorimeter which is now under construction.

Conclusion

Single-crystal sapphire fibers can be grown routinely, at speeds up to 8 mm/min, and with a diameter stability of better than 0.1% feedback controlled. The fibers are chemically inert, mechanically strong and transparent from the UV to the mid-IR. Measured fundamental-mode scattering losses of unclad 150 μ m c-axis fibers are 0.3 dB/m in the visible and less than 0.07 dB/m at 3.39 μ m. Elaborate diameter control techniques are probably not necessary for simple light-guiding. Intentional diameter modulation, however, may eventually lead to interesting fiber devices.

Future work should prove that better diameter control can lead to lower scattering losses. Higher-speed growth, fiber cladding and the use of non-crystalline source material for the growth of longer fibers are all technological issues which need to be addressed. Single-crystal sapphire fiber development has nevertheless reached the stage at which the fibers are ready for immediate use in some applications requiring their unique properties.

Acknowledgments

The authors wish to thank the following people for their contributions to this research: Ken Fesler, for help in polishing fibers; Andrew Gurbaxani and Adnah Postenauer, for making the bending strength measurement; Rosemarie Koch, for optical microscopy; Eric Lin for computer acquisition of diameter data; and John Nightingale for permission to reprint figures from his dissertation.

The work was funded by the Air Force Office of Scientific Research, Contract #F49620-85-C-0062, the Joint Services Electronics Program, Contract #NO0014-84-K-0327, and the Stanford University Center for Materials Research, Contract #CMR-83-16982.

G.A. Magel gratefully acknowledges the support of the Fannie and John Hertz Foundation. D.H. Jundt is supported by the Institute of International Education in the form of a Fulbright Grant.

References

1. Burrus, C.A., and Stone, J., "Single Crystal Fiber Optical Devices : A Nd:YAG Fiber Laser", *Appl. Phys. Letts.* 26, p.318 (1975).
2. Fejer, M., Byer, R.L., Feigelson, R., and Kway, W., "Growth and Characterization of Single Crystal Refractory Oxide Fibers", *Proc. SPIE* 320, p.50 (1982).
3. Fejer, M., Nightingale, J.L., Magel, G.A., and Byer, R.L., "Laser Assisted Growth of Optical Quality Single Crystal Fibers", *Proc. SPIE* 460, p.26 (1984).
4. Fejer, M., Nightingale, J.L. Magel, G.A. and Byer, R.L., "Laser Heated Miniature Pedestal Growth Apparatus for Single Crystal Optical Fibers", *Rev. Sci. Instrum.* 55, p.1791 (1984).
5. Nightingale, J.L., The Growth and Optical Applications of Single Crystal Fibers, Ph.D. Dissertation, Stanford University, 1985 and Tiller, W.A., and Nightingale, J.L., to be published.
6. Fejer, M., Magel, G.A., Byer, R.L., "High Speed High Resolution Fiber Diameter Variation Measurement System", *Appl. Opt.* 24, p.2362 (1985).
7. Magel, G.A., Fejer, M., Nightingale, J.L., and Byer, R.L., "Controlled Growth of Single Crystal Optical Fibers", paper ThH2, CLEO '85, Baltimore, MD. May 21-24, 1985.
8. Brenner, S.S., "Factors Influencing the Strength of Whiskers", in Fiber Formable Materials, American Society for Metals, p.11 (1965).
9. Mehan, R.L., and Herzog, J.A., "Mechanical Properties of Whiskers", in Whisker Technology, Levitt, A.P., Ed., Wiley, pp.157-195 (1970).
10. LabSphere, Inc., P.O. Box 70, North Sutton, NH. 03260.
11. Sparks, M.G., and DeShazer, L.G., "Theoretical Overview of Losses in Infrared Fibers", *Proc. SPIE* 266, p.3 (1981).
12. Hordvik, A., Bendow, B., Lipson, H.G., Skolnik, L.H., and Brown, R.N., "Studies of Absorption in mid-IR Window Materials", in Symposium on Optical Materials for High Power Lasers, 8th, Boulder, Colorado, pp.50-57 (1976).
13. Extra Pure Grade Verneuil Craquelle Sapphire, Adolf Meller Co., P.O. Box A6001, Providence, Rhode Island 02940.

Electrooptic Sampling in GaAs Integrated Circuits

BRIAN H. KOLNER, STUDENT MEMBER, AND DAVID M. BLOOM, MEMBER, IEEE

(Invited Paper)

Abstract—Electrooptic sampling has been shown to be a very powerful technique for making time-domain measurements of fast electronic devices and circuits. Previous embodiments relied on a hybrid connection between the device under test and a transmission line deposited on an electrooptic substrate such as LiTaO₃. The hybrid nature of this approach leads to device packaging difficulties and can result in measurement inaccuracies and performance degradation at very high frequencies. Since GaAs is electrooptic and an attractive material for high speed devices, we have devised an approach of direct electrooptic sampling of voltage waveforms in the host semiconductor. In this paper, we review the principles and limitations of electrooptic sampling and discuss this new noninvasive technique for electronic probing with applications to characterizing high speed GaAs circuits and devices.

I. INTRODUCTION

THE speed of solid-state electronic and optoelectronic devices has steadily increased over the years, continually challenging our ability to measure them. Indeed, the improvements in instrumentation have often been driven by these constant advances in device performance. Sampling oscilloscopes can resolve risetimes approaching 25 ps, but state-of-the-art transistors employing novel structures have already broken the 10 ps barrier [1] and photoconductive switches have been demonstrated with subpicosecond response times [2].

On the other hand, techniques for ultrashort optical pulse generation and measurement have improved at an even faster rate and, today, light pulses as short as 8 fs have been generated [3]. The question of how to utilize these ultrashort light pulses to make electrical measurements has been addressed by several workers over the years using a variety of methods [4]–[7]. Recently, a new electrooptic sampling technique, first reported by Valdmanis *et al.*, was used to repetitively sample the electric field below a transmission line excited by a photoconductive switch [8]. Later, Kolner *et al.* demonstrated a similar system which was used to characterize the performance of a 100 GHz bandwidth GaAs Schottky photodiode [9].

We have recently employed this electrooptic sampling technique to directly probe electrical waveforms propagating on a GaAs substrate containing active devices and transmission line structures [10], [11]. Our approach eliminates the need for hybrid connections between the

device under test and an external electrooptic crystal thus allowing noncontact, noninvasive optical probing of GaAs circuits with picosecond time resolution.

In this paper, we review the basic principles of electrooptic sampling and the factors that influence the ultimate time resolution and voltage sensitivity. Second, we discuss methods of noninvasive probing of microwave and digital GaAs integrated circuits by using phase-lock techniques to synchronize a mode-locked laser to a microwave synthesizer and electrooptically sample a circuit in a manner analogous to a sampling oscilloscope. Finally, we present the results of measurements made on a GaAs monolithic microwave integrated circuit (MMIC) that demonstrates the power and flexibility of this new technique.

II. APPROACHES TO NONINVASIVE ELECTRICAL MEASUREMENTS

Most previous electrooptic sampling systems relied on a hybrid connection between the device under test and a transmission line formed on an electrooptic substrate such as LiTaO₃ [8], [9], [12]–[14]. The electric field of the transmission line was then probed transversely [Fig. 1(a)] with ultrashort optical pulses from a mode-locked laser. Although these systems demonstrated outstanding speed and sensitivity, their hybrid nature represents a compromise when very wide bandwidth measurements are anticipated. The physical connection between the device under test and an LiTaO₃ transmission line will, for example, introduce parasitic capacitances and inductances that could seriously affect the accuracy of the measurement. One approach that attempted to minimize the effects of this transition was to form a coplanar transmission line at the active device and continue the line to the edge of the substrate where a coplanar transmission line on LiTaO₃ with exactly the same dimensions was joined [15]. In this case, the active device was a photoconductive switch formed on a Cr-doped GaAs substrate. Although the physical dimensions of the coplanar lines were exactly matched, the large discontinuity in dielectric constants (ϵ_r (GaAs) = 12.3, ϵ_r (LiTaO₃) = 43), implies that a mode mismatch and reactive energy storage effects occur at the boundary [16].

Another approach to electrooptic sampling in LiTaO₃ relied on placing the electrooptic crystal in contact with (or close proximity to) the transmission line to be sampled [14], [17]. The sampling beam was passed through the crystal where fringing fields from the transmission line produced the phase retardation. Using this method, a sampling crystal can be positioned anywhere on a circuit where a measurement is to be made, thereby avoiding a hard-

Manuscript received July 16, 1985; revised September 19, 1985. This work was supported in part by the Air Force Office of Scientific Research and the Joint Services Electronics Program.

B. N. Kolner was with the Edward L. Ginzton Laboratory, Stanford University, Stanford, CA 94305. He is now with Hewlett-Packard Laboratories, Palo Alto, CA 94304.

D. M. Bloom is with the Edward L. Ginzton Laboratory, Stanford University, Stanford, CA 94305.

IEEE Log Number 8406315

0018-9197/86/0100-0079\$01.00 © 1986 IEEE

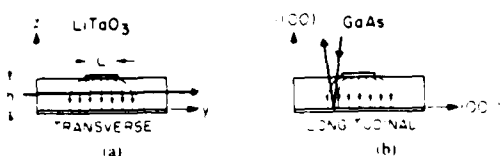


Fig. 1 Microstrip sampling geometries with indicated crystallographic axes

wired connection. In spite of the flexibility of this approach, the presence of the sampling crystal will cause a lumped dielectric loading of the transmission line resulting in waveform distortion, particularly at high frequencies.

The hybrid sampling techniques discussed to this point have all demonstrated remarkable performance, but in each case some perturbation of the device or circuit was required to make the measurement. The nature of these perturbations is such that they manifest themselves only at very high frequencies where electrooptic sampling shows its greatest advantage over all other time domain measurement techniques. So a new approach is called for.

The majority of high speed electronic and optoelectronic devices made today use the GaAs system. GaAs is a cubic crystal but does not possess a center of inversion symmetry, thus, it exhibits the linear electrooptic effect. This is rather fortuitous because it implies that electrooptic sampling measurements can be made *in situ* in the host material of the fastest electronic devices without the necessity of a hybrid connection to another electrooptic crystal.

To realize a measurement system based on this concept, two criteria must be satisfied. First, the conventional crystal orientations used in manufacturing devices and circuits must be compatible with the allowed directions for the electrooptic interactions. Fortunately, the industry standard wafer orientation is (100) and this lends itself to a very convenient sampling geometry where the probe beam enters the top side of the wafer and reflects off the ground plane below, interacting with only the [100] electric field component of the transmission line fringing fields [Fig. 1(b)]. Because the probe beam propagates along the electric field lines, we refer to this as the "longitudinal" sampling geometry. Second, sources of ultrashort optical pulses must be available in the wavelength region where GaAs is transparent. Recent advances in fiber/grating pulse compression techniques have resulted in the efficient compression of modelocked Nd:YAG pulses to < 5 ps [18]–[21]. At a wavelength of 1.06 μm , these pulses are below the band gap of GaAs and are well suited to electrooptic sampling.

Apart from its noninvasive character, the longitudinal sampling geometry has some unique advantages over its transverse counterpart. In the case of transverse sampling, the strength of the electrooptic interaction depends on the width and height of the transmission line. As L is increased or h decreased, a fixed voltage on the line will produce a larger sampling signal because the interaction distance and the electric field have increased. Thus, the

sampling signal strength depends on the transmission line impedance as well as the voltage on it. In the longitudinal GaAs case, increasing the height lowers the electric field for a fixed voltage, but the interaction distance increases and the two effects exactly cancel. Therefore, the strength of the sampling signal is independent of the transmission line impedance and, in fact, gives a measure of the absolute voltage at that point on the line. Of course, this is true to the extent that the fringing fields provide a phase retardation comparable to the maximum experienced directly beneath the top electrode. (In the initial experiments, there was evidence to indicate that this is the case.)

The principal advantage of the longitudinal geometry is the versatility of the probe. Because the beam interacts with fringing fields, virtually any point on a GaAs circuit can be probed, as long as there is an optically transparent path through the substrate adjacent to a conductor. This is especially useful in measuring complicated integrated circuits, such as monolithic microwave integrated circuits or MMIC's. These circuits are typically comprised of many active and passive elements on a common substrate with access to the input and output ports via a 50Ω transmission line system. Using the LiTaO_3 system, the sampling transmission line can be placed only at the input and output ports of the device and will not yield much useful information about the circuit's internal workings. Again, the transition between the two substrates (and possibly connectors) will introduce reflections. This, combined with the problem of transmission line dispersion would put the accuracy of the measurement in serious doubt. At best, a "black box" characterization of the circuit would be obtained.

In defense of the hybrid sampling approach, we would add that there is still much interest in high speed devices fabricated in silicon and this approach is useful for characterizing them to moderate frequencies.

III. ELECTROOPTIC SAMPLING: PRINCIPLE AND RESOLUTION LIMITATIONS

In order to utilize ultrashort light pulses to make electrical measurements, a mechanism for the interaction between optical and radio frequency fields is required. This mechanism is provided by the electrooptic effect and is covered extensively in the literature [22], [23]. Briefly, the electrooptic effect is the change in the optical index of refraction in an anisotropic crystal caused by a dc or slowly varying electrical field. An optical beam passing through the crystal experiences a phase shift between two orthogonal polarization components which can then be converted to an amplitude variation by passage through a polarizer. The whole assembly constitutes a Pockels cell light modulator and it is the key element in any electrooptic sampling system.

In this section, we examine the principle of operation of an electrooptic sampling system using microstrip transmission lines and transverse optical probe beams as a model. The results are completely general and apply to all sampling systems whether based in LiTaO_3 or GaAs.

The transfer function of a Pockels cell relates the trans-

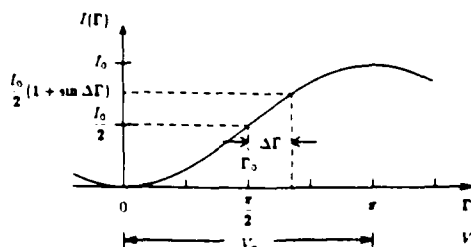


Fig. 2. Light intensity versus net phase retardation Γ or applied voltage V for a Pockels cell light modulator. Static retardation Γ_0 shown at quarter-wave bias point with signal term $\Delta\Gamma$ as a perturbation

mitted light intensity to the applied voltage and is given by

$$I = I_0 \sin^2 \left(\frac{\Gamma_0 + \Delta\Gamma}{2} \right) \quad (1)$$

where Γ_0 is the static phase retardation and $\Delta\Gamma$ is the additional retardation induced by the applied electric field (Fig. 2). The static phase retardation plays an important role as the operating point or "bias point." In order to maintain the most linear relationship between the applied voltage and the transmitted light intensity, the modulator must be biased such that $\Gamma_0 = \pi/2$. This point is usually referred to as the *quarter-wave* bias point because it corresponds to a net quarter wave of phase shift between the two polarization components of the optical beam. The voltage required to switch the modulator from the "off" to the "on" state is similarly known as the *half-wave* switching voltage (V_s) and corresponds to a total retardation of π radians. Thus, at the quarter-wave bias point, we can write (1) as

$$I = \frac{I_0}{2} (1 + \sin \Delta\Gamma) = \frac{I_0}{2} \left(1 + \sin \pi \frac{V}{V_s} \right) \quad (2)$$

The basic components of an electrooptic sampling system are illustrated in Fig. 3. In this arrangement, the impulse response of a high speed GaAs Schottky photodiode is to be measured. The photodiode has been connected to a microstrip transmission line deposited on an electrooptic crystal which, together with a polarizer and orthogonally oriented analyzer, constitutes the Pockels cell light modulator. A train of picosecond optical pulses from a mode-locked laser is split into three beams with the first beam incident on a scanning autocorrelator used for laser diagnostics. The second, lower beam is used to illuminate the photodiode under test which injects a current pulse onto the transmission line with each optical pulse. If the duration of the optical pulse is short compared to the impulse response of the photodiode, then the propagating electric field represents the photodiode impulse response. A high frequency electrooptic modulator has been included in the excitation path to put modulation sidebands on the photocurrent so that a narrow-band receiver can be used to improve the signal-to-noise ratio (Section IV). The remaining pulses in the upper beam are routed through a delay leg so that when they arrive at the transmission line,

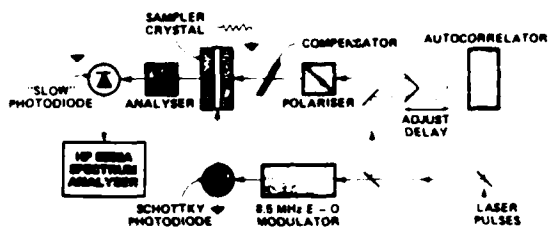


Fig. 3. Schematic diagram of the electrooptic sampling system used to characterize high speed GaAs photodiodes

they will exactly coincide with the photocurrent waveform produced by a replica of that same pulse. As each pulse passes through the electric field beneath the line, it interacts with a small portion of the photocurrent waveform and experiences a modulation proportional to the amplitude of the field there. For a fixed path delay between the two beams, the pulses "sample" only one portion of the waveform and thus the average power in the sampling beam is constant. Now, if the delay is adjusted so that the sampling beam path is slightly longer, then the sampling pulses will arrive at the transmission line a little later and interact with a later portion of the photocurrent waveform. As a result, the average power in the sampling beam will be different, representative of the magnitude of the photocurrent at that later point in time. By adjusting the relative path lengths between the excitation and sampling beams, the equivalent impulse response of the high speed photodiode is mapped out in terms of the average sampling beam power exiting the Pockels cell.

Adjustment of the relative path delay can be accomplished in several ways. The most common method is to mount a cube-corner reflector on a mechanically driven stage and route either beam through it. An alternative approach is to use a spinning prism assembly in which the beams are refracted through varying path lengths. This, however, requires a greater length of glass, producing dispersion as well as linearity problems. Another solution is to use two picosecond light sources running at slightly different pulse rates. The sampling pulses constantly "walk" through the excitation pulses and no moving parts are required. Regardless of the approach, the rate at which the measured waveform is acquired determines the bandwidth presented at the sampler output. As we will see, most of the system noise contributions have uniform power spectral densities, thus narrower bandwidths and slower scan rates give higher signal-to-noise ratios.

Fig. 4 shows a detailed view of the interaction between the propagating microwave field $E(x, y, z, t)$ and the optical sampling pulse $I(x, y, z, t)$. In this diagram, a microstrip transmission line supports a $+y$ -propagating electric field interacting with a $+x$ -propagating sampling pulse. A variable time delay τ is included in the arrival time of the sampling pulse. The output signal intensity $I_{\text{sig}}(t, \tau)$ represents the sampling pulse profile after being affected by the field-induced phase retardation. When there is no overlap between the fields, $I_{\text{sig}}(t, \tau) = 0$. Since the slow photodiode measuring the sampling beam power can-

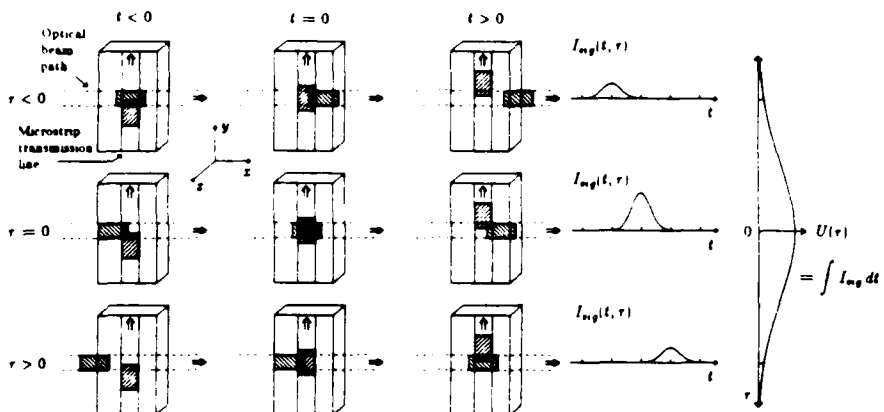


Fig. 4. Interaction between electrical fields and optical sampling pulses in the electrooptic sampler. Sampling pulses propagating in the $+z$ direction accumulate phase retardation by interaction with $+z$ propagating electric fields. Output signal intensity $I_{sg}(t, \tau)$ is proportional to the overlap of the fields and is thus a function of the relative time delay τ . As τ varies from zero, the pulses overlap less and contribute less to $I_{sg}(t, \tau)$. The pulse energy $U(\tau)$ is proportional to the area under $I_{sg}(t, \tau)$ and thus depends on τ in the same way.

not respond to the instantaneous power waveform, we integrate $I_{sg}(t, \tau)$ to find the energy $U(\tau)$ in the sampling pulse which is then a measure of the average beam power. The function $U(\tau)$ describes the net energy in a sampling pulse that is affected by the electro-optic interaction in the sampling crystal. It is proportional to the cross-correlation between the electrical and optical fields and can be written as [24]

$$U(\tau) = \iiint_{-\infty}^{\infty} A(n_x, n_y, n_z, r_{ik}) I(x - v_t(t - \tau), y, z) \cdot E(x, y - v_s t, z) dx dy dz dt \quad (3)$$

where $A(n_x, n_y, n_z, r_{ik})$ is a coefficient containing information about the indexes of refraction and the electrooptic tensor r_{ik} .

Because of the finite sizes of the field distributions, the transit times associated with their interaction limit the impulse response of the electrooptic sampling system. These transit time effects can be quantified by considering each one separately and assuming that the others temporarily play no role.

4. Optical Transit Time Effect

In the time interval required for a sampling pulse to propagate across a transmission line, the electric field waveform also propagates down the line. Rather than sampling a fixed point on the waveform, the optical pulse measures an average of the waveform over that interval. To see how this affects the impulse response, assume that the waveform is a propagating impulse function and the optical beam diameter is negligible. Then, the sampling pulse would experience uniform retardation while interacting with the waveform and no retardation otherwise,

resulting in a "rectangular" impulse response for the sampling system. We refer to this impulse response degradation as the *optical transit time effect* (OTT) and model it mathematically in (3) by using appropriate descriptions for the optical and electrical fields. Successively applying the sifting property to (3) yields the impulse response (neglecting constants)

$$U(\tau)_{OTT} = E_s(-v_t \tau, 0, 0) \quad (4)$$

where v_t is the propagation velocity (c/n) of the sampling pulse. Thus, the sampled response maps out the τ -profile of the electric field as a function of the time delay τ . If we approximate the electric field as being entirely contained under the transmission line (i.e., no fringing fields), then

$$U(\tau)_{OTT} = \text{rect} \left(\tau \frac{v_t}{L} \right) = \text{rect} \left(\tau \frac{c}{nL} \right) \quad (5)$$

is the impulse response where the "rect" function is defined as

$$\text{rect}(\tau) = \begin{cases} 1 & |\tau| \leq \frac{1}{2} \\ 0 & |\tau| > \frac{1}{2} \end{cases} \quad (6)$$

The full width at half maximum (FWHM) of this response is easily seen to be

$$\Delta\tau_{OTT} = \frac{nL}{c} \quad (7)$$

Since the Fourier transform of the rect(τ) function is $\sin(\pi f)/\pi f$, the system frequency response has a -3 dB bandwidth of

$$f_{-3\text{dBOTT}} = 0.443 \frac{c}{nL} \quad (8)$$

where nL/c is the optical transit time through the transmission line electric field.

B. Electrical Transit Time Effect

The OTT accounted for the degradation of the impulse response due to the sampling beam propagating across the width of the transmission line and the resultant impulse response was calculated by assuming that all fields had infinitesimal spatial and temporal extent except for the width of the transmission line field. The *electrical transit time effect* (ETT) accounts for the degradation of the impulse response due to the electrical waveform propagating across the radial profile of the sampling beam. In order to calculate the ETT, we assume that all fields are infinitesimal except for the radial profile of the sampling beam. From (3) the impulse response becomes

$$U(\tau)_{\text{ETT}} = I(0, v, \tau, 0). \quad (9)$$

This time, the beam waist profile in the y direction is mapped as a function of the time delay τ . If we assume a lowest order Gaussian mode with spot size $2w$, the impulse response can be written

$$U(\tau)_{\text{ETT}} = \exp\left(-\frac{2c^2}{\epsilon_{\text{eff}} w^2} \tau^2\right) \quad (10)$$

where ϵ_{eff} is the effective dielectric constant of the transmission line. The pulse width at half maximum is

$$\Delta\tau_{\text{ETT}} = \frac{w}{c} \sqrt{2 \ln 2 \epsilon_{\text{eff}}} \quad (11)$$

and, by applying a Fourier transform, we obtain a Gaussian frequency response with -3 dB bandwidth

$$f_{-3\text{dB}_{\text{ETT}}} = \sqrt{\frac{\ln 2}{\epsilon_{\text{eff}} \pi w}} \frac{c}{\pi w}. \quad (12)$$

C. Optical Pulsewidth Limit

The effect of using a finite time width sampling pulse on the system resolution is intuitively obvious. The time duration of the sampling pulse is a finite "window" through which all field measurements are made. Again, if we assume all dimensions shrink to infinitesimal values and apply the sifting property to (3), the impulse response due to a finite optical pulsewidth (OPW) is

$$U(\tau)_{\text{OPW}} = I(-v, \tau, 0, 0). \quad (13)$$

As expected, the optical envelope is mapped out via the time delay τ . For a Gaussian time waveform with pulsewidth τ_0 (FWHM) the impulse response is

$$U(\tau)_{\text{OPW}} = \exp(-4 \ln 2 (\tau/\tau_0)^2). \quad (14)$$

Transformation to the frequency domain yields a system bandwidth of

$$f_{-3\text{dB}_{\text{OPW}}} = \frac{0.441}{\tau_0} \quad (15)$$

There is an interesting consequence of using the same

laser pulse to drive the photodiode as well as to measure its response. We saw that the sampling system impulse response was a cross correlation between the spatial profiles of the traveling electric fields and the sampling optical fields. When the transmission line is driven by a photodiode, the voltage on the line is the convolution between the excitation pulse $I(t)$ and the photodiode impulse response $h(t)$. Thus, we can write the sampler output signal as

$$V(t) = I(t) \star [I(t) * h(t)] \quad (16)$$

where \star indicates cross correlation and $*$ indicates convolution. Since the operations of convolution and correlation are associative [25], we can rewrite (16) as

$$V(t) = [I(t) \star I(t)] * h(t). \quad (17)$$

Hence, we find that the system response is given by the convolution of the autocorrelation function of the laser pulse $[I(t) \star I(t)]$ with the photodiode impulse response. Since we have an independent method of measuring the autocorrelation function using second harmonic generation [26], we can deconvolve the contribution of the optical pulse width. The deconvolution can easily be carried out using Fourier transform techniques; however, noise will be introduced into the calculation at very high frequencies where both the measured waveform spectrum and the autocorrelation spectrum have rolled off considerably

D. Practical Resolution Limitations

We can now calculate the transit times in the sampling system for a typical microstrip transmission line on a GaAs MMIC. Using the parameters

$$\begin{aligned} h &= 100 \mu\text{m} && \text{(substrate thickness)} \\ w &= 5 \mu\text{m} && \text{(beam radius)} \\ n &= 3.5 && \text{(optical index)} \\ \epsilon_{\text{eff}} &= 9 && \text{(effective dielectric constant)} \end{aligned} \quad (18)$$

we obtain the following resolution limits:

$$\begin{aligned} \Delta\tau_{\text{OTT}} &= 2.3 \text{ ps} & f_{-3\text{dB}_{\text{OTT}}} &= 190 \text{ GHz} \\ \Delta\tau_{\text{ETT}} &= 60 \text{ fs} & f_{-3\text{dB}_{\text{ETT}}} &= 5.3 \text{ THz.} \end{aligned} \quad (19)$$

The optical transit time effect dominates because of the high index of GaAs and the double pass through the substrate.

In principle, there is a way to reduce or eliminate the transit time effects. If a component of the microwave group velocity can be matched with a similar component of the sampling beam, at least one of the transit times can be eliminated [8]. In Fig. 4, if we tilt the sampling beam with respect to the transmission line, the y -component of the group velocities can be matched and the optical transit time effect disappears. This technique is effective in the transverse LiTaO_3 sampler but in GaAs the microwave and optical velocities are nearly the same and the sampling beam would have to be tilted below the critical angle, thus pre-

cluding the use of the top-side sampling geometry of Fig. 1(b).

IV. VOLTAGE SENSITIVITY AND NOISE ISSUES

4. Minimum Detectable Voltage and Signal-to-Noise Ratio

The minimum detectable voltage on the electrooptic transmission line corresponds to the voltage that will produce a signal in the receiver equal to the sum of all the noise contributions. The three principal sources of noise are laser shot noise, Johnson noise, and excess laser noise. By "excess laser noise," we mean all phase and amplitude noise arising from gain or cavity length fluctuations in the laser. These noise contributions are present in the "slow" photodiode that detects the average power in the sampling beam and because they are uncorrelated, they add on a mean-square or power basis. Thus, if we consider the noise in terms of mean-square current spectral densities, we can write the total receiver noise as

$$\bar{I}_N = \bar{I}_{N_{\text{shot}}} + \bar{I}_{N_{\text{J}}} + \bar{I}_{N_{\text{ex}}}$$
 (20)

where

$$\begin{aligned} \bar{I}_{N_{\text{shot}}} &= 2qI_{\text{avg}} & \text{A}^2 \text{Hz shot noise} \\ \bar{I}_{N_{\text{J}}} &= 4kT R_L & \text{A}^2 \text{Hz Johnson noise} \\ \bar{I}_{N_{\text{ex}}} &= \text{characteristic of laser} & \text{A}^2 \text{Hz excess noise} \end{aligned}$$
 (21)

and

I_{avg} = average photodiode current

$$R_L = \text{photodiode load resistor.}$$
 (22)

The shot noise and Johnson noise will always be present to some degree, but the effect of the excess laser noise can be reduced or practically eliminated by suitable modulation of the signal propagating on the transmission line. This adds a modulation component to the sampling beam as it passes through the transmission line. If the modulation frequency is chosen to be outside the excess noise spectrum, a narrow-band receiver can be tuned to this frequency to select the transmission line signal out of the total sampling beam photocurrent.

The frequency spectrum of excess laser noise can be observed directly with a photodiode and RF spectrum analyzer. A typical spectrum from a synchronously-pumped, mode-locked dye laser is shown in Fig. 5. The lower trace is the noise floor of the spectrum analyzer. We see that the excess noise spectrum has diminished to the level of the noise floor by about 5 MHz. Conventional lock-in receiver techniques usually employ mechanical chopping wheels resulting in modulation frequencies of a few kilohertz. From Fig. 5 we see that there is a substantial amount of noise at these low frequencies and that by chopping above ≈ 5 MHz, a 50 dB signal-to-noise improvement is obtained. This is easily accomplished by using an acousto-optic or electrooptic modulator in the beam path to the device under test.

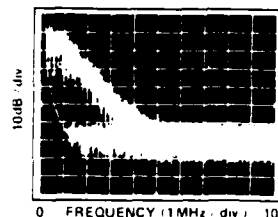


Fig. 5. Noise spectrum of a synchronously pumped mode-locked dye laser recorded with a photodiode and RF spectrum analyzer. Beam blocked in lower trace

Assuming that the excess noise can be neglected, we can calculate the signal-to-noise ratio (S/N) and derive the minimum detectable voltage. For a photodiode connected to a load resistor R_L , the signal power dissipated is

$$P_{\text{sig}} = \bar{I}_{\text{avg}}^2 R_L$$
 (23)

and the total noise power is

$$P_{\text{noise}} = (\bar{I}_{N_{\text{shot}}} + \bar{I}_{N_{\text{J}}}) BR_L$$
 (24)

$$P_{\text{noise}} = 2qI_{\text{avg}}BR_L + 4kTB$$
 (25)

where B is the receiver bandwidth. Thus, we can write the signal-to-noise ratio as

$$S/N = \frac{P_{\text{sig}}}{P_{\text{noise}}} = \frac{\bar{I}_{\text{avg}}^2 R_L}{2qI_{\text{avg}}BR_L + 4kTB}$$
 (26)

From (26), we see that when the Johnson noise term dominates the total noise power, S/N varies as \bar{I}_{avg}^2 while when the shot noise dominates, S/N varies only linearly. Therefore, I_{avg} and R_L should be chosen so that the shot noise dominates.

Next, we derive expressions for \bar{I}_{avg} and I_{avg} based on the form of the signal on the transmission line. The total optical intensity I passing through an electrooptic modulator was shown to be

$$I = I_0 \sin^2 \left(\frac{\Gamma_0 + \Delta\Gamma}{2} \right) = \frac{I_0}{2} (1 - \cos(\Gamma_0 + \Delta\Gamma))$$
 (27)

where I_0 is the intensity incident on the electrooptic crystal. Applying a trigonometric identity and assuming that $\Delta\Gamma \ll 1$, (27) can be rewritten as

$$I = \frac{I_0}{2} [1 - \cos \Gamma_0 + \Delta\Gamma \sin \Gamma_0].$$
 (28)

Using this beam to illuminate the receiver photodiode will produce a total photocurrent given by

$$I_{\text{total}} = \frac{I_0}{2} [1 - \cos \Gamma_0 + \Delta\Gamma \sin \Gamma_0]$$
 (29)

where I_0 is the maximum photodiode current for a given beam intensity I_0 .

When the transmission line is driven by a light modulated optoelectronic device, the voltage on the line is given by

$$V(t) = V_0 \left(1 - m \sin^2 \frac{\omega_m}{2} t \right)$$
 (30)

where, for convenience, we assume the device produces a sinusoidal signal at a frequency ω_m . V_0 is the peak voltage on the line and m is the modulation index. Notice that this is an asymmetrical driving function; the deviation from static retardation

$$\Delta\Gamma = \pi \frac{V(t)}{V_r} \quad (31)$$

is positive only.

Combining (29)–(31) we can write the total photocurrent as

$$i_{\text{total}} = \frac{i_0}{2} \left[1 - \cos \Gamma_0 + \pi \frac{V_0}{V_r} \left(1 - m \sin^2 \frac{\omega_m t}{2} \right) \sin \Gamma_0 \right]. \quad (32)$$

By expanding the \sin^2 term, we can separate out the average term and the time varying term since they contribute to the received noise power and signal power, respectively.

$$i_{\text{avg}} = \frac{i_0}{2} \left[1 - \cos \Gamma_0 + \pi \frac{V_0}{V_r} \left(1 - \frac{m}{2} \right) \sin \Gamma_0 \right] \quad (33)$$

$$i_{\text{sig}} = m \frac{i_0}{4} \pi \frac{V_0}{V_r} \cos \omega_m t \sin \Gamma_0. \quad (34)$$

If we assume that the modulation index is maximum ($m = 1$), then the mean-square shot noise current density is

$$\overline{i_{\text{SV}}^2} = 2q i_{\text{avg}} = q i_0 \left(1 - \cos \Gamma_0 + \frac{\pi}{2} \frac{V_0}{V_r} \sin \Gamma_0 \right) \quad (35)$$

and the mean-square signal current is

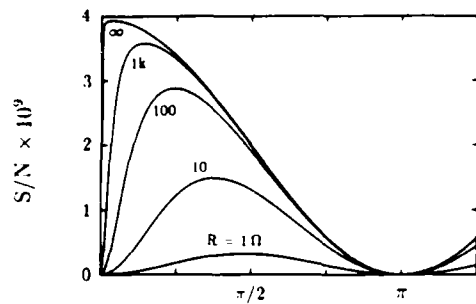
$$\overline{i_{\text{sig}}^2} = \frac{i_0^2}{32} \left(\frac{\pi V_0}{V_r} \right)^2 \sin^2 \Gamma_0. \quad (36)$$

We can now write the signal-to-noise ratio as

$$S/N = \frac{i_0^2}{32qB} \left(\frac{\pi V_0}{V_r} \right)^2 \frac{\sin^2 \Gamma_0}{i_0 \left(1 - \cos \Gamma_0 + \frac{\pi}{2} \frac{V_0}{V_r} \sin \Gamma_0 \right) + 4kT/qR_L} \quad (37)$$

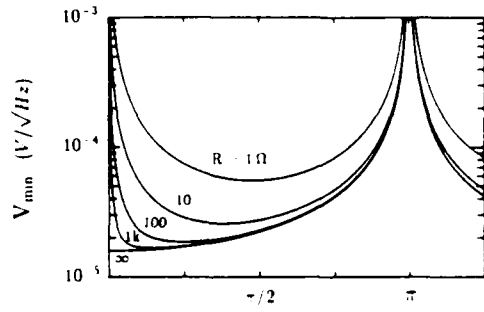
We have purposely left the static retardation Γ_0 as a free parameter in this equation so that we may study its effect on the signal-to-noise ratio [27]. Fig. 6 displays (37) plotted as a function of Γ_0 with various values of R_L from 1Ω to $10K \Omega$ including $R_L \rightarrow \infty$. We see that when shot noise dominates ($R_L \rightarrow \infty$), the signal-to-noise ratio improves by a factor of two as $\Gamma_0 \rightarrow 0$ compared to operating at the quarter-wave bias point $\Gamma_0 = \pi/2$. However, as Γ_0 is reduced, so is the signal. If a finite load resistance is included, at some point the Johnson noise will be comparable with the signal and the signal-to-noise ratio will reduce as Γ_0 is reduced. This trend is evident in Fig. 6.

The factor $\pi V_0/2V_r \sin \Gamma_0$ in the denominator of (37)



STATIC RETARDATION Γ_0

Fig. 6. Signal-to-noise ratio versus static phase retardation Γ_0 for various photodiode load resistances. Curves are drawn for GaAs assuming $V_0 = 1$ on the transmission line, a maximum receiver photocurrent of 20 mA and a bandwidth of 1 Hz .



STATIC RETARDATION Γ_0

Fig. 7. Minimum detectable voltage V_{min} versus static retardation Γ_0 for the same load resistances as in Fig. 6. Curves are drawn for GaAs assuming a maximum receiver photocurrent of 20 mA and a bandwidth of 1 Hz .

arises as a contribution to the average current (and hence the shot noise) because of the asymmetrical modulation of the transmission line waveform (i.e., the voltage on the transmission line is always positive so the average optical power is increased). The magnitude of this term is only significant for very large values of V_0/V_r ($\geq 10^{-3}$) and then it only makes a difference for very small values of Γ_0 . Calculations show that when V_0/V_r is increased from 10^{-4} to 10^{-1} , the coefficient to the right of $(V_0/V_r)^2$ in (37) is reduced by half. However, the total signal-to-noise ratio has increased by 0.5×10^6 and, hence, this effect can be neglected (recall that for typical signals, $V_0 \ll V_r$).

With this approximation in mind, we set (37) equal to one and solve for voltage V_{min} which represents the minimum detectable voltage (normalized to 1 Hz bandwidth).

$$V_{\text{min}} = \frac{8}{i_0} \frac{V_r}{\pi} \sqrt{q} \frac{i_0 \sin^2 \Gamma_0/2 + 2kT/qR_L}{\sin^2 \Gamma_0} \quad V/\sqrt{\text{Hz}}. \quad (38)$$

It is interesting to explore the variation in the minimum detectable voltage with Γ_0 . This is presented in Fig. 7 where V_{min} is plotted versus Γ_0 for the same load resis-

tances as in Fig. 6. As expected, the minimum detectable voltage decreases at the same points where the signal-to-noise ratio improves.

Equation (38) can be simplified if we assume shot noise limited operation at the quarter-wave bias point. Then, $\Gamma_0 = \pi/2$, $i_0 = 2i_{avg}$ and the Johnson noise term is eliminated leaving

$$V_{min} = 4 \frac{V_s}{\pi} \sqrt{\frac{q}{i_{avg}}} \quad V/\sqrt{Hz} \quad (39)$$

For a microstrip transmission line on GaAs ($V_s = 4.4$ kV) with an average receiver photocurrent of 10 mA, we find

$$V_{min} = 22 \mu V/\sqrt{Hz}$$

B. Dynamic Range

The minimum detectable voltage represents the lower bound to the system sensitivity. As the signal voltage is increased from V_{min} , the \sin^2 dependence of the output will eventually result in a deviation from a linear response. This puts a limit on the maximum applied voltage V and thus the dynamic range can be defined as the ratio of these two extrema.

$$\text{dynamic range} = 20 \log \frac{V}{V_{min}} \text{ dB} \quad (40)$$

The limit on V is somewhat arbitrary and depends on the amount of nonlinearity that can be tolerated. By combining some of the previous equations we can get an idea of what range of V/V_{min} will produce a given deviation from linearity and, thus, characterize the dynamic range of the electrooptic sampler.

Let us define the "fractional deviation from linearity" as

$$d^* = \left| \frac{P_{lin} - P_{act}}{P_{act}} \right| \quad (41)$$

where P_{act} is the *actual* output power given by

$$P_{act} = P_0 \sin^2 \left(\frac{\Gamma_0}{2} + \frac{\pi V}{2V_s} \right) \quad (42)$$

and P_{lin} is the small signal linear response

$$P_{lin} = \frac{P_0}{2} \left[1 - \cos \Gamma_0 + \pi \frac{V}{V_s} \sin \Gamma_0 \right] \quad (43)$$

Equation (41) is plotted in Fig. 8 for several values of Γ_0 from $\pi/64$ to $\pi/2$. Earlier, it was stated that operating at the quarter-wave bias point was desirable from the standpoint of linearity. This is certainly apparent from the figure where curve (d), corresponding to quarter-wave bias, indicates that a dynamic range of 140 dB results in less than 1 percent deviation from linearity. However, it is interesting to see that even by lowering the operating point to $\Gamma_0 = \pi/64$, a dynamic range of > 100 dB can be achieved for 1 percent nonlinearity (provided that shot noise limited operation is maintained).

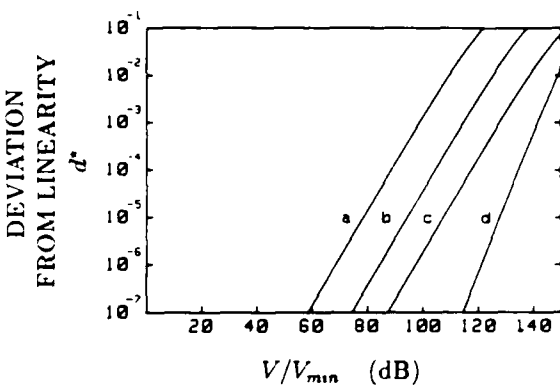


Fig. 8. Deviation from linear response d^* plotted as a function of the system dynamic range V/V_{min} where V is the signal voltage being measured. Curves are shown for 4 values of static retardation: (a) $\Gamma_0 = \pi/64$, (b) $\Gamma_0 = \pi/16$, (c) $\Gamma_0 = \pi/4$, (d) $\Gamma_0 = \pi/2$.

C. Optical Rectification

The linear electrooptic effect causes a change in the polarization field of a propagating wave in a dielectric when a dc or slowly varying electric field is applied to the dielectric. The inverse electrooptic effect, on the other hand, produces a dc polarization field in a dielectric when an optical wave passes through it. The magnitude of the polarization is proportional to the instantaneous power density of the optical field and the effect is called "optical rectification."

In the electrooptic sampler, the picosecond sampling pulses will generate a polarization field due to optical rectification and the resulting induced voltage may interfere with the signal being measured. We can make an estimate of the strength of the optical rectification signal by assuming that the area of the crystal illuminated by the sampling beam acts as a transient voltage source V_0 with a series capacitance C . Since the induced voltage waveform propagates in both directions on the transmission line, the source sees a resistance $R = Z_0/2$ where Z_0 is the characteristic impedance of the line. The voltage V_0 that appears on the transmission line thus satisfies the differential equation

$$\frac{dV_0}{dt} + \frac{1}{RC} V_0 = \frac{dV_1}{dt} \quad (44)$$

which has the general solution

$$V_0 = e^{-i\omega RC} \left[\int e^{i\omega RC} \frac{dV_1}{dt} dt + \text{constant} \right]. \quad (45)$$

Next, we need to relate the source voltage V_0 to the optically induced polarization P_{VL} . It can be shown that when the optical beam fills the width of a capacitor loaded with an optically nonlinear dielectric, the voltage at the plates is given by [28], [29],

$$V_0 = P_{VL} \frac{d}{\epsilon} \quad (46)$$

where d is the beam diameter and ϵ is the dielectric permittivity. In our sampling geometry where the probe beam enters through the top of the (100) grown GaAs wafer and reflects off the ground plane, d is replaced by the substrate thickness h and (46) becomes

$$V(t) = \frac{n^3 r_{41} h}{\epsilon c} I(t) \quad (47)$$

where $I(t)$ is the intensity envelope of the sampling pulse. For simplicity, we assume $I(t)$ is triangular in shape with pulsedwidth τ and peak value I_0 . Solving (45) with (47) as the driving function results in a peak voltage

$$V_0(0) = \frac{n^3 r_{41} h}{\epsilon c} I_0 \frac{RC}{\tau} [1 - \exp(-\tau/RC)] \quad (48)$$

appearing on the transmission line. Thus, using the following parameters appropriate for a 100 μm thick GaAs MMIC

$$r_{41} = 1.2 \times 10^{-12} \text{ m/V}$$

$$n = 3.44$$

$$d = 10 \mu\text{m}$$

$$\epsilon = 12.3 \times \epsilon_0$$

$$I_0 = 6.4 \times 10^7 \text{ W/cm}^2$$

$$RC = 2.1 \text{ fs}$$

$$\tau = 5 \text{ ps}$$

$$h = 100 \mu\text{m}$$

we calculate a peak voltage of

$$V_0(0) = 41 \mu\text{V}.$$

This is very small compared to typical voltages to be measured in the electrooptic sampler, yet it is comparable to the minimum detectable voltage in a 1 Hz receiver bandwidth. It is interesting to note that this signal is being produced at the same rate as the sampling pulses and if the waveform being measured has a chopping-frequency component, then the optical rectification signal will never be detected.

In spite of the weak effect, optical rectification from femtosecond pulses is currently being investigated as a source of far-infrared radiation for transient spectroscopy in a series of elegant experiments by Auston *et al.* [30] and Cheung and Auston [31].

V. ELECTROOPTIC SAMPLING IN GaAs

A. Electrooptic Effect in GaAs

Gallium arsenide belongs to the cubic zincblende group with crystal symmetry $43m$. The electrooptic tensor for this group has the form

$$r_{mk} = \begin{pmatrix} 0 & 0 & 0 \\ 0 & 0 & 0 \\ 0 & 0 & 0 \\ r_{41} & 0 & 0 \\ 0 & r_{41} & 0 \\ 0 & 0 & r_{41} \end{pmatrix} \quad (49)$$

When an electric field is applied to the crystal, a birefringence is induced and the initially spherical index ellipsoid is distorted. The intersection of the index ellipsoid and a plane normal to the direction of optical propagation defines an ellipse whose major and minor axes give the allowed polarization directions and the associated indices of refraction. For GaAs, the ellipsoid is described by

$$\frac{x^2 + y^2 + z^2}{n_0^2} + 2r_{41}(E_{x,y}z + E_{y,x}z + E_{x,y}y) = 1 \quad (50)$$

where x , y , and z are parallel to the crystallographic axes [100], [010], and [001], respectively.

The most common orientation for GaAs wafers in the integrated circuits industry is (100) (i.e., the normal to the wafer surface is in the [100] direction) [32]. Since the most convenient geometry for optical probing is one in which the beam enters the wafer normal to its surface, we investigate the index ellipse for [100] propagation. In the $x = 0$ plane, we have

$$\frac{y^2 + z^2}{n_0^2} + 2r_{41}E_{x,y}z = 1 \quad (51)$$

which has principal axes y' and z' at 45° with respect to y and z and corresponding indexes [33]

$$n_y' = n_0 + \frac{1}{2} n_0^3 r_{41} E_x$$

$$n_z' = n_0 - \frac{1}{2} n_0^3 r_{41} E_x. \quad (52)$$

Note that for light incident along x , only the x component of the applied electric field contributes to the induced birefringence. Thus, for an arbitrary electric field distribution in a (100) wafer of GaAs, the single pass phase retardation is given by

$$\Gamma = \frac{2\pi}{\lambda} n_0^3 r_{41} V_{12} \quad (53)$$

where V_{12} is the potential difference between the front and back side of the wafer. For the microstrip transmission line geometry of Fig. 1(b), a focused beam of light which enters the GaAs wafer at a point adjacent to the top conductor and reflects from the ground plane experiences a round trip retardation of

$$\Gamma = \frac{4\pi}{\lambda} n_0^3 r_{41} V \quad (54)$$

where V is the potential of the top conductor.

For light propagating along x , the result of (53) is com-

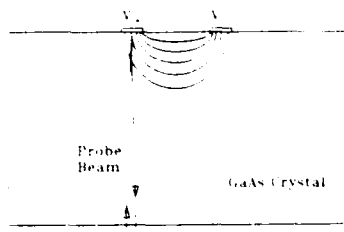


Fig. 9. Backside electrooptic sampling geometry

TABLE I
COMPARISON OF GaAs TO LiTaO₃ FOR THE MICROSTRIP SAMPLING GEOMETRIES OF FIG. 1

	GaAs	LiTaO ₃
Electro-optic figure of merit	$n^3 r_{31} = 60$	$n^3 r_{33} - n^3 r_{13} = 229$
Half-wave voltage V_z	4.4 kV	4.63 (h/L) kV
Minimum detectable voltage	22 μ V/ \sqrt{Hz}	188 μ V/ \sqrt{Hz}

$\lambda = 1.06 \mu m$, $Z_0 = 50 \Omega$, $I_{ss} = 10 \text{ mA}$

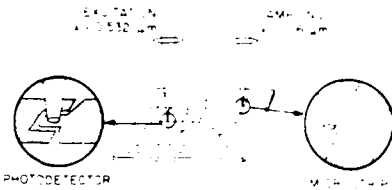
pletely general. The phase retardation sensed by the laser beam is proportional to V_z , regardless of the electric field distribution. Recently, Freeman *et al.* [34] have used this fact to probe a GaAs digital integrated circuit using a novel backside probing geometry (Fig. 9).

B. Comparison of Sensitivities: GaAs Versus LiTaO₃

Let us define a figure of merit for the electrooptic modulator as a basis for comparing the magnitude of the physical effect. We know that the net phase retardation depends on the electric field and a coefficient containing the indexes of refraction and the electrooptic tensor. In Table I we list the coefficients for GaAs and LiTaO₃ as the "electrooptic figure of merit." They have been calculated assuming a wavelength of 1.06 μm . We see that the value for LiTaO₃ is almost a factor of four larger than that for GaAs. If we calculate the half-wave voltages V_z , we see that in the case of LiTaO₃, V_z depends on the ratio h/L and for GaAs, the value is fixed. Finally, since the minimum detectable voltage depends on V_z , GaAs is almost an order of magnitude more sensitive because for a 50 Ω transmission line on LiTaO₃, $h/L \approx 0.1$. Thus, although LiTaO₃ transverse sampling appears at the outset to be the stronger of the two, its dependence on the line impedance makes longitudinal sampling in GaAs the more sensitive approach.

C. Optical Sources

A key element in any electrooptic sampling system is a continuous train of ultrashort optical pulses. The state of the art in ultrashort pulse generation in the visible part of the spectrum has come a long way in the last decade mainly due to advances in mode-locked ring dye lasers [35], [36]. For electrooptic sampling in GaAs, the wavelength of the sampling beam must be long enough so that

Fig. 10. Optical excitation of a GaAs integrated circuit using frequency-doubled pulses from the 1.06 μm sampling beam

the photon energy is below the bandgap, assuring transparency of the semiconductor to the beam. This occurs at about 900 nm. Unfortunately, sources of ultrashort pulses beyond 900 nm are not nearly as developed as their visible counterparts. Mode-locked Nd: glass lasers produce bursts of Q -switched pulses at 1.06 μm with picosecond duration but there is no correlation between pulses from different bursts. Mode-locked color-center lasers have the advantage of tunability and high average power output [37], but the stability of the color-center crystals is not good and the laser must be synchronously pumped by another mode-locked laser.

Continuous-wave mode-locked Nd: YAG lasers, on the other hand, are commercially available and very reliable. They can produce average powers up to 10 W at pulse rates of 100 MHz. The disadvantage of these lasers is the pulselwidth: typically 80 ps. One of the techniques that helped the development of ultrashort pulse sources in the visible was pulse compression by means of single-mode fibers and diffraction grating delay lines, pioneered by Grischkowsky [38]–[42]. This technique uses self-phase modulation in single-mode fibers to spectrally broaden and chirp a pulse as it propagates through the fiber. The pulse is then passed through a pair of diffraction gratings which act as a matched filter and compress the new frequency components [43]. We have successfully applied this technique to the compression of the rather long Nd: YAG pulses and have obtained 1.8 ps pulses at an 82 MHz rate with an average power of 500 mW [18], [19]. The shapes of these pulses are not entirely optimum, however, owing to the nonlinear frequency chirp on the wings of the pulses exiting the fiber. By spectrally filtering these frequency components, Heritage *et al.* have demonstrated a significant improvement in the shapes of the compressed Nd: YAG pulses [20].

In previous electrooptic sampling systems using visible pulses, a source of radiation for exciting photodiodes or other optoelectronic devices was always available. In the GaAs sampler, the wavelength was chosen specifically to avoid the generation of charge carriers and, hence, the pulses cannot be used to directly excite semiconductor devices. However, because of the very high peak powers involved, the pulses can be efficiently frequency doubled in KTP or other suitable crystals. The result is a pair of synchronized pulse trains, one above and one below the bandgap. Photodetectors can then be incorporated on a GaAs integrated circuit and driven by the second harmonic beam acting as electrical impulse generators to drive the rest of the circuit which can then be probed by the fundamental

beam (Fig. 10). Because the excitation pulses were derived from the sampling beam, this method is free from timing jitter.

D. Experimental Results

1) *GaAs Reflectance Modulator*: The first step toward demonstrating a high speed sampling system in GaAs was to demonstrate a basic low-frequency electrooptic modulator [44]–[46]. Choosing the longitudinal interaction geometry as a test case, a simple reflectance modulator was constructed in order to verify the sensitivity of the fringing field interaction.

At 1.5 mw HeNe laser operating at $1.15 \mu\text{m}$ was used as the infrared source. The linearly polarized output was converted to circular polarization with a Soliel-Babinet compensator adjusted for quarter wave retardation. The beam was focused with a standard $5 \times$ microscope objective onto a GaAs wafer adjacent to a microstrip transmission line where it entered the crystal and reflected off the ground plane on the back side. After the beam exited the crystal, the microscope objective recollimated it parallel to the incident beam and slightly displaced where a mirror directed it to the analyzer and photodiode. The transmission line was driven with a sine wave generator with 1 V peak-to-peak amplitude at a frequency of 1 kHz.

Taking into account the 30 percent Fresnel reflection of the incident light from the surface of the GaAs, we measured a half-wave switching voltage of 10.5 kV. This is a factor of two high and the error may have to do with the nature of the distribution of the fringing fields (i.e., the potential is lower immediately adjacent to the transmission lines). Also, if a large spot size is used and is centered on the fringing field, some of the beam might be reflected by the top conductor of the transmission line, reducing the electrooptic interaction.

As the optical beam was moved away from the transmission line, the signal diminished as expected due to the local confinement of the electric fields. However, when an additional visible HeNe laser ($\lambda = 632 \text{ nm}$) was used to flood-illuminate the surface of the GaAs in the vicinity of the sampling beam, the signal returned to its original value. This suggests that a conductive surface is being photogenerated and that charge from the transmission line is accumulating there, reestablishing an electric field in the sampling beam. The photoconductive surface may play an important role in future measurements because it can be used to optically alter, or introduce, new conductive patterns on any GaAs wafer. This might be useful for introducing known reflections as timing markers in time domain reflectometry measurements, or, as a way of rapidly designing new transmission-line structures without intermediate processing steps.

2) *Photodiode Characterization*: In this experiment, we measured the impulse response of a GaAs photodiode that was excited by the second harmonic of the sampling beam [10]. Although the photodiode made a hybrid connection to the GaAs microstrip transmission line, the principle of excitation and sampling of an active GaAs device was demonstrated.

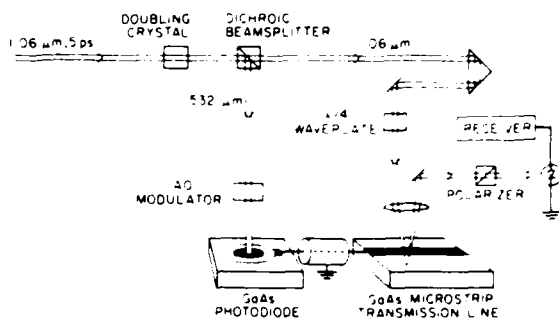


Fig. 11. Schematic diagram of an electrooptic sampling system for direct probing in GaAs substrates.

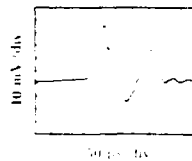


Fig. 12. Impulse response of a $50 \mu\text{m}$ diameter GaAs photodiode measured by electrooptic sampling of a GaAs microstrip transmission line (horizontal 50 ps/div , vertical $\approx 10 \text{ mV/div}$).

The experimental set up is indicated schematically in Fig. 11. It functions in an identical manner to the apparatus shown in Fig. 3, but with a different optical source. Instead of a synchronously pumped dye laser, we used a Spectra-Physics model 3000 Nd: YAG laser in conjunction with a model 3600 pulse compressor to produce a train of 5 ps pulses at a rate of 82 MHz. The doubling crystal was KTP and an acoustooptic modulator was used to chop the excitation beam at 20.9 MHz. Fig. 12 shows the impulse response of a $50 \mu\text{m}$ diameter GaAs Schottky photodiode [47] measured with this system.

3) *MMIC Testing*: The real power and flexibility of our sampling approach can be demonstrated best when applied to measurements made in complex integrated circuits. Weingarten and Rodwell have sampled the output of a four stage GaAs FET traveling wave amplifier (TWA, courtesy of G. Zdziuk, Varian Associates), measuring electronic distortion induced by changes in the power supply bias [11], [48]. In this experiment, instead of driving the device under test with a photodiode, it was connected to a microwave synthesizer (HP 8340A), phase-locked to the laser mode-locker driver and operating at a fixed frequency. The frequency was chosen to be an exact multiple of the fundamental sampling rate plus 1 Hz so that the sampling pulses walked through the driving sinusoid at a rate of 1 Hz. Pulse modulating the synthesizer at 10 MHz, allowed a narrow-band receiver to be used for signal-to-noise enhancement. Since the spectrum analyzer used as the 10 MHz receiver displayed only the rms value of the sampled waveform a small amount of the 10 MHz chopping signal was injected into the input so that it summed vectorially with the photodiode signal to produce a true bipolar waveform.

With the synthesizer tuned to 4.1 GHz and the TWA

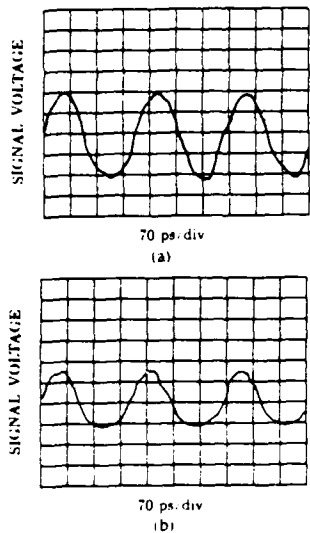


Fig. 13. Voltage output of a four stage GaAs FET traveling wave amplifier measured by electrooptic sampling in the GaAs substrate. (a) Normal drain-source biasing. (b) Reduced drain-source biasing demonstrating soft clipping distortion. Frequency = 4.1 GHz. (Horizontal: 70 ps/div. vertical: 200 mV/div.)

biased normally, the waveform shown in Fig. 13(a) was measured by electrooptically sampling the TWA at the output of its last stage. Reducing the drain-to-source voltage from +4 to +1.5 V caused the TWA to operate in the "triode" region. Fig. 13(b) shows the soft clipping on the negative peaks as well as the reduction in gain that resulted from this bias condition. The distortion present in both waveforms is due to jitter in the arrival time of the sampling pulses and is covered in detail in Section VI.

4) *Digital GaAs Integrated Circuit*: In an experimental setup similar to that just described for the TWA, Freeman *et al.* [34] have utilized the backside probing geometry of Fig. 9 to sample the serial output waveform from an 8-bit multiplexer/demultiplexer [49] operating at a clock rate of 2.6 GHz. The eight parallel input lines were statically set to the digital word 11110100. By probing the 2 μ m wide line leading to the output buffer stage, the serial bit stream shown in Fig. 14 was obtained.

VI. HARMONIC MIXING, PHASE NOISE, AND TIMING JITTER

Because there is a random variation in the period between pulses in a mode-locked pulse train, any sampling measurement of an arbitrary waveform using these pulses (such as in the amplifier just described) will reflect this variation. A fluctuation of even 10 ps translates to a phase fluctuation of 36° for a 10 GHz sinusoid. The timing jitter in mode-locked lasers is a random process that is not easy to model or predict. We can, however, determine the rms magnitude of the jitter by integrating the frequency spectrum of the fluctuations. In this section, we describe how the electrooptic sampler functions as a general wide-band harmonic mixer and how it can be used to study phase

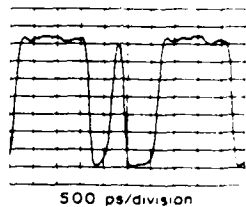


Fig. 14. Electrooptically sampled serial output waveform of a 2.6 GHz multiplexer/demultiplexer measured using the backside probing geometry of Fig. 9. Parallel input word is 11110100

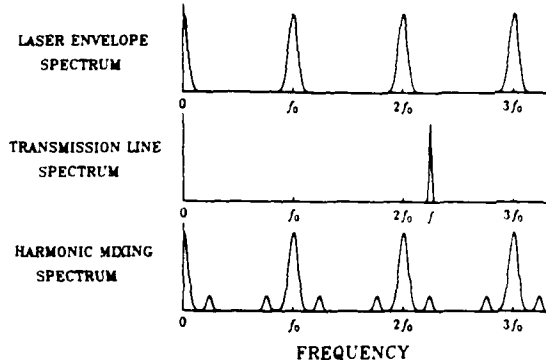


Fig. 15. Frequency spectra describing electrooptic harmonic mixing. Picosecond pulses from the electrooptic sampler mix with the transmission line signal to produce the indicated harmonic mixing spectrum in the receiver photocurrent.

noise arising from the pulse-to-pulse timing jitter in mode-locked lasers.

Electrooptic modulation of a light beam illuminating a photodiode produces a photocurrent that is proportional to the product of the light intensity and the modulating voltage. Because of the product relationship, the modulator/photodiode combination can be viewed as a mixer. The picosecond pulses in the electrooptic sampler represent the local oscillator signal and the transmission line voltage represents the RF input signal. In the frequency domain (Fig. 15), any signal at frequency f propagating on the transmission line will mix with all of the harmonics of the fundamental sampling rate f_0 . Sidebands, due to the convolution of these two spectra will appear at frequencies $nf_0 \pm f$. We refer to this process as "electrooptic harmonic mixing." Unlike electronic balanced mixers, both the local oscillator and the RF input signals appear at the output (IF) port.

If the transmission line is driven with a sinusoidal signal, a replica of the nearest harmonic will appear between dc and $f_0/2$ where it can be conveniently viewed on a spectrum analyzer or other receiver. The phases of the microwave signals are preserved and any fluctuations or phase noise will be transferred to the base-band signal. Thus, the phase noise of the down-converted harmonic can be studied without using a high speed photodiode, yielding information about the timing jitter in the pulse train.

A typical harmonic spectral component is shown in Fig.

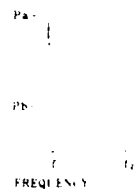


Fig. 16. Typical laser envelope harmonic spectral component. P_c = carrier power. P_b = phase noise power at any offset from the carrier. (See text for explanation of f_1 and f_2 .)

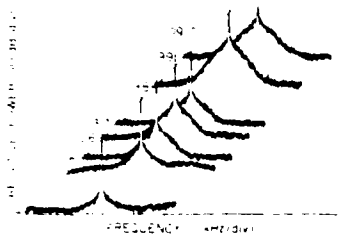


Fig. 17. Laser envelope harmonic spectral components down-converted to 10 MHz by harmonic mixing in the electrooptic sampler. Center frequency of each component equals $n \times 82$ MHz, where n is the harmonic number.

16. It consists of a delta function at nf_0 and a phase noise pedestal arising from the pulse-to-pulse jitter. For small phase fluctuations, the relative phase noise power can be shown to vary as the square of the harmonic number n [50]. The phase noise-to-carrier power ratio for a given sinusoidal component of the noise is given by

$$\frac{P_b}{P_c} = \frac{(n\omega_0\tau_0)^2}{2} \quad (55)$$

where

P_b = phase noise power at some offset frequency

P_c = carrier power

$\omega_0 = 2\pi \times$ sampling rate

τ_0 = peak timing jitter at frequency of P_b .

Fig. 17 shows a series of harmonic spectra from the mode-locked and compressed Nd: YAG laser mixed down to 10 MHz. To obtain these spectra, signals up to 16 GHz ($n = 199$) were applied to the transmission line from a microwave synthesizer (HP 8340A) that was phase-locked to the mode-locker driver (HP 3325A). The growth of the phase noise sidebands is clearly evident. By measuring the relative intensity of the phase noise and plotting it against the actual frequency of the harmonic (nf_0), the rate of sideband growth can be compared to the theory. In Fig. 18, these data are plotted on a log-log graph against a slope = 2 line. The data follow the square-law dependence well with the deviation at the high end assumed to result from the higher modulation index causing a nonlinear departure from the small-signal theory.

With a picture of one of the spectral components in

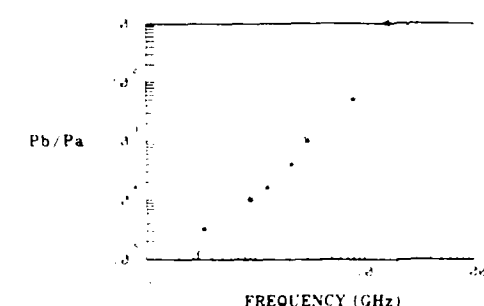


Fig. 18. Relative growth of phase noise power as a function of harmonic frequency ($n \times 82$ MHz). Solid line of slope = 2 corresponds to theoretical square-law dependence.

hand, we can deduce the extent of the timing fluctuations because the total power in the phase noise sidebands, P_{DSB} , can be shown to be related to the rms timing jitter [50], [51]. To calculate the total double side-band noise power, the phase noise spectrum is integrated from some low frequency f_1 near the carrier (nf_0) to some higher frequency f_2 where the phase noise falls to the level of the AM and Johnson noise. Since the apparent width of the carrier component depends on the resolution bandwidth of the spectrum analyzer, using a narrower bandwidth allows f_1 to move closer to the carrier and lower frequency phase fluctuations to contribute to the total side-band power. Thus, any calculation of timing jitter using this method must specify the low frequency cutoff f_1 . The expression relating the rms timing jitter to the carrier and phase noise powers is

$$\Delta t_{rms} = \frac{T}{2\pi n} \sqrt{\frac{P_{DSB}}{P_c}} \quad (56)$$

where

$$P_{DSB} = 2 \int_{f_1}^{f_2} \frac{P_b(f)}{B} df \quad (57)$$

and B = spectrum analyzer resolution bandwidth and $T = 1/f_0$.

In our experiments we used two spectrum analyzer bandwidth settings. In the first case with the bandwidth $B = 10$ Hz, the low-frequency cutoff f_1 ranged between 10 Hz and 32 Hz. In the second case, $B = 30$ Hz and f_1 varied from 105 Hz to 150 Hz. The upper frequency limit f_2 was typically 1 kHz-2 kHz.

The rms timing jitter calculated from the phase noise spectra and (56) is plotted in Fig. 19 for five harmonic components from $n = 11$ to $n = 98$. Although there is a spread of several picoseconds in the jitter for each of the two resolution bandwidths, the slopes connecting the two data points of each harmonic number are nearly the same, indicating a similar trend in increasing jitter as lower frequency components are included. The data suggest an upper limit of 11 ps rms jitter for fluctuation frequencies above 10 Hz. We have not yet identified the source of the

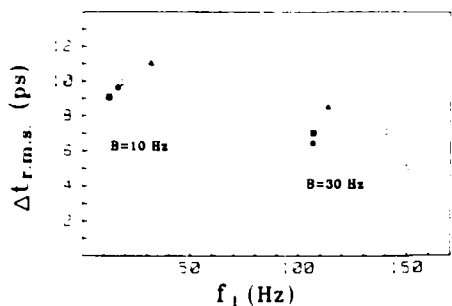


Fig. 19. Rms timing jitter of a cw mode-locked and compressed Nd:YAG laser. Data derived by integrating phase noise power spectra from f_1 to f_2 (see Fig. 15). Five harmonic spectra represented using indicated spectrum analyzer bandwidths

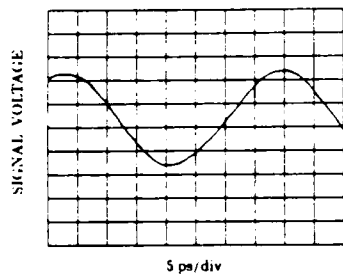


Fig. 20. 26.4 GHz sine wave from a microwave synthesizer (HP 8340A) measured by electrooptic sampling in GaAs after active stabilization of the mode-locked Nd:YAG laser

timing jitter but we believe it may result from intensity fluctuations in the CW flashlamp that pumps the Nd:YAG rod.

As previously mentioned, timing fluctuations of this magnitude can seriously degrade the accuracy of microwave measurements at modest frequencies. In order for electrooptic sampling of microwave signals at very high frequencies to be viable, some method of reducing the timing jitter will have to be employed. Cotter [52] has reported on a method of phase-locking the outputs of mode-locked argon ion and synchronously pumped dye lasers to a reference microwave synthesizer. M. Rodwell is currently pursuing a similar approach in our lab and has succeeded in reducing the timing jitter of our Nd:YAG laser to less than 2 ps rms [48]. Fig. 20 shows a section of a 26.4 GHz sine wave as measured on the electrooptic sampler with substantially reduced timing error distortion.

VII. SUMMARY

We have described a new electrooptic sampling technique that allows noninvasive electrical characterization of GaAs circuits and devices. The technique is based on using the intrinsic electrooptic effect in GaAs to amplitude modulate picosecond pulses as they probe the fringing fields adjacent to conductors on the semiconductor substrate. The time resolution and voltage sensitivity have been reviewed and indicate that picosecond response with $22 \mu\text{V}/\sqrt{\text{Hz}}$ sensitivity is achievable. We have demonstrated the effectiveness of the system by synchronous excitation and

characterization of photodiodes, measuring electronic distortion in a monolithic microwave integrated circuit, and probing the output of a digital GaAs i.c.

Currently, the performance of the sampler for measuring high-frequency signals is limited by the timing jitter in the picosecond source. Using the sampler as an electrooptic harmonic mixer, we have measured the magnitude of the effect and are pursuing ways of reducing it.

We feel this new sampling technique holds great promise as a tool for studying and developing very high speed GaAs and other compound semiconductor devices.

VIII. ACKNOWLEDGMENT

The authors wish to thank G. Zdziuk of Varian Associates for supplying the GaAs FET traveling wave amplifier, and K. Weingarten and M. Rodwell for useful discussions and assistance in making some of the measurements. We appreciate the careful reading and critiqueing of this manuscript by J. Freeman, B. Auld, N. Kendzierski, and N. Kolner. Special thanks go to the Hewlett-Packard Company, where our initial electrooptic sampling work in LiTaO₃ was done, and to Spectra-Physics and Hewlett-Packard for generous equipment donations and loans which helped make this research possible.

REFERENCES

- [1] N. C. Cirillo, Jr., and J. K. Abrokwa, "8.5-picosecond ring oscillator gate delay with self-aligned gate modulation-doped n+ (Al_xGa_{1-x})As GaAs FETs," presented at 43rd Ann. Device Res. Conf., Boulder, CO, June 1985, paper IIA-7.
- [2] P. M. Downey, "Subpicosecond response times from ion bombarded InP," in *Topical Meet. Picosecond Electron Optoelectron. Tech. Dig.*, Mar. 1985, paper THAG-1, New York: Springer-Verlag, 1985.
- [3] W. H. Knox, R. L. Fork, M. C. Downer, R. H. Stolen, C. V. Shank, and J. A. Valdmanis, "Optical pulse compression to 8 fs at a 5-kHz rate," *Appl. Phys. Lett.*, vol. 46, pp. 1120-1121, 1985.
- [4] P. LeFur and D. H. Auston, "A kilovolt picosecond optoelectronic switch and Pockel's cell," *Appl. Phys. Lett.*, vol. 28, pp. 21-23, 1976.
- [5] R. C. Alferness, N. P. Economou, and L. L. Buhl, "Picosecond optical sampling technique for measuring the speed of fast electro-optic switch/modulators," *Appl. Phys. Lett.*, vol. 37, pp. 597-599, 1980.
- [6] P. R. Smith, D. H. Auston, and W. M. Augustyniak, "Measurement of GaAs field-effect transistor electronic impulse response by picosecond optical electronics," *Appl. Phys. Lett.*, vol. 39, pp. 739-741, 1981.
- [7] F. J. Leonberger, C. E. Woodward, and R. A. Becker, "4-bit 428-mega-sample/s electro-optic guided-wave analog-to-digital converter," *Appl. Phys. Lett.*, vol. 40, pp. 565-568, 1982.
- [8] J. A. Valdmanis, G. Mourou, and C. W. Gabel, "Picosecond electro-optic sampling system," *Appl. Phys. Lett.*, vol. 41, pp. 211-212, 1982.
- [9] B. H. Kolner, D. M. Bloom, and P. S. Cross, "Electro-optic sampling with picosecond resolution," *Electron. Lett.*, vol. 19, pp. 574-575, 1983.
- [10] B. H. Kolner and D. M. Bloom, "Direct electro-optic sampling of transmission-line signals propagating on a GaAs substrate," *Electron. Lett.*, vol. 20, pp. 818-819, 1984.
- [11] B. H. Kolner, K. J. Weingarten, M. J. W. Rodwell, and D. M. Bloom, "Picosecond electro-optic sampling and harmonic mixing in GaAs," *Topical Meet. Picosecond Electron Optoelectron. Tech. Dig.*, paper WB4-2, Incline Village, NV, Mar. 1985, New York: Springer-Verlag, 1985.
- [12] Janis A. Valdmanis, Gerard A. Mourou, and C. W. Gabel, "Subpicosecond electrical sampling," *IEEE J. Quantum Electron.*, vol. QE-19, pp. 664-667, 1983.
- [13] Brian H. Kolner, David M. Bloom, and Peter S. Cross, "Picosecond optical electronic measurements," *SPIE Proc.*, vol. 439, pp. 149-152, 1983.
- [14] J. A. Valdmanis, G. Mourou, and C. W. Gabel, "Subpicosecond electrical sampling," *SPIE Proc.*, vol. 439, pp. 142-148, 1983.

[15] G. A. Mourou and K. E. Meyer, "Subpicosecond electro-optic sampling using coplanar strip transmission lines," *Appl. Phys. Lett.*, vol. 45, pp. 492-494, 1984.

[16] R. E. Collin, *Foundations for Microwave Engineering*, New York: McGraw-Hill, 1966.

[17] K. E. Meyer and G. A. Mourou, "Electro-optic sampling: Field mapping with subpicosecond resolution," in *Proc. Int. Conf. on Picosecond Electronics and Optoelectronics: Lasers, Detectors, Devices*, Mar. 1985, paper WB3-1, New York: Springer-Verlag, 1985.

[18] J. D. Kafka, B. H. Kolner, T. Baer, and D. M. Bloom, "Compression of pulses from a continuous wave mode-locked Nd:YAG laser," *Opt. Lett.*, vol. 9, pp. 505-508, 1984.

[19] B. H. Kolner, J. D. Kafka, D. M. Bloom, and T. M. Baer, "Compression of mode-locked Nd:YAG pulses to 18 ps," in *Ultralast Phenomena IV*, New York: Springer-Verlag, 1984.

[20] J. P. Heritage, R. N. Thurston, W. J. Tomlinson, A. M. Weiner, and R. H. Stolen, "Spectral windowing of frequency-modulated optical pulses in a grating compressor," *Appl. Phys. Lett.*, vol. 42, pp. 57-59, 1983.

[21] A. S. L. Gomes, W. Sibbett, and J. R. Taylor, "Generation of subpicosecond pulses from a continuous wave mode-locked Nd:YAG laser using a two-stage optical compression technique," *Opt. Lett.*, vol. 10, pp. 338-340, 1985.

[22] I. P. Kaminow, *An Introduction to Electrooptic Devices*, New York: Academic, 1974.

[23] I. F. Nye, *Practical Principles of Optics*, 2nd ed., Oxford, U.K.: Clarendon Press, 1974.

[24] B. H. Kolner, "Picosecond electro-optic sampling in GaAs," Ph.D. dissertation, Stanford Univ., Stanford, CA, 1985.

[25] R. N. Bracewell, *The Fourier Transform and Its Applications*, New York: McGraw-Hill, 1978.

[26] F. P. Jeppe and C. V. Shank, "Techniques for measurement of ultra-short light pulses," S. L. Shapiro, Ed., New York: Springer-Verlag, 1977, pp. 53-122.

[27] S. Williamson and G. Mourou, "Picosecond electro-electron oscilloscope," in *Topics in Meas. Phys., Opt., Electron., Optoelectron., Tech. Dig.*, Mar. 1985, postdeadline paper PDP2.

[28] Y. R. Shen, *The Principles of Nonlinear Optics*, New York: Wiley, 1984.

[29] J. F. Ward, "Absolute measurement of an optical rectification coefficient in ammonium dihydrogen phosphate," *Phys. Rev.*, vol. 143, pp. 569-574, 1966.

[30] D. H. Auston, K. P. Cheung, J. A. Valdmanis, and D. A. Kleiman, "Cherenkov radiation from femtosecond optical pulses in electro-optic media," *Phys. Rev. Lett.*, vol. 53, pp. 1555-1558, 1984.

[31] K. P. Cheung and D. H. Auston, "Distortion of ultrashort pulses on total internal reflection," *Opt. Lett.*, vol. 10, pp. 218-219, 1985.

[32] R. E. Williams, *Gallium Arsenide Processing Techniques*, Dedham, MA: Artech House, 1984.

[33] Susumu Nambu, "Electro-optical effect of zincblende," *J. Opt. Soc. Amer.*, vol. 51, pp. 76-79, 1961.

[34] J. L. Freeman, Jr., S. K. Diamond, H. Fong, and D. M. Bloom, "Electro-optic sampling of planar digital GaAs integrated circuits," *Appl. Phys. Lett.*, vol. 47, pp. 1083-1084, 1985.

[35] R. L. Fork, Charles V. Shank, R. Yen, and C. A. Hirshmann, "Femtosecond optical pulses," *IEEE J. Quantum Electron.*, vol. QE-19, pp. 500-506, 1983.

[36] J. A. Valdmanis, R. L. Fork, and J. P. Gordon, "Generation of optical pulses as short as 27 femtoseconds directly from a laser balancing self phase modulation, group velocity dispersion, saturable absorption and saturable gain," *Opt. Lett.*, vol. 10, pp. 131-133, 1985.

[37] L. E. Mollenauer and D. M. Bloom, "Color center laser generates picosecond pulses and several watts cw over the 1.24-1.45 μ m range," *Opt. Lett.*, vol. 14, pp. 247-249, 1979.

[38] D. Grischkowsky and A. C. Balant, "Optical pulse compression based on enhanced frequency chirping," *Appl. Phys. Lett.*, vol. 41, pp. 1-3, 1982.

[39] B. Niklaus and D. Grischkowsky, "12 + pulse compression using optical fibers," *Appl. Phys. Lett.*, vol. 42, pp. 1-3, 1983.

[40] C. V. Shank, R. L. Fork, R. Yen, and R. H. Stolen, "Compression of femtosecond optical pulses," *Appl. Phys. Lett.*, vol. 40, pp. 761-763, 1982.

[41] A. M. Johnson, R. H. Stolen, and W. M. Simpson, "80 + single-stage compression of frequency doubled Nd:yttrium-aluminum-garnet laser pulses," *Appl. Phys. Lett.*, vol. 44, pp. 729-731, 1984.

[42] W. J. Tomlinson, R. H. Stolen, and C. V. Shank, "Compression of optical pulses chirped by self phase modulation in fibers," *J. Opt. Soc. Amer. B*, vol. 1, pp. 139-149, 1984.

[43] E. B. Treacy, "Compression of picosecond light pulses," *Phys. Lett.*, vol. 28A, pp. 34-35, 1968.

[44] Lui Ho and C. E. Butler, "Electro-optic devices in optical fibers," *Appl. Opt.*, vol. 2, pp. 641-648, 1963.

[45] A. Yariv, C. A. Mead, and J. V. Barker, "GaAs as an electro-optic modulator at 10.6 microns," *IEEE J. Quantum Electron.*, vol. QE-12, pp. 243-245, 1966.

[46] T. E. Walsh, "Gallium arsenide electro-optic modulators," *RC-TR*, vol. 27, pp. 323-335, 1966.

[47] S. Y. Wang, D. M. Bloom, and D. M. Collins, "20 GHz bandwidth GaAs photodiode," *Appl. Phys. Lett.*, vol. 42, pp. 190-192, 1983.

[48] K. J. Weingarten, M. J. W. Rodwell, H. K. Heintz, B. H. Kolner, and D. M. Bloom, "Direct electro-optic sampling of GaAs," *Appl. Electron. Lett.*, vol. 21, pp. 765-766, 1985.

[49] G. D. McCormick, A. G. Rode, and E. W. Strid, "A GaAs MSL 8-bit multiplexer and demultiplexer," in *Proc. 1982 GaAs IC Symp.*, Beaverton, OR, pp. 25-28, courtesy of Triquint Semiconductor, Inc.

[50] J. Kluge, "Synchronously pumped dye lasers for ultrashort light pulse generation," Ph.D. dissertation, Univ. Essen, Fed. Rep. Germany, 1984.

[51] W. P. Robins, *Phase Noise in Signal Sources*, England: Prentice-Hall, 1982.

[52] D. Cotter, "Technique for high-speed electro-optic sampling," *Optics Preprint 44*, New York: Springer-Verlag, 1984.

Brian H. Kolner (S'85) was born in Chicago, IL, on June 22, 1955. He received the B.S. degree in electrical engineering from the University of Wisconsin, Madison, in 1979 and the M.S. and Ph.D. degrees in electrical engineering from Stanford University, Stanford, CA, in 1981 and 1985, respectively.

From 1979 to 1983 he was a part-time employee with Hewlett-Packard Laboratories, Palo Alto, CA, where he worked on surface acoustic wave devices, integrated optical directional coupler modulators, and electro-optic sampling. He has also collaborated with Spectra-Physics Corporation and Bell Communications Research. In 1985 he rejoined the Staff at Hewlett-Packard Laboratories where his current interests include high-speed electronic and optoelectronic devices, electro-optic sampling, optical pulse compression, and ultralast phenomena.



Dr. Kolner is a member of the Optical Society of America.

David M. Bloom (S'68, M'76, M'81) was born in October 10, 1948 in Brooklyn, NY. He received the B.S. degree in electrical engineering from the University of California, Santa Barbara, in 1970 and the M.S. and the Ph.D. degrees in electrical engineering from Stanford University, Stanford, CA, in 1972 and 1975, respectively.

From 1975 to 1977 he was employed by Stanford University as a Research Associate. During this period he was awarded the IBM Postdoctoral Fellowship. From 1977 to 1979 he was employed by Bell Telephone Laboratories, Holmdel, NJ, where he conducted research on optical phase conjugation, ultralast optical pulse propagation in fibers, and tunable color-center lasers. From 1979 to 1983 he served on the Staff and later as a Project Manager at Hewlett-Packard Laboratories, Palo Alto, CA. While there he conducted and managed research on fiber-optical devices, high-speed photodetectors, and picosecond electronic measurement techniques. In late 1983 he joined the Edward L. Ginzton Laboratory, W. W. Hansen Laboratories of Physics, Stanford University, where he is currently an Associate Professor of Electrical Engineering. His current research interests are ultralast optics and electronics.

Dr. Bloom was awarded the 1980 Adolph Lomb Medal of the Optical Society of America for his pioneering work on the use of nonlinear optical processes to achieve real-time conjugate wavefront generation. In 1981 he was elected a Fellow of the Optical Society of America in recognition of his distinguished service in the advancement of optics. He is the 1985 IEEE/LEOS Travelling Lecturer.

A GUIDED WAVE MONOLITHIC RESONATOR RUBY FIBER LASER

J.L. NIGHTINGALE and R.L. BYER

Applied Physics Department, Edward L. Ginzton Laboratory, C-Physics, Stanford University, Stanford, CA 94309, USA

Received 24 July 1985

Single crystal ruby fibers, cooled with liquid nitrogen, have been operated as end pumped lasers. The fiber laser is a guided wave device with a length of 15 mm and a mean diameter of 60 μm . The laser resonator structure is monolithic, consisting of an aluminum mirror coated on one fiber end face and an uncoated opposite end face serving as an output coupler. Using an argon ion laser pump source, cw output powers of several mW were obtained.

Single crystal optical fibers offer the promise of compact, rugged and highly efficient end-pumped laser oscillators. The chief advantage of the fiber geometry is the inherent excellent spatial overlap between the confined pump radiation and the oscillator's fundamental optical mode [1]. This offers the potential for simple butt coupling of fiber oscillators to laser diode and light emitting diode pump sources.

Realization of practical crystal fiber lasers will require the development of a guided wave, monolithic resonator oscillator. In this paper we report the first such device, a liquid nitrogen cooled ruby fiber laser.

The 77 K ruby system was chosen for demonstration of a monolithic resonator crystal fiber oscillator because of its high laser gain. The high gain allows laser operation despite the large resonator losses which were present in these fiber oscillators. A major disadvantage of a ruby oscillator at present is the lack of a sufficiently bright semiconductor light source to serve as the oscillator pump. An argon ion laser was used as the pump source in the present experiment. Demonstration of a guided wave, monolithic resonator oscillator in ruby represents a significant step toward development of practical light emitting diode or laser diode pumped fiber oscillators in other materials such as Nd:YAG.

Both cw [2] and laser pumped [3,4] liquid nitrogen cooled ruby lasers have been reported in bulk crystal samples. Short crystal fiber lengths (< 10 mm) have previously been used to make miniature room tempera-

ture ruby [5] as well as Nd:YAG [6-8] and Nd:Y₂O₃ [9] lasers. These miniature lasers employed external mirrors adjacent to the fiber to form the resonator cavity. The finite mirror thickness precluded efficient butt coupling to LED pump sources [7] and complicated laser diode pumping [8]. For almost all these lasers the fiber's length was less than or comparable to the Rayleigh length of the fiber's lowest order optical mode. In this situation the mode only weakly interacts with the fiber surface and pump beam confinement is limited.

In our work the laser resonator structure is simply formed by the fiber waveguide and the polished fiber end faces. The single crystal fibers tested had diameters which ranged between 60 μm and 83 μm . The maximum fiber length was 15 mm. The lowest order optical mode for such a fiber has a beam waist approximately one-third the fiber diameter. For a 60 μm diameter fiber this yields a beam waist of 20 μm , implying a Rayleigh length in ruby of 3.2 mm. A 15 mm long fiber laser of this diameter is thus approximately five Rayleigh lengths long and may be considered a guided wave device. In these fibers the waveguide interface is the ruby-liquid nitrogen boundary at the fiber periphery. The large refractive index difference between these materials (1.76 to 1.21), coupled with fiber diameter variations of approximately 2%, leads to substantial waveguide losses.

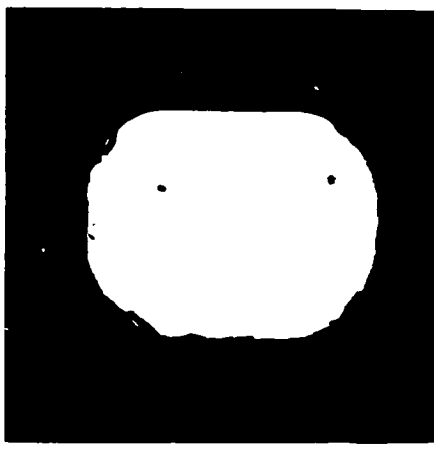
The ruby fibers used were grown by the miniature pedestal growth technique [5-10], using an apparatus

developed in our laboratory [11]. In this method fiber crystallographic orientation is accomplished by use of an oriented seed crystal which nucleates the crystal growth. Two different orientations were grown in this study: $\langle 1\bar{1}00 \rangle$ (fiber axis 90 degrees to c -axis) and $\langle 0001 \rangle$ (fiber axis parallel to c -axis). The crystallographic orientation of the fibers was verified by Laue X-ray diffraction and laser absorption techniques. The fiber's cross-section reflects the characteristic growth habits of the crystal. The $\langle 0001 \rangle$ axis fibers have a slightly rounded hexagonal cross section [5] while $\langle 1\bar{1}00 \rangle$ axis fibers display a rounded rectangular shape.

The $\langle 0001 \rangle$ axis fibers were grown at 3.0 mm/min using a single 3.1 diameter reduction. The source rod diameter was 250 μm yielding a final fiber diameter of 83 μm . 60 μm diameter $\langle 1\bar{1}00 \rangle$ axis fibers were grown using two 3.1 diameter reductions from a 540 μm diameter source rod. The growth speed for both diameter reductions was 4.5 mm/min.

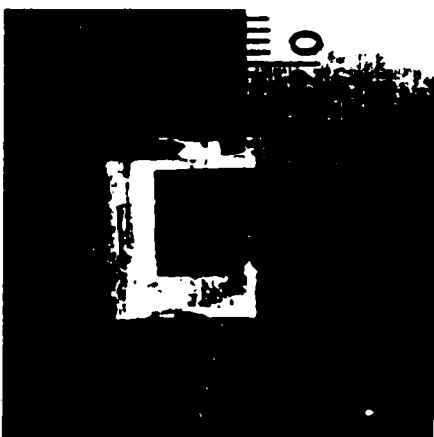
The starting material for all laser fibers was single crystal ruby with a chromium concentration of 0.79 wt%. The fiber's chromium concentration is less than that of the feed material due to evaporation of chromium during the growth process [5,12]. Using laser absorption through thin cross sections of fiber samples we measured a chromium concentration of 0.090 wt% in the $\langle 1000 \rangle$ axis fibers and 0.15 wt% in the $\langle 1\bar{1}00 \rangle$ axis fibers.

The fiber end faces were fabricated by mounting the fibers in a slotted sapphire block. The fiber and block lengths were identical, allowing both fiber end faces to be polished without removing the fiber from the slot. The sapphire block end faces were optically polished flat to within 2 μm per centimeter and parallel to within 1 minute of arc. Assuming that the fiber rests squarely in the slot the same tolerances would apply to the fiber. Unfortunately, the fiber has a tendency to bend and wander within the slot. This leads to the end faces being skewed with respect to the fiber axis as well as a loss of end face parallelism. Based on the slot width, the uncertainty in the end face orientation is one degree. We are currently modifying the polishing procedure by using narrower slots which should improve the orientation accuracy to ~ 2 minutes of arc. A photograph of a polished $\langle 1\bar{1}00 \rangle$ fiber is shown in fig. 1a. Fig. 1b shows the fiber mounted in an aluminum holder. The holder supports the fiber during laser tests.



50 μm

(a)



(b)

Fig. 1. (a) Cross section of a polished $\langle 1\bar{1}00 \rangle$ axis ruby fiber. The fiber's major and minor axis dimensions are 58 μm and 46 μm respectively. The minor axis corresponds to the $\langle 0001 \rangle$ direction. (b) Photograph showing a single crystal ruby fiber mounted in its fiber holder. The holder supports the fiber during laser tests.

After removal from the polishing fixture an optically thick reflective aluminium coating is vapor deposited on one fiber end face. The aluminium coating is easier to apply than a multilayer dielectric coating and thus was used for this device demonstration. The reflectivity of the aluminium coating was measured to be 75%. This simple polished and coated fiber constitutes both the laser medium and the resonator structure.

The overall system for ruby laser operation is shown in fig. 2. The ruby laser fiber is permanently mounted in the machined aluminium holder to facilitate handling. The holder supports the fiber at two points near the fiber ends. A quartz tube supports the fiber holder while the entire assembly is immersed in liquid nitrogen. The cut away central section of the holder allows liquid nitrogen to directly contact the fiber during laser operation. The uncoated fiber end protrudes about 1 mm into the quartz tube. Silicone vacuum grease and silicone rubber serve as sealants to prevent liquid nitrogen from entering the tube and covering the fiber end. A helium gas atmosphere, maintained over the fiber, prevents condensation on the end face. Pump radiation, from an argon ion laser operating at 514.5 nm, is focused into the uncoated fiber end and separated from the resultant ruby laser radiation by means of a dichroic mirror.

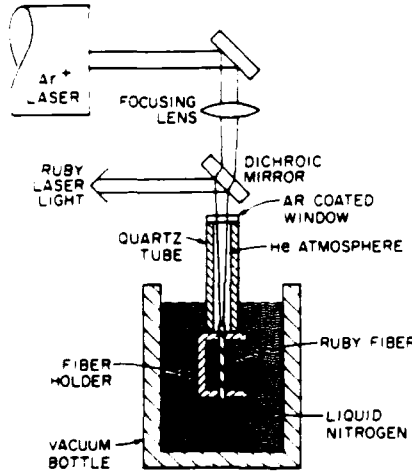


Fig. 2. Experimental set-up used in the cw monolithic resonator ruby fiber laser tests.

Table 1
Summary of results for two different monolithic resonator ruby fiber oscillators

Characteristics	Fiber	
	1	2
Length (mm)	7.7	15.0
Mean diameter (μm)	83	60
Chromium concentration (wt%)	0.15	0.090
Laser threshold with uncoated reflector (mW)	550	620
Laser threshold with aluminium reflector (mW)	300	410
Maximum ruby laser output with aluminium reflector (mW)	3.9	2.0
Calculated round trip cavity loss (L in eq. (1)), loss in % equals $100[1 - \exp(-L)]$	2.4	4.2
Slope efficiency with Al mirror (%)	1.3	0.67

Table 1 summarizes results for two fiber oscillators. Fiber 1 is a relatively short, large diameter, fiber with a fiber length comparable to the Rayleigh length of the lowest order optical mode. Fiber 2 is a true guided wave device as discussed earlier. For both these fibers, laser oscillation could be obtained even with the aluminium mirror removed from the rear fiber end face. In this case the Fresnel reflection from the ruby-liquid nitrogen dielectric interface yields a rear mirror reflectivity of 3.4%. The laser threshold values listed include the pump beam Fresnel losses off the fiber output coupler. The aluminium mirror on fiber 2 was slightly damaged reducing its reflectivity by an estimated 20% from its undamaged value.

The difference in the laser thresholds for the two different rear mirror reflectivities allows us to estimate the resonator losses. Equating the laser gain and losses at threshold for the three level ruby laser system leads to the relation [13]

$$\frac{2\alpha_0 g_1 (KP_{th} - (1 + \kappa) g_2/g_1)}{g_2(1 + \kappa)(KP_{th} + 1)} = L - \ln R_1 R_2. \quad (1)$$

where α_0 is the absorption coefficient between the ground state and laser level ($\alpha_0 = 0.20 \text{ cm}^{-1}$ at room temperature for a chromium density of 0.05 wt%), L is the fiber length, g_1, g_2 are the degeneracy factors for the ground state and upper laser level ($g_2/g_1 = 1/2$),

K is a constant dependent on the upper state lifetime and the pump beam absorption cross-section, P_{th} is the pump power at threshold, κ is the thermal distribution of population between the split upper laser level ($\kappa = 0.58$ at 77 K), L is the round trip cavity loss not including mirror reflectivity losses and R_1, R_2 are the mirror reflectivities.

In order to use the two different threshold conditions to solve eq. (1) for L we must determine the absorption cross section α_0 . Assuming an isothermal fiber at 77 K, α_0 can readily be calculated knowing the fiber's chromium density. However, since the transition line center shifts by 0.0045 nm/K [13], temperature variations within the fiber can reduce α_0 . Since the laser transition is the same as the common fluorescence transition, measurement of the ruby fluorescence spectrum allows determination of α_0 .

The fluorescence spectrum was measured with a 0.007 nm resolution spectrometer using the geometry shown in fig. 2. To avoid laser oscillation complicating the spectra, fiber samples identical to those tested as laser oscillators were used except that the bottom fiber end was not polished. Fig. 3 illustrates a typical fluorescence spectrum obtained with 390 mW of pump power. Note the long wavelength tail and the asymmetric nature of the central peak. This asymmetric shift towards longer wavelengths is consistent with pump radiation heating of the fiber. The measured transition full width at half maximum is 0.033 nm which is 4.7 times the natural linewidth of 0.007 nm. Spectra taken at other pump powers all display a long wavelength asymmetry with a linewidth at least 4.3

times the natural linewidth. The peak of all spectra occurred at the same wavelength indicating no overall shift in fiber temperature with pump power. The absolute value of the peak wavelength is 693.43 ± 0.01 nm, which is consistent with the previous measurements at 77 K [13].

A potential problem with these spectroscopic measurements is line broadening due to self-absorption or line narrowing due to stimulated emission. A conservative estimate of the former effect shows that for a uniformly pumped, uniform temperature fiber, with no ground state depletion, the self-absorption would broaden the spectra by less than a factor of three. Ground state depletion at the laser threshold would reduce the absorption by at least a factor of two, reducing the broadening to a maximum of 2.2 times the natural linewidth. Since the observed broadening is approximately twice this value, the line center shift due to temperature variations is the dominant broadening mechanism. Including temperature broadening in the analysis reduces the calculated self-absorption broadening to negligible levels. Similarly, stimulated emission does not significantly narrow the spectra in fiber samples with an unpolished end face. Such narrowing would be associated with a faster than linear increase in the fluorescence power with pump power which was not observed with these samples.

The value of α_0 to be used in eq. (1) can now be calculated by integrating the measured spectrum at threshold and equating the area under the natural and broadened spectral distribution. The results, (tabulated in table 1), indicate a lossy cavity with a round trip loss of 90% and 98.5% for fibers 1 and 2 respectively. These calculated losses are sensitive to the absorption coefficient value used in eq. (1) and should be taken as only an estimate of the cavity loss. Neglecting material scattering and absorption in the fiber, the losses must stem from either waveguide imperfections or end-face misalignment. The fact that the loss L in the weakly-guiding fiber is roughly half that of the guided wave device suggests that these effects are of comparable importance.

The cw laser output was quasi-steady state with power variations of only $\pm 10\%$. Maximum laser output powers of 3.9 mW and 2.9 mW were observed with fibers 1 and 2 respectively. The pump power in both cases was 750 mW of 514.4 nm radiation. No large scale spiking was seen due to the high cavity losses and

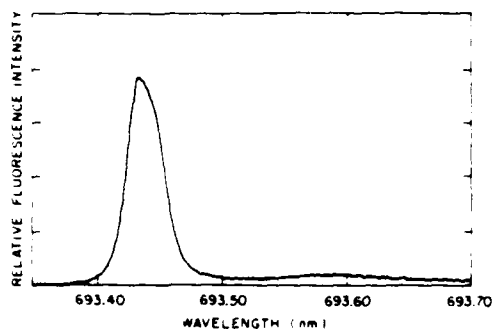


Fig. 3. Ruby fluorescence spectrum at 390 mW of pump power.

highly multi-mode transverse beam profile. The laser beam divergence for both fibers was approximately ten times the diffraction limit. The measured slope efficiency was 1.3% and 0.67% for fibers 1 and 2 respectively.

In conclusion we have demonstrated the first guided wave monolithic resonator crystal fiber device. Ruby laser performance was hampered by the high cavity losses stemming from waveguide scattering and mirror misalignment. Improvements in these areas would allow room temperature laser operation with pump power thresholds well below 100 mW. The lack of sufficiently bright semiconductor light sources in the ruby pump bands will discourage further development of ruby fiber oscillators. However, the experience gained here will prove useful to the development of optical fiber oscillators in other crystal materials such as Nd:YAG.

We gratefully acknowledge useful discussions with M.M. Fejer, M. Digonnet and D.L. O'Meara, all of Stanford University. We are thankful to J.J. Vrheil for polishing the fibers and to L.C. Goddard for the coatings.

This work was supported by the Air Force Office of Scientific Research, Contract #F49620-84-0327, the Joint Services Electronics Program, Contract #N00014-84-K-0327, The National Science Foundation, Contract #DMR-80-20248, and the Lawrence National Laboratories at Livermore, CA, Contract #8518101.

J.L. Nightingale acknowledges the support of the Newport Corporation through the Newport Research Award.

References

- [1] M.J.F. Digonnet and C.J. Gaeta, *Appl. Optics* 24 (1985) 333.
- [2] D.F. Nelson and S. Boyle, *Appl. Optics* 1 (1962) 1981.
- [3] M. Birnbaum and C.L. Fincher, *Appl. Phys. Letts.* 12 (1968) 225.
- [4] A. Szabo, *J. Appl. Phys.* 46 (1975) 802.
- [5] C.A. Burrus and J. Stone, *J. Appl. Phys.* 49 (1978) 3118.
- [6] C.A. Burrus and J. Stone, *Appl. Phys. Letts.* 26 (1975) 318.
- [7] J. Stone and C.A. Burrus, *Fiber and Integrated Optics* 2 (1979) 19.
- [8] M.J.F. Digonnet and H.J. Shaw, *Diode pumped fiber laser, Final Technical Report for AFWAL, TR-83-1110* (July 1983).
- [9] J. Stone and C.A. Burrus, *J. Appl. Phys.* 49 (1978) 2281.
- [10] J.S. Haggerty, *N.A.S.A., Cr-120948*, 1972.
- [11] M.M. Fejer, J.L. Nightingale, G.A. Magel and R.L. Byer, *Rev. Sci. Instr.* 55 (1984) 1791.
- [12] R.C. Pastor, H. Kimura, L. Podokisk and M.A. Pearson, *J. Chem. Phys.* 43 (1965) 3948.
- [13] W. Koechner, *Solid state laser engineering* (Springer-Verlag, New York, N.Y., 1976).

IBM

Journal of Research and Development

Volume 30, Number 4, July 1986

Tunneling microscopy from 300 to 4.2 K

by S. A. Elrod
A. Bryant
A. L. de Lozanne
S. Park
D. Smith
C. F. Quate

Copyright 1986 by International Business Machines Corporation. See individual articles for copying information. Pages containing the table of contents and "Recent papers by IBM authors" may be freely copied and distributed, in any form. ISSN 0886-46

Tunneling microscopy from 300 to 4.2 K

by S. A. Elrod
A. Bryant
A. L. de Lozanne
S. Park
D. Smith
C. F. Quate

A scanning tunneling microscope (STM) has been developed for operation over the full temperature range from 300 to 4.2 K. At room temperature, the instrument has been used to produce topographic images of grain structure in a copper-titanium alloy foil and of atomic structure on a Pt(100) surface. At low temperatures, the instrument can be used in a new spectroscopic mode, one which combines the high spatial resolution of the STM with the existing technique of electron tunneling spectroscopy. This new capability has been demonstrated by using the microscope to probe spatial variations in the superconducting character of a niobium-tin alloy film.

Introduction

While the use of tunneling for microscopy is a fairly recent development, its use as a spectroscopic tool underlies several well-established fields. In the case of tunneling spectroscopy, however, electron flow has conventionally been between planar electrodes separated by a solid insulating barrier. At low temperatures, the current-voltage ($I-V$) characteristics of such sandwich tunnel junctions are found to be rich in spectroscopic information. This information has been successfully related to such diverse physical phenomena as superconductivity of the electrodes [1], inelastic tunneling associated with photons, phonons, or molecular excitations [2], and resonant tunneling through barrier states [3]. All of

these phenomena have characteristic energies below several hundred millielectron volts; low temperatures (≤ 4.2 K) are therefore required to reduce thermal smearing to an acceptable level.

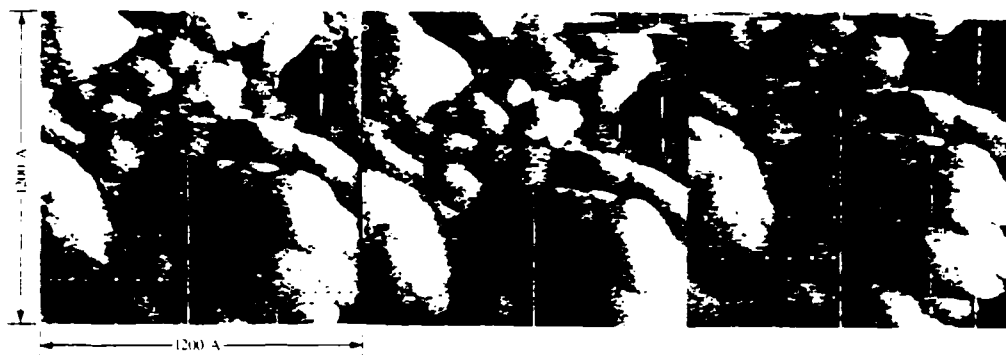
A major disadvantage of conventional planar structures is that the desired spectroscopic information is spatially averaged over the full area of the junction. While junctions as small as $1200 \times 3000 \text{ \AA}$ have been fabricated [4], these dimensions are still considerably larger than the characteristic length over which properties of interest might be expected to vary. For the case of superconductors, the relevant scale is set by the coherence length, which can range from thousands to tens of angstroms. For resonant or inelastic tunneling, large variations can be expected to occur over the size of a single molecule. Conventional tunnel junctions also suffer from the liability that the interpretation of results can be confused by unwanted effects of the nonideal solid tunneling barrier.

The low-temperature tunneling microscope described in this paper was developed in order to capitalize on the demonstrated lateral resolution of the scanning tunneling microscope and to combine it with the powerful and well-established technique of tunneling spectroscopy. It was hoped that the resulting instrument would allow for the possibility of spectroscopic studies of surfaces with a lateral resolution approaching atomic dimensions. In addition to very high lateral resolution, the low-temperature tunneling microscope would offer the advantage of an ideal (vacuum) barrier. The instrument would also afford easy access to the electrodes, making possible the introduction of molecular species for inelastic tunneling spectroscopy [2].

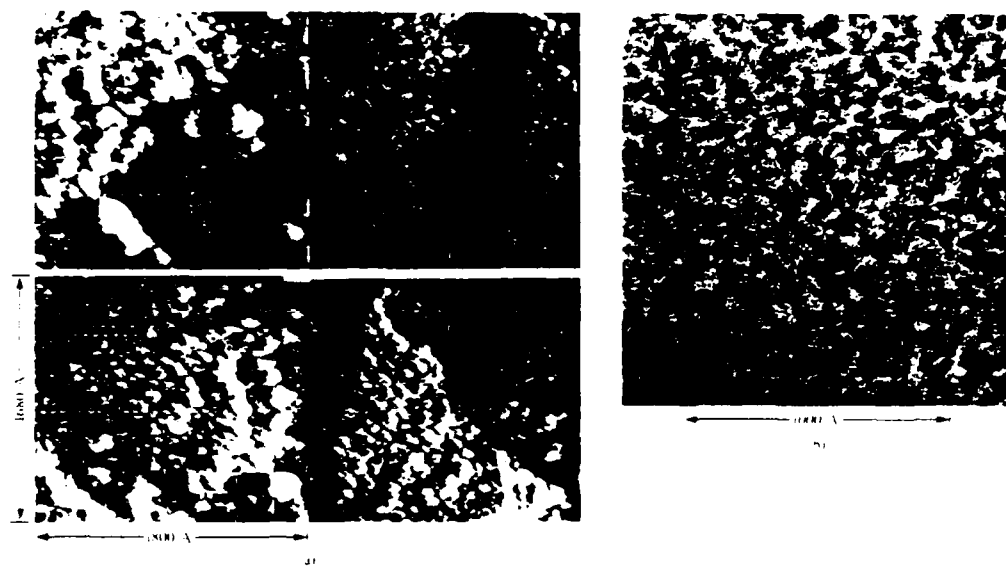
Room-temperature studies

During the development of the low-temperature instrument, several room-temperature studies were conducted. The exponential dependence of tunneling current on

©Copyright 1986 by International Business Machines Corporation. Copying in printed form for private use is permitted without payment of royalty provided that (1) each reproduction is done without alteration and (2) the *Journal* reference and IBM copyright notice are included on the first page. The title and abstract, but no other portions, of this paper may be copied or distributed royalty free without further permission by computer-based and other information-service systems. Permission to republish any other portion of this paper must be obtained from the Editor.



Three topographic images of the same region of a copper-titanium alloy foil. The images were taken in rapid succession to demonstrate reproducibility.



(a) STM images of four different portions of the surface of the copper-titanium foil. (b) TEM image of a similar copper-titanium foil.

interelectrode spacing was verified [5]. As a check on microscope performance, topographic studies of several metal surfaces were made. These studies provided a valuable

check on such important attributes as resolution and image reproducibility. STM images of grain structure in a copper-titanium alloy foil compared favorably with TEM images

Images of a single-crystal surface of Pt(100) showed reproducible features with atomic resolution ($\approx 3 \text{ \AA}$). Details of the topographic mode of STM operation are described elsewhere [5-7].

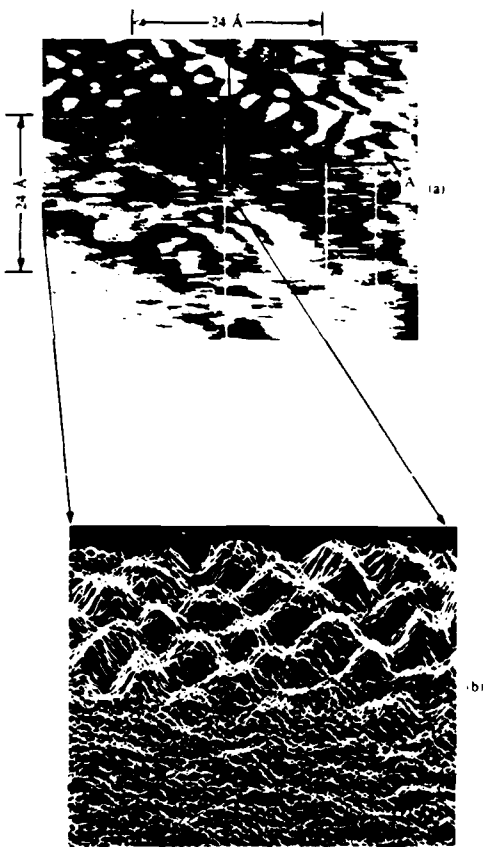
An alloy foil of copper and titanium [8] exhibited very rich structure under topographic examination with the STM. As described elsewhere [8], the sample was prepared by co-sputtering copper and titanium to form an amorphous film of $\text{Cu}_{40}\text{Ti}_{60}$. The film was annealed at 418°C and quenched into a metastable microcrystalline phase having a characteristic grain size of $\approx 60 \text{ \AA}$.

The sample was imaged at a gap resistance of $250 \text{ k}\Omega$ with a tungsten tip at a dc tip voltage of -1.5 mV . It was argon-ion-beam-milled (500 V at 0.26 mA/cm^2 for two minutes), then transferred in air to the STM. Imaging was accomplished at 10^{-7} torr the following day. Images were taken in four minutes with a 1-Hz line rate. Image quality seemed to improve after the tip was touched to the surface with an applied voltage of -30 V and then "walked" to a new location. To compensate for an overall tilt of the sample, data were ac coupled to a significant degree. The z calibration therefore depended on the data frequency and is not included.

Figure 1 shows three images taken in rapid succession. The images show high sensitivity to grain structure and are very reproducible. Shown in **Figure 2(a)** are four STM images taken at different locations on the surface. For comparison, a TEM image of a similar sample [8] has been included in **Figure 2(b)**. We note that while the TEM averages over the entire sample thickness, the STM is surface-sensitive only.

The capability of the STM to resolve atomic features was demonstrated using a platinum sample having a (100) surface. The sample was prepared by cleaning in solvents and then heating in vacuum to approximately 800°C at a pressure of 10^{-6} torr. The tunneling tip was "prepared" by touching it to the surface with an applied voltage of -30 V . The sample was imaged at a gap resistance of $250 \text{ k}\Omega$ and a dc tip voltage of -25 mV . As was the case with the images from the copper-titanium sample, data were ac coupled; the z calibration is therefore not included.

Figure 3(a) shows a region of the platinum surface. The upper left portion of the image shows a square array of atomlike features. The average nearest-neighbor distance is measured to be 3.2 \AA . This portion of the image is also depicted in **Figure 3(b)** in the more conventional amplitude trace format. The expected nearest-neighbor distance for an unreconstructed surface of Pt(100) is 2.8 \AA . The discrepancy with the measured value of 3.2 \AA is within the calibration error of the piezoelectric drives. While it is tempting to identify the square array as the platinum lattice, several cautions are in order. The cleaning procedure which we adopted was modest and is known to leave residual carbon on the surface [9]. In addition, we acknowledge that none of

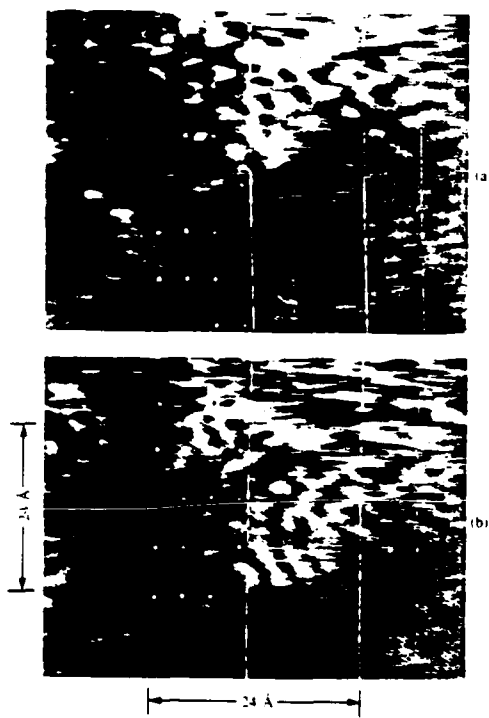


(a) Region of a Pt(100) surface. A square array of atomlike features is identified in the upper left corner. The average nearest-neighbor distance is 3.2 \AA . At location A, a discontinuity is indicated, possibly due to tip switching. (b) Top left corner of (a) is depicted in the more conventional amplitude trace format.

the conventional tools (Auger, LEED) was used to ascertain the degree of surface order and cleanliness. While the measurements are thus nonideal, they nevertheless demonstrate that atomic resolution has been achieved.

Figure 4 shows two images taken in rapid succession to verify that the observed atomic features are reproducible. Each image was obtained in 50 seconds. One feature has been selected; it is indicated by arrows in the images. The displacement of atomic features is believed to be due to thermal drift or piezoelectric creep.

Image interpretation is not always as straightforward as the above results might suggest. In particular, we recognize



Two consecutive images of the same area of a PdIn₂ surface. A feature which can be seen in both images is identified by arrows.

two problems, both associated with the unknown geometry of the tunneling tip. The first is the fundamental problem involved in trying to separate the effects of an unknown tip geometry from those due to surface topography. One can even imagine the extreme case in which a very flat tip is itself imaged by a sufficiently rough surface. The most desirable situation is clearly one in which the surface is atomically flat.

The second problem is associated with the switching of tunneling current between minitips [6]. For a tip with a sufficiently flattened end, switching might even occur between minitips located microns apart. Tip-switching effects have been intermittently observed in most of the topographic studies conducted by our group. In images, these appear as abrupt boundaries between regions which seem unrelated. The effects are most pronounced after the tip has been moved to a new location on the sample, and they seem to decrease with time. For the images presented in this paper (with the possible exception of Figure 3), tip-switching effects are believed to be absent.

Low-temperature studies [10]

The low-temperature tunneling microscope (LTTM) offers the first opportunity to conduct spectroscopic studies of surfaces with a lateral resolution approaching atomic dimensions. Of all the physical phenomena which can give rise to identifiable spectroscopic features in the tunneling I - V characteristic, superconductivity of the electrodes has one of the largest and most distinctive signatures. Superconductive tunneling was therefore chosen as the first spectroscopy with which to test the capabilities of the new instrument.

For two reasons, the surface of superconducting Nb₃Sn was selected as the one to be studied. First, independent measurements [11] indicated the possible presence of microscopic spatial inhomogeneities, which would provide a contrast mechanism for spectroscopic imaging. Second, the energy gap of Nb₃Sn is among the largest known (3.3 mV) [11] and should be readily discriminated in the tunneling I - V characteristic.

As a normal tip is scanned over the superconducting Nb₃Sn surface, a single parameter is extracted from the I - V characteristic to provide a direct measure of the local superconductivity. Images produced in this fashion show strong spatial variations, with reproducible transitions between fully normal and fully superconducting behavior on length scales as small as 13 nm. Images taken above and below the critical temperature confirm that the observed effects are due to superconductive tunneling. Additional confirmation comes from a successful fit of the measured I - V curves to a simple superconductor-insulator-normal metal (SIN) tunneling model [7].

Poppe and Schroder [12] have developed an apparatus similar to the LTTM described in this paper. We also acknowledge the low-temperature tunneling work of Moreland et al. [13], who use flexible substrates to control the interelectrode spacing. In both cases, the authors obtain excellent tunneling characteristics, although in neither case has a scanning capability (i.e., microscopy) yet been demonstrated.

• Spectroscopic imaging

- The I - V characteristic of an SIN junction can provide detailed information on the properties of the superconducting electrode [1]. With respect to the ohmic case, the most pronounced alteration in the I - V characteristic is associated with a gap in the excitation density of states of the superconductor.

For spatially resolved LTTM studies of superconductivity, one would ideally like to measure the full I - V curve at every point on the sample surface. The local value of the energy gap could then be deduced by fitting the individual I - V curves to a simple SIN tunneling model [1, 6]. For this pilot study of the LTTM's capabilities, however, a simplified approach was taken.

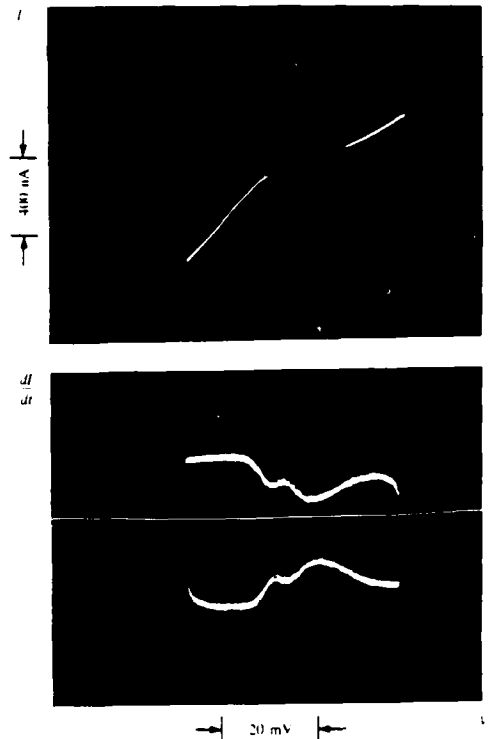
For spectroscopic studies, the gap voltage is triangle-wave modulated at 1 kHz. The analog time derivative of the junction current (dI/dt) is displayed as a function of junction voltage, yielding a sensitive measure of the local electronic structure but differing from the conventional dynamic conductance (dI/dV) by a factor of dV/dt . At the same time that the $I-V$ curve is being swept at 1 kHz, the ac current is detected with a lock-in amplifier to provide a signal proportional to the gap resistance averaged over the full $I-V$ curve. This signal is further amplified to provide feedback to the piezoelectric drive which controls the interelectrode spacing. Since the 1-kHz sweep rate is fast compared to the feedback response, the only effect of the latter is to stabilize the average gap resistance at the desired equilibrium value.

As the tip is scanned laterally, the magnitude of dI/dt changes with variations in superconductivity and/or topography. Some care must therefore be taken to sort out the different effects on the tunneling current. In order to obtain a spectroscopic image of the sample, we choose to extract a single parameter from the $I-V$ curve which is a direct measure of the local superconductivity but excludes the effects of changing topography. This is accomplished by sampling the zero-bias value of dI/dt and normalizing it to the average gap resistance.

We justify this particular choice of spectroscopy signal in the following way. We assume that the basic physics of the tunneling process, and hence the shape of the $I-V$ characteristic curve, remains unchanged as the gap resistance varies (due to topography) about its equilibrium value. In a simple SIN tunneling model, the normal state resistance enters the problem only as an overall normalization factor. With the assumptions noted above, the normalization procedure yields a signal which equals unity for normal metal-insulator-normal metal (NIN) junctions (independent of topography) and zero for ideal SIN junctions at $T = 0$. A more detailed justification for this procedure is given in [6].

• LTTM results for Nb₃Sn

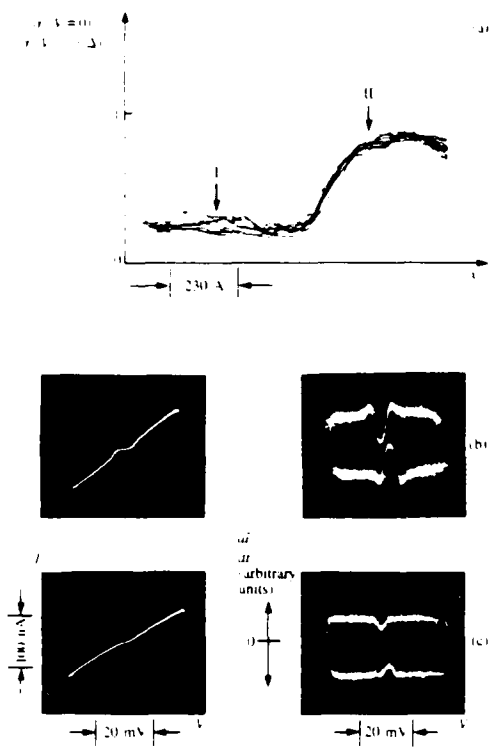
In order to minimize the oxide contribution to the tunneling barrier, iridium was used for the normal metal tip. The sample which was examined was a thin film of Nb₃Sn with an inductively measured critical temperature of 18 K. To reduce the possibility of lattice damage (and resultant degradation of superconductivity) from the cleaning procedure, the sample was not ion-milled as in previous experiments [5], but rather was briefly etched in a 10% aqueous solution of HF immediately before being installed in the tunneling unit. Following pumpdown and cooling to 4.2 K, helium exchange gas was introduced into the vacuum space (resulting in a pressure increase to 5×10^{-5} torr). Cold-plate baffles ensured that only helium gas reached the sample. Tunneling measurements were made in the exchange gas.



Prior to tip cleaning. Traces of I vs. V and dI/dt vs. V for a Nb₃Sn sample and an iridium tip at a temperature of 6 K.

Prior to the tip-cleaning procedure described below, $I-V$ curves were unstable, with gross features superimposed on the less pronounced (if present) superconducting gap. Maxima and minima in dI/dt at voltages from 0 to 100 mV, along with either sign of overall second derivative, were measured. Similar effects were observed for nonsuperconducting samples. The $I-V$ characteristic in Figure 5 is representative of the type frequently encountered. The figure shows both I vs. V and dI/dt vs. V for a Nb₃Sn sample and an iridium tip at a gap resistance of 50 k Ω and a temperature of 6 K.

The superconducting gap of Nb₃Sn is expected to be in the range of 2.3 to 4.5 mV [11]. Any gap structure present in Figure 5 is totally obscured by background distortions of the $I-V$ characteristic. Similar effects were observed at gap resistances up to 1 M Ω , and for different sample and tip materials. $I-V$ characteristics of the type shown in Figure 5 were unstable, changing among a myriad of different shapes on a time scale of seconds.



a. Repeated spectroscopic normalized zero-bias conductance line scans over a region of the Nb₃Sn sample, showing a continuous spatial transition between normal and superconducting behavior
 b. and c. I-V characteristics corresponding to locations I and II

Possible explanations for the observed *I*-*V* characteristics include (1) low effective barrier height, (2) resonant tunneling, and (3) inelastic tunneling. In the first case, we refer to nonohmic contributions to the tunneling current which become significant when the applied voltage is no longer much less than the barrier height [14]. Very low barrier heights (≈ 0.1 eV) would result in nonlinear behavior at the low voltages shown in Figure 5. Such barrier heights have been intermittently observed with the STM [6]; their origin is not well understood. In any case, the simple explanation of low barrier height would only account for a monotonic increase in the dynamic conductance about its minimum value.

The second possibility is that of resonant transmission through an impurity situated somewhere between the tunneling electrodes [3]. Field-emission studies [15] of

resonant tunneling through adsorbed species suggest that large effects on the *I*-*V* characteristic are to be expected. Observed time-dependent effects in the STM would correspond to the migration of molecules on the sample or tip, possibly under the influence of the high electric field (10 V/m) near the tip. The helium exchange gas used in these experiments may have participated in such resonant tunneling effects.

The third possibility is that of inelastic tunneling associated with the excitation of vibrational modes of molecules situated between the tip and surface. For planar junctions [2], inelastic tunneling spectra show peaks which agree closely with known infrared and Raman-mode energies. Conductance changes of $\leq 1\%$ are observed for monolayer impurity coverage on planar junctions. Enhancement by a factor of three has recently been predicted for the STM [16]. This is still too small to account for the observed structure in Figure 5.

At moments of particular stability, *I*-*V* curves could be made to change reproducibly and continuously among different shapes by scanning the tip laterally. Changes of this type occurred down to scan sizes of several angstroms, providing partial evidence that the observed effects were due to single atoms or molecules.

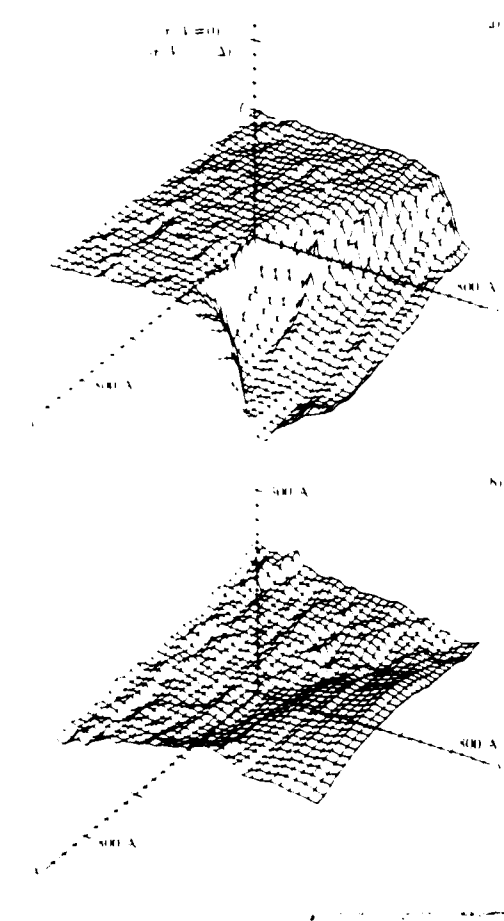
While these effects are very interesting and deserve further study, they tend to wreak havoc on any effort to obtain spectroscopic images of superconductivity. The imaging technique described above assumes an ohmic *I*-*V* characteristic for voltages significantly greater than the superconducting gap. *I*-*V* characteristics like that shown in Figure 5 would give wildly varying spectroscopic image signals having no relationship to the local superconductivity

A tip-cleaning procedure was used to eliminate such effects. With -30 V applied to the tip, the gap spacing was reduced until current flowed. Initially, the current would increase uncontrollably, reaching the resistor-limited value of 1.2 μ A. After several attempts, it became possible to control the current at 200 nA. The current was maintained at this value for several minutes. *I*-*V* curves taken after this procedure were stable and essentially ohmic. However, the procedure resulted in the extinction of superconductivity over the full field of view of the scanner (2000×2000 \AA). It was therefore necessary to move the tip to a new location with the magnetic walker [17] in order to observe superconducting features. Results reported in the remainder of this paper were taken after using this tip-cleaning procedure.

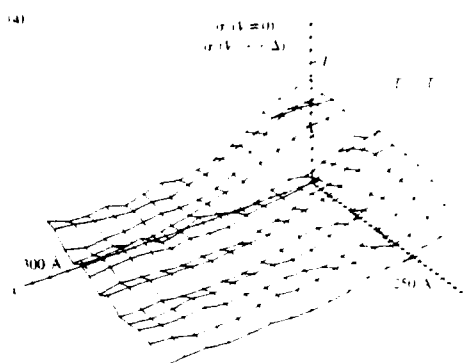
Shown in Figure 6 are repeated spectroscopic line-scans over a region of the sample, generated using the spectroscopic signal extraction technique described above. They show a continuous spatial transition between normal and superconducting regions which occurs over a distance of 230 \AA . This is larger than, and therefore consistent with, the coherence length of Nb₃Sn (≈ 40 \AA). *I*-*V* characteristics for

locations I and II are shown in the figure, as are the time derivatives used to obtain the spectroscopic signal.

Shown in Figure 7 is a full x - y image of the spatial variations of superconductivity over a region of the Nb₃Sn surface. For this image, scanning was in the x direction; each x line-scan was taken 20 times and signal-averaged by computer. Images taken in immediate succession show excellent reproducibility; rotation of the scanning direction by 90 degrees did not alter the image appreciably. Also shown in the figure are topographic data which were obtained concurrently. The spectroscopic image shows a



(a) Full x - y images of the superconducting character of the Nb₃Sn sample. The distance between successive grid lines is 27 Å. The vertical axis is the normalized zero-bias conductance, as discussed in the text. (b) Topographic data obtained concurrently.



Spectroscopic images obtained (a) below and (b) above the critical temperature

transition between normal and superconducting regions which is defined by an arc in the x - y plane. The topographic image shows a similar boundary between the two regions: the superconducting region appears topographically flat, while the normal region shows more texture. Possible explanations for observed variations are discussed below. We note that a significant fraction of the data for Nb₃Sn do not show such variations, but rather show exclusively superconducting or normal behavior.

Figure 8 shows spectroscopic images taken over a region of the sample below and above its critical temperature. Taken at 6.2 K, part (a) shows a distinct transition between normal and superconducting regions. Warming the sample above 20 K with a resistive heater resulted in the spectroscopic image shown in part (b). This figure demonstrates the success of the spectroscopic signal extraction technique in normalizing out topographic variations.

- Possible causes for observed variations

There are several possible causes for the spatial variations of superconductivity observed in this sample. The first is the presence of microscopic inhomogeneities on a scale of less than 1 μm . The presence of such inhomogeneities is suggested by heat capacity measurements [18], which show a spread in the transition temperature of niobium-tin samples. This is an unlikely explanation for the sample (25 at% Sn) used in these studies, however, because it is outside the composition range (20 at% to 24 at% Sn) for which a spread in T_c is observed.

On the other hand, the best tunnel junctions fabricated using stoichiometric Nb₃Sn films still show a large spread in the superconducting gap (2.3 mV to 4.1 mV) [11]. The origin of this spread is not understood, but it can be successfully modeled by assuming the presence of microscopic domains having a distribution of energy gaps [11].

The second possibility is gap anisotropy [19], which would introduce spatial variations due to the different orientations of neighboring microcrystals. This cannot, however, explain the full variation between normal and superconducting behavior depicted in Figure 7. Furthermore, the Nb₃Sn films used in this study typically grow with a preferred [200] orientation normal to the substrate [11]. Tunneling therefore proceeds along that direction unless there is substantial texture on the surface.

The last possibility is that the variations are due to damage created either by previous ion milling [5] or by the tip-cleaning procedure described above. The latter is perhaps the most likely current explanation, since the superconductive tunneling is locally extinguished after tip cleaning.

It should be emphasized that regardless of the cause of the variations observed on this sample, the results demonstrate a direct measurement of the superconducting gap on a scale two to three orders of magnitude finer than previous techniques.

Acknowledgments

We thank F. Hellman, A. F. Marshall, and S. Park for generously contributing samples for these studies. This research was sponsored by the IBM Corporation, the Defense Advanced Research Projects Agency, the Office of Naval Research, and the Joint Services Electronics Program.

References and note

1. L. Solymar. *Superconductive Tunneling and Applications*. Wiley-Interscience Publishers, New York, 1972.
2. *Tunneling Spectroscopy*. P. K. Hansma, Ed., Plenum Press, New York, 1982.
3. S. J. Bending and M. R. Beasley. *Phys. Rev. Lett.* **55**, 324 (1985); M. Ya. Azbel. *Solid-State Commun.* **45**, No. 7, 527 (1983).
4. C. T. Rogers and R. A. Buhrman. *IEEE Trans. Magnetics* **MAG-19**, No. 3, 453 (1983).

5. S. Elrod, A. L. de Lozanne, and C. F. Quate. *Appl. Phys. Lett.* **45**, No. 11, 1240 (1984).
6. Scott Alan Elrod. Ph.D. Thesis, Stanford University, California, 1985.
7. A. L. de Lozanne, S. A. Elrod, and C. F. Quate. *Phys. Rev. Lett.* **54**, No. 22, 2344 (1985).
8. A. F. Marshall, Y. S. Lee, and C. A. Stevenson. *Acta Metall.* **31**, No. 8, 1225 (1983).
9. J. L. Gland and G. A. Somorjai. *Surf. Sci.* **38**, 157 (1973).
10. Sections of this paper have been excerpted from Ref. [1] and from A. L. de Lozanne and S. A. Elrod. *Bull. Amer. Phys. Soc.* **30**, No. 3, 322 (1985).
11. D. Rudman, F. Hellman, R. H. Hammond, and M. R. Beasley. *J. Appl. Phys.* **55**, No. 10, 3544 (1984); D. Rudman. Ph.D. Thesis, Stanford University, California, 1982.
12. U. Poppe and H. Schroder. *Proceeding of the 17th Conference on Low-Temperature Physics* LT-17, 835 (1984).
13. J. Moreland, S. Alexander, M. Cox, R. Sonnenfeld, and P. K. Hansma. *Appl. Phys. Lett.* **43**, No. 4, 387 (1983).
14. J. Simmons. *J. Appl. Phys.* **34**, No. 6, 1793 (1963) and *J. Appl. Phys.* **34**, No. 9, 2581 (1963).
15. J. W. Gadzuk. *Phys. Rev. B* **1**, 2110 (1970).
16. G. Binnig, N. Garcia, and H. Rohrer. *Phys. Rev. B* **32**, No. 2, 1356 (1985).
17. Douglas P. E. Smith and Scott A. Elrod. *Rev. Sci. Instrum.* **56**, No. 10, 1970 (1985).
18. F. Hellman, D. A. Rudman, S. R. Early, and T. H. Geballe. *Bull. Amer. Phys. Soc.* **27**, 347 (1982).
19. *Anisotropy Effects in Superconductors*, H. W. Weber, Ed., Plenum Press, New York, 1977.

Received July 2, 1985, accepted for publication November 8, 1985

Scott A. Elrod *Xerox Corporation, Palo Alto Research Center, Palo Alto, California 94304* Dr. Elrod received an A.B. degree in physics from Earlham College, Richmond, Indiana, in 1981 and a Ph.D. in applied physics from Stanford University, California, in 1985. His Ph.D. research was directed toward the development of a low-temperature tunneling microscope. Dr. Elrod is currently a Visiting Scientist at the Xerox Palo Alto Research Center.

Andres Bryant *Edward L. Ginzton Laboratory, Stanford University, Stanford, California 94305* Mr. Bryant received a B.S.E. in 1982 from the University of Maine at Orono and an M.S.E. in 1984 from Stanford University, California. He is currently working toward a Ph.D. in electrical engineering at Stanford. He was a recipient of IBM fellowships in 1983 and 1984. Mr. Bryant's research interests include the scanning tunneling microscope and its application to mass storage and nanolithography.

Alex L. de Lozanne *Department of Physics, University of Texas at Austin, 200 West 21st Street, Austin, Texas 78712* Dr. de Lozanne is an Assistant Professor. Previously he held the Chodorow Fellowship in Applied Physics at Stanford University, under which this work was done. His Ph.D. thesis (Stanford University, California, 1982) on high critical temperature Josephson devices was directed by Professor M. R. Beasley. He received his bachelor's degree with highest distinction from Purdue University, Lafayette, Indiana, in December 1976. His academic honors include the Danforth, IBM, and Chodorow fellowships, the R. W. King Award, and election to Phi Beta Kappa, Phi Kappa Phi, and Sigma Pi Sigma.

Sang-II Park *Edward L. Ginzton Laboratory, Stanford University, Stanford, California 94305* Mr. Park received a B.S. in physics from Seoul National University, Seoul, Korea, in 1981. He is currently a Ph.D. candidate in applied physics at Stanford, working on room-temperature STM especially directed toward surface physics.

Douglas P. E. Smith *Edward L. Ginzton Laboratory, Stanford University, Stanford, California 94305* Mr. Smith received his A.B. in 1981 from Dartmouth College, Hanover, New Hampshire, and worked from 1981 to 1983 at the IBM Thomas J. Watson Research Center. Since 1982 he has been a doctoral student in the Applied Physics Department at Stanford. His present research concerns low-temperature scanning tunneling microscopy and the use of field ion microscopy to clarify the nature of the STM tip.

Calvin F. Quate *Edward L. Ginzton Laboratory, Stanford University, Stanford, California 94305* Dr. Quate is a Professor of Applied Physics and Electrical Engineering. He received a B.S. degree in 1944 from the University of Utah, Salt Lake City, and a Ph.D. degree in 1950 from Stanford University, California, both in electrical engineering. In 1984 he became a Senior Research Fellow at Xerox Corporation, Palo Alto Research Center. Dr. Quate is a member of the American Physical Society, the National Academy of Engineering, and the National Academy of Sciences. He is a Fellow of the Acoustical Society, the American Academy of Arts and Sciences, and the Institute of Electrical and Electronics Engineers; and an Honorary Fellow of the Royal Microscopical Society. He was awarded the IEEE Morris N. Liebmann Award in 1981 and the Rank Prize for Opto-Electronics in 1982. His research interests include imaging, scanning microscopy, and new concepts for data storage.

Characterization of proton-exchanged waveguides in MgO:LiNbO_3

M. Digonnet, M. Fejer, and R. Byer

Edward L. Ginzton Laboratory, W. W. Hansen Laboratories of Physics, Stanford University, Stanford, California 94305

Received December 31, 1984; accepted February 26, 1985

We report the fabrication and characterization of proton-exchanged waveguides in MgO -doped LiNbO_3 , a high-optical-damage threshold material. Results indicate waveguide characteristics similar to those of waveguides fabricated in undoped LiNbO_3 except for slower diffusion rates and freedom from etching of the surface when pure benzoic acid is used as a proton source. An optical-damage threshold of 70 kW/cm^2 was measured at $0.5145 \mu\text{m}$ in a MgO:LiNbO_3 waveguide, corresponding to a factor-of-2 improvement over undoped LiNbO_3 .

It was shown by Zhong *et al.*¹ and more recently by Bryan *et al.*² that LiNbO_3 doped with approximately 5% or more MgO exhibits a remarkably reduced photorefractive response compared with undoped LiNbO_3 . It is believed that the reduced photorefractive response is due to the increased photoconductivity of the MgO:LiNbO_3 .² Such a material offers great promise for nonlinear and integrated optics, for which induced photorefractivity (optical damage) has been a serious limitation in the past. It must be noted that the enhanced photoconductivity may cause deleterious effects in devices requiring the application of low-frequency electric fields.

As a first step toward the demonstration of efficient nonlinear guided-wave devices, it was interesting to fabricate proton-exchanged waveguides in MgO:LiNbO_3 . Compared with other waveguide fabrication processes in LiNbO_3 , proton exchange has been shown to be a rapid low-temperature process and to yield waveguides with interesting applications in polarization filtering and birefringence control.³ In this Letter we report the fabrication of H^+ -exchanged waveguides in MgO:LiNbO_3 and describe the waveguide characteristics and power handling at short wavelengths.

Waveguides were fabricated in x- and y-cut 5% MgO -doped LiNbO_3 crystals grown by Crystal Technology, Palo Alto, California. The now standard technique of proton exchange in a melt of benzoic acid containing varying amounts of lithium benzoate was used.⁴ Benzoic acid has been shown to have an appropriate dissociation constant, melting temperature, and stability as a liquid for use in this process.^{1,4} The addition of lithium benzoate to the melt provides a means of controlling the proton concentration in the exchanged region, which has a strong bearing on the crystal structure and the optical properties and quality of the waveguide.⁵

The acid melt, containing between 0 and 2 mol % lithium benzoate, was contained in a glass flask equipped with a condensing column. The column was used to reduce material loss and composition change of the melt, as the waveguide characteristics have been

shown to depend strongly on the concentration of Li^+ ions in the melt.⁴ The wafer to be exchanged was held in a glass tube provided with lateral cuts to let the liquid penetrate inside the tube. All exchanges were performed at the boiling temperature of the melt, about 249°C in pure acid and 246 and 243°C for melts containing 1 and 2% lithium benzoate, respectively. This arrangement yielded easily reproducible results.

After fabrication the waveguide index profiles were characterized using the prism-coupling launching-angle measurement to determine the effective indices of the guided modes. The guide index profile was then recovered from the mode indices with a standard inverse WKB method. Figure 1 shows a typical set of index profiles measured at different wavelengths for an x-cut MgO:LiNbO_3 waveguide exchanged for 3 h in pure benzoic acid. The profiles exhibit the same step-index shape as is characteristic of proton-exchanged waveguides in undoped LiNbO_3 with an increase of the ex-

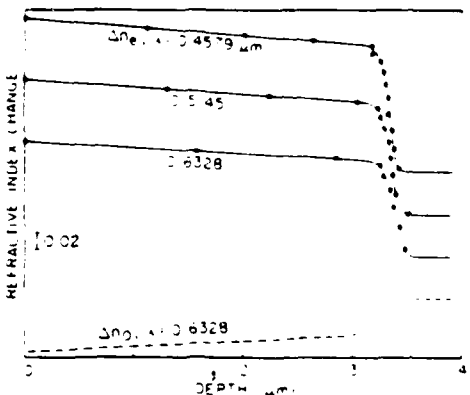


Fig. 1. Typical n_x and n_z profiles of a proton-exchanged waveguide in MgO:LiNbO_3 . The x-cut wafer was processed for 3 h in pure benzoic acid at 245°C . The profiles were shifted vertically for clarity.

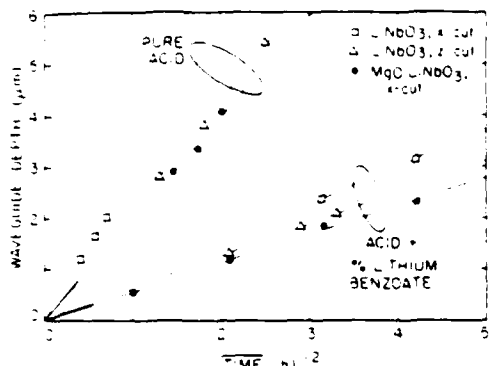


Fig. 2. Waveguide depth versus the square root of the exchange time in doped and undoped LiNbO_3 treated in melts of different compositions.

extraordinary index (of the order of 0.135 at the wavelength of $\lambda = 0.6328 \mu\text{m}$) and a decrease of the ordinary index. This result indicates that the presence of MgO in the crystal lattice does not significantly alter the exchange process.

The negative ordinary index profile was measured by launching a wave at an angle θ to the usual propagation direction (along y) in an x -cut waveguide. The resulting index step Δn seen by the wave is then a known combination of Δn_s and Δn_e , from which the latter can easily be extracted. Alternatively, one can measure the critical angle θ_c for which the wafer no longer supports a guided mode. This method yielded the value of $\Delta n_e = -0.06 \pm 0.006$, in good agreement with previously published values for the undoped material.⁴

We show in Fig. 2 the evolution of the waveguide depth with the square root of the exchange time for waveguides fabricated in MgO -doped and -undoped LiNbO_3 in melts of different compositions. The dependence is linear, which suggests a diffusionlike behavior for both materials. One can thus characterize the exchange rate by the diffusion coefficient D , defined by $d = (4Dt)^{1/2}$, where d is the depth (at half-maximum) of the waveguide and t the exchange time. As is shown in Fig. 3, the exchange rate decreases as the Li^+ melt concentration is increased, following an exponential law previously established for undoped LiNbO_3 .⁵ The exchange rate is lower in z -cut than in x -cut wafers for the undoped material, and is even lower in the x -cut orientation for the doped material. This result is similar to the situation in Ti-diffused LiNbO_3 , where the presence of Ti slows down the proton-exchange rate.⁶ Note that the exchange rate is still very high with melts containing up to 1% of lithium benzoate: a single-mode waveguide can be fabricated in less than a few minutes.

Waveguides were also fabricated in y -cut $\text{MgO}:\text{LiNbO}_3$ in pure benzoic acid with no evidence of surface etching up to the maximum exchange time that was tested, about 4 h. Again, this observation parallels that of other authors concerning proton exchange in waveguides previously doped with titanium.⁷ The diffusion

rates were found to be essentially the same for x -cut and y -cut $\text{MgO}:\text{LiNbO}_3$.

Figure 4 illustrates the index changes Δn_s measured in two $\text{MgO}:\text{LiNbO}_3$ waveguides at different wavelengths and the corresponding single-pole Sellmeier curve to which they were fitted. The index change was found to vary substantially across the visible and near-infrared ranges, from about 0.18 at $0.4579 \mu\text{m}$ to 0.12 at $0.820 \mu\text{m}$ for waveguides made in pure acid. This fairly strong Δn_s dispersion indicates a higher index dispersion for $\text{Li}_{1-x}\text{H}_x\text{NbO}_3$ (whether or not doped with MgO) than for unexchanged LiNbO_3 for the wide range of proton concentration x that was tested. For a given Li concentration, we found that Δn_s was larger in the doped than in the undoped material by about $2-3 \times 10^{-3}$ for x -cut samples. Δn_s decreases linearly with increasing Li concentration in the melt, with essentially the same slope for the MgO -doped (x -cut) and undoped (x and z cuts) material. We measured a slope $d(\Delta n_s)/d[L_1^+]$ of $-0.019/\text{mol} \cdot \text{cm}^2$ at $\lambda = 0.6328 \mu\text{m}$.

Several authors reported aging of proton-exchanged LiNbO_3 waveguides, apparent as a reduction of the surface index and of the waveguide depth over a period of a few days, especially in waveguides fabricated in pure acid.⁸ The same phenomena were observed in $\text{H}^+:\text{MgO}:\text{LiNbO}_3$ waveguides. Stronger mode coupling was also noticed in waveguides exchanged in pure acid. Postannealing, a process that was shown to eliminate these difficulties,⁹ is clearly also needed for doped LiNbO_3 to control the crystal phase of the exchanged layer and stabilize its surface index. Since we did not anneal our waveguides after exchange, we performed all the measurements described here approximately one day after the wafer was removed from the melt to keep our results consistent.

Zero-field photorefractive sensitivity (optical damage) in both types of waveguides was observed to have a fairly high threshold at short wavelengths. Up to about 1 mW of light was coupled into our waveguides for routine characterization without apparent long-term effects on the waveguide index, even at $0.4579 \mu\text{m}$.

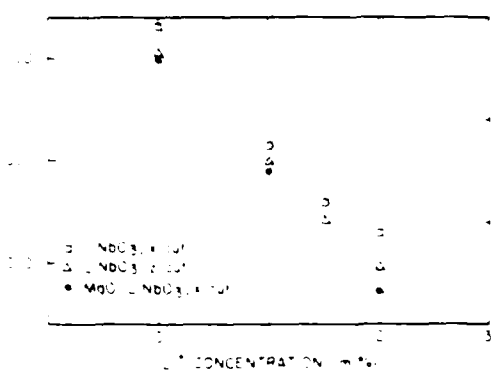


Fig. 3. Comparison of proton-diffusion rate in doped and undoped LiNbO_3 as a function of the Li^+ concentration in the melt.

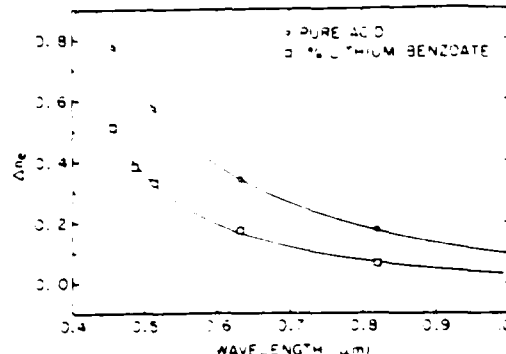


Fig. 4. Δn , dispersion of x-cut MgO-doped LiNbO₃ waveguides for two Li⁺ concentrations in the melt.

Quantitative measurements also indicated a good short-term tolerance to relatively high optical intensities. Short-term optical-damage thresholds were measured by prism coupling a 0.5145- μm beam focused in the waveguide plane to a 40- μm -diameter spot size with a cylindrical lens. The TE₀ mode output was apertured with a narrow slit and recorded as a function of time for different power levels. Damage appeared as a broadening of the output mode in the plane of the waveguide and was recorded as a drop of the measured power. The short-term-damage threshold was arbitrarily defined as the coupled power at which the recorded output dropped by 10% in 1 min. Damage thresholds were slightly higher in annealed samples (annealing was performed by bringing the wafers up to about 250°C and letting them cool slowly over several hours). Initial measurements indicate a threshold of 13 mW in a nine-mode undoped LiNbO₃ waveguide and 10.5 mW in a three-mode MgO:LiNbO₃ waveguide. This corresponds to an intensity of 35 and 70 kW/cm², respectively, one of the highest intensities achieved to date in a LiNbO₃ waveguide at this wavelength and about 4 orders of magnitude higher than we observed in Ti-diffused LiNbO₃ guides.

It should be noted that the photorefractive sensitivity of a LiNbO₃ waveguide is a complicated function of the optical and thermochemical history of the device. The simple test described here is useful for the comparison of short-term damage effects in various waveguides, but it must be recognized that more-sensitive measurement techniques⁹ would undoubtedly find damage effects at intensities much lower than those reported here.

It was recently reported that proton-exchanged waveguides in undoped LiNbO₃ have significantly increased dark conductivity. This enhanced dark con-

ductivity probably accounts for the relatively small advantage of highly photoconductive MgO:LiNbO₃ over the undoped material for proton-exchanged waveguides.¹⁰ Further tests are now under way to improve the power tolerance of the waveguides.

In conclusion, we have characterized the parameters of proton-exchanged waveguides in high-damage-threshold MgO:LiNbO₃ and have compared these with waveguides made in undoped LiNbO₃. The major differences include a slower proton-diffusion rate and no etching of the y face in MgO:LiNbO₃ waveguides, as has also been observed in Ti-diffused, proton-exchanged waveguides. A factor-of-2 improvement in optical damage threshold (about 70 kW/cm²) at 0.5145 μm was achieved in a proton-exchanged MgO-doped LiNbO₃ waveguide compared with a waveguide made of undoped LiNbO₃.

This research was supported jointly by Litton Systems, Inc., the U.S. Air Force Office of Scientific Research (contract F49620-84-0327), the Joint Services Electronics Program (contract N00014-84-K-0327), the National Science Foundation (contract DMR-80-20248), and the Lawrence National Laboratories, Livermore (contract 3518101).

We are grateful to Crystal Technology, Inc., for providing us with the MgO:LiNbO₃ used in these measurements. The authors are also indebted to David O'Meara for the preparation of the samples and to Mei Lu for her help in the waveguide fabrication.

M. Digonnet is with Litton Systems, Inc., Chatsworth, California, and is a Visiting Scholar at Stanford University.

References

1. G.-G. Zhong, in *Proceedings of 12th International Quantum Electronics Conference* (IEEE catalog no. 80-CH1561-0) (Optical Society of America, Washington, D.C., 1980), p. 631.
2. D. A. Bryan, R. Cerson, and H. E. Tomaschke, *Appl. Phys. Lett.* **44**, 847 (1984).
3. J. L. Jackel, C. E. Rice, and J. J. Veselka, *Appl. Phys. Lett.* **41**, 607 (1982).
4. M. DeMicheli, J. Botineau, S. Neveu, P. Sibillot, D. B. Ostrowsky, and M. Papuchon, *Opt. Lett.* **8**, 114 (1983).
5. J. L. Jackel, C. E. Rice, and J. J. Veselka, *Electron. Lett.* **19**, 387 (1983).
6. C. E. Rice and J. L. Jackel, *Mat. Res. Bull.* **19**, 591 (1984).
7. J. L. Jackel and C. E. Rice, *Proc. Soc. Photo-Opt. Instrum. Eng.* **460**, 43 (1984).
8. M. DeMicheli, J. Botineau, P. Sibillot, D. B. Ostrowsky, and M. Papuchon, *Opt. Commun.* **42**, 101 (1982).
9. R. A. Becker, *Soc. Photo-Opt. Instrum. Eng.* **460**, 75 (1984).
10. R. A. Becker, *Proc. Soc. Photo-Opt. Instrum. Eng.* **517**, 194 (1984).

High-speed high-resolution fiber diameter variation measurement system

Martin M. Fejer, Gregory A. Magel, and Robert L. Byer

A fiber diameter variation measurement system is described which is capable of measuring transparent fibers with 0.02% diameter resolution and 6- μm axial resolution at a measurement rate of 1 kHz and with a working distance of >100 mm. The principles of its operation are discussed in detail, and experimental confirmation of its performance is reported. A theoretical calculation of the optimum obtainable diameter resolution for a given set of experimental parameters is also presented.

I. Introduction

There is considerable current interest in the growth and application of single crystal fibers for nonlinear optical, miniature laser, and acoustic devices.¹⁻⁴ Our efforts to apply the miniature pedestal growth technique^{1,5} to the growth of refractory oxide fibers have shown that closed-loop control of the fiber diameter is necessary to achieve the diameter control requisite for useful device applications.

The crystal growth process involves melting the tip of a source rod with a tightly focused CO₂ laser, dipping the seed crystal into the melt, and then effecting a diameter reduction by pulling the seed more rapidly than feeding in the source. Since there is no viscous draw-down region, small scale diameter variations tend to be frozen into the fiber instead of being stretched to long periods and low amplitudes as in glass fiber pulling. It is thus necessary to measure the fiber diameter with high axial resolution in addition to good diameter resolution. The CO₂ laser focusing optics and the short thermal time constant of the molten zone impose additional constraints on the working distance and measurement rate.

While the diameter control tolerances and the growth parameters depend in detail on the material and device application involved, the following criteria specify a measurement system useful for a broad range of crystal

fiber applications: diameter variation resolution better than 0.1% for fiber diameters between 20 and 500 μm ; axial resolution better than 10 μm ; working distance >100 mm; and measurement rate faster than 100 Hz.

The forward scattering pattern from a fiber illuminated by a laser beam perpendicular to the fiber axis can be used to measure the diameter of the fiber.⁶ A fiber diameter measurement device based on counting the number of fringes scattered into a particular angular range has been described previously.⁷ While the speed and resolution of the above system are suitable for our application, the optical system for imaging the requisite large 60° angular range becomes quite unwieldy at 100 mm working distances. Moreover, the lack of any provision for axial resolution, i.e., selection of a thin section whose diameter is to be measured, limits the usefulness of the previous diameter measurement approach for single-crystal fiber growth. The remainder of this paper describes the design of the electronic and optical systems developed to implement fiber diameter variation measurements. Experimental verification of the system performance is also presented.

II. Measurement Approach

It is possible to simplify substantially the optical system by accurately tracking the position of the center of a single fringe scattered at a large angle rather than attempting to count a large number of fringes. An anamorphic optical system can be used to obtain improved axial resolution by focusing the laser beam perpendicular to the fiber axis.

A simplified diagram of the fiber diameter measurement approach is shown in Fig. 1. A plane wave of wavelength λ illuminates the fiber. A fringe scattered at an angle θ is imaged onto a photodiode array by a lens of focal length f in a Fourier transform configuration. The center-to-center spacing of the elements of the diode array is s .

The authors are with Stanford University, Applied Physics Department, Ginzton Laboratory, Stanford, California 94305.

Received 12 March 1985.

0873-791X/85/152362-07\$02.00/0.

© 1985 Optical Society of America.

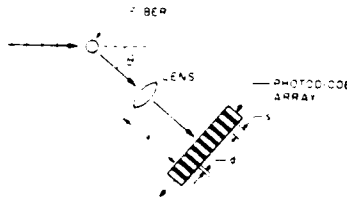


Fig. 1. Schematic of the fiber diameter measurement approach. An incident plane wave of wavelength λ scatters off a fiber. The resulting interference pattern is projected by a lens of focal length f onto a photodiode array with element spacing s and element width d .

To determine the resolution of the system, it is necessary to calculate the shift in angle of a peak due to a given change in fiber diameter.

A. Transparent Fiber

As discussed in Ref. 6, the fringe spacing of an unclad transparent fiber can be described analytically by considering the path length difference $\Lambda(\theta)$ between rays refracted through and reflected off the fiber at a given angle θ as shown in Fig. 2. The interference between these rays in the far field gives rise to a series of approximately sinusoidal fringes. The power scattered per unit angle at an angle θ can be written as

$$P(\theta) = a_1(\theta) + a_2(\theta) \cos k \Lambda(\theta), \quad (1)$$

where $k = 2\pi/\lambda$. An approximate ray optics calculation of the amplitude functions $a_1(\theta)$ and $a_2(\theta)$ is presented in the Appendix. The path length difference $\Lambda(\theta)$ is given by⁶

$$\Lambda(\theta) = 2\rho[\sin^2 \theta + (n^2 + 1 - 2n \cos^2 \theta)^{1/2}] + \lambda/4, \quad (2)$$

where n is the index of refraction of the fiber, and ρ is the fiber radius.

From Eqs. (1), (2), and (A13)–(A16) it can be shown that $a_1(\theta)$ and $a_2(\theta)$ vary sufficiently slowly that it is adequate to take the maxima of the scattering pattern to lie at the maxima of the cosine function in Eq. (1). The angular position θ_j of the j th bright fringe is then given implicitly by

$$k \Lambda(\theta_j) = 2\pi(j + j_0), \quad (3)$$

where $\Lambda(\theta = 0) = (j_0 + \delta)\lambda$, and where j_0 is an integer and $\delta < 1$.

The change in position on the diode array of the j th fringe Δx in response to a change $\Delta \rho$ in the fiber radius is

$$\Delta x = \frac{\partial \theta_j}{\partial \rho} / \Delta \rho. \quad (4)$$

With our detection system, the minimum resolvable position change is the diode spacing s . Thus the minimum resolvable radius change is

$$\Delta \rho_{\min} = \frac{(s)}{f} \left| \left(\frac{\partial \theta_j}{\partial \rho} \right) \right|^{-1}. \quad (5)$$

We can calculate $\partial \theta_j / \partial \rho$ from Eqs. (2) and (3) and find

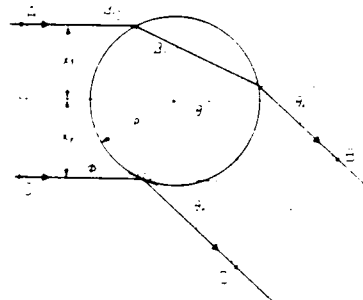


Fig. 2. Geometry of reflected and transmitted rays that interfere to form the fringe pattern. The path difference between AB and CD is given by $\Lambda(\theta)$ in Eq. (2) when $H_1 = H_2 = H$. Angles and lengths indicated are used in the Appendix to calculate scattering amplitudes $a_1(\theta)$ and $a_2(\theta)$ referred to in Eq. (1).

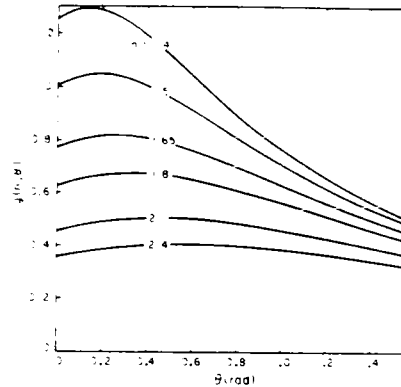


Fig. 3. Plot of sensitivity function $g(n, \theta)$ defined by Eqs. (6) and (7). Solid lines show $g(n, \theta)$ vs θ for various values of n .

$$\frac{\partial \theta_j}{\partial \rho} = \frac{-2}{\rho} \frac{\sin^2 \theta_j + (n^2 + 1 - 2n \cos^2 \theta_j)^{1/2}}{\rho \cos^2 \theta_j + n(n^2 + 1 - 2n \cos^2 \theta_j)^{1/2} \sin^2 \theta_j}. \quad (6)$$

If we write this relationship in the form

$$\frac{\partial \theta_j}{\partial \rho} = -\frac{1}{\rho} g^{-1}(n, \theta_j), \quad (7)$$

we arrive at a simple form for the diameter resolution:

$$\left(\frac{\Delta \rho}{\rho} \right)_{\min} = \frac{s}{f} g(n, \theta_j). \quad (8)$$

The function $g(n, \theta)$ is plotted in Fig. 3 and is seen to be bounded for cases of interest by $0.3 \leq g \leq 1.3$.

Note also that the resolution is independent of the laser wavelength. The qualitative explanation is that for a given $\Delta \rho$, the decrease with wavelength in the number of fringes below θ_j is exactly canceled by a larger fractional shift per fringe, leading to exactly the same shift in the position of the j th peak.

For a transparent fiber with $n = 1.5$ and a measurement system with $s = 50 \mu\text{m}$, $f = 100 \text{ mm}$, and $\theta_j = 1.2 \text{ rad}$, we find from Fig. 3 that $g = 0.63$ and calculate from Eq. (8) that $(\Delta \rho / \rho)_{\min} = 3.2 \times 10^{-4}$.

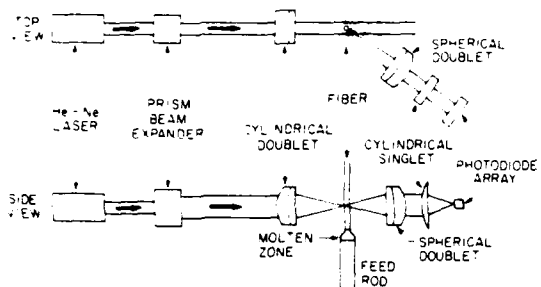


Fig. 4. Schematic diagram of the fiber diameter measurement optical system.

The dynamic range limitation occurs when the fringe moves off the diode array which consists of M elements. This occurs for $(\Delta\rho/\rho)_{\max} = \pm(M/2)(s/f)g(n, \theta)$, where we have chosen to track the fringe originally at the center of the array.

For $M = 512$ and the other values as above, we calculate that $(\Delta\rho/\rho)_{\max} = \pm 8\%$.

B. Opaque Fiber

The scattering pattern of an opaque fiber can also be written in the form of Eq. (1). It can be shown from scalar diffraction theory that for $\theta \geq \lambda/\pi w_0$, where w_0 is the beam waist in the plane perpendicular to the fiber axis, that

$$a_1(\theta) = a_2(\theta) = \frac{P_0\lambda}{2\pi^{5/2} w_0 \theta^2} \quad (9)$$

where P_0 is the incident laser power and that

$$\Lambda(\theta) = 2\rho\theta - (\lambda/2) \quad (10)$$

Since there is no refracted ray, the physical interpretation of Λ given earlier obviously no longer applies.

From Eqs. (3), (7), and (10) it is found that for an opaque fiber,

$$g(n, \theta) = g(\theta) \approx 1/\theta \quad (11)$$

III. Optical System

A. Illumination

A block diagram of the optical system is shown in Fig. 4. The arrangement for illuminating the fiber consists of a prism beam expander and a cylindrical lens to provide the transverse focusing necessary for axial resolution. A 120-mm focal length cylindrical doublet and an input beam waist of 8 mm were chosen to meet

the working distance specification and provide a line focus halfwidth of $3 \mu\text{m}$ with a He-Ne laser beam. The fiber position is tightly controlled in our apparatus, so it is not necessary to expand the beam in the direction perpendicular to the fiber axis.

B. Imaging the Fringe Pattern

The Fourier transform lens projects the fringe onto the photodiode array and determines the diameter variation resolution of the system through Eq. (8). It also serves to reduce the sensitivity of the fringe position on the diode array to movement of the fiber. In the absence of lens aberration there is no first-order variation of sensitivity across the diode array beyond that caused by $\partial g/\partial \theta$ and no first-order dependence of fringe position on the diode array on fiber position. Using a 100-mm focal length plano-convex Fourier transform lens leads to a 1% variation of sensitivity across the detector and a theoretical window for fiber motion of several hundred microns without an error of magnitude s in fringe position. A spherical doublet corrected for infinite conjugate ratio was chosen, which significantly reduces these effects as is discussed in Sec. VI.

The final cylindrical lens, in conjunction with the Fourier transform lens, concentrates the light onto the photodiode array.

IV. Electronics

The purpose of the electronic system is to lock onto one of the peaks of the interference pattern and track the location on the diode array of the center of that peak as it moves in response to diameter changes in the fiber. This task is complicated by the variations observed in peak amplitude and contrast ratio.

Figure 5 is a schematic of the electronic system designed to track an interference fringe. The output of the photodiode array, a section of which is shown in Fig. 6(a), is a series of 512 voltage levels clocked serially at a 0.5-MHz rate. The measurement is initiated by choosing a single fringe near the center of the photodiode array. The window signal [Fig. 6(b)] brackets the chosen fringe of the interference pattern and gates the boxcar integrator, whose output [Fig. 6(c)] is the average voltage of the bracketed fringe. The comparator output thus changes state on the steeply changing portions of the fringe signal. Control circuit 1 in Fig. 5 latches the output of the counter at the rising and falling edges of the comparator output that occur during the window interval. The sum of the two latch outputs thus rep-

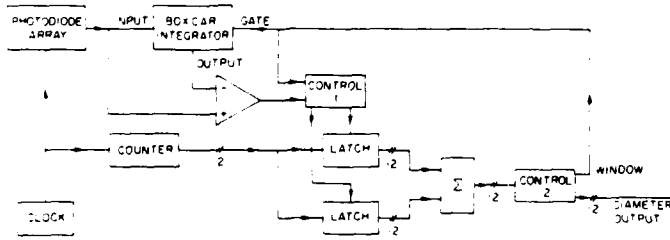


Fig. 5. Schematic diagram of the fiber diameter measurement electronic system.

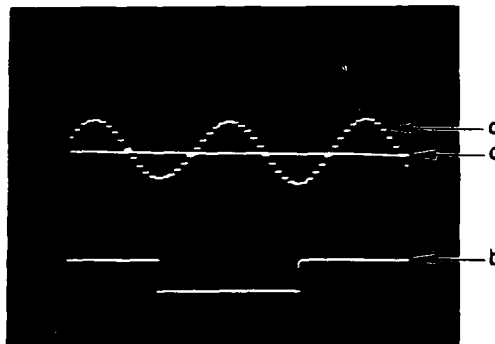


Fig. 6. Typical electronic signals: (a) output of a section of the photodiode array; (b) window signal bracketing fringe to be tracked; (c) output of boxcar integrator equal to the average value of the fringe selected by the window signal.

resents twice the value of the center of the fringe. Control circuit 2 compares this value of the center to the previous measurement. If the difference is too large, the measurement is assumed to be due to an anomalous optical or electronic event, and the output is not updated. If the new point is valid, the current fringe position measurement is transferred to the output and the window position is changed by the same increment. This cycle repeats every scan of the diode array, i.e., approximately once per millisecond.

The signal thus derived contains information only on diameter changes, not absolute diameter. If absolute diameter information were desired, additional signal processing would be necessary. At the beginning of a measurement, one absolute determination of the diameter would be made. Changes in the diameter would be measured using the technique described here. The accuracy of the diameter measurement would be determined by the accuracy of the absolute measurement technique, while the speed and resolution of the measurement would be determined by the fringe tracking system. Thus, a relatively slow method, e.g., the Fourier transform technique of Ref. 8, could be used for the absolute diameter measurement without adverse effect on the measurement rate.

V. Optimum Resolution

The linear increase in diameter resolution with the focal length of the Fourier transform lens predicted by Eq. (5) reaches an ultimate limit due to noise and non-uniform sensitivity of the elements of the photodiode array. To see where this limit occurs, it is necessary to calculate the focal length for which the difference in the output voltages of the adjacent photodiodes at the comparator threshold is less than the noise. The voltage output of the m th element of the photodiode array is given by

$$V_m = \frac{d}{f} R_m P(\theta_m) + v_m, \quad (12)$$

where θ_m is the angular position of the m th element, R_m is the responsivity of the m th element (in volts per

joule), τ is the measurement time interval, d is the width of an element of the array, v_m is the noise voltage on the m th element, and $P(\theta)$ is given by Eq. (1).

The difference in the output of adjacent diode elements is

$$\delta V_m = V_{m+1} - V_m \quad (13)$$

or

$$\delta V_m = \left(\frac{d}{f} \right) \tau [P(\theta_{m+1}) R_{m+1} - P(\theta_m) R_m] + (v_{m+1} - v_m) \quad (14)$$

Keeping only terms up to first order in a Taylor series expansion of $P(\theta)$ we have

$$\delta V_m = \left(\frac{d}{f} \right) \tau \left[\sum_j R_m \frac{dP}{d\theta} \Big|_{\theta_m} + (R_{m+1} - R_m) P(\theta_m) \right] + (v_{m+1} - v_m) \quad (15)$$

The first term in Eq. (15) can be evaluated from Eq. (1). If we assume $da_1/d\theta \ll a_2 k \partial \Delta / \partial \theta$, we have

$$\delta V = U + E, \quad (16)$$

where

$$U = \frac{sd}{f^2} \tau R_m a_2(\theta_m) k \frac{d\Delta}{d\theta} \Big|_{\theta_m},$$

$$E = \frac{d}{f} \tau (R_{m+1} - R_m) a_1(\theta_m) + (v_{m+1} - v_m)$$

The first term U in Eq. (16) is the result for an ideal noiseless uniform diode array, while E represents deviations due to nonuniform response and noise. Note that U decreases more rapidly with f than does E . If f_{opt} is chosen so that $U = E$, there is a one-diode uncertainty in the location of the peak center. Thus we can find the optimum focal length f_{opt} for a given observation angle θ by solving

$$U(f_{\text{opt}}, \theta) = E(f_{\text{opt}}, \theta). \quad (17)$$

Noting the relation between $(\Delta\rho/\rho)$ and f_{opt} given in Eq. (8) and using Eqs. (16), (17), and (A12), we obtain a quadratic equation for the maximum usable resolution at a given angle:

$$0 = -[\bar{a}_2 h(\theta)/g^2](\Delta\rho/\rho)^2 + (\bar{a}_1/2\pi g)(\delta R/R)(\lambda/\rho)h(\Delta\rho/\rho) + (2\sqrt{2\pi})^{-1}(E_0/P_0\tau)(s/d)(a_0/\rho)(\lambda/\rho), \quad (18)$$

where $\delta R/R$ is the fractional variation of the photodiode responsivity and

$$h(\theta) = \frac{1}{\rho} \frac{\partial \Delta}{\partial \theta} \\ = \cos(\frac{1}{2}\theta) + n \sin(\frac{1}{2}\theta)(n^2 + 1 - 2n \cos^2(\frac{1}{2}\theta))^{-1/2}$$

Here $E_0 = R_m v_m$ is a noise equivalent energy, and \bar{a}_1 and \bar{a}_2 are the dimensionless scattering coefficients defined in Eqs. (A13) and (A14). Solving Eq. (18) for $(\Delta\rho/\rho)$ and minimizing the result with respect to θ yield θ_{opt} , the optimum θ for a given experimental situation. Substituting θ_{opt} into Eq. (18) yields $(\Delta\rho/\rho)_{\text{opt}}$, the optimum resolution.

Figure 7 plots θ_{opt} vs the log of a dimensionless parameter ϵ defined by

$$\epsilon = (2\pi^3)^{-1/4} \left(\frac{\delta R}{R} \right) \left(\frac{P_0 \tau d}{E_0 s w_0} \frac{\lambda}{\rho} \right)^{1/2}. \quad (19)$$

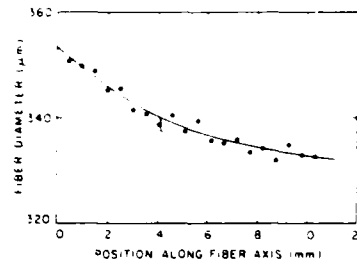


Fig. 9. Diameter vs length of a 350- μm diam glass fiber. The solid line was measured using the fringe tracking apparatus; the closed circles were measured using an optical microscope.

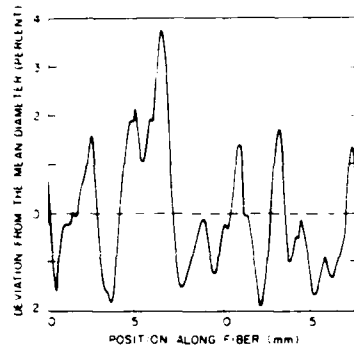


Fig. 10. Diameter change vs length for a 50- μm diam ruby fiber grown under open-loop conditions by the fiber growth apparatus described in Ref. 1.

sured. The former limit is due to lens aberration, while the latter is due to curvature of the phase front of the He-Ne beam in the direction perpendicular to the fiber axis. This latter window could be enlarged by collimation of the beam in that direction.

VII. Conclusion

We have designed and built a fiber diameter variation measurement system which has measured the diameter variation of transparent fibers having diameters between 25 and 300 μm , with 0.02% diam resolution and 6- μm axial resolution at a 1-kHz measurement rate and with a working distance of >100 mm. Modifications, such as a longer focal length Fourier transform lens, could increase the diameter resolution by 1 order of magnitude. This device is being used to provide real time measurements of the diameter variation of single-crystal refractory oxide fibers during growth.

The authors are grateful to Michel Digonnet and Keith Bennett for many helpful suggestions. Gregory Magel gratefully acknowledges the support of the Fannie and John Hertz Foundation. This work was supported by the U.S. Air Force under contract F49620-84-C-0021 and by the Joint Services Electronics Program under contract N00014-84-K-0327.

Appendix: Ray Calculation of Fringe Amplitudes

To obtain the amplitude of the fringe pattern of a transparent fiber, it is necessary to combine the amplitudes of the reflected and refracted rays, taking into account the phase difference between them.⁷ The power scattered between θ and $\theta + d\theta$ is given by

$$P(\theta) = P_r(\theta) + P_t(\theta) + 2\sqrt{P_r(\theta)P_t(\theta)} \cos k\Delta(\theta), \quad (\text{A1})$$

where $P_r(\theta)$ and $P_t(\theta)$ are the power per unit angle in the reflected and transmitted rays, respectively.

We assume the geometry shown in Fig. 2 with a uniform incident power per unit length I to obtain P_r and P_t . From conservation of energy it is clear that

$$P_r(\theta) = I R(\theta) \left| \frac{dx_r(\theta)}{d\theta_r} \right|, \quad (\text{A2})$$

$$P_t(\theta) = I T(\theta) \left| \frac{dx_t(\theta)}{d\theta_t} \right|, \quad (\text{A3})$$

where $R(\theta)$ and $T(\theta)$ are the power reflection and transmission coefficients.

If we assume that the incident beam of total power P_0 is Gaussian with a halfwidth w_0 , which is much larger than the fiber radius a , then $I = (2/\pi)^{1/2}(P_0/w_0)$. The necessary geometrical relationships to calculate the other quantities appearing in Eqs. (A2) and (A3) can be obtained from Fig. 2 and Snell's law. We see that

$$\frac{d\phi}{dx_r} = \frac{-1}{\rho \sin \phi}. \quad (\text{A4})$$

Since $\theta_r = 2\phi$, we can immediately write

$$\frac{d\theta_r}{dx_r} \Big|_{\theta_r=2\phi} = \frac{-2}{\rho \sin^{1/2} \theta_r}. \quad (\text{A5})$$

Noticing that

$$\theta_r = 2(\beta_0 - \beta_1), \quad (\text{A6})$$

where

$$\beta_1 = \sin^{-1}(x_t/\rho), \quad (\text{A7})$$

$$\beta_0 = \sin^{-1}(x_t/\rho), \quad (\text{A8})$$

we obtain

$$\frac{d\theta_r}{dx_r} \Big|_{\theta_r=2\phi} = \frac{2}{\rho} \left(\frac{1}{\cos \beta_0} - \frac{1}{\cos \beta_1} \right). \quad (\text{A9})$$

R and T can now be obtained from Fresnel's equations. Assuming the incident light to be polarized parallel to the fiber axis, we have

$$R(\theta) = \frac{(\sin^{1/2} \theta - n \cos \gamma)^2}{(\sin^{1/2} \theta + n \cos \gamma)^2}, \quad (\text{A10})$$

$$T(\theta) = \frac{4n \cos \beta_0 \cos \beta_1}{(\cos \beta_0 + n \cos \beta_1)^2}. \quad (\text{A11})$$

where $\gamma \equiv \sin^{-1}[(1/n) \cos^{1/2} \theta]$.

Finally, we can combine Eqs. (A1)–(A11) to obtain

$$P(\theta) = P_0 \left(\frac{2}{\pi} \right)^{1/2} \left(\frac{\rho}{w_0} \right) [\bar{a}_1(\theta) + \bar{a}_2(\theta) \cos k\Delta(\theta)], \quad (\text{A12})$$

where $\bar{a}_1(\theta)$ and $\bar{a}_2(\theta)$ are given by the following equations:

$$\bar{a}_1(\theta) = \frac{1}{2} \left[R(\theta) \sin^{1/2} \theta + T(\theta) \left(\frac{1}{\cos \beta_0} - \frac{1}{\cos \beta_1} \right)^{-1} \right]; \quad (\text{A13})$$

$$\tilde{a}_2(\theta) \approx \left[\kappa(\theta) \tilde{r}(\theta) \sin^2(\theta) \left(\frac{1}{\cos \beta_0} - \frac{1}{n \cos \beta_1} \right)^{-1} \right]^{1/2} \quad (A14)$$

The fringe amplitude coefficients a_1 and a_2 appearing in Eq. (1) in Sec. II are then given by

$$a_1(\theta) \approx P_0 \left(\frac{2}{\pi} \right)^{1/2} \left(\frac{\rho}{u} \right) \tilde{a}_1(\theta), \quad (A15)$$

$$a_2(\theta) \approx P_0 \left(\frac{2}{\pi} \right)^{1/2} \left(\frac{\rho}{u} \right) \tilde{a}_2(\theta) \quad (A16)$$

These results are also used in Sec. V to calculate the optimum resolution of the diameter measurement system.

References

1. M. M. Fejer, J. L. Nightingale, G. A. Magel, and R. L. Bver, "Laser Heated Miniature Pedestal Growth Apparatus for Single Crystal Optical Fibers," *Rev. Sci. Instrum.* **55**, 1791 (1984).
2. J. Stone and C. A. Burrus, "Self Contained LED-Pumped Single Crystal Nd:YAG Fiber Lasers," *Fiber Integrated Opt.* **2**, 19 (1979).
3. T. J. Bridges, J. S. Hasiak, and A. R. Strand, "Single Crystal AgBr Infrared Optical Fibers," *Opt. Lett.* **5**, 85 (1980).
4. G. D. Boyd, L. A. Coldren, and R. N. Thurston, "Acoustic Clad Fiber Delay Lines," *IEEE Trans. Sonics Ultrason.* **SU-24**, 246 (1977).
5. C. A. Burrus and J. Stone, "Single Crystal Fiber Optical Devices, A Nd:YAG Fiber Laser," *Appl. Phys. Lett.* **26**, 318 (1975).
6. L. S. Watkins, "Scattering from Side-Illuminated Clad Glass Fibers for Determination of Fiber Parameters," *J. Opt. Soc. Am.* **64**, 767 (1974).
7. D. H. Smithgall, L. S. Watkins, and R. E. Frazee, Jr., "High-Speed Noncontact Fiber-Diameter Measurement Using Forward Light Scattering," *Appl. Opt.* **16**, 2395 (1977).
8. M. A. G. Abushagur and N. George, "Measurement of Optical Fiber Diameter Using the Fast Fourier Transform," *Appl. Opt.* **19**, 2031 (1980).
9. A similar analysis for determination of fiber location in silicone coatings appears in D. H. Smithgall, "Light Scattering Model for the Determination of Fiber Location in Silicone Coatings," *Appl. Opt.* **21**, 1326 (1982).

PICOSECOND
ELECTRO-OPTIC SAMPLING
IN GALLIUM ARSENIDE

by

Brian Howard Kolner

G.L. No. 3912

A Dissertation

Contract

AFOSR 84-0139

August 1985

Abstract

The performance of high speed electronic devices has progressed rapidly over the years, continually challenging the limits of modern instrumentation to characterize them. At the same time, techniques for ultrashort optical pulse generation and measurement have improved at an even faster rate and today, light pulses of just a few optical cycles have been generated. The question of how to utilize these ultrashort light pulses to make electrical waveform measurements has been addressed by several workers using a variety of methods. The new technique of electro-optic sampling is a particularly effective method and is the central theme of this dissertation.

Electro-optic sampling utilizes ultrashort light pulses to repetitively sample the electric fields of transmission lines deposited on electro-optic crystals. Most high speed electronic and optoelectronic devices being developed today are fabricated in GaAs and related compound semiconductors which, fortuitously, possess an intrinsic electro-optic effect. As a result, sub-band gap optical pulses can be used to noninvasively probe the devices and circuits in the host semiconductor without degrading their performance.

This work describes the principles and limitations of electro-optic sampling applied to the characterization of high speed electronic and optoelectronic devices. Subpicosecond temporal resolution and sensitivities of several microvolts per root Hertz are shown to be achievable. Experiments measuring GaAs photodiodes and a monolithic microwave integrated circuit demonstrate the power of this new technique while studies of transmission line dispersion and laser pulse timing fluctuations exhibit its flexibility.

This new approach of direct electro-optic sampling represents a significant advance in measurement technology and holds promise as a useful tool for studying and developing very high speed devices made in GaAs and related semiconductor materials.

7-GHz acoustic transmission through a Hertzian contact

B. L. Heffner, G. S. Kino, and B. T. Khuri-Yakub

Edward L. Ginzton Laboratory, W. W. Hansen Laboratories of Physics, Stanford University, Stanford, California 94305

Received 29 March 1985; accepted for publication 17 April 1985

Transmission of acoustic waves through a Hertzian contact is demonstrated at 7 GHz. A zinc oxide transducer on a sapphire buffer rod is used to excite acoustic pulses which propagate into a sapphire flat through a direct Hertzian contact. Measurement of the reflected pulses yields a transmission loss through the contact of 1.2 dB.

Acoustic pulse echo techniques have been found useful in a great variety of applications. It is possible to avoid bonding an acoustic transducer directly to the material under investigation by bonding it instead to an acoustic buffer rod with a spherically shaped front surface. The rod is pressed against the material to be tested, forming a Hertzian contact. Transmission of longitudinal and shear acoustic waves through such a contact has been demonstrated at frequencies up to 1 GHz.^{1,2} We have now observed similar results at 7 GHz and have measured the transmission loss through the contact to be 1.19 ± 0.08 dB.

The demonstration of low-loss transmission through a Hertzian contact is significant because of the high frequency and correspondingly short wavelength involved. An intermediate coupling medium, such as a thin gold foil, had commonly been used in previous contacts. At 7 GHz, the acoustic wavelength in sapphire is $1.59 \mu\text{m}$, and attenuation through a $25\text{-}\mu\text{m}$ -thick foil is approximately 25 dB, making it unsuitable for low-loss contacts. In our experiment, the two sapphire pieces were pressed directly together. The short wavelength and lack of a soft coupling medium made the contact very sensitive to proper cleaning. However, the shorter wavelength promises better resolution in pulse echo measurements. In addition, acousto-optic effects become more pronounced as the wavelength approaches that of light. The authors plan to apply the current results to optical modulation.

The acoustic devices used in this experiment are shown schematically in Fig. 1. A single-crystal sapphire buffer rod and a flat test sample of the same material, both of circular cross section with the *c* axis oriented parallel to the cylindrical axis, were used. A zinc oxide acoustic transducer was sputtered on the flat face of the buffer rod, centered over the opposing spherical face which would form the Hertzian contact. The circular transducer was fabricated by photolithography, and had a diameter of $40 \mu\text{m}$.

A Hertzian contact results when any two rigid bodies are forced together into a "point" contact. The high stress in the neighborhood of this point causes elastic deformations, bringing the bodies into contact over a finite region. The stress and strain fields and the size of the contact region have been calculated for certain special cases.³ In our experiment the spherical face of a buffer rod (radius $R = 20 \text{ cm}$) was pressed against a flat. The radius a_c of the resulting circular contact region is given by

$$a_c = (FBR)^{1/3}, \quad (1)$$

where F is the force on the bodies, and B is an elastic constant

of the materials used. The buffer rod was mounted on a compliant metal sheet and pressed against the flat with a force of about 5 N. With $B \approx 3 \times 10^{-12} \text{ m}^2 \text{ N}^{-1}$ for sapphire, this force gives a calculated contact diameter on the order of $250 \mu\text{m}$.

In order for a reflected pulse to be detected, the plane of the transducer and the back surface of the flat must be parallel, so the alignment of the two sapphire pieces is critical. To align the pieces, a $125\text{-}\mu\text{m}$ -thick gold foil was first inserted between them. The tilt stage holding the flat was scanned while observing the first reflection P_{10} for a null, which indicated that acoustic power was coupled into the foil. After aligning the flat to the center of this relatively broad null, the sapphire pieces were momentarily separated and the foil was removed. The alignment was then fine tuned to find the much sharper null of P_{10} , resulting from the direct contact.

The transducer resonance was experimentally found to be centered at 6.95 GHz. The device was driven by a series of rf pulses 20 ns wide, with a 100-kHz repetition rate. Each pulse was reflected many times between the spherical and flat faces of the buffer rod. At each reflection from the flat face, the acoustic pulse generated an output from the transducer which was monitored using a circulator in the rf line. In this way we were able to measure the timing and peak powers of the various acoustic reflections.

The acoustic velocity v_s along the *c* axis in sapphire is $11\,100 \text{ ms}^{-1}$. The thickness of the buffer rod (D_s) was 1.0 mm and that of the flat (D_f) was 0.7 mm . As expected, the reflections inside the coupler produced a series of echoes separated in time by $2D_s/v_s$. When the spherical face of the coupler was pressed against the flat to form a Hertzian contact, a strong echo at time $2D_s + D_f/v_s$ indicated a reflection from the back face of the flat and hence acoustic transmission through the contact. Considering all possibilities of

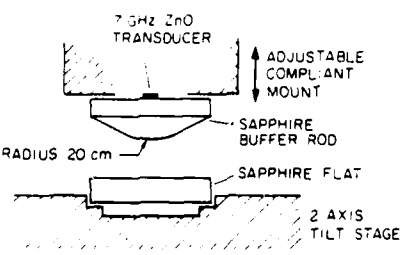


FIG. 1. Sapphire buffer rod and flat mounted on an alignment jig. The two pieces are pressed together to form a Hertzian contact.

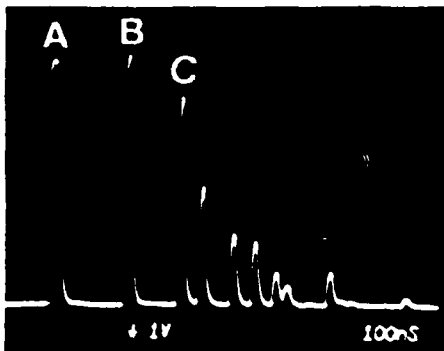


FIG. 2. 7.06-GHz acoustic reflections in a sapphire buffer rod pressed against a flat. (a) Electric mismatch of driving pulse. (b) First acoustic reflection from Hertzian interface. (c) First acoustic reflection from back surface of flat.

multiple reflections, echoes are expected at times

$$t_{mn} = \frac{2nD_r + 2mD_f}{v_s} \quad m = 0, 1, 2, \dots \quad (2)$$

$$n = 1, 2, 3, \dots$$

Figure 2 shows the rf pulses generated by the echoes. The timing of the pulses agrees with Eq. (2), confirming our interpretation of the echoes.

By measuring the peak powers P_{mn} of a series of reflected pulses, it is possible to calculate the power reflection and transmission coefficients R and T of the Hertzian contact. Echoes corresponding to $n = 1$ and $m = 0, 1, 2, 3$ were chosen for measurement in order to avoid reflections from the transducer and the attendant errors involved in estimating the transducer efficiency. The pattern of reflections leading to these echoes is shown schematically in Fig. 3. In this figure, k accounts for the constant incident peak power and transducer efficiency. The function β accounts for diffraction loss using the Fraunhofer approximation, and for an assumed material loss of 11 dB/cm. We assume that all power is reflected at the free surface of the flat, that R and T are the same approaching the contact from either direction, and that no power is dissipated within the contact.

Peak power measurements were made at five frequencies spaced at 50-MHz intervals centered about 6.95 GHz. Only two peak powers and the relation $R + T = 1$ were needed to determine k , R , and T , but four power measurements were made in order to test the validity of our system model. According to our theory, the quantities

$$\frac{\beta(2D_r + 4D_f)P_{11}}{\beta(2D_r + 2D_f)P_{12}}$$

and

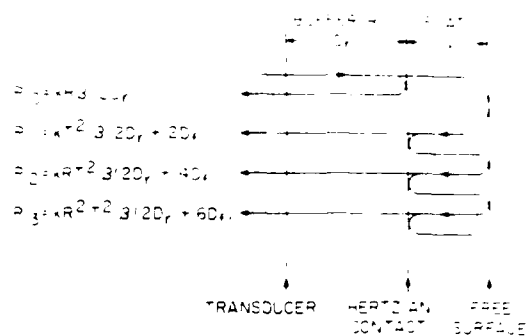


FIG. 3. Path of reflections used to calculate transmission through the contact.

$$\frac{\beta(2D_r + 6D_f)P_{12}}{\beta(2D_r + 4D_f)P_{13}}$$

are equal. These quantities were experimentally observed to be 6.19 ± 0.11 dB and 6.23 ± 0.25 dB respectively, confirming that our model of the system is consistent with observation. The reflection and transmission coefficients of the Hertzian contact were found to be

$$R = -6.21 \pm 0.25 \text{ dB}, \quad T = -1.19 \pm 0.08 \text{ dB}.$$

This result can be modeled by an impedance discontinuity at the contact, in which case the calculated impedance reduction from sapphire is 0.62. Such a reduction by imperfect contact due to asperities or dirt might be expected.

We have therefore shown that it is possible to obtain good transmission of 7-GHz acoustic waves through a Hertzian contact. This principle leads to the possibility of carrying out nondestructive testing in structural ceramics, semiconductors, and other materials at very high frequencies with correspondingly high resolution. It also suggests the possibility of obtaining very high-frequency modulation of optical signals without fabricating transducers on optical components.

We wish to thank Steve Burns for suggesting the possibility of acoustic transmission through a Hertzian contact. This work was supported by the Office of Naval Research through the Joint Services Electronics Program on contract No. N00014-84-K-0327. Brian Heffner is supported by a fellowship from the Fannie and John Hertz Foundation.

¹B. T. Khuri-Yakub and G. S. Kino, *Appl. Phys. Lett.* **30**, 78 (1977).

²W. Yee, Engineer's thesis, Stanford University 1972.

³See, for example, L. D. Landau and E. M. Lifshitz, *Theory of Elasticity*, translated by J. B. Sykes and W. H. Reid (Pergamon, New York, 1959), pp. 30-77.

Laser-heated miniature pedestal growth apparatus for single-crystal optical fibers

M. M. Fejer, J. L. Nightingale, G. A. Magel, and R. L. Byer

Applied Physics Department, Edward L. Ginzton Laboratory of Physics, Stanford University, Stanford, California 94305

(Received 21 December 1983; accepted for publication 20 July 1984)

We have designed and built a single-crystal fiber growth apparatus. The apparatus employs novel optical, mechanical, and electronic control systems that enable the growth of high optical quality single-crystal fibers. We have grown oriented single-crystal fibers of four refractory oxide materials, Al_2O_3 , $\text{Cr:Al}_2\text{O}_3$, Nd:YAG, and LiNbO_3 . These materials exhibit similar growth characteristics and yield fibers of comparable quality. Fibers as small as $20\text{ }\mu\text{m}$ in diameter and as long as 20 cm have been grown. Measured optical losses at $1.06\text{ }\mu\text{m}$ for a 10-cm-long, $170\text{-}\mu\text{m-diam}$ $\text{Cr:Al}_2\text{O}_3$ fiber were 0.074 dB/cm .

INTRODUCTION

The unique combination of material properties and geometry found in single-crystal optical fibers offers intriguing capabilities in a variety of optical devices. Three refractory oxide materials typify the broad range of potential applications.

The large nonlinear coefficients of LiNbO_3 suggest its use for modulators, signal processors, and parametric sources. Miniature lasers made from Nd:YAG fibers¹ have been known for several years. Such active fibers might also be used as in-line amplifiers in conventional glass fiber systems. Sapphire's high melting point and favorable optical properties make it useful in applications such as high-temperature thermometry.²

The optimal growth or preparation technique to achieve fiber devices in a variety of single-crystal materials is not yet clear. The methods thus far proposed fall into four categories: hot rolling,³ edge defined growth and its variants,⁴⁻⁶ Bridgman growth in capillary tubing,^{7,8} and miniature pedestal growth.^{9,10} The first three growth approaches require a crucible or die with materials that are compatible with the crystal growth conditions. In addition, the small diameter capillaries or orifices necessary to define crystal growth boundaries have to be produced with the same diameter tolerances that apply to the finished fiber. In order to avoid these problems we have chosen to pursue the laser heated pedestal growth method¹⁰ first applied to optical fiber growth by Burrus and Stone.¹¹

Our prior efforts to produce optical fiber devices using the pedestal growth method have been hampered by poor fiber quality.¹² In particular, diameter fluctuations and resultant surface irregularities have led to unacceptably large optical transmission losses. We believe these diameter fluctuations stem from mechanical and optical irregularities occurring during fiber growth rather than from some fundamental crystal growth instability. We have thus designed and built a crystal growth apparatus to produce optical quality single-crystal fibers. The present paper focuses on the

fiber growth apparatus and reports our initial growth results.

I. REQUIRED FIBER CHARACTERISTICS

The growth of single-crystal fibers is motivated by their application to passive, active, and nonlinear optical devices. The device application determines the required crystal fiber characteristics. Important crystal fiber parameters include length, diameter, and optical attenuation.

Optical loss can stem from a number of causes including bulk crystal imperfections, index of refraction variations, diameter fluctuations, and surface defects. The first two causes of loss are present in conventional crystal growth while the latter two are unique to the fiber geometry. The optical loss induced by surface defects and diameter fluctuations depends strongly on the azimuthal dependence and spatial frequency of the perturbation. We estimate losses on the order of 25% for a 1% random diameter fluctuation in a 5-cm-long, $25\text{-}\mu\text{m-diam}$ fiber.

The optical losses can be reduced by using a diffused cladding if the diffusion depth is large compared to the scale length of the diameter variations. Diffused cladding could be accomplished in different ways; for example, out diffusion of Cr^{+3} ions from ruby fibers¹³ or in diffusion of protons in *c*-axis LiNbO_3 fibers.¹⁴

Most optical crystal fiber devices require fiber lengths less than 5 cm with fiber diameters below $200\text{ }\mu\text{m}$. Small fiber diameters are particularly important in nonlinear optical devices, since tight beam confinement leads to improved nonlinear conversion efficiency. In some passive device applications, such as high-temperature sapphire thermometry,² the acceptable optical losses can be quite large and thus fiber diameter variations of several percent are tolerable. Nonlinear interactions, particularly those involving a fiber within a resonator, are more sensitive to diameter fluctuations. We estimate that for a nondiffused cladding, diameter fluctuations must be in the 0.1%–1% range for a useful nonlinear fiber. We have designed and built a crystal growth

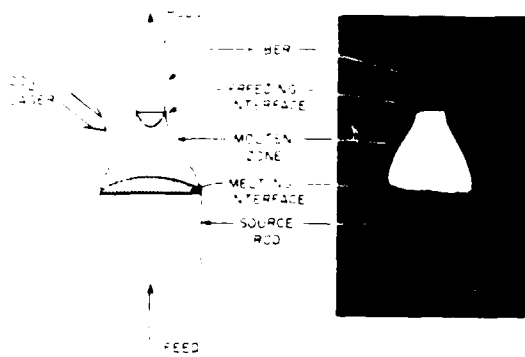


FIG. 1 Schematic diagram and corresponding photomicrograph of fiber growth. The photomicrograph depicts growth of a 190- μm LiNbO₃ fiber from a 570- μm -diam source rod. The fiber is supported from above by wetting an oriented seed crystal (not shown). The growth ridges faintly visible on the fiber are discussed later in the text.

apparatus to grow fibers with these length, diameter, and diameter stability characteristics.

II. DESCRIPTION OF GROWTH APPARATUS

A. Design overview

Figure 1 illustrates the miniature pedestal growth of a single-crystal fiber. A tightly focused CO₂ laser, emitting 10.6- μm radiation is the heat source used to melt the refractory material. The source rod may be fabricated from single-crystal,¹¹ polycrystalline, sintered,¹² or pressed powder¹³ material. The seed rod defines the crystallographic orientation of the fiber. Growth proceeds by simultaneous upward translation of the seed and source rods with a molten zone positioned between them. The laser focal spot, and consequently the molten zone, remain fixed during fiber growth. The source rod to fiber diameter ratio is set by mass conservation to be the square root of the fiber to source rod translation rate. Typical fiber growth rates range from 1–10 mm/min with diameter reductions of approximately three.

In our system ground rods 500 μm in diameter serve as the initial source for fiber crystal growth. The small rod di-

ameter provides the ability to grow materials with melting points exceeding 2000°C using only a few watts of laser power. An initial growth step reduces the 500- μm -diam rods to a 170- μm -diam fiber. Subsequent diameter reductions using the fiber as a source rod are also possible.

In order to achieve a constant fiber diameter, stable fiber growth conditions must be realized. This in turn dictates smooth source feed and fiber pull rates, stable laser power, and symmetric heat input into the molten zone.

B. Optical system

A block diagram and photograph of the fiber growth apparatus are shown in Figs. 2 and 3, respectively. A 15-W polarized waveguide CO₂ laser (California Laser, model 82-15000-P-W)¹⁴ served as the heat source for crystal growth. The water-cooled laser cavity is temperature stabilized and produces a polarized HE₁₁ output mode with power fluctuations less than 1%.

The laser power and beam pointing are most stable if the laser is allowed to run at constant high power. Therefore, an electro-optic power control system is used to vary the laser power incident on the molten zone. The system consists of a ZnSe quarter-wave plate, CdTe electro-optic crystal, and ZnSe polarizer/analyzer. The measured system dynamic range is greater than 100:1. Provisions for modulating the incident laser power have been incorporated into the control circuitry to allow growth of a fiber with controlled diameter variations. Such periodic variations could serve as a distributed Bragg reflector eliminating the need for conventional mirrors in fiber resonator devices.

The CO₂ laser beam (invisible) emerging from the polarizer is combined with a HeNe laser beam (visible) on a dichroic mirror. The visible coincident HeNe beam facilitates CO₂ alignment down the remainder of the optical train. After passing through a ZnSe focusing telescope and some beam steering optics, the CO₂ beam enters the controlled atmosphere growth chamber.

Within the growth chamber a novel optical system focuses the laser beam onto the fiber in a 360° axially symmet-

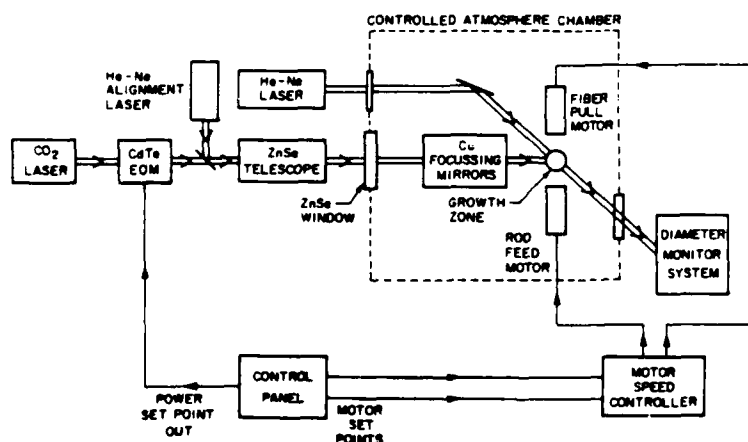


FIG. 2 Block diagram of fiber growth apparatus.

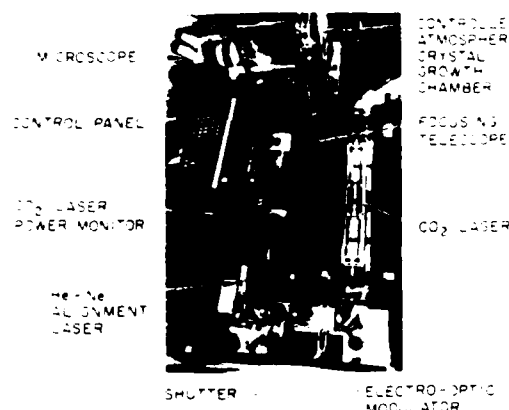


FIG. 3. Photograph of fiber growth apparatus. The diameter measurement system is not installed. A plastic dust cover which normally protects the optical train has been removed for the photograph.



ric distribution as shown in Fig. 4. The symmetric irradiance prevents cold spots in the growth zone and represents a significant improvement over the previously used two-beam,¹³ rotating periscope,¹⁷ or ellipsoidal¹⁸ focusing systems. An optical element incorporated into the design is a reflaxicon,¹⁹ which consists of an inner cone surrounded by a larger coaxial cone. In order to achieve good optical performance it is critical that the reflaxicon's two cones be accurately aligned.

A mated surface design, using diamond turned copper optical components, manufactured by Pneumo Precision,²⁰ assures centering of the two cone axes. A gold coating on the copper optical surfaces enhances reflectivity and protects the copper substrate. The reflaxicon and parabolic mirror provide near diffraction limited $f/2$ focusing, yielding a minimum spot size of $30\mu\text{m}$. This tight focus is important for the stable growth of small diameter fibers. The focal spot size can be controlled by modifying the input beam divergence with the focusing telescope. Motorized x-y stages on the fiber and source rod translation devices permit adjustment of the fiber position with respect to the fixed laser focal spot.

C. Mechanical system

Previous miniature pedestal growth systems have used lead screw translation. The lead screw fiber translation approach has the drawback that the fiber support point moves away from the melt zone as the fiber grows. The growth zone is thus increasingly sensitive to mechanical perturbations for small diameter and/or long fibers. Moreover, lead screw travel limits the total fiber length.

To alleviate these problems we adopted the belt drive system shown in Fig. 5. The fiber is driven by a polyester cord reinforced urethane belt, which in turn is driven by a dc motor through a speed reducing gearhead. An optical encoder, attached to the dc motor, allows locking the motor speed to a stable reference frequency. A V groove etched in silicon²¹ and overcoated with SiO_2 guides the fiber to prevent

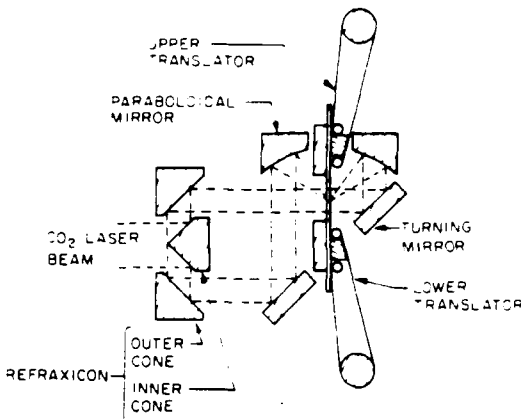


FIG. 4. Photograph of sapphire fiber growth showing optical focusing elements and head of lower translator. A cross-sectional diagram of focusing optics and translators is also shown.

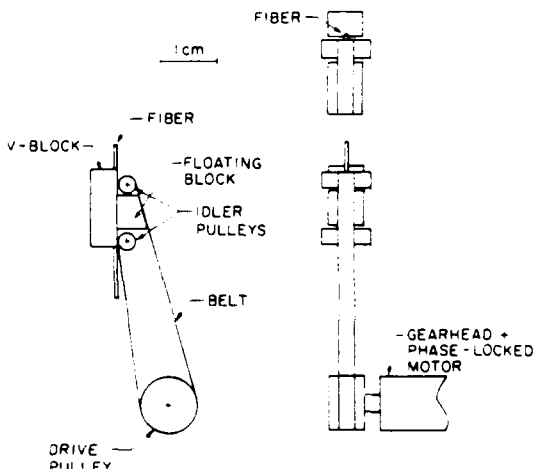


FIG. 5. Detail of fiber translator

side-to-side wobble. It provides a smooth, hard sliding surface along the fiber axis.

A phase-locked control circuit enables stable dc motor operation over a 100:1 speed range with acquisition times of 100 ms. A useful control option allows fixing the fiber to source rod speed ratio while adjusting growth speed. Since the fiber diameter has starting transients in the initial phases of growth, a slow growth rate allows time for the operator to make adjustments. As equilibrium conditions are reached growth speed can be conveniently increased without changing the fiber diameter.

The motor control system ensures motor velocity stabilization to frequencies above the mechanical response time of the drive system. Gear noise introduced in the speed reducing gearhead between the dc motor and belt drive pulley is a possible source of fiber translation fluctuation. The magnitude of this noise is not known. However, measurements of the actual fiber translation velocity indicate a jitter of less than 3%, the measurement resolution.

Fiber motion orthogonal to the translation direction is limited only by fiber straightness and diameter uniformity. Uniform diameter source rods are fabricated using a Boccadoro²¹ model FB40 centerless grinder. We have ground rods of Al_2O_3 , YAG, and LiNbO_3 to diameters of 300–600 μm in lengths up to 12 cm, with a taper of less than 1 $\mu\text{m}/\text{cm}$. For these source rods, the measured side-to-side wobble during translation is less than 3 μm , the measurement resolution.

During growth the molten zone is situated 1 cm above the lower translator. The upper translator has two operating positions, 1 and 3.5 cm above the melt. The raised position allows growth of an approximately 3-cm-long fiber without the newly grown fiber contacting the translator. The seed for this growth is typically an oriented crystal mounted in a capillary tube.

Longer fiber lengths are obtained using the lower position of the upper translator and a previously grown 3-cm-long fiber as a seed crystal. In this case both the newly grown fiber and the seed crystal pass through the upper translator. The diameter of the fiber must be matched to that of the seed crystal to within $\pm 10\%$ to avoid jamming the translator. The small irregularities in fiber diameter resulting from the joint between the seed crystal and new growth can give rise to unacceptably large molten zone side-to-side wobble. This forces the addition of an 8-mm-long glass capillary tube guide mounted onto the end of the upper translator. For growth of a 170- μm -diam fiber a 200- μm -diam guide provides the necessary position stability.

D. Diameter measurement system

Another important feature of the growth apparatus is a high-speed noncontact diameter measurement system. As currently used the system monitors the fiber diameter during growth. A planned improvement in the growth apparatus will be to use the diameter measurement system to provide an error signal in a diameter stabilization feedback loop. In order to grow fibers with 0.1% diameter stability at 1 mm/min growth rates the diameter measurement system must have a measurement rate >100 Hz, a diameter resolution

$<0.05\%$, an axial resolution as small as 5 μm , and a working distance >100 mm to avoid obstruction of the CO_2 focusing system. No commercial system was available which met all these criteria.

We designed and built the fiber diameter system shown schematically in Fig. 6. A helium-neon laser beam illuminates one side of the fiber. The rays passing through the fiber and those reflected off the fiber surface interfere in the far field to form a series of light and dark fringes whose period is inversely proportional to the fiber diameter.²² By imaging the interference pattern on a photodiode array and electronically tracking one of the fringes as it changes position in response to fiber diameter changes, a voltage proportional to the diameter change is derived. As built, the system has a diameter resolution better than 0.02%, an axial resolution of 5 μm , and a measurement rate of 1 kHz. A detailed description of the diameter measurement system is given by Fejer, Magel, and Byer.²⁴

III. RESULTS

Four crystalline materials have been grown to date: sapphire (Al_2O_3), sapphire with 0.05 wt.% chromium (ruby), YAG with 0.9 wt.% neodymium, and lithium niobate (LiNbO_3). Growth characteristics of the chromium doped ruby were identical to those of the pure sapphire. Growth orientations for the fibers were (001) for sapphire, (111) for YAG, and both (001) and (100) for lithium niobate. Fibers as small as 20 μm in diameter and as long as 20 cm have been grown (see Table I). Fiber growth speeds ranged from 0.3 to 30 mm/min.

Typical diameter reductions are approximately three to one. Larger diameter reductions result in less stable growth and yield fibers with larger diameter fluctuations. Smaller diameter reductions yield good quality fibers but require more steps to reach the desired diameter. The observed correlation between diameter reduction and growth stability agrees qualitatively with the theoretical analysis of Surek and Coriell.²⁵

Even though the melting temperatures range from 2045° to 1260 °C for these materials, their fiber growth characteristics are similar. Molten zone length is determined by the incident laser power. For optimum growth conditions the laser power was adjusted to yield the molten zone shape depicted in Fig. 7. For all materials investigated the molten zone shape is similar with a height

AD-A189 143

JOINT SERVICES ELECTRONICS PROGRAM APPENDIX(U) STANFORD 3/3

UNIV CA SAN DIEGO EDWARD L GINZTON LAB OF PHYSICS

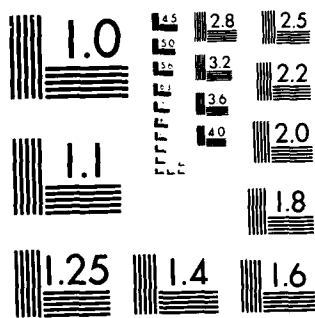
D M BLOOM ET AL. 15 OCT 87 GL-4287 M88014-84-K-0327

F/G 9/1

ML

UNCLASSIFIED

END
DATE
FORMED
8-1



MICROCOPY RESOLUTION TEST CHART
NATIONAL BUREAU OF STANDARDS 1963 A

TABLE I. Length, diameter, and crystallographic orientation for some single-crystal fibers grown with the apparatus.

Material	Orientation	Length (cm)	Diameter (μm)
Al_2O_3	(001)	20	170
		3.0	50
$\text{Al}_2\text{O}_3 + 0.05 \text{ wt. \% Cr}$	(001)	10.0	170
		3.0	20
YAG + 0.9 wt. % Nd	(111)	3.0	110
		3.0	40
LiNbO_3	(001)	3.0	50
		3.0	170

0.9 ± 0.15 for a 3 to 1 diameter reduction. Typical power levels necessary to grow from 500- μm Al_2O_3 or LiNbO_3 rods are 4.8 and 1.5 W, respectively.

In Fig. 7 the growing fiber is invisible since its smooth sides scatter much less light than those of the ground source rod. The solid-liquid growth interface is evident as the slightly darker bowl-shaped region at the top of the molten zone. The curvature of this isothermal surface reflects the radial temperature gradients present. The measured angle between the growing fiber and the molten zone at the periphery (meniscus angle) is 12° and 8° ($\pm 2^\circ$) for sapphire and YAG, respectively. This angle is a material constant independent of fiber growth speed or diameter. Our measured meniscus angle for sapphire ($12^\circ \pm 2^\circ$) is slightly below but not inconsistent with the $17^\circ \pm 4^\circ$ value previously measured by Dreeben, Kim, and Schujko.²⁸

A well-defined meniscus angle could not be measured in lithium niobate due to the highly anisotropic fiber cross section. *A*-axis lithium niobate fibers show a rectangular cross section with two protruding ridges, while *c*-axis lithium niobate has three sharply defined growth ridges. These ridges are clearly shown in Figs. 8(a) and 8(b). The ridges run smoothly and continuously down the length of the fiber as shown in Fig. 8(c). The growth ridges found in LiNbO_3 are not evident in either sapphire or YAG fibers, both of which show a slightly rounded hexagonal cross section.

Another feature evident in Fig. 8(c) is the excellent fiber

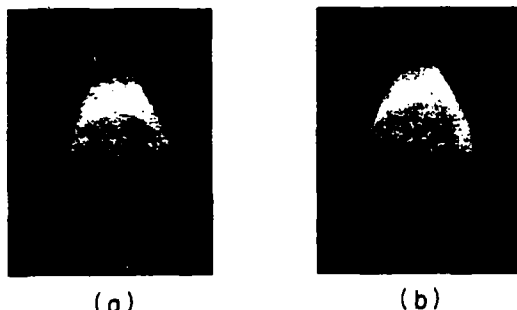


FIG. 7. Both photomicrographs illustrate a 3 to 1 diameter reduction from a 500- μm -diam source rod. Materials are (a) Al_2O_3 , melting point 2045 °C and (b) Nd:YAG, melting point 1970 °C. Notice the similarity to Fig. 1 showing LiNbO_3 , melting point 1260 °C.

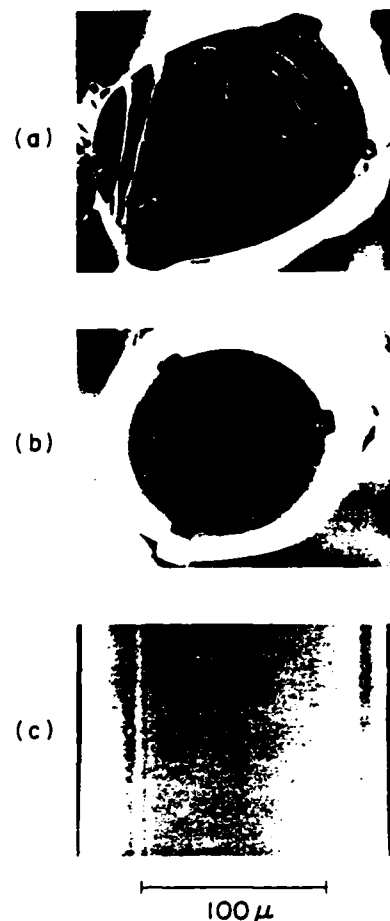


FIG. 8. Scanning electron micrographs of LiNbO_3 fibers: (a) cleaved cross section of *a*-axis fiber, (b) cross section of *c*-axis fiber, (c) surface of *c*-axis fiber. The internal concentric ring pattern and dark central area in (b) are artifacts of the procedure used to obtain the cross section. In (c) note the sharply defined growth ridges at the right boundary and near the left edge.

diameter control and surface quality. No fiber irregularities exist on the micron scale lengths visible in the figure. On a longer scale length we have demonstrated a rms diameter variation of 1% over a 1 cm length of fiber.

Typical variations in fiber diameter are shown in Fig. 9. This 55- μm -diam ruby fiber was grown at 4.5 mm/min from a 165- μm -diam source rod. The previously described diameter measurement apparatus was used to measure the deviations about the mean diameter. The rms diameter variation over the entire fiber length is 1.7%. The last centimeter of fiber shows a 1% rms diameter variation.

To date all growth has been performed with the growth chamber open to the atmosphere. The as-grown LiNbO_3 fibers have a brownish cast resulting from oxygen loss during growth. Annealing the fiber at 1000 °C in an oxygen atmosphere for several hours recovers a water-white crystal color.

A 10-cm-long, 170- μm -diam ruby fiber grown at 3.0 mm/min showed 72% transmission of an incident 1.06- μm

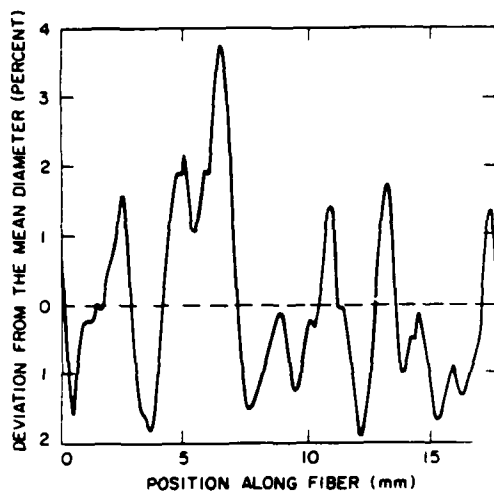


FIG. 9 Diameter variations in a 55- μm -diam ruby fiber measured with the noncontact diameter measurement system.

Nd:YAG laser beam. Taking into account the Fresnel reflection losses from the fiber end faces, the fiber optical loss can be calculated as 1.7%/cm or equivalently, 0.074 dB/cm. In this test no optical cladding was used, the guiding dielectric interface being the ruby fiber surface and the surrounding air.

IV. DISCUSSION

The single-crystal fiber growth apparatus has proven very reliable and easy to use. Over the past year six different operators have grown a total of more than 350 fibers. As many as 14 fibers have been grown on a single day. The time necessary to change from growing one material to another is small, approximately 30 min.

The novel design of the apparatus has allowed the growth of single-crystal fibers with a diameter stability of 1% per centimeter of length. The growth morphology of the crystal fibers is similar to that seen in bulk Czochralski crystal growth. The noncircular nature of the fiber cross section does not introduce additional optical loss since the cross section is invariant with length.

In our initial efforts to propagate light down these fibers we have measured optical losses of <2% per cm over distances of several centimeters. Losses of this level are acceptable in some device applications such as sapphire fiber thermometry. Efficient active and nonlinear devices demand somewhat lower optical losses. We have designed and constructed a single-crystal fiber growth apparatus based on a laser heated miniature pedestal growth technique. Oriented single-crystal fibers have been grown with diameters of 500

to 20 μm . Planned improvements in fiber diameter control and fiber cladding techniques should allow realization of single-crystal fiber-optical devices.

ACKNOWLEDGMENTS

We gratefully acknowledge useful discussions with M. Digonnet, D. L. O'Meara, T. Y. Fan, W. Kozlovsky, G. A. Kotler, R. S. Feigelson, R. K. Route, and W. Kway, all of Stanford University. We are thankful for the technical support provided by D. Buseck, S. Greenstreet, J. J. Vrheil, M. M. Simkin, K. L. Doty, A. Ospina, B. A. Williams, and P. A. Thompson. This work was supported by the Joint Services Electronics Program, Contract No. N00014-75-C-0632, the Air Force Office of Scientific Research, Contract No. 83-0193, The Stanford University Center for Materials Research, Contract No. CMR-80-20248, and the Lawrence National Laboratories at Livermore, Contract No. 8518101. G. A. Magel gratefully acknowledges the support of the Fannie and John Hertz Foundation.

- ¹J. Stone and C. A. Burrus, *Fiber Integrated Opt.* **2**, 19 (1979).
- ²R. R. Dils, *J. Appl. Phys.* **54**, 1198 (1983).
- ³J. A. Harrington, *Proc. SPIE* **227**, 85 (1980).
- ⁴J. Bridges, J. S. Hasiak, and A. R. Strand, *Opt. Lett.* **5**, 85 (1980).
- ⁵H. E. La Belle, Jr. and A. I. Mlavsky, *Mater. Res. Bull.* **6**, 571 (1971).
- ⁶B. Chalmers, H. E. La Belle, Jr., and A. I. Mlavsky, *Mater. Res. Bull.* **6**, 681 (1971).
- ⁷J. L. Stevenson and R. B. Dyott, *Electron. Lett.* **10**, 449 (1974).
- ⁸H. P. Weber, P. F. Liao, B. C. Tofield, and P. M. Bridenbaugh, *Appl. Phys. Lett.* **26**, 692 (1975).
- ⁹D. B. Gasson and B. Codkayne, *J. Mater. Sci.* **5**, 100 (1970).
- ¹⁰J. S. Haggerty, NASA Report No. Cr-120948, 1972.
- ¹¹C. A. Burrus and J. Stone, *Appl. Phys. Lett.* **26**, 318 (1975).
- ¹²M. Fejer, R. L. Byer, R. Feigelson, and W. Kway, *Proceedings of the SPIE Advances in Infrared Fibers II* (1982), p. 320.
- ¹³C. A. Burrus and L. A. Coldren, *Appl. Phys. Lett.* **31**, 383 (1977).
- ¹⁴J. L. Jackel, C. E. Rice, and J. J. Vaselka, Jr., *Appl. Phys. Lett.* **41**, 607 (1982).
- ¹⁵J. Stone and C. A. Burrus, *J. Appl. Phys.* **49**, 2281 (1978).
- ¹⁶California Laser Corporation, 1070 Commerce Street, San Marcos, CA 92069.
- ¹⁷J. E. Midwinter, *Optical Fibers for Transmission* (Wiley, New York, 1979), p. 194.
- ¹⁸U. C. Paek, *Appl. Opt.* **13**, 1383 (1974).
- ¹⁹W. R. Edmonds, *Appl. Opt.* **12**, 1940 (1973).
- ²⁰Pneumo Precision Incorporated, Precision Park, Keene, NH 03431.
- ²¹F. Boccadoro, Via Dr. Varesi, CH-6600 Locarno, Switzerland.
- ²²C. M. Schroeder, *BSLT* **57**, 91 (1978).
- ²³D. H. Smithgall, L. S. Watkins, and R. E. Frazee, Jr., *Appl. Opt.* **16**, 2395 (1977).
- ²⁴M. M. Fejer, G. A. Magel, and R. L. Byer (to be published).
- ²⁵T. Surek and S. R. Cornell, *J. Cryst. Growth* **37**, 253 (1977).
- ²⁶W. Bardsley, F. C. Frank, G. W. Green, and D. T. J. Hurle, *J. Cryst. Growth* **23**, 341 (1974).
- ²⁷T. Surek, *J. Appl. Phys.* **47**, 4384 (1976).
- ²⁸A. B. Dreeben, K. M. Kim, and A. Schujko, *J. Cryst. Growth* **50**, 126 (1980).

November 1984 / Vol. 9, No. 11 / OPTICS LETTERS

Compression of pulses from a continuous-wave mode-locked Nd:YAG laser

J. D. Kafka

Spectra-Physics, Inc., 1250 West Middlefield Road, Mountain View, California 94042

B. H. Kolner

Edward L. Ginzton Laboratory, Stanford University, Stanford, California 94305

T. Baer

Spectra-Physics, Inc., 1250 West Middlefield Road, Mountain View, California 94042

D. M. Bloom

Edward L. Ginzton Laboratory, Stanford University, Stanford, California 94305

Received July 9, 1984; accepted August 10, 1984

We have compressed the 80-psec pulses from a cw mode-locked Nd:YAG laser by a factor of 45. The pulse compressor uses single-mode optical fiber and a compact grating-pair dispersive delay line.

Using the technique of optical pulse compression, we have generated 1.8-psec pulses from a cw mode-locked Nd:YAG laser. Our pulse compressor incorporates a novel grazing-incidence delay line that is compact and reduces the ellipticity of the output beam. We have achieved pulse-compression ratios of 45:1 and generated visible picosecond pulses by second-harmonic generation.

In 1968, Treacy¹ reported experiments in which he compressed chirped optical pulses with a grating pair. Duguay and Hansen² compressed 500-psec mode-locked pulses from a He-Ne laser by a factor of 2 by using a phase modulator and a Gires-Tournois interferometer. McMullen³ proposed the compression of 10- to 100-nsec pulses with a pair of gratings separated by 100 m. More recently, Nikolaus and Grischkowsky^{4,5} used the effect of self-phase modulation in a single-mode optical fiber to chirp an optical pulse and then compressed the pulse by using a grating pair. Johnson *et al.*⁶ have used this technique with a grating separation of 7 m to compress the 33-psec pulses from a frequency-doubled, mode-locked cw Nd:YAG laser by a factor of 80.

We have designed a compact and efficient grating-pair configuration using a unique grazing-incidence technique.^{3,7,8} To achieve high efficiency, the grating is used close to the Littrow condition. For a given wavelength, it is possible to choose a grating such that the Littrow condition is satisfied at grazing incidence (80°). When the grating pair is employed at grazing incidence, the distance between the gratings can be reduced by 2 orders of magnitude. In addition, the ellipticity of the output beam is greatly decreased. De-

tails of the grazing-incidence design will be discussed in a subsequent theoretical paper. The efficiency of a pulse compressor is dependent primarily on the losses in the optical fiber. An advantage of pulse compression at 1.06 μ m is that, at this wavelength, single-mode optical fiber has less than 1 dB/km loss, allowing long lengths of fiber to be used.

A Spectra-Physics Model 3000 cw mode-locked Nd:YAG laser was used to generate 80-psec pulses at a repetition rate of 82 MHz with 8 W of average power. Although our coupling efficiency was typically 50%, the output power from the fiber was limited to 1 W by Raman generation. After propagation through 300 m of single-mode optical fiber, the pulse width remained unchanged, but the bandwidth broadened from 0.03 to 3.5 nm. The fiber used was not polarization-preserving fiber; however, no drift in the output polarization was

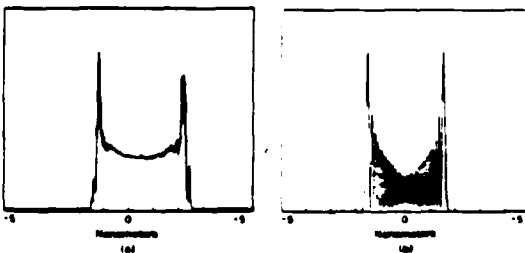


Fig. 1. (a) Experimental and (b) theoretical output spectrum from the fiber.

0146-9592/84/110505-02\$2.00/0

© 1984, Optical Society of America

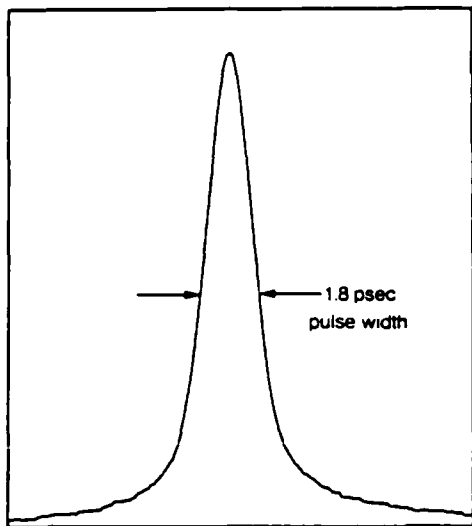


Fig. 2. Autocorrelation of 1.06-μm pulse. The pulse width is 1.8 psec (FWHM), assuming a Gaussian pulse shape.

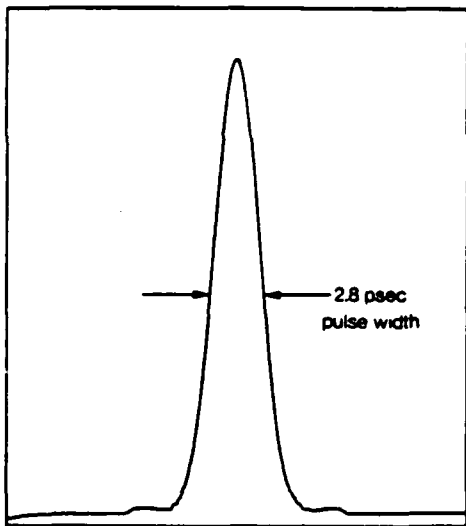


Fig. 3. Autocorrelation of 532-nm pulse after optimization of compressor throughput. The pulse width is 2.8 psec (FWHM), assuming a Gaussian pulse shape.

observed over time periods of several hours. The output spectrum is shown in Fig. 1 along with a theoretical spectrum calculated assuming no group-velocity dispersion.⁹ This assumption is justified because we operate at a wavelength and pulse width at which the effects of group-velocity dispersion that are due to wavelength and pulse width are minimal.¹⁰

The dispersive delay consisted of a single 1800-line/mm grating and a roof prism reflector separated by 17 cm. The shortest pulse observed was 1.0 psec; however, typical pulse widths, shown in Fig. 2, were 1.8 psec, assuming a Gaussian pulse shape. The theory predicts a pulse width of 1.6 psec.⁹ The 500 mW of output power at 1.06 μm was frequency doubled by using a 5-mm KTP crystal, and we obtained 40 mW of power at 532 nm.

Recently, we optimized the compressor to achieve maximum throughput and obtained 2 W of average power at 1.06 μm. Using a 5-mm KTP crystal, we generated 500 mW of second-harmonic power, yielding a conversion efficiency of 25%. In this configuration, the pulse width broadened to 2.8 psec at 532 nm (Fig. 3).

In conclusion, we have built a compact pulse compressor by using a novel grazing-incidence technique. The device is capable of compressing the 80-psec pulses from a cw mode-locked Nd:YAG laser by a factor of 45. Synchronized picosecond pulses at 532 nm can easily be generated. The compressed cw mode-locked Nd:YAG laser is a completely solid-state picosecond source with high repetition rate and high average power.

References

1. E. B. Treacy, Phys. Lett. 28A, 34 (1968).
2. M. A. Duguay and J. W. Hansen, Appl. Phys. Lett. 14, 14 (1969).
3. J. D. McMullen, Appl. Opt. 18, 737 (1979).
4. B. Nikolaus and D. Grischkowsky, Appl. Phys. Lett. 42, 1 (1983).
5. B. Nikolaus and D. Grischkowsky, Appl. Phys. Lett. 43, 228 (1983).
6. A. M. Johnson, R. H. Stolen, and W. M. Simpson, Appl. Phys. Lett. 44, 729 (1984).
7. Patent pending.
8. E. B. Treacy, IEEE J. Quantum Electron. QE-5, 454 (1969).
9. B. H. Kolner, J. D. Kafka, D. M. Bloom, and T. M. Baer, "Compression of mode-locked Nd:YAG pulses to 1.8 picoseconds," in *Picosecond Phenomena IV* (Springer-Verlag, New York, 1984).
10. W. J. Tomlinson, R. H. Stolen, and C. V. Shank, J. Opt. Soc. Am. B 1, 139 (1984).

DIRECT ELECTRO-OPTIC SAMPLING OF TRANSMISSION-LINE SIGNALS PROPAGATING ON A GaAs SUBSTRATE

Indexing terms: Integrated optics. Electro-optics

We report a new picosecond electro-optic sampling probe suitable for noncontact electronic characterisation of high-speed monolithic GaAs integrated circuits.

In this letter we report the first picosecond electro-optic sampling measurement made directly in GaAs. Using compressed picosecond pulses at 1.06 μ m and the electro-optic effect inherent in GaAs, we have sampled the fringing electric field of a microstrip transmission line deposited on the <100> face of a GaAs substrate. Frequency-doubled pulses at 0.532 μ m were used to excite a Schottky photodiode which served as an electrical signal generator connected to the transmission line (Fig. 1). Because the excitation beam was derived from the same source as the sampling beam, time synchronism was assured.

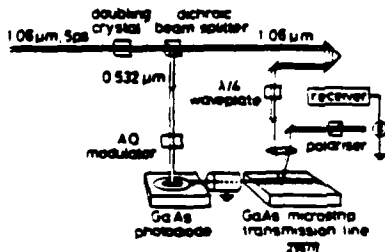


Fig. 1 Schematic diagram of system for electro-optic sampling in a GaAs substrate

Receiver is a spectrum analyser tuned to the acousto-optic modulation frequency of 20.9 MHz

Our previous efforts at electro-optic sampling have utilised a hybrid assembly consisting of a high-speed photodiode and a lithium tantalate microstrip transverse light modulator.^{1,2} Although initial results from that work demonstrated very wide bandwidth capabilities, the hybrid assembly presented a significant packaging difficulty. At frequencies of approximately 100 GHz, wires as short as a few tens of micrometres contributed significant inductance and hence degraded device performance. Thus, for ultrahigh-speed devices a monolithic approach was desirable.

Fortunately, GaAs is electro-optic and quite suitable for use in electro-optic sampling. Various geometries are feasible for use with a variety of transmission-line structures. One of the most versatile and sensitive geometries is illustrated in Fig. 2a. For <100> cut wafers of GaAs (the most commonly used orientation in integrated-circuit applications), the sampling optical beam passes through the wafer at a point adjacent to the upper conductor of a microstrip transmission line and is reflected back by the ground plane conductor on the bottom side of the wafer. This longitudinal geometry has a number of

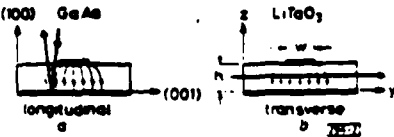


Fig. 2 Microstrip sampling geometries with indicated crystallographic axes

advantages over the transverse geometry originally employed in LiTaO_3 (Fig. 2b). First it can be employed on the same wafer used to fabricate the photodetector and other devices and circuit elements. Second, multiple sampling points can easily be incorporated into the wafer allowing complex high-speed circuits to be characterised. Finally, the sensitivity or minimum detectable voltage of the longitudinal geometry is independent of the characteristic impedance of the transmission line. In fact, for a 50Ω system, the sensitivity is calculated to be nearly ten times better than that of the transverse LiTaO_3 electro-optic sampler (Table 1).

Table 1 COMPARISON OF GaAs TO LiTaO₃ FOR THE MICROSTRIP SAMPLING GEOMETRIES OF FIG. 2

	GaAs	LiTaO ₃
Electro-optic figure of merit $n^2 r_{11} \times 10^{-12} \text{ m V}$	$n^2 r_{11} = 60$	$n^2 r_{33} - n^2 r_{13} = 229$
Halfwave voltage $V_{1/2}$	4.4 kV	4.63 (h w) kV
Minimum detectable voltage	22 $\mu\text{V} \text{ Hz}^{-1}$	188 $\mu\text{V} \text{ Hz}^{-1}$

Values in the Table are calculated for $\lambda = 1064 \text{ nm}$, a transmission-line impedance of 50Ω and a sampling beam detector average current of 10 mA

A new aspect of this approach is the need for a two-wavelength picosecond optical source. A short-wavelength pulse is required to excite the photodetector while a long-wavelength pulse is needed to probe the fields in the GaAs. An Nd:YAG laser is an ideal source for this application in terms of wavelength. The fundamental laser output at 1064 nm is well below the absorption edge of GaAs and can be used as the sampling beam. The second harmonic output obtained by frequency-doubling to 0.532 nm is ideal for exciting the photodetector. While reliable CW mode-locked lasers are commercially available, the minimum pulselength is limited to 50–100 ps. These pulses are too long to be used for high-speed sampling. However, recent work on fibre-grating pulse compressors has resulted in the efficient compression of CW mode-locked Nd:YAG pulses to $< 5 \text{ ps}$.³

In our experiment a Spectra-Physics model 3000 CW mode-locked Nd:YAG laser generated 80 ps pulses at an 82 MHz rate and was followed by a Spectra-Physics model 3600 fibre-grating pulse compressor. The compressor produced a train of 5 ps pulses at 1064 nm with 400 mW average power. These pulses were frequency-doubled in a KTP crystal and separated by a dichroic beam splitter to yield 40 mW average power at 0.532 nm . An acousto-optic modulator was used to chop the beam at 20.9 MHz. This frequency was chosen to be above the excess noise produced by the Nd:YAG laser and the pulse compressor. The beam power was reduced to a few milliwatts before being focused onto the Schottky photodiode. The remaining power in the 1064 nm sampling beam was routed through a right-angle prism mounted on a stepper-motor driven delay stage that provided a variable delay of up to 500 ps. The beam was then passed through a quarter-wave plate adjusted for circular polarisation and was focused into the GaAs adjacent to the microstrip transmission line. Electric fields from the transmission line along the $\langle 100 \rangle$ axis induced birefringent axes along the $\langle 011 \rangle$ and $\langle 011 \rangle$ directions. As the circularly polarised probe beam passed in and out of the crystal, the voltage-induced birefringence elliptically polarised the light which was analysed with a polariser oriented along $\langle 010 \rangle$. The photodiode detecting the sampling beam was followed by a narrowband receiver; in this case an HP 8566B spectrum analyser was tuned to 20.9 MHz. As the time delay between the excitation and sampling beam are changed, the intensity of the sampling beam (and hence the magnitude of the signal at 20.9 MHz) maps out the equivalent photodiode response. Fig. 3 shows the impulse response of a $50 \mu\text{m}$ -diameter GaAs Schottky photodiode measured with this sampling system. The ringing after the main peak is due to reflections from the package.

To confirm the sensitivity of the modulation characteristics of the GaAs, we applied a low-frequency (1 kHz) signal directly to the microstrip transmission line. By comparing

amplitude of the AC photocurrent to that of the DC photocurrent we estimated the half-wave switching voltage to be 10 kV or about twice the predicted value.

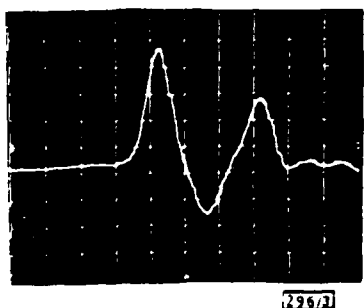


Fig. 3 Impulse response of a $50 \mu\text{m}$ -diameter GaAs photodiode measured by electro-optic sampling of a GaAs microstrip transmission line.

50 ps/div

As the infra-red sampling beam was moved away from the transmission line, the signal diminished as expected due to the local confinement of the electric fields. However, when an HeNe laser was used to illuminate the surface of the GaAs in the vicinity of the sampling beam, the signal returned to its original value. This suggests that a conductive surface is being photogenerated and that charge from the transmission line is accumulating there, re-establishing an electric field in the sampling beam. The photoconductive surface may play an important role in future measurements because it can be used to optically alter, or introduce new, conductive patterns on any GaAs wafer. This might be useful for introducing known reflections as timing markers in time-domain-reflectometry measurements, or as a way of rapidly designing new transmission-line structures without intermediate processing steps.

In summary, we have demonstrated electro-optic sampling directly in a GaAs substrate. We used a dual-wavelength picosecond optical source to simultaneously excite a GaAs photodiode and measure the birefringence induced in a GaAs transmission line by the electro-optic effect. We demonstrated the photoconductive extension of the transmission line and suggested possible uses for this interesting property. Finally, we would like to point out that, although this experiment was based on two discrete devices for signal generation and sampling, the technique is ideally suited for noninvasive characterisation of high-speed monolithic GaAs integrated circuits.

B. H. KOLNER
D. M. BLOOM

*Edward L. Ginzton Laboratory,
Stanford University,
Stanford, CA 94305, USA*

20th July 1984

References

1. KOLNER, B. H., BLOOM, D. M., and CROSS, P. S. 'Electro-optic sampling with picosecond resolution'. *Electron. Lett.*, 1983, 19, pp. 574–575
2. KOLNER, B. H., BLOOM, D. M., and CROSS, P. S. 'Picosecond optical electronic measurements'. *Proc. SPIE*, 1983, 439, pp. 149–152
3. KOLNER, B. H., KAPPA, J. D., BLOOM, D. M., and BAER, T. W. 'Compression of mode-locked Nd:YAG pulses to 1.8 picoseconds'. *Proceedings of topical meeting on ultrafast phenomena, 12–15 June 1984, Monterey, California* (Springer-Verlag, Berlin), to be published

COMPRESSION OF MODE-LOCKED Nd:YAG PULSES TO 1.8 PICoseconds

B.H. Kolner, J.D. Kafka*, D.M. Bloom and T.M. Baer*

Edward L. Ginzton Laboratory
Stanford University
Stanford, California 94305

*Spectra-Physics Corporation
Laser Products Division
1250 W. Middlefield Road
Mountain View, California 94042

ABSTRACT

Pulses from a cw mode-locked Nd:YAG laser have been compressed by 45 times to 1.8 picoseconds using single-mode optical fiber and a compact grating pair dispersive delay line. An average power of 500 mW was obtained corresponding to 25% throughput efficiency. Using a 5 mm long KTP crystal, an average power of 40 mW was generated at 532 nm.

To be published in "The Proceedings of the Topical Meeting on Ultrafast Phenomena, June 12-15, 1984, Monterey, California", Springer-Verlag, Berlin, 1984.

COMPRESSION OF MODE-LOCKED Nd:YAG PULSES TO 1.8 PICoseconds

B.H. Kolner, J.D. Kafka*, D.M. Bloom and T.M. Baer*

Edward L. Ginzton Laboratory, Stanford University, Stanford, California 94305

*Spectra-Physics Corporation, Laser Products Division, 1250 W. Middlefield Road, Mountain View, California 94042

In this paper we report the compression of 80 picosecond long mode-locked Nd:YAG pulses to 1.8 picoseconds by using self-phase modulation in single-mode optical fibers and a grating pair dispersive delay line. Although we generated pulses as short as 1.0 picoseconds, pulsewidths of 1.8 picoseconds were more routinely obtained. Our compressor incorporated a novel grazing incidence delay line which greatly reduced the grating separation. We achieved pulse compression ratios of 45:1 and generated visible picosecond pulses by second harmonic generation. For fixed wavelength applications the compressed cw mode-locked Nd:YAG laser provides a completely solid state source of picosecond pulses. In addition, the compressed pulses should improve the performance of synchronously pumped tunable lasers.

Pulse compressors based on self-phase modulation in single-mode optical fibers have been demonstrated in the visible spectrum [1-4]. Previous workers typically used short duration pulses and grating configurations exhibiting low dispersion. The results of these experiments suggested that compression of longer pulses would require inconveniently large grating separations [5]. However, analysis of grating pair dispersive delay lines shows that the dispersion is a widely varying function of input angle, groove density and wavelength [6-8]. We discovered that grazing incidence and high diffraction angles increases the dispersion by more than two orders of magnitude. Thus, only tens of centimeters of grating separation are required to compress 100 picosecond Nd:YAG pulses. To realize high efficiency the gratings are used close to the Littrow condition. At any wavelength it is possible to choose a grating ruling that satisfies the Littrow condition at grazing incidence (80 degrees).

In our experiment a Spectra-Physics Model 3000 cw mode-locked Nd:YAG laser generated 80 picosecond pulses at 82 MHz with 8 watts average power. The beam was attenuated to 2 watts to prevent stimulated Raman scattering and focused into 300 meters of single-mode fiber. The coupling efficiency was typically 50%. At the fiber output the pulsewidth was unchanged but the bandwidth broadened from 0.3 \AA to 35 \AA due to self-phase modulation. The broadened frequency spectrum is shown in Figure 1a.

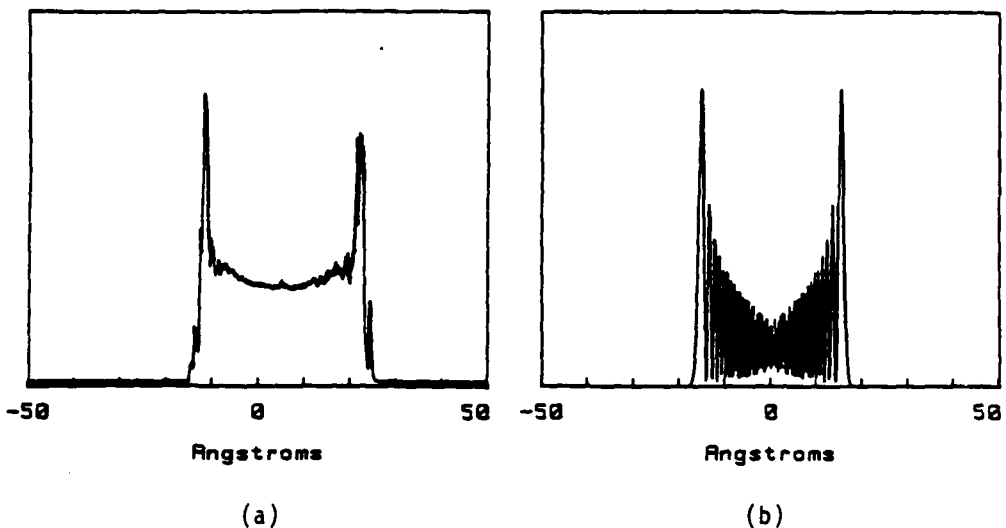


Fig. 1 a) Measured frequency spectrum of the self-phase modulated pulse. b) Calculated frequency spectrum for $A=150$.

The output pulses passed through a pair of 1800 lines/mm gratings with a separation of 33 cm. We achieved compressed pulses with an average power of 500 mW and duration of 1.8 picoseconds, measured by second harmonic autocorrelation (Figure 2). Using a 5 mm long KTP crystal, an average power of 40 mW was generated at 532 nm.

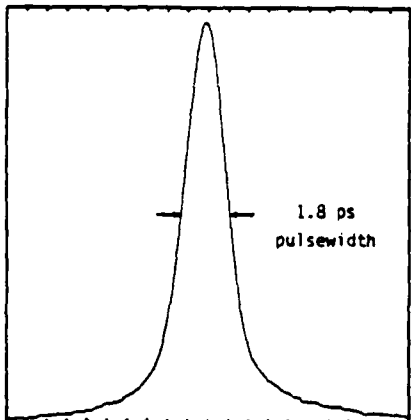


Fig. 2 Measured autocorrelation waveform of compressed Nd:YAG pulse (1 ps/div). The indicated FWHM pulsewidth assumes a Gaussian envelope.

We predicted the amount of spectral broadening and subsequent pulse compression by assuming that the fiber causes self-phase modulation only

and that group velocity dispersion is negligible. These assumptions are justified in our experiments because a 100 picosecond pulse at 1.06 microns requires a 400 km fiber to double in width due to group velocity dispersion. The effect of the self-phase modulation is to introduce into the phase of the electric field a contribution $\phi(t)$ that is proportional to the intensity envelope $I(t)$.

$$E(L,t) = E_0(L,t) \cdot \exp[j(k_0 L + \phi(t) - \omega t)]$$

$$\phi(t) = A \cdot I(t) / I_0$$

The dimensionless parameter A is defined as:

$$A = \frac{2\pi L n_2 I_0}{\lambda_0 n_0 c \epsilon_0}$$

where: L = fiber length
 n_0 = linear index of refraction
 n_2 = nonlinear index of refraction
 I_0 = peak intensity
 λ_0 = free space wavelength
 ϵ_0 = free space permittivity

We obtain the compressed time domain waveform by Fourier transforming the electric field, multiplying by the grating pair transfer function [6], and inverse transforming the product. The spectral broadening, optimum grating spacing, and minimum pulsewidth are characterized by the parameter A. For the power densities in our experiments, A is approximately 150. We used this value to predict a spectral broadening ratio of 155 and a final pulsewidth of 1.6 picoseconds assuming a Gaussian pulse shape. This is in good agreement with our experimental results. The theoretical spectra of the chirped pulse is shown in Figure 2b.

Self-phase modulation in single-mode fibers in the absence of group velocity dispersion (GVD) produces a frequency sweep (chirp) across the pulse that is linear in the center of the pulse only [1,2]. The grating pair is a matched filter for a linear frequency sweep and thus parts of the pulse with a nonlinear chirp do not contribute to an optimally compressed pulse. Furthermore, when the parameter A increases, more of the pulse is chirped nonlinearly and the expected increase in compression ratio suffers. This explains why we obtained a pulse compression ratio of 45:1 while the frequency spectrum broadened by 117:1. Figure 3 shows the theoretical spectral broadening and pulse compression ratios as a function of A. This situation is not as severe in fibers with group velocity dispersion because the GVD tends to linearize the chirp over more of the pulse.

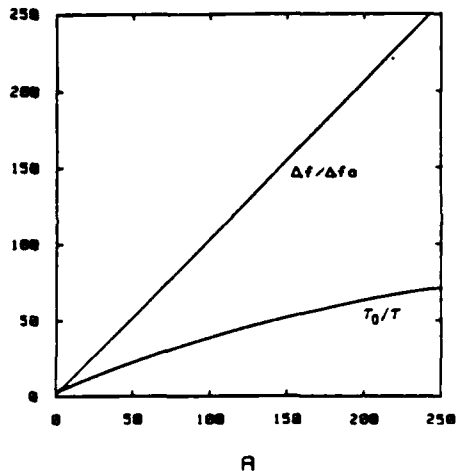


Fig. 3 Theoretical spectral broadening ratio $\Delta f/\Delta f_0$ and pulse compression ratio T_0/T as a function of the parameter A.

Δf = final FWHM bandwidth
 Δf_0 = initial FWHM bandwidth
 T = final FWHM pulsewidth
 T_0 = initial FWHM pulsewidth

In conclusion, we have built an efficient and compact pulse compressor using a single-mode optical fiber and a grazing incidence grating delay line. With this device we compressed 80 picosecond pulses from a cw mode-locked Nd:YAG laser to 1.8 picoseconds. We also generated synchronized pulses at 532 nm with 8% conversion efficiency. The compressor offers a simple, compact alternative to synchronously pumped dye or color center lasers for the generation of picosecond pulses in the near infrared.

REFERENCES

1. B. Nikolaus and D. Grischkowsky, App. Phys. Lett. 42, 1 (1983)
2. B. Nikolaus and D. Grischkowsky, App. Phys. Lett. 43, 228 (1983)
3. C.V. Shank, R.L. Fork, R Yen, R.H. Stolen, App. Phys. Lett. 40, 761 (1982)
4. A.M. Johnson, R.H. Stolen, W.M. Simpson, App. Phys. Lett., 44, 729 (1984)
5. W.J. Tomlinson, R.H. Stolen and C.V. Shank, J. Opt. Soc. Am. B, 1, 139 (1984)
6. E.B. Treacy, IEEE J. Quant. Elect., QE-5, 454 (1969)
7. E.B. Treacy, Physics Letters, 28A, 34 (1968)
8. J.D. McMullen, Applied Optics 18, 737 (1979)

A Reprint from the

PROCEEDINGS

Of SPIE-The International Society for Optical Engineering



Volume 460

Processing of Guided Wave Optoelectronic Materials

January 24-25, 1984
Los Angeles, California

Laser assisted growth of optical quality single crystal fibers

M. M. Fejer, J. L. Nightingale, G. A. Magel, R. L. Byer
Applied Physics Department, Stanford University, Stanford, California 94305

©1984 by the Society of Photo-Optical Instrumentation Engineers
Box 10, Bellingham, Washington 98227 USA Telephone 206/676-3290

Laser assisted growth of optical quality single crystal fibers

M.M. Fejer, J.L. Nightingale, G.A. Magel and R.L. Byer

Applied Physics Department, Stanford University, Stanford,
California 94305

Abstract

Single crystal fibers of four refractory oxide materials (Al_2O_3 , $\text{Cr:Al}_2\text{O}_3$, Nd:YAG and LiNbO_3) have been grown by a miniature pedestal growth technique. The growth apparatus employs novel electronic control, mechanical and optical systems enabling growth of high optical quality fibers. All four materials exhibit similar growth characteristics and yield fibers of comparable quality. Measured optical waveguide losses at 632.8 nm for a 5 cm long 170 μm diameter $\text{Cr:Al}_2\text{O}_3$ fiber were 0.04 dB/cm.

Introduction

The ability to fabricate optical waveguides in materials other than glass offers new and interesting device opportunities. In particular, waveguides formed from single crystal fibers offer the potential to make devices that utilize the unique optical and nonlinear optical properties of single crystals in a guided wave structure.

In this paper we report the growth of single crystal fibers using a laser assisted miniature pedestal growth technique.^{1,2,3} To implement the growth of small diameter, oriented, single crystal fibers, we have designed and constructed a fiber growth apparatus, that uses a waveguide CO_2 laser source and a unique symmetrical optical focusing system.^{4,5}

The advantages of single crystal fibers are best illustrated by considering potential applications. The applications, in turn, generate a set of criteria that the single crystal fibers must meet if they are to be useful in devices. Following the discussion of applications and fiber parameters, we describe the growth apparatus and recent growth results. We then review optical measurements of single crystal fibers and summarize progress toward single crystal fiber devices.

Applications and properties of single crystal fibers

The growth of single crystal fibers is motivated by their application to linear and nonlinear optical devices that are not possible in glass fibers. For convenience, we classify devices as passive, active and nonlinear. Table I lists examples of possible single crystal fiber applications within these classes and illustrates each application area by some representative materials. In addition to device applications, the rapid growth of single crystal fibers makes them useful for material surveys.

Table I. List of 4 different classes of applications and some specific devices in each class. Some representative crystalline materials for each application are given in the right hand column.

Passive Devices	
Lightguide	Al_2O_3
Thermometer	
Polarizer	
Active Devices	
Laser amplifier	$\text{Nd}^{+++}:\text{YAG}$
Laser oscillator	$\text{Cr}^{+++}:\text{Al}_2\text{O}_3$
Nonlinear Devices	
Modulator	$\text{Ti}^{+++}:\text{Al}_2\text{O}_3$
Mixer	LiNbO_3
Harmonic generator	
Parametric oscillator	
Materials Surveys	
Laser host-ion combinations	$\text{Ti:Al}_2\text{O}_3$

To date we have grown single crystal fibers of Al_2O_3 , $\text{Cr:Al}_2\text{O}_3$, Nd:YAG and LiNbO_3 , in the orientations, lengths, and diameters shown in Table II. This list is representative and not intended to be complete, since more than thirty materials have been grown by this technique at Stanford University.⁶

The optical attenuation of a single crystal fiber is determined by a number of factors including crystal defects, impurity concentration, compositional inhomogeneities and diameter fluctuations.

Fiber diameter control is of concern since random diameter fluctuations of only 1% can lead to modal conversion and scatter losses in the range of 5% cm^{-1} . However, for a typical case, diameter fluctuations of 0.1% yield calculated losses of only 0.05% cm^{-1} . Periodic diameter modulation of

the fiber also leads to scatter losses. However, if properly controlled, periodic fiber diameter modulation may be useful as a Bragg mirror or filter.

Table II. Representative Single Crystal Fibers

Material	Orient- ation	Length (cm)	Diameter (μ m)
Al_2O_3	$\langle 001 \rangle$	20 3.5	170 50
$\text{Al}_2\text{O}_3 + 0.05 \text{ wt \% Cr}$	$\langle 001 \rangle$	10.0 3.0	170 95
YAG + 0.9 wt % Nd	$\langle 111 \rangle$	3.5	110
LiNbO_3	$\langle 001 \rangle$ $\langle 100 \rangle$	3.5 3.0	50 170

The optical loss resulting from diameter variations can be reduced by using a diffused cladding if the diffusion depth is large compared to the scale length of the diameter variations. Such a cladding might be achieved in LiNbO_3 by diffusing protons into the fiber using known techniques.⁷

To date fibers grown with our apparatus have shown diameter fluctuations on the order of several percent under open loop growth conditions. We have designed and plan to implement closed loop diameter control during fiber growth

using a novel diameter measurement apparatus.⁸ Fiber diameter uniformity of 0.1% should be achieved using this system.

The device applications of single crystal fibers shown in Table I determine the fiber parameters necessary for good device performance. Important crystal fiber parameters include length, diameter, and optical loss. Table III summarizes typical single crystal parameters required for thermometry using an Al_2O_3 fiber⁹ and for second harmonic generation using a LiNbO_3 fiber.

Table III. Typical single crystal fiber parameters for device applications

Passive device (Thermometry using sapphire)	
length	- 20 cm
diameter	- 70 microns
diameter variations	- 1%
Nonlinear device (SHG using lithium niobate)	
length	- 5 cm
diameter	- 25 microns
diameter variations	- 0.1%
efficiency	- 0.1%/mW

High temperature thermometry is possible using blackbody emission guided along a sapphire fiber. Since the sapphire fiber can be optically coupled to a glass fiber only the portion of fiber exposed to high temperatures need be sapphire. We thus anticipate relatively short, e.g. 20 cm, fiber lengths to be useful. Constraints on fiber flexibility generally determine the maximum allowable fiber diameter. A 70 μ m diameter sapphire fiber can be readily bent on a 1 cm radius of curvature, adequate for most applications.

This device is not particularly sensitive to optical loss or mode coupling within the fiber. The allowable diameter variations are, therefore, relatively loose, on the order of 1%.

To date high temperature sapphire thermometry has made use of short sapphire rods coated with iridium metal at the tip.⁹ Recently we have grown 170 μ m diameter fibers of sapphire up to 20 cm in length for this application. We have also successfully doped the end of the sapphire fiber with metal to provide an integral, stable, blackbody source. Tests are now in progress to demonstrate the use of sapphire fibers as a flexible, high temperature, high speed thermometer.

Nonlinear devices using crystal fibers promise higher frequency conversion efficiency than conventional devices since fibers allow a tight beam confinement over a long interaction length. For example a 5 cm long 25 μ m diameter LiNbO_3 fiber offers a factor of 50 efficiency improvement compared to second harmonic generation in a bulk crystal. Since this device requires low loss single mode optical propagation in the fiber, the diameter control tolerances are tight, on the order of 0.1%. Thus high conversion efficiency is possible with incident powers on the order of 100 mW, which is the power level now available in single mode diode laser sources.

Crystal growth apparatus

We have designed and built a growth apparatus to produce single crystal fibers of the quality required for device applications. The apparatus uses a laser heated miniature pedestal growth technique first applied to optical fiber growth by Burrus and Stone.¹⁰ Figure 1 illustrates growth of a single crystal fiber using the laser heated miniature pedestal growth technique.

A waveguide CO_2 laser is focused onto the molten zone by a combination refraxicon/parabolic mirror optical system shown schematically in Fig. 2. A source rod is translated into the focused laser beam via a belt drive translation system. The source rod may be

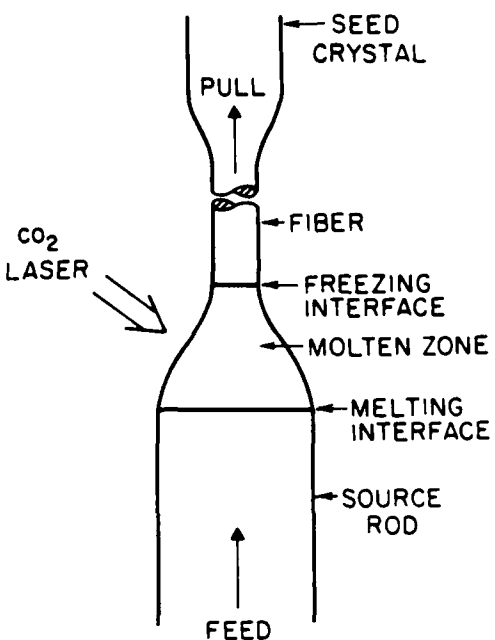


Figure 1. Schematic of miniature pedestal growth.

fabricated from either single crystal, polycrystalline, or hot pressed powder material.

To initiate growth an oriented seed rod is dipped into the molten zone. The seed rod defines the crystallographic orientation of the fiber. Growth proceeds by simultaneously translating the lower and upper fiber source and seed rods. Conservation of mass determines the fiber diameter reduction as the square root of the feed rate to pull rate ratio. Diameter reductions of 3:1 are typical. Greater diameter reductions are difficult due to the onset of growth instabilities.

Miniature pedestal growth differs from the viscous drawdown of a glass fiber since, unlike glass, crystals have a definite solid/liquid phase transition. The molten zone is a true liquid being held in place by surface tension.

In order to achieve a stable fiber diameter, stable fiber growth conditions must be realized. This in turn dictates a stable mechanical apparatus, smooth feed and pull rates, stable laser power and symmetric heat input into the molten zone.

The optical system shown schematically in Fig. 2 uses copper mirrors to focus the CO₂ laser source onto the molten zone. The refraxicon, in combination with the f/2 focusing parabolic mirror, yields a symmetric focus with a 30 μm diameter. The tight focus allows the growth of small diameter fibers.

The translation system shown in Fig. 2 uses a seamless-belt drive system driven by a phaselocked dc motor. The fiber is held in a 'V-groove' etched in a silicon substrate that is oxidized to form a hard silicon dioxide surface. This drive system is in turn controlled by a digital logic system that allows control of the growth rate and diameter reduction ratio.

The present growth apparatus yields fibers with 2% diameter variations over centimeter lengths. The growth of more uniform fibers will require active control of the fiber diameter during growth. Figure 3 shows a schematic of the fiber growth apparatus including a fiber diameter measurement and control system. Since no commercial fiber diameter system met our sensitivity, speed, and working distance requirements, we have designed and built the non-contact diameter measurement system shown in Fig. 4.

The fiber diameter measurement system uses a helium-neon laser to illuminate the fiber. The beam is tightly focused using a cylindrical lens to define the measurement zone along the fiber. In the other plane the beam is scattered by the fiber and imaged onto a

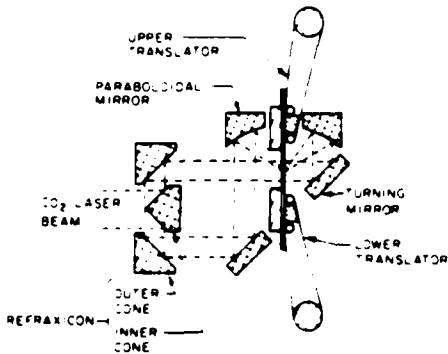


Figure 2. Schematic of focusing system and fiber translation devices.

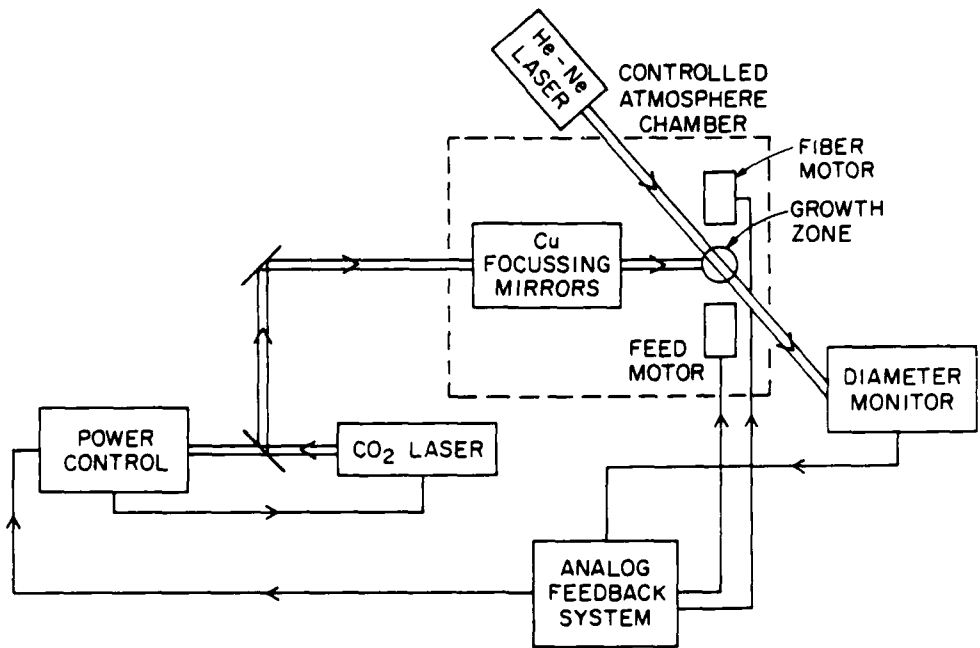


Figure 3. Schematic of fiber growth apparatus.

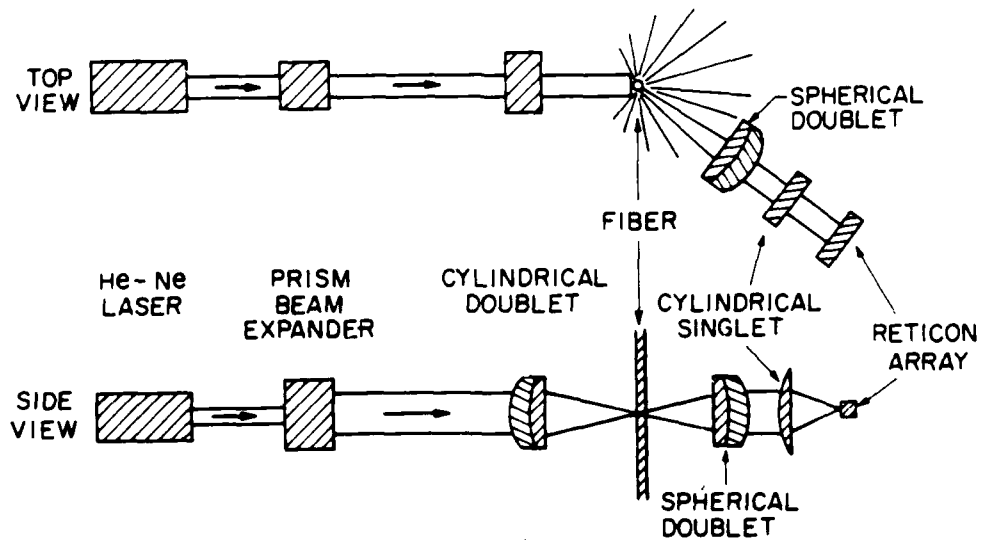


Figure 4. Schematic of diameter measurement system.

a photodiode array where interference fringes are detected.¹⁰ The interference pattern is analyzed to provide an output signal proportional to the fiber diameter. Recent measurements have shown that the diameter sensitivity is $\pm 500 \text{ \AA}$ at a measurement rate of 1 kHz.

The diameter measurement system has not yet been incorporated into the growth apparatus. Thus all fibers grown to date have been without diameter feedback control.

Fiber growth results

In the six months that the fiber growth apparatus has been operational four crystalline materials have been grown: sapphire, ruby, Nd:YAG and LiNbO₃. Table II summarizes the length, diameter and orientation of the single crystal fibers. We initiated our growth studies by concentrating on sapphire and chromium doped sapphire or ruby because of availability and ease of growth. Experience with sapphire has enabled us to extend growth studies to Nd:YAG and to LiNbO₃. To date we have grown both a-axis and c-axis LiNbO₃ with diameters as small as 50 μm and lengths to 3.5 cm.

Typical fiber growth rates range between 1 and 10 mm/min . While these growth rates are slow compared to glass fiber pulling rates, they are orders of magnitude faster than bulk crystal Czochralski growth rates. Since fiber lengths of 5 cm are adequate for many applications useful fiber lengths can be grown in approximately twenty minutes.

The growth apparatus is designed to yield fiber diameters of between 500 and 20 μm . However, smaller diameter fibers to 6 μm have been grown under special circumstances.⁶ The initial feed rods are fabricated to 500 μm diameter using a centerless grinder. Diameter reductions of 3 to 1 are normally used during growth. Smaller diameter fibers are grown using previously grown fibers as source rods. The CO₂ laser power required to grow A₂O₃ and LiNbO₃ fibers from 500 μm diameter feed rods are 4.8 and 1.5 watts respectively. The difference is chiefly due to the different melting temperatures of the materials, 1945°C for sapphire and 1260°C for LiNbO₃. The required laser power reduces to less than 1 W for fibers grown from 170 μm diameter feed rods.

Sapphire, Nd:YAG and LiNbO₃ all display similar growth characteristics. Figure 5 shows the molten zone shape for A₂O₃. The molten zone shape is similar for the other materials. For optimum growth stability the laser power is adjusted to yield a molten zone with a height-to-width ratio of near unity for a 3:1 diameter reduction ratio.

The single crystal fiber growth morphology is similar to that seen in bulk Czochralski growth. For example, $\langle 111 \rangle$ axis Nd:YAG fibers show a slightly rounded hexagonal cross-section as shown in Fig. 6. LiNbO₃ grown along the optic axis shows a characteristic 3-fold symmetry with growth ridges running parallel to the crystal length as shown in Fig. 7.

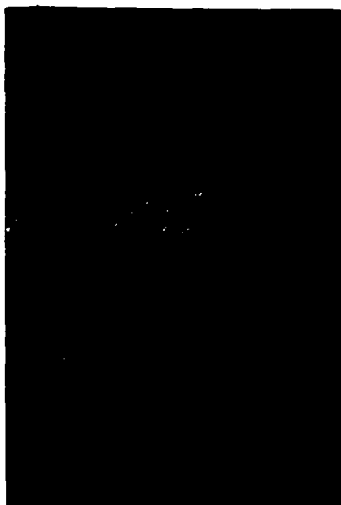


Figure 5. Photomicrograph showing growth of a 170 μm diameter A₂O₃ fiber from a 500 μm diameter source rod. The growing fiber is invisible since its smooth sides scatter very little light.



Figure 6. Scanning electron microscope photograph of cross-section of Nd:YAG fiber.



Figure 7a. Scanning electron microscope photograph of cross-section of LiNbO_3 fiber showing pronounced 3-fold growth ridges. The internal concentric ring pattern and dark central area are artifacts of the procedure used to obtain the cross-section.

Since the fiber cross-section is invariant with length, the growth morphology should not be detrimental to optical applications.

Early single crystal fibers showed fine scale diameter fluctuations along the fiber length with a scale of $1 - 10 \text{ }\mu\text{m}$. Crystals grown with the current machine are free of these irregularities as shown in Fig. 7b. At a longer length scale we have demonstrated diameter stability to $\pm 2\%$ over fibers several centimeters in length.

Optical measurements

We recently have initiated optical property measurements on single crystal fibers. For example, we have measured an optical waveguide loss of 0.04 dB/cm at 632.8 nm in a 5 cm long $170 \text{ }\mu\text{m}$ diameter ruby fiber. Comparable losses have been measured in other fibers. For these measurements the single crystal fibers were not cladded so that guiding was provided by the crystal-air dielectric interface. We anticipate lower propagation losses as we grow improved optical fibers and employ more refined cladding techniques.

Sapphire fibers as now grown are suitable for some light-guide applications such as thermometry. For example, we have demonstrated optical propagation in a sapphire fiber heated to 1500°C with no significant change in transmission at the elevated temperatures.

Summary

In summary we have designed and built a fiber growth apparatus to produce high quality single crystal fibers. The apparatus uses the miniature pedestal growth technique which permits the growth of crystal fibers in a wide range of materials. The apparatus is designed to handle fiber diameters as small as 20 microns with fiber lengths exceeding 20 cm . Diameter stability to $\pm 2\%$ has been demonstrated over fiber lengths of several centimeters. The optical attenuation of these fibers is 0.04 dB/cm . These fibers are of sufficient quality for simple passive device applications such as high temperature thermometry.

A fiber diameter measurement system has been built which when installed in the growth apparatus should improve the diameter stability and the optical attenuation by an order of magnitude. We anticipate these fibers will be of sufficient quality for a host of active and nonlinear device applications.

Acknowledgements

We gratefully acknowledge useful discussions with M. Digonnet, G.A. Kotler, R.S. Feigelson, R.K. Route, W. Kway, W. Kozlovsky and T.Y. Fan, all of Stanford University.

We thank D. Buseck, S. Greenstreet, J.J. Vrheil, M.M. Simkin, K.L. Doty, A. Ospina, B.A. Williams and P.A. Thompson for technical support.

This work was supported by the Joint Services Electronics Program, Contract #NO0014-75-C-0632, the Air Force Office of Scientific Research, Contract #83-0193 and the Stanford University Center for Materials Research, Contract #CMR-80-20248.

G.A. Magel gratefully acknowledges the support of the Fannie and John Hertz Foundation.

References

1. Jaggerty, J.S., N.A.S.A. Cr-120948, 1972.
2. Burrus, C.A., and Stone, J., Appl. Phys. Letts. 36, p.318 (1975).
3. Stone, J., and Burrus, C.A., Fiber and Integrated Optics, 2, p.19 (1979).
4. Fejer, M., Byer, R.L., Feigelson, R.S., and Kway, N., Proceedings of the S.P.I.E. Advances in Infrared Fibers II, p.320 (1982).
5. Fejer, M.M., Nightingale, J.L., Magel, G.A., Byer, R.L., to be published.
6. Feigelson, R.S., Proceedings of the Fifth International Summer School on Crystal Growth, Davos, Switzerland, 1983.
7. Jackel, J.L., Rice, C.E., and Vasilka, J.J. Jr., Appl. Phys. Letts. 41, p.607 (1982).
8. Fejer, M.M., Magel, G.A., and Byer, R.L., to be published.
9. Dils, R.R., J. Appl. Phys. 54, p.1198 (1983).
10. Smithgall, D.H., Watkins, L.S., and Frazee, R.E. Jr., Applied Optics, 16, 1395 (1977).

Reprinted from PROCEEDINGS OF THE
ULTRASONICS SYMPOSIUM, Oct 31, Nov 1, 2, 1983

ACOUSTIC WAVE REFLECTION FROM FERROELASTIC DOMAIN WALLS

S.W. Meeks[†] and B.A. Auld

Edward L. Ginzton Laboratory
Stanford University
Stanford, CA, 94305

ABSTRACT

A theoretical model of acoustic plane wave reflection from a ferroelastic domain wall is presented. Values of the reflection coefficients at normal incidence are calculated for two ferroelastics: Neodymium Pentaphosphate (NPP) and Gadolinium Molybdate (GMO). Previous work has shown that NPP has an exceptionally large reflection coefficient for certain reflection geometries. We attribute the large reflection coefficient to a vibrating domain wall. The theory presented in this paper is used to model variable delay lines, bandpass and bandstop filters based on the moving wall concept.

1. Introduction

Ferroelastic materials have the unique property of exhibiting stress-switchable configurational states. These regions of distinctly different configurational states, called ferroelastic domains, exhibit distinct physical properties and the boundaries between domains, or domain walls, are therefore surfaces of abrupt change in material properties. The existence of switchable and latching boundaries of this nature provide a basis for a variety of acoustical and optical devices such as variable acoustic delay lines, variable acoustic stopband filters, optical diffraction gratings, and optical phasematching gratings. The two materials considered in this paper are the pure ferroelastic: Neodymium Pentaphosphate (NPP) and the ferroelastic-ferroelectric:Gadolinium Molybdate (GMO).

Figure 1 shows the acoustic slowness surfaces (the inverse of phase velocity versus angle) for quasilongitudinal (QL) and quasishhear (QS) propagation in the xz plane of NPP. The left side of the figure is the slowness surface in domain state 1 and the right in domain state 2. The dashed line separating the two states corresponds to a domain wall. The slowness surfaces reflect about the z axis when the material switches from one domain state to another. This changes the angle of the major axis of the surfaces. If one considers a non-normally incident wave and one remembers Snell's law, the possibility of a discontinuity in acoustic velocity can be clearly seen. A normally incident QL or QS wave has no velocity discontinuity. However, we will show there is a mechanical displacement polarization

discontinuity. The y-polarized pure shear not shown in Fig. 1) suffers no polarization discontinuity hence it does not reflect and will not be considered further. An analogous situation occurs with the z polarized pure shear wave in GMO.

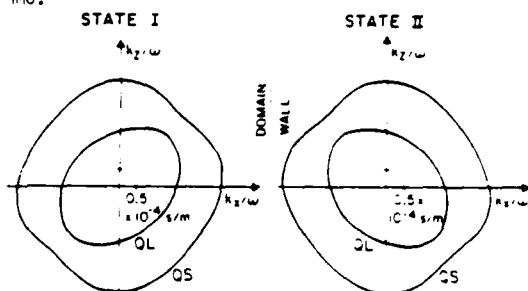


Figure 1 Change in NPP Slowness Surfaces for the Two Possible Domain States.

2. Acoustic Reflections from a GMO Domain Wall

Ferroelastic-ferroelectric twins (domains) in GMO form with domain walls in the (110) or (110) crystallographic plane. The situation for a (110) plane domain wall is illustrated in the upper part of Fig. 2. Figure 2 also illustrates the important point that the "a" and "b" crystal axes of orthorhombic GMO are exchanged when the domain state is switched. It is this exchange of crystal axes which leads to different acoustic properties and hence reflections from the domain wall. The bottom half of Fig. 2 shows a simplified model of a GMO domain wall which neglects the 21 minute angle between the crystal faces in the two domains and also the piezoelectricity of GMO.

The bottom half of Fig. 2 also shows the incident, reflected, and transmitted acoustic waves which must be matched at the domain wall to obtain a solution. To solve this reflection problem one must first solve the Christoffel equation² for propagation in the xy plane of an orthorhombic crystal. This analysis will consider only normal incidence since this is the only case for which an analytical solution is possible. To obtain the reflection coefficients one must match at the domain wall the x and y components of the particle velocity and the traction force for the

five waves shown in Fig. 2 giving a system of 4 linear equations for the scattered amplitudes. The particle velocities \vec{v} are obtained from the solutions of the Christoffel equation, and the traction forces \vec{T} on the wall for normal incidence are

$$\vec{T} = \pm \rho v_p \vec{v} \quad (1)$$

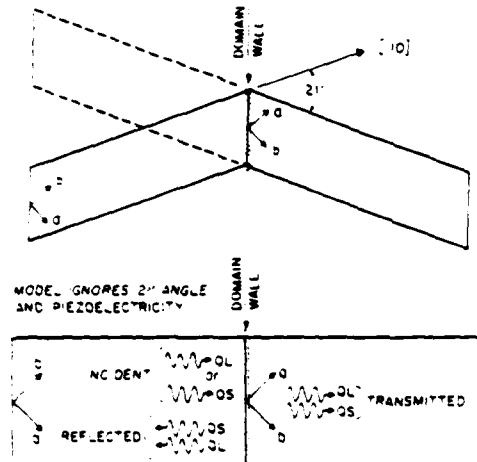


Figure 2 Model of a GMO Domain wall.

where ρ is the density, v_p the phase velocity, and the minus (plus) sign refers to a positive (negative) traveling wave. As stated earlier the reflection coefficient for normal incidence in both GMO and NPP is due entirely to a polarization change at the domain wall. In GMO the QS and QL waves change their polarization angle by about 10 degrees when crossing the domain wall.

The solution of the resulting system of equations yields the following expressions for the amplitude reflection coefficients in GMO at normal incidence

$$R_{EE} = \frac{v_{Qe}^2 - v_{QS}^2}{v_{QS}^2 + v_{Qe}^2 - v_{QL} v_{QS} (C_1^2 C_4^2 + C_2^2 C_3^2) / (C_1 C_2 C_3 C_4)} \quad (2a)$$

$$R_{SS} = -R_{EE} \quad (2b)$$

$$R_{SE} = R_{ES} = \frac{(v_{QS} v_{Qe} - v_{Qe}^2) (C_2^2 C_3 C_4 + C_1 C_2 C_4^2)}{C_1 C_2 C_3 C_4 (v_{QS}^2 + v_{Qe}^2) - v_{Qe} v_{QS} (C_1^2 C_4^2 + C_2^2 C_3^2)} \quad (2c)$$

where,

$$C_1 = \left(\frac{\sqrt{2}}{2}\right)(1+u_1); C_2 = \left(\frac{\sqrt{2}}{2}\right)(1+u_2); C_3 = \left(\frac{\sqrt{2}}{2}\right)(u_1-1);$$

$$C_4 = \left(\frac{\sqrt{2}}{2}\right)(u_2-1)$$

$$u_2 = \frac{1 - 2[C_{66} + (C_{11}/2) + (C_{22}/2) - C']^{-1} [(C_{11}/2) + (C_{66}/2)]}{[C_{66} + (C_{11}/2) + (C_{22}/2) - C']^{-1} [C_{12} + C_{66}]}$$

$$C' = \sqrt{[C_{66} + (C_{11}/2) + (C_{22}/2)]^2 - 4C} \quad (3)$$

$$C = [C_{11}/2 + (C_{66}/2)][(C_{66}/2) + (C_{22}/2)] - (C_{12} + C_{66})^2/3, \quad (4)$$

with Q_1 the same as Q_2 except for a positive sign before C' . The QS and QL phase velocities of GMO at normal incidence are v_{QS} and v_{Qe} , respectively and the doubly subscripted constants are elements of the elastic stiffness matrix for GMO. The magnitude of the calculated values are shown in Table I and compared with measured values.

3. Acoustic Reflections from an NPP Domain wall

Figure 3 shows the change in crystal axes as one crosses an "a" domain wall in the pure ferroelastic NPP (or any (RE)PP where $RE=Ld-Tb$). The lower half of Fig. 3 shows the simplified model which neglects the 1 degree angle between the faces in the two domains and assumes $C_{46} = 0$, as shown by experiment.⁶ The solution of this reflection problem proceeds in a manner similar to that for GMO. The predicted reflection coefficients are in general larger than GMO since the change in polarization is 24 degrees when crossing the NPP domain wall, compared with 10 degrees, the expressions for the reflection coefficients at normal incidence are

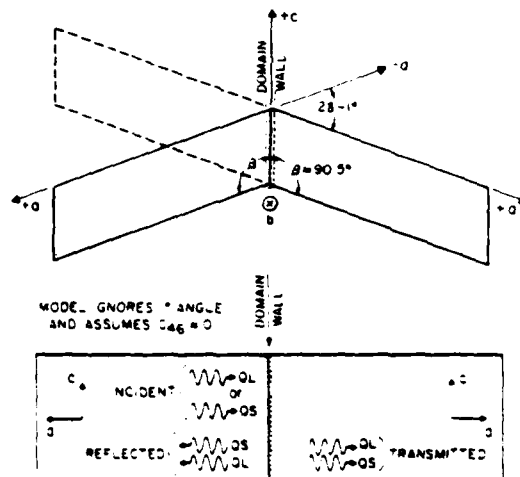


Figure 3 Model of an NPP or LPP Domain wall.

$$R_{EE} = \frac{v_{Qe}^2 - v_{QS}^2}{v_{Qe}^2 + v_{QS}^2 - v_{QS} v_{Qe} (v_3^2 + v_4^2) / (u_3 u_4)} \quad (4a)$$

$$R_{SE} = R_{ES} = \frac{v_{QS} v_{Qe} - v_{Qe}^2 + (u_3 v_{Qe} v_{QS}) / u_4}{v_{Qe}^2 + v_{QS}^2 - v_{QS} v_{Qe} (v_3^2 + v_4^2) / (u_3 u_4)} \quad (4b)$$

$$R_{ss} = \frac{v_{qs}^2 - v_{qe}^2 + v_{qe} v_{qs} v_3 v_4}{v_{qe}^2 - v_{qs}^2 - v_{qs} v_{qe} (v_3^2 + v_4^2) / (v_3 v_4)}, \quad (4c)$$

where v_{qs} and v_{qe} are the NPP quasimode and quasimode phase velocities at normal incidence obtained from the Christoffel equation and

$$v_{qs} = \frac{c_{55} - c_{11} \pm \sqrt{(c_{11} - c_{55})^2 + 4c_{15}^2}}{2c_{15}}, \quad (5)$$

and the doubly subscripted constants are the elastic constants of NPP. Since the elastic constants of NPP were not available we used the constants of the La isomorph LPP.⁶ Calculated and experimental values of the magnitude of the reflection coefficients are given in Table I.

The most interesting point in Table I is the comparison between the theoretical and experimental values of R_{ss} . Lemons and Colgren³ attribute the anomalously large reflection of a GDO domain wall to vibration of the domain wall. We have observed under a microscope the vibration of an NPP domain wall when reflecting a high intensity (350 watts per square centimeter) acoustic shear wave. A physical picture of a vibrating wall driven by an incident shear wave is shown in Fig. 4. An incident shear wave with the polarization shown in Fig. 4 has a stress component in the direction needed to switch the configuration state. The wall responds to the acoustic wave by switching the configuration states over a number of unit cells, and vibrating between the initial and final positions shown. In so vibrating the wall absorbs and reradiates the acoustic energy as a shear wave. The reflection coefficients R_{ss} and R_{sl} are not modified in this way, since the incident longitudinal wave does not have the proper stress components to switch the configurational state and the wall therefore does not vibrate. Consequently, experimental values of R_{ss} and R_{sl} for NPP should show good agreement with theory, as in GDO (Table I).

4. Domain Wall Grating Acoustic Filters

Figure 5 shows one possible ferroelastic bandstop filter structure, in which a regular array of domain walls is injected into a crystal.¹ The theory of Sittig and Coquin⁷ gives mid band reflection and transmission factors for a constant spacing grating,

$$RF = \frac{z^{2N} - 1}{z^{2N} + 1}; \quad TFI = \frac{2z^N}{z^{2N} + 1} \quad (6)$$

where z = impedance mismatch ratio between domains and N = number of sections in grating. The mismatch ratio for NPP is 1.52, obtained by

calculating an effective mismatch ratio using a 2 medium planewave model and R_{ss} . The above equations indicate that an array of only 10 domains in NPP will have -30.5 dB transmission in the stopband with excellent sidelobe suppression. The high stopband rejection is due to the large reflection coefficient of a single NPP domain wall. The spacing of the domain walls in NPP at 50 MHz is 34 microns for the shear wave and 62 microns for the longitudinal wave. In GDO under the same conditions is 23 and 39 microns, respectively.

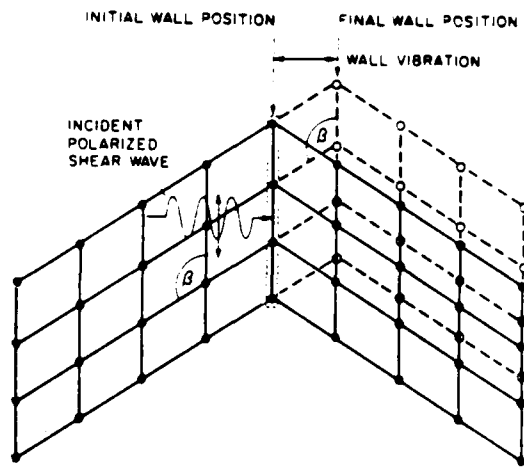


Figure 4 Vibrating Domain Wall in NPP

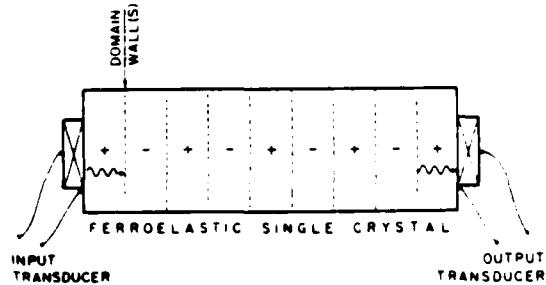


Figure 5 Ferroelastic Bandstop Filter.

Since the mismatch ratio for GDO is much smaller, many more domain walls are required for similar performance. An array in GDO and NPP with the above spacings may be created by a transverse mechanical injection technique,¹ or by applying a periodic electric field (GDO only). A third means proposed for creating an array is to apply a uniform static stress and an intense acoustic field to the crystal. This creates through nonlinear elasticity a spatially varying static stress. The crystal is then raised above its Curie point, with the acoustic field applied.

upon cooling through the transition the domain should appear in an array with the same periodicity as the nonlinearly generated static stress. The period of the SMO (or NPP) array may be controlled by changing the frequency of the acoustic wave used to generate the spatially varying static stress. In this structure the normally incident acoustic wave will experience some anisotropic walkoff, but the direction of walkoff is reversed in successive domain sections (Fig. 1) and cancels after passage through an even number of sections. The SMO filter will probably be more useful as a passband filter, since a small reflection factor is required.

b. Conclusions

We have presented analytical expressions for the reflection coefficients R_{SS} , $R_{SS'}$, $R_{S'}$ of SMO and NPP ($\text{E}=\text{La-TD}$). The R_{SS} reflection coefficients of SMO and NPP are anomalously large, due to wall vibration. Wall vibration in NPP under an intense acoustic field has been visually

observed. A physical picture of how a domain wall vibrates under a properly polarized intense acoustic shear wave has been presented. Calculations indicate that a type of bandstop or bandpass filter may be created by injecting arrays of domain walls into NPP and GMO crystals. These ferroelastic filters will have desirable transmission or reflection spectra, will have no "walkoff", and will be tunable. For a bandpass filter it is necessary to operate in a reflection mode or to use pairs of grating arrays as reflection mirrors spaced to create a standing wave 'cavity', as in SAW technology. These grating structures may also be applicable in tunable SAW filters. In this case full cross-section domain walls (Fig. 5) are likely to be undesirable because of coupling into bulk waves, but arrays of blade domains (narrow wedge-shaped domains attached to the crystal surface) offer an alternative.

[†]On educational sabbatical from the Naval Research Laboratory, JSRD, Orlando, FL.

Table I. Reflection Coefficients

SMO		NPP		
Theoretical dB	Experimental dB	Theoretical dB	Experimental dB	
R_s	-40.3	-40	-26.3	----
$R_{S'}$	-17.2	-29	-29.6	----
R_{SS}	-40.3	-28(max); -38(min)	-26.0	-13.7*

*Measured at 6.4 MHz for a guided mode in a rod-like sample.

c. Acknowledgments

This work was supported by the Office of Naval Research (Contract N00014-75-C-0632) and the NSF-MRL Program through the Center for Materials Research at Stanford University.

d. References

1. S.W. Meeks, et al., "Interaction of Acoustic Waves and Ferroelastic Domain Walls" in Ferroelectrics (to be published).
2. R.A. Auld, Acoustic Fields and Waves in Solids, Wiley-Interscience, New York, 1973, Vol. 1, Ch. 7.
3. J.T. Hochli, Phys. Rev. B, 6, 1814 (1972).
4. R.A. Lemons and L.A. Godfrey, 1978 Ultrasonics Symposium Proceedings, 188.
5. H.P. Weber et al., Phys. Rev. B, 11, 1152 (1975).
6. G. Errandonea, Phys. Rev. B, 21, 5221 (1980).
7. E. Sittig and G. Coquin, IEEE Trans. Sonics and Ultrasonics, SU-15, 111 (1968).

Observations of Higher-Order Laser-Induced Surface Ripples on $\langle 111 \rangle$ Germanium

P. M. Fauchet and A. E. Siegman

Edward L. Ginzton Laboratory,
Stanford University, Stanford, CA 94305, USA

Received 24 June 1983 Accepted 24 July 1983

Abstract. We report the observation and analysis of higher-order optical diffraction patterns arising from linear combinations of the primary laser-induced gratings or ripples on germanium surfaces. These higher-order surface structures presumably arise from nonlinear interactions between superimposed primary gratings with different grating wave vectors. For gratings produced by normally incident laser beams on Ge $\langle 111 \rangle$ surfaces, the diffraction patterns exhibit a strongly hexagonal symmetry.

Observations of laser-induced periodic surface structures extend back over nearly two decades [1, 2]. There has been a recent upsurge of interest, however, in these periodic ripple structures which can be written into surfaces of a wide variety of materials using an equally wide variety of laser beams. The phenomenon has been accurately described as universal [3], since such ripples can be produced on the surfaces of semiconductors, metals, dielectrics or liquids, using laser signals ranging from single cw beams or repeated Q-switched laser pulses at intensities well below the expected damage thresholds for some materials [4, 5] to picosecond laser pulses at intensities near or above the melting threshold [6, 7].

Van Driel and his co-workers have proposed one analysis which explains the formation of these periodic ripples based on the concept of "radiation remnants" scattered from irregular surface structures [4, 5]; while we have given an analysis which appears to contain a similar physical content, based on calculating the various diffracted orders of light produced by a periodically rippled or modulated surface and then examining the interference between these orders at the sample surface [7]. Numerous references to earlier work are given in [4, 7].

Since these laser-induced surface structures have periods close to the incident laser wavelength, they can be viewed, with some difficulty, using microphotography

or SEM photography. Another powerful and elegant way to look at these ripples was recently introduced by van Driel and co-workers [4], and by Haneman and Nemanich [8]. The ripple structures are studied simply by illuminating the rippled surface with a shorter wavelength probe laser beam at near-normal incidence, and observing the back-diffracted light on a screen located close to the sample. This technique is, of course, a close analog to x-ray scattering by periodic atomic layers, since the periodic structures being observed are of the same order as the probing wavelength. This method allows a more accurate determination of the grating periods and directions in the surface ripple pattern, and a more complete characterization of their properties.

Van Driel et al. [3] have described the circular diffraction pattern that is observed in this fashion when the ripples are produced by an excitation beam arriving at normal incidence, as well as the pattern of two intersecting ovals produced by an excitation beam arriving at off-normal incidence. These patterns are indicative of scattering from the primary or first-order gratings formed by the excitation beam. In this paper we report the observation and analysis of complicated multiple higher-order grating diffraction patterns, of which some typical forms are illustrated in Fig. 1. These diffraction patterns indicate the formation of more complex surface structures that arise from non-

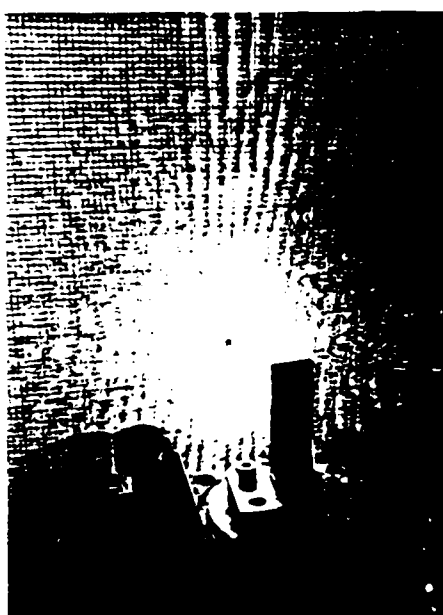
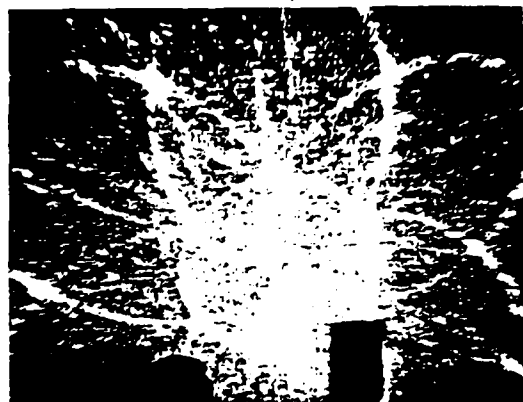
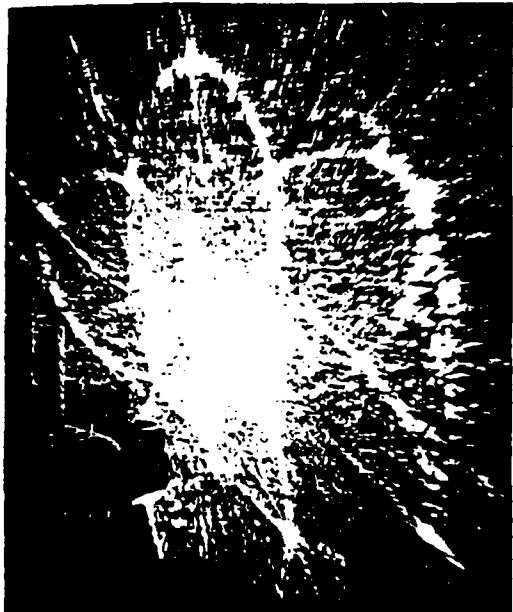


Fig. 1. (a) Hexagonal symmetry pattern observed after illumination with circularly polarized light at normal incidence. (b) Complex diffraction pattern observed after illumination with p-polarized light at $\theta = 50^\circ$.

linear or higher-order interactions between gratings having different wave-vectors. They also give the first indication of periodic structures whose orientation is tied to the underlying crystal structure of the sample, rather than just to the optical properties of the excitation and probe beams.

1. Grating Formation and Diffraction Analysis

The preliminary observations reported here were made in essentially the same fashion as those of the Toronto group [3,4], namely by illuminating a (111) germanium surface with a series of excitation pulses at 1.06 μm . In our work these pulses consist of either repeated single picosecond pulses or, more commonly, of repeated Q-switched bursts of such mode locked pulses, with different angles of arrival and different polarization characteristics in different experiments. The gratings were probed and the diffraction patterns observed using either greatly attenuated 532 nm light derived from the same laser by harmonic generation or a 454.5 nm beam from an argon-ion laser, arriving in both cases at normal incidence to the sample.

1.1. Grating Formation Process

To analyze the grating-formation process as well as the light diffraction from these gratings, we employ a coordinate system with x, y axes in the plane of the surface and z axis normal to the surface, as illustrated in the inset to Fig. 2a. An excitation beam with propagation vector \mathbf{k}_0 is assumed to be incident on the surface traveling at an angle θ to the normal in the x, z plane. Let \mathbf{k}_g be the wave vector for a periodic surface grating that is to be produced in the sample surface (the x, y plane), and \mathbf{k}_s be the propagation vector for the scattered light (or, if one chooses, for the surface wave excitation) that is to be generated in the grating formation process.

From experimental evidence, as well as the currently accepted theories for the grating formation process, the scattered wave \mathbf{k}_s has a propagation vector which is very nearly in the plane of the surface, and a magnitude which is usually, though not always, equal to within a few per cent to that of the excitation wave-vector. The Bragg condition that $\mathbf{k}_0 + \mathbf{k}_g = \mathbf{k}_s$ in the plane of the surface, and the magnitude condition that $\mathbf{k}_s \approx \mathbf{k}_0$, then lead to the conditions that

$$k_0 \sin \theta \pm k_{gx} = k_{sx} \quad \text{and} \quad \pm k_{gy} = k_{sy} \quad (1)$$

with the constraint that $k_{sx}^2 + k_{sy}^2 \approx k_0^2$.

To further simplify our notation, suppose we normalize the magnitude of the grating wave vector to the magnitude of the incident wave vector by writing $\mathbf{g} \equiv \mathbf{k}_g / k_0$. The x and y components of the normalized

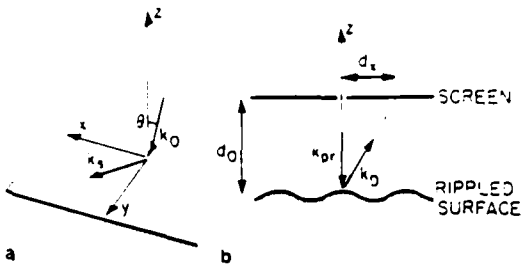


Fig. 2 (a) Geometry for ripple formation. (b) Geometry for surface diffraction

grating wave vector are then given by

$$(g_x \pm \sin \theta)^2 + g_y^2 = 1. \quad (2)$$

That is, for off-normal incidence the normalized grating vectors lie on two intersecting circles of radius unity having their centers at $g_x = \pm \sin \theta$, $g_y = 0$.

1.2. Probe Beam Diffraction Process

Let us now analyze the diffraction of a probe beam from a surface structure with grating wave vector \mathbf{g}_r . (We use the notation \mathbf{g}_r because the higher-order gratings have total wave vectors that are combinations of the primary wave vectors \mathbf{g} given by (2) above.) Suppose the surface is illuminated at normal incidence with a probe beam whose frequency is r times higher, or wavelength r times shorter than the initial excitation beam, so that $\mathbf{k}_{pr} = r \mathbf{k}_0$. The transverse wave vector components of the resulting diffracted beam, which we denote by $\mathbf{k}_D \equiv (k_{Dx}, k_{Dy}, k_{Dz})$, will then be given by

$$k_{Dx} = g_{rx} k_0, \quad k_{Dy} = g_{ry} k_0$$

and the normal component of \mathbf{k}_D , traveling away from the surface, will then be necessarily given by

$$k_{Dz} = \sqrt{r^2 k_0^2 - k_{Dx}^2 - k_{Dy}^2}. \quad (3)$$

An observation screen located at some distance d_s from the sample (Fig. 2b) intersects this diffracted beam at distances d_x and d_y from the probe beam axis that are given by

$$d_x = (k_{Dx} k_{Dz}) d_0, \quad d_y = (k_{Dy} k_{Dz}) d_0. \quad (4)$$

Combining these results gives for the diffracted spot locus on the screen the equations

$$\frac{d_x}{d_0} = \frac{g_{rx}}{\sqrt{r^2 - g_{rx}^2 - g_{ry}^2}}, \quad \frac{d_y}{d_0} = \frac{g_{ry}}{\sqrt{r^2 - g_{rx}^2 - g_{ry}^2}}. \quad (5)$$

We now consider the total gratings \mathbf{g}_T observed in our experiments.

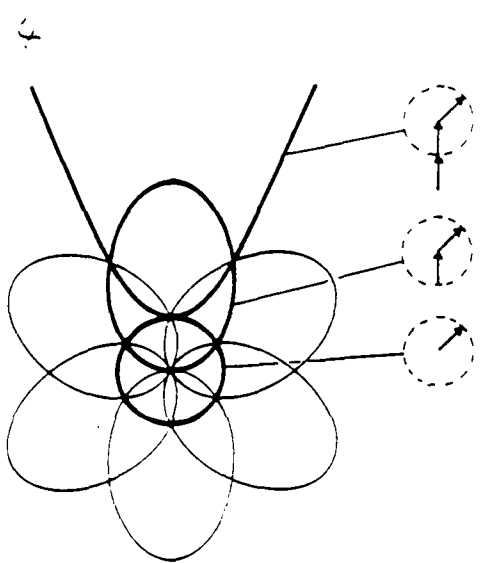


Fig. 3. Predicted diffraction pattern given by (7). The full hexagonal pattern is shown for $m=0$ and 1. From $m=2$, only the pattern formed by $l=0$ is shown; for the other values of l , simply rotate by multiples of 60° . The fit is perfect.

2. Higher-Order Grating Observations

Previous workers have described the diffraction patterns produced by diffraction from the primary laser-induced gratings given by (2), i.e., by those gratings for which $\mathbf{g}_T \equiv \mathbf{g}$. That is, the primary gratings correspond to surface ripples with purely sinusoidal height profiles that vary with position over the surface in the form $h(\mathbf{r}) \approx \sin(k_g \cdot \mathbf{r})$, where \mathbf{g} is a solution to (2) and \mathbf{r} is position in the x, y plane.

We are reporting here the observation of diffraction patterns from higher-order gratings that result from nonlinear interaction between these primary laser-induced gratings. Suppose that two such primary gratings with wave vectors \mathbf{g}_a and \mathbf{g}_b are present, and that the surface profile has some nonlinear dependence on these primary gratings of the form $h(\mathbf{r}) \approx [\sin(k_a \cdot \mathbf{r}) - \sin(k_b \cdot \mathbf{r})]^2$, where both \mathbf{g}_a and \mathbf{g}_b are separate solutions to (2). One would not be surprised to find such a nonlinear dependence when a new set of ripples is written across a previously existing set of any significant depth. The surface profile will then contain higher-order spatial frequency components with total grating wave vectors given by sums of the form

$$\mathbf{g}_T = \mathbf{g}_a + \mathbf{g}_b + \dots \quad (6)$$

where $\mathbf{g}_a, \mathbf{g}_b$, etc., are different primary solutions of the laser-induced grating equation (2). These "product" gratings might result from a nonlinear response of the surface when for example a weak grating with wave vector \mathbf{g}_a begins to grow on a surface which already

possesses a stronger pre-existing grating of wave vector \mathbf{g}_b .

Among the distinct types of such nonlinear grating behavior on germanium, we observe two of special interest having either hexagonal or rectangular symmetry.

2.1. Hexagonal Symmetry Patterns

For normal incidence of the writing beam and a wide variety of laser polarizations ranging from elliptical to circular, the diffraction patterns we observe have the distinct six-fold azimuthal symmetry illustrated in Fig. 1a. The various arcs in each branch can then be interpreted as arising from a combination of one or more discrete grating \mathbf{g} -vectors lying along the six-fold axes of symmetry, plus an additional grating wave vector \mathbf{g}_0 which rotates around the entire circular locus given by (2) with $\sin\theta = 0$.

That is, all of these arcs can be interpreted as diffraction patterns given by gratings with the total grating wave vector

$$\mathbf{g}_T = m \cos(l\pi/3)x + m \sin(l\pi/3)y + \mathbf{g}_0, \quad (7)$$

where x and y are unit vectors in the surface plane; m is an integer ≥ 0 ; l is an integer ranging from 0 through 5; and \mathbf{g}_0 rotates in a unit circle in the x, y plane. Figure 3 shows the expected diffraction pattern produced by this formula for various values of m . This azimuthal symmetry variation does not seem to be associated with anything in the experimental optics, and must presumably come from the similar underlying symmetry of the $\langle 111 \rangle$ germanium surface.

2.2. Rectangular Symmetry Patterns

When the writing beam strikes the surface at oblique incidence, the observed higher-order grating patterns become considerably more complex, but the observed patterns generally reflect an overall rectangular rather than hexagonal surface symmetry.

To analyze this, let us call the two primary solutions associated with the $\pm \sin\theta$ terms in (2) \mathbf{g}_+ and \mathbf{g}_- . The triple patterns for off-normal incidence are then generally dominated by three essentially linear patterns running parallel or perpendicular to the x and y axes. These dominant ripple patterns are the large-period and small-period ripples extending perpendicular to the x axis, with wave vectors $\mathbf{g}_{+1} = l - \sin\theta$ and $\mathbf{g}_{-1} = l + \sin\theta$, and periods $\lambda_+ \equiv \lambda(l - \sin\theta)$ and $\lambda_- \equiv \lambda(l + \sin\theta)$, respectively; plus the perpendicular ripples with wave vector $\mathbf{g}_{\perp} = \cos\theta$ and spacing $\lambda_{\perp} \equiv \lambda \cos\theta$. (These perpendicular ripples correspond to the intersection of the two circles along the y -axis.)

Straight-line ripples corresponding to these three general types are the most common first-order fringes in both separate and overlapping regions of the illuminated spots. The relative dominance of the three types of ripples is discussed below.

The nonlinear ripples we observe can then be explained in general as combinations of one or more of these three basic ripple types, plus possibly some component of the general intersecting circles given by (2). That is, we can always write the total diffraction wave vector \mathbf{g}_T in the general form

$$\mathbf{g}_T = m_+ \mathbf{g}_+, x + m_- \mathbf{g}_-, x + m_+ \mathbf{g}_+, y - M_+ \mathbf{g}_+ - M_- \mathbf{g}_-, \quad (8)$$

where the m 's and M 's are all integers, and \mathbf{g}_+ and \mathbf{g}_- are solutions in the x, y plane as given by (2). All the rectangular patterns we have seen can be fit by this expression.

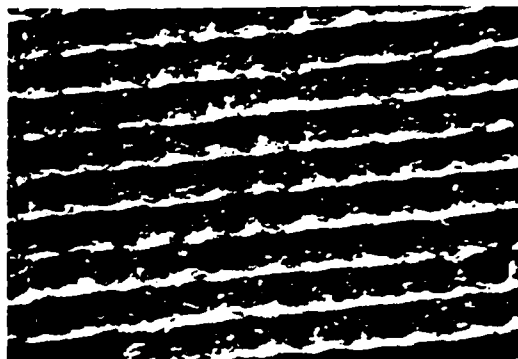
2.3. Surface Photographs

Figure 4 illustrates a few examples from many we have observed, showing the kinds of surface profiles that go with both the rectangular and hexagonal symmetry diffraction patterns. Note that on normally excited samples local regions of the same sample may illustrate both distinctly hexagonal and distinctly square (since $\theta = 0^\circ$) surface morphology. It can be difficult to distinguish this in diffraction patterns, however, since the probe spot usually illuminates both types of region simultaneously, and the purely square portion is lost in the more dominant hexagonal diffraction patterns.

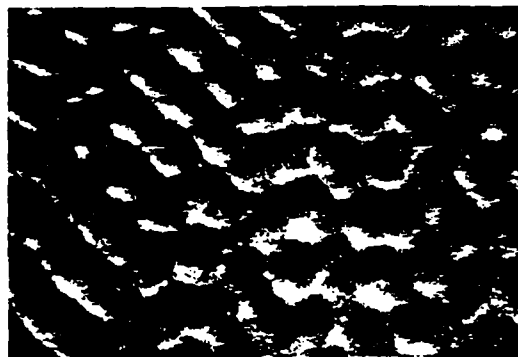
3. Discussion

Both the diffraction patterns and the surface profiles are in general complex and varied functions of the illumination conditions (angle of incidence, polarization, intensity, and number of shots). We can only make the following tentative generalizations from our experiments:

- 1) For lower writing intensities (less than 100 mJ/cm^2) we generally see only the primary diffraction patterns developing even after a sizeable number of shots.
- 2) At higher writing intensities (greater than or on order of 200 mJ/cm^2) we see first order rings after a very few shots; and then the complex higher-order structures developing as the number of shots increases further.
- 3) For higher writing intensities, the patterns begin to degrade as the number of shots becomes still larger, with the regular patterns degrading into more or less random speckle patterns.
- 4) At high writing intensities with linear or only slightly elliptical polarization we generally see first the



a



b



c

Fig. 4 (a) Square surface pattern obtained after illumination with almost linearly polarized light at normal incidence. The incident electric field is vertical (20 kV , $\times 10,000$). (b) Hexagonal surface pattern obtained after illumination with circularly polarized light at normal incidence (20 kV , $\times 10,400$). (c) The depth of the corrugations can become comparable to the excitation wavelength (20 kV , $\times 18,800$).

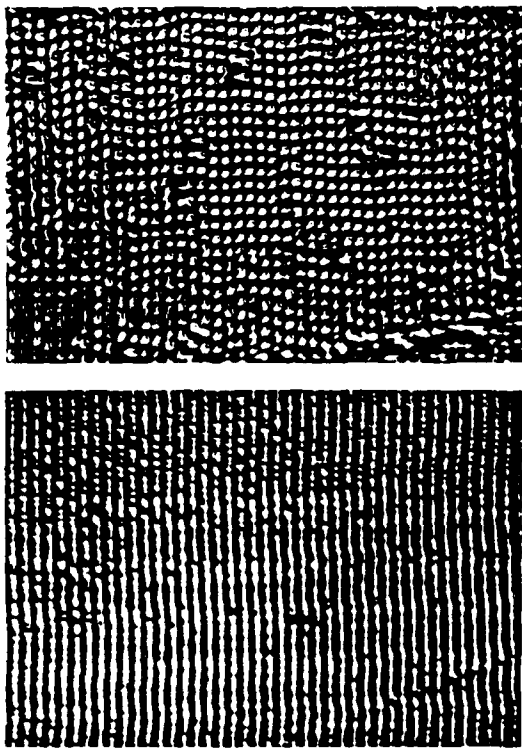


Fig. 5. Development of square patterns after repetitive illumination with high intensity pulses

development of linear ripples with grating wave vector parallel to the E field. These then develop into deeper ripples with the same wave vector. Perpendicular ripples then begin to occur and nonlinear interactions then produce a generally rectangular or square pattern (Fig. 5).

5) Probing with a small probe spot in different regions of any one illuminated spots can yield significantly different illumination patterns over the "skeleton"

given by the above analysis, indicating that the ripple patterns are not entirely uniform within the writing spot. This is particularly noticeable for circular polarization at non-normal incidence, where different regions of the illuminated spot contain significantly different ripple patterns.

6) As a rule, the g_{\perp} ripples almost always display a very high degree of linearity (very small angular spread) as contrasted with the somewhat more irregular and angularly dispersed g_{\parallel} and g_{\perp} ripples.

7) For non-normal writing beams between $\theta=0^\circ$ and $\theta \approx 40^\circ$ the large spacing g_{\perp} ripples are dominant while the g_{\parallel} and g_{\perp} ripples are much fainter. For $\theta > 40^\circ$ the g_{\perp} ripples tend to dominate although all of the different patterns are present in the diffraction patterns.

8) We do not seem to see any qualitative difference between the results obtained with multiple illumination with 80 nsec mode locked and Q-switched pulse trains or multiple single-pulse-selected subnanosecond pulses at 1.06 μm .

Acknowledgements. The technical assistance of C. Barker, R. Koch, and C. Zercher is gratefully acknowledged. This research was supported by the Air Force Office of Scientific Research, and the Joint Services Electronics Program at Stanford.

References

1. M. Birnbaum, *J. Appl. Phys.* **36**, 3688 (1965)
2. M. Bertolotti, P. Mariotti, D. Sette, L. Stagni, G. Vitali, *Radial. Eff. I.* 161 (1969)
3. H. M. Van Driel, J. E. Sipe, Jeff F. Young, *Phys. Rev. Lett.* **49**, 1955-1958 (Dec. 1982)
4. J. E. Sipe, Jeff F. Young, J. S. Preston, H. M. Van Driel, *Phys. Rev. B* **27**, 1141-1154 (Jan. 1983)
5. Jeff F. Young, J. S. Preston, H. M. Van Driel, J. E. Sipe, *Phys. Rev. B* **27**, 1155-1172 (Jan. 1983)
6. P. M. Fauchet, A. E. Siegman, *Appl. Phys. Lett.* **40**, 324-326 (May 1982)
7. Zhou Guosheng, P. M. Fauchet, A. E. Siegman, *Phys. Rev. B* **26**, 5366-5381 (Nov. 1982)
8. D. Haneman, R. J. Nemanich, *Solid State Commun.* **43**, 203 (1982)

Evidence for a dense electron-hole plasma close to the melting phase transition in silicon

P. M. Fauchet and A. E. Siegman

Edward L. Ginzton Laboratory, Stanford University, Stanford, California 94305

(Received 10 February 1983; accepted for publication 19 September 1983)

We have studied both theoretically and experimentally the dynamics of laser-induced electron-hole plasmas created at the surface of silicon using the strong synergy observed during simultaneous illumination by two picosecond pulses of different wavelengths. In a range of intensities up to those capable of producing a phase transition, we find good agreement between the results of our experiments and the predictions of a conventional model for pulsed laser heating.

PACS numbers: 71.35. + z, 72.30. + q, 64.70.Dv, 79.20.Ds

Recently there has been considerable interest in the physics of pulsed laser annealing and laser-induced phase transitions in solids, including some controversy concerning the mechanism of pulsed laser annealing itself. Most researchers have held that energy transfer from an optically excited electron-hole plasma to the lattice takes place in picoseconds, creating as a result a molten layer at the surface of the sample.¹ Other researchers, however, have proposed that this energy transfer could be considerably slower, in which case there would be a more complicated form of phase transition.²

Picosecond time-resolved experiments³⁻⁵ are capable of testing these hypotheses. Such experiments have indicated for example that when the intensity of a 532-nm excitation beam applied to a Si surface is raised above some threshold, melting indeed appears to occur in a matter of picoseconds, as evidenced by an abrupt jump in the reflectivity of a 1.06- μm probe beam.^{4,5} For excitation pulses just below the melting threshold the reflectivity drops slightly, indicating the presence of a dense electron-hole plasma at the surface. It is difficult, however, to study this plasma in detail for densities below $\sim 10^{21} \text{ cm}^{-3}$, because this density only slightly modifies the reflectivity of the probe beam.⁶

We introduce in this letter a novel technique to study in more detail the plasma close to but below the melting phase transition and also to test the validity of the thermal model describing semiconductor heating and annealing with ultra-short pulses. In our experiments, either of two Nd:yttrium aluminum garnet (YAG) lasers generates 30 to 100 ps pulses at 1.06 μm and 532 nm. A visible pulse at 532 nm with intensity below melting threshold is then used to "prepare" the sample, i.e., to create a dense electron-hole plasma at the surface, while still only slightly increasing the lattice temperature. The intensity of an infrared pulse at 1.06 μm , which is delayed with respect to the visible pulse by variable increments up to plus or minus several nanoseconds, is then adjusted to just melt the surface, as revealed by postmortem examination using a microscope.

The absorption of 1.06- μm radiation in silicon occurs predominantly via free-carrier absorption, and therefore measurements of melting threshold using 1.06- μm pulses alone are very sensitive to surface preparation and doping level. In our experiment, however, the initial free-carrier

concentration is set by the 532-nm pulse, so that we can control the free-carrier absorption for the IR pulse. As the IR pulse delay is increased, the carrier density decreases under the combined action of recombination and diffusion, and the IR intensity required to melt thus increases. On the other hand, when the IR pulse precedes the visible pulse, little or no effect is expected, since no plasma is present. We thus have a method for probing the dynamics of electron-hole plasmas in semiconductors at densities below those obtained at melting threshold, a region where only small reflectivity changes are observed. (Our method must be distinguished from the earlier two-pulse work of Auston *et al.*,⁷ in which an initial 532-nm pulse melted the Si surface, and the addition of a 1.06- μm pulse prolonged the melt duration.)

To quantify these predictions, we have used a computer model similar to that of Lietola and Gibbons,⁸ in which we solve numerically a set of three coupled partial differential equations describing the spatial and temporal evolution of the carrier density and the electronic and lattice temperatures in silicon under laser illumination. We have included the temperature dependences of all parameters (e.g., absorption coefficient, band gap, etc.) but have neglected diffusion during illumination by the picosecond pulses. We find excellent agreement between the predictions of our modified code and the results of Ref. 9.

In Fig. 1 we show the evolution of the lattice temperature predicted by our code for a crystalline Si surface under simultaneous illumination by two rectangular 100-ps pulses at 532 nm and 1.06 μm . As the 532-nm intensity is increased a denser electron-hole plasma is created, so that under the action of free-carrier absorption at 1.06 μm , the final temperature increases more rapidly, and the melting point is reached at earlier times during the pulse. The thermalization time of the hot carriers in this model was chosen equal to 1 ps, a reasonable assumption.¹⁰ These predictions are rather insensitive to the exact temperature variation of the band gap and the absorption coefficient, but are very sensitive to the value of the free-carrier absorption cross section at 1.06 μm , $\sigma_0 = 5.1 \times 10^{-18} (T/300) \text{ cm}^2$ (Ref. 10).

The contours in Fig. 2 then indicate the combined pulse intensities at 532 nm and 1.06 μm that are required to just reach melting threshold on a *c*-Si surface for cases where the IR pulse arrives before, coincident with, or after the visible

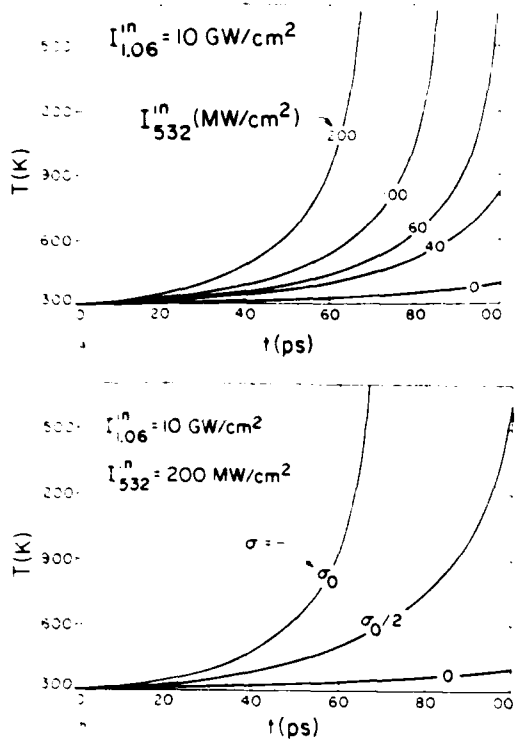


FIG. 1. Calculated time evolution of c-Si surface temperature during simultaneous illumination at 1.06 μm and 532 nm. The intensities are measured inside the material. (a) Different pulse intensities at 532 nm. (b) different free-carrier absorption cross sections.

pulse. The synergistic effect of the visible pulse on the IR pulse absorption for coincident pulses (i.e., $\tau_d = 0$) is strongly apparent. For example, at a fixed fluence $F_{532} = 0.1 \text{ J/cm}^2$, the amount of IR energy needed to reach melting decreases rather suddenly by a factor of 7, from 1.8 to 0.25 J/cm^2 , for a 1.06- μm pulse arriving coincident with rather than slightly before the 532-nm pulse. This effect is very large when compared to the $\sim 15\%$ drop in IR reflectivity observed in Ref. 5 during an excite-and-probe experiment with similar excitation energy. Without free-carrier absorption or other synergistic effects, the curve at zero delay becomes essentially a straight line between the intersection points on the two axes. Also of interest is the rather rapid increase in 1.06- μm fluence needed to obtain melting when the IR pulse arrives after the 532-nm pulse, and the increase of this effect at higher visible energies. The latter is due in large part to the faster recombination rate for the denser electron-hole plasma at higher visible intensities.

We have performed a series of such two-pulse melting experiments to demonstrate this type of delay-dependent synergism on various types of Si and GaAs samples. In Fig. 3, we show for example data of this type taken on ion-implanted (100) Si (10^{15} cm^{-2} As⁺ @ 100 keV) for various IR pulse delays relative to the 532-nm pulse. We shall present in a later paper more complete results obtained with GaAs and different Si samples. We merely note here that the thresholds may differ greatly according to the type of sample, but that some synergy is always present.

The synergistic effect predicted for c-Si in Figs. 1 and 2 is clearly also observed in the ion-implanted Si results shown in Fig. 3. Computer simulations such as in Figs. 1 and 2 were also carried out for the ion-implanted case, taking into account the highly damaged nature of the surface layer. There are uncertainties in some of the parameters for such ion-implanted layers, but in order to reproduce the experimentally observed synergy, it was always necessary to include a large free-carrier absorption cross section. A good fit to the experimental results was obtained for the following parameters (at room temperature): $\alpha(532) = 2 \times 10^4 \text{ cm}^{-1}$, $\alpha(1.06) = 10^3 \text{ cm}^{-1}$, $\sigma = 2 \times \sigma_0$, $\tau_{\text{recomb}} = 10 \text{ ps}$, $\tau_{\text{lat}} = 0.1 \text{ ps}$, with the latent heat of fusion included. The peak plasma density reaches $\sim 10^{21} \text{ cm}^{-3}$ for large visible energy fluence.

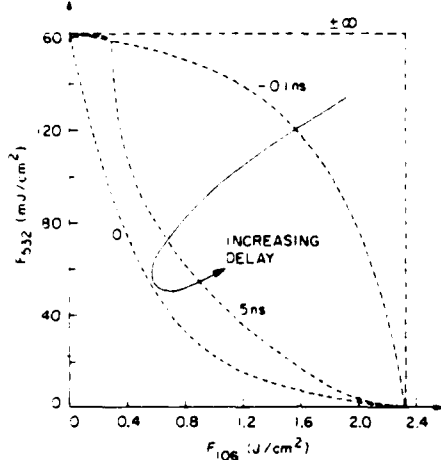


FIG. 2. Calculated threshold fluences required to melt a c-Si surface by simultaneous or separate illumination by two 100-ps square pulses at 532 nm and 1.06 μm . Here, $\sigma = \sigma_0$.

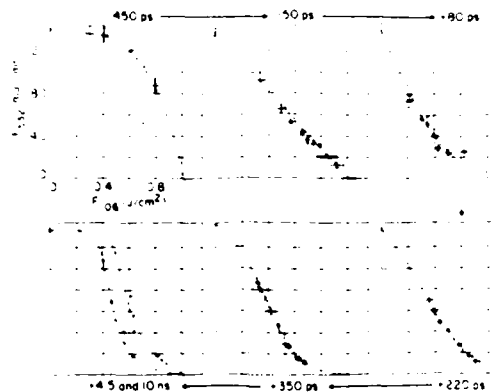


FIG. 3. Observed pulse-energy melting thresholds on As-implanted Si for joint illumination by ~ 40 ps pulses at 532 nm and 1.06 μm for various relative delays of the IR pulse as indicated in the figures. The broken lines are guides for the eye except in the top right figure where it represents the computer fit with parameters given in the text.

If free-carrier absorption is not included, the predicted results in ion-implanted silicon lie on a nearly straight line joining the thresholds for single beam melting at 532 nm and 1.06 μm , respectively. Such a straight line is what Newstein *et al.*¹¹ obtained after simultaneous illumination of arsenic-implanted Si samples with 60-ns pulses at 532 nm and 1.06 μm . With nanosecond pulses, the plasma density remains low at all times, and the lack of significant free-carrier absorption precludes any synergistic effect.

From the results in Fig. 3, we deduce that the synergistic effect of the electron-hole plasma is predominant when the IR pulse arrives between about one pulse width before to about ~ 300 ps after the visible pulse. The subsequent increase of the IR intensity required to melt reflects both the decay of the EHP and also the much slower heat diffusion that takes place on a nanosecond time scale. At large 532-nm fluences, the combined effect of diffusion and recombination is more pronounced, in qualitative agreement with the predictions for *c*-Si. We are presently working on a detailed fit of these and other experimental curves.

In conclusion, we have shown that the Lietoila-Gibbons model for highly excited semiconductors appears to be in agreement with our two-pulse experiments over a large range of excitation energies. The technique we have used, involving melting with two pulses at very different wavelengths, is useful where conventional excite and reflectivity-probe techniques are more difficult, i.e., for intensities one order of magnitude or so below onset of phase transition. The rather slow decay of the electron-hole plasma in Si compared to that obtained by others⁴ is a consequence of both

lower 532-nm excitation energies and the sensitivity of our method to lower electron-hole plasma densities. This technique may also be of technological importance, especially when applied to simultaneous illumination by Nd YAG and carbon dioxide lasers.

This research was supported by the Air Force Office of Scientific Research and the Joint Services Electronics Program at Stanford University. We thank Professor Gibbons and his group for useful conversations. The technical assistance of D. Ress is appreciated.

A. E. Bell, *RCA Rev.* **40**, 294 (1979); D. H. Auston, C. M. Surko, T. N. C. Venkatesan, R. E. Slusher, and J. A. Golovchenko, *Appl. Phys. Lett.* **33**, 437 (1978);
 J. A. Van Vechten, R. Tsu, and F. W. Saris, *Phys. Lett.* **A 74**, 422 (1979);
 H. W. Lo and A. Compaan, *Phys. Rev. Lett.* **44**, 1604 (1980);
 K. Gamo, K. Murakami, M. Kawabe, S. Nambu, and Y. Aoyagi, in *Laser and Electron-Beam Solid Interactions and Materials Processing*, edited by J. F. Gibbons, L. D. Hess, and T. W. Sigmon (North-Holland, New York, 1981), p. 97;
 J. M. Liu, H. Kurz, and N. Bloembergen, *Appl. Phys. Lett.* **41**, 643 (1982) and MRS Symposium A, Boston, November 1982;
 D. von der Linde and N. Fabricius, *Appl. Phys. Lett.* **41**, 991 (1982);
 This limit is somewhat lowered for experiments performed on SOS samples, where interference effects play a role (see Ref. 4);
 D. H. Auston, J. A. Golovchenko, and T. N. C. Venkatesan, *Appl. Phys. Lett.* **34**, 558 (1979);
 A. Lietoila and J. F. Gibbons, *Appl. Phys. Lett.* **40**, 624 (1982); *J. Appl. Phys.* **53**, 3207 (1982);
 J. M. Liu, R. Yen, H. Kurz, and N. Bloembergen, *Appl. Phys. Lett.* **39**, 755 (1981);
 K. G. Svartesson and N. G. Nilsson, *J. Phys. C* **12**, 3837 (1979);
 M. C. Newstein, K. C. Liu, and R. Kaplan, in *Laser and Electron Beam Processing of Materials*, edited by C. W. White and P. S. Peercy (Academic, New York, 1980), p. 303.

UNCLASSIFIED

SECURITY CLASSIFICATION ON THIS PAGE

REPORT DOCUMENTATION PAGE

a. REPORT SECURITY CLASSIFICATION ON Unclassified	b. RESTRICTIVE MARKINGS
c. SECURITY CLASSIFICATION AUTHOR	
d. DECLASSIFICATION/DOWNGRADING SCHEDULE	
e. PERFORMING ORGANIZATION REPORT NUMBER(S) GL 4287	
fa. NAME OF PERFORMING ORGANIZATION Edward L. Ginzton Laboratory Stanford University	fb. OFFICE SYMBOL Code: 2E254
fc. ADDRESS (City, State and Zip Code) Stanford University Stanford, California 94305	fd. ADDRESS (City, State and Zip Code) 800 North Quincy Street Arlington VA 22217-5000
fe. FUNDING SPONSORING ORGANIZATION Joint Services Electronics Program	ff. OFFICE SYMBOL
fg. ADDRESS (City, State and Zip Code) N.J. Davis (414) Head, Electronics Division Office of Naval Research 800 North Quincy Street Arlington, VA 22217-5000	fh. ADDRESS (City, State and Zip Code)
i. TITLE REPORT APPENDIX: ANNUAL PROGRESS REPORT, 1 APRIL 1986 THROUGH 31 MARCH 1987	

2. PERSONAL AUTHORS Bloom, C.M., Byer, R.L., Kino, G.S., Quate, C.F., Shaw, M.L., Siegman, A.E., Khuri-Yakub, B.T., Au, J., B.A. and others			
3a. TYPE OF REPORT Annual Progress Report	3b. TIME COVERED From: 1 APR 86 To: 31 MAR 87	3c. DATE OF REPORT (Yr Mo Day) 87 10/15	3d. PAGE COUNT e6
6. SUPPLEMENTARY NOTATION The views, opinions and/or findings contained in this report are those of the authors and should not be construed as an official Dept of Defense position, policy or decision unless otherwise documented.			

7. COSAT CODES	18. SUBJECT TERMS (Continue on reverse if necessary & identify by block no.)
FEED GROUP	SUB GROUP

9. ABSTRACT (Continue on reverse if necessary & identify by block no.)
--

THIS IS A BOUND COLLECTION OF PUBLICATIONS CITING THE SPONSORSHIP OF JSEP CONTRACT NO0014-84-K-0327: Atomic Resolution with the Atomic Force Microscope; Optical Detection of Charge Modulation in Silicon Integrated Circuits Using a Laser Diode Probe; Observation of Dislocations in Graphite by Scanning Tunneling Microscopy; Atomic Resolution Imaging of a Nonconductor by Atomic Force Microscopy; A Noninvasive Optical Probe for Detecting Electrical Signals in Silicon Integrated Circuits; A Real-Time Confocal Scanning Optical Microscope; A Switchable Fiber-Optic Tap Using the Acousto-Optic Bragg Interaction; All-Fiber-optic Gyroscopes; Deposition of Piezoelectric Films on Single-Mode Fibers and Applications to Fiber Modulators; Switchable Fiber-Optic Tap Using Acoustic Transducers Deposited Upon the Fiber Surface; Optical Sensors for Range and Depth Measurements; Images of a Lipid Bilayer at Molecular Resolution by Scanning Tunneling Microscopy; Real Time Digital Signals in a Silicon Bipolar Junction Transistor Using a Noninvasive Optical Probe; Anomalous Distance Dependence in Scanning Tunneling Microscopy; Monolithic Nd:YAG Fiber Laser; Optical Interactions with Solids; Switchable Fiber-Optic Tap Using the Acousto-Optic Bragg Interaction; Noninvasive Sheet Charge Density Probe for Integrated Silicon Devices; Deposition of Oriented Zinc Oxide on an Optical Fiber; Low Loss Single-Crystal Sapphire Optical Fibers"; Electrooptic Sampling in GaAs Integrated Circuits; A Guided Wave Monolithic Resonator Ruby Fiber

20. DISTRIBUTION/AVAILABILITY OF ABSTRACT UNCLASSIFIED/UNLIMITED [x] SAME AS RPT [] OTIC USERS []	21. ABSTRACT SECURITY CLASSIFICATION Unclassified
22a. NAME OF RESPONSIBLE INDIVIDUAL S.E. Harris, Director, Edward L. Ginzton Laboratory	22b. TELEPHONE NUMBER (415) 723-0224
22c. OFFICE SYMBOL UNCLASSIFIED	

DD FORM 1473, 84 MAR 83 APR edition may be used until exhausted. All other editions obsolete.

UNCASSIFIED

SECURITY CLASSIFICATION OF THIS PAGE

REPORT DOCUMENTATION PAGE (CONTINUATION)

E. SUBJECT TERMS (Continued)

F. ABSTRACT (Continued)

Laser; Tunneling Microscopy from 300 to 42k; Characterization of Proton Exchanged Waveguides in MgO: Nd₃; High Speed, High Resolution Fiber Diameter Measurement System; Picosecond Electro-Optic Sampling in Gallium Arsenide; 2 GHz Acoustic Transmission through a Hertzian Contact; Laser Heated Meltature Pedestal Growth Apparatus for Single Crystal Optical Fibers; Compression of Pulses from a Continuum-wave Mode-locked Nd:YAG Laser; Direct Electrooptic Sampling of Transmission Line Signals Propagating on a GaAs Substrate; Compression of Mode-locked Nd:YAG Pulses to 18 ps; Laser Assisted Growth of Optical Quality Crystal Fibers; Acoustic Wave Reflection from Ferroelastic Domain Walls; Observations of higher-order laser induced surface ripples on ^{75}Se germanium; Evidence for a dense electron-hole plasma close to the melting phase transition in s - con;

ATE
MED
8